

AD-A210 145

COORDINATED SCIENCE LABORATORY
College of Engineering

ELECTROMAGNETIC SCATTERING FROM A STRUCTURED SLAB COMPRISED OF PERIODICALLY PLACED RESISTIVE CARDS

Roy E. Jorgenson
Raj Mittra

SDTIC
ELECTE
JUL 05 1989

cb H

UNIVERSITY OF ILLINOIS AT URBANA-CHAMPAIGN

Approved for Public Release. Distribution Unlimited.

8 0 0 0 0 4 8

REPORT DOCUMENTATION PAGE

Form Approved
OMB No. 0704-0188

1a. REPORT SECURITY CLASSIFICATION Unclassified		1b. RESTRICTIVE MARKINGS None	
2a. SECURITY CLASSIFICATION AUTHORITY		3. DISTRIBUTION / AVAILABILITY OF REPORT Approved for public release; distribution unlimited	
2b. DECLASSIFICATION / DOWNGRADING SCHEDULE			
4. PERFORMING ORGANIZATION REPORT NUMBER(S) UILLU-ENG-89-2218		5. MONITORING ORGANIZATION REPORT NUMBER(S)	
6a. NAME OF PERFORMING ORGANIZATION Coordinated Science Lab University of Illinois	6b. OFFICE SYMBOL (If applicable) N/A	7a. NAME OF MONITORING ORGANIZATION Office of Naval Research	
6c. ADDRESS (City, State, and ZIP Code) 1101 W. Springfield Ave. Urbana, IL 61801		7b. ADDRESS (City, State, and ZIP Code) Arlington, VA 22217	
8a. NAME OF FUNDING / SPONSORING ORGANIZATION Joint Services Electronics Program	8b. OFFICE SYMBOL (If applicable)	9. PROCUREMENT INSTRUMENT IDENTIFICATION NUMBER N00014-84-C-0149	
8c. ADDRESS (City, State, and ZIP Code) Arlington, VA 22217		10. SOURCE OF FUNDING NUMBERS	
		PROGRAM ELEMENT NO.	PROJECT NO.
		TASK NO.	WORK UNIT ACCESSION NO.
11. TITLE (Include Security Classification) Electromagnetic Scattering from a Structured Slab Comprised of Periodically Placed Resistive Cards			
12. PERSONAL AUTHOR(S) Jorgenson, R. E. and Mittra, R.			
13a. TYPE OF REPORT Technical	13b. TIME COVERED FROM _____ TO _____	14. DATE OF REPORT (Year, Month, Day) 1989 May	15. PAGE COUNT 270
16. SUPPLEMENTARY NOTATION			
17. COSATI CODES		18. SUBJECT TERMS (Continue on reverse if necessary and identify by block number)	
FIELD	GROUP	SUB-GROUP	
		electromagnetic scattering, structured slab, Green's function	
19. ABSTRACT (Continue on reverse if necessary and identify by block number)			
<p>The structured slab, which is constructed by arranging cells composed of thin, lossy, dielectric cards on a one- or two-dimensional lattice, is an important material in the aerospace industry because of its high strength-to-weight ratio. Recently, the structured slab has also been used to reduce the radar cross section of various aircraft. It is important, therefore, to characterize how an electromagnetic wave scatters from this slab. The structured slabs discussed in this report are constructed by repeating lossy strips periodically in one dimension or lossy plates in two dimensions.</p> <p>An electric field integral equation is formulated which has as its unknown the electric current flowing in a single unit cell of the structure. The periodicity of the structure is accounted for by using an efficiently calculated periodic Green's function. The loss is modeled by the resistive boundary condition. The integral equation is solved by the method of moments using subdomain basis functions. The generalized scattering matrix is calculated and the propagating reflection coefficients are plotted as a function of frequency for various structures.</p>			
20. DISTRIBUTION / AVAILABILITY OF ABSTRACT <input checked="" type="checkbox"/> UNCLASSIFIED/UNLIMITED <input type="checkbox"/> SAME AS RPT. <input type="checkbox"/> DTIC USERS		21. ABSTRACT SECURITY CLASSIFICATION Unclassified	
22a. NAME OF RESPONSIBLE INDIVIDUAL		22b. TELEPHONE (Include Area Code)	22c. OFFICE SYMBOL

19. Abstract (continued)

The oblique scattering from one-dimensional arrays of strips is examined for various configurations of unit cells and various resistances. A depolarizing effect of the structure is found to be a function of incident angle and symmetry in the unit cell. The reflection from two-dimensional arrays of plates connected to form slabs of zigzag plates and honeycombs is also examined. The symmetry of the honeycomb unit cell minimizes the coupling between the TE and TM polarizations.

The structured slab is usually very thick in terms of wavelengths so that the incident electromagnetic energy can be absorbed effectively. To solve a thick structure in a straightforward manner requires too many unknowns; therefore, the final subject discussed in this thesis is how to extrapolate the scattering characteristics of a thick slab from the solution of a thin slab. Three methods are examined: cascading the generalized scattering matrix of a thin slab, which cannot account for currents flowing between the thin slabs; finding the modes in a lossy structure and mode matching, which is numerically intensive; using a few basis functions to model the interior current in a thick slab. The basis functions are constructed through the application of Prony's method.

NAVY

Approved For	<input checked="" type="checkbox"/>
Classification	SECRET
Authority	
Approved For	
Classification	
Authority	

A-1

**ELECTROMAGNETIC SCATTERING FROM A STRUCTURED SLAB
COMPRISED OF
PERIODICALLY PLACED RESISTIVE CARDS**

by

Roy E. Jorgenson and Raj Mittra
Electromagnetic communication Laboratory
University of Illinois
Urbana, Illinois

Abstract

The structured slab, which is constructed by arranging cells composed of thin, lossy, dielectric cards on a one- or two-dimensional lattice, is an important material in the aerospace industry because of its high strength-to-weight ratio. Recently, the structured slab has also been used to reduce the radar cross section of various aircraft. It is important, therefore, to characterize how an electromagnetic wave scatters from this slab. The structured slabs discussed in this report are constructed by repeating lossy strips periodically in one dimension or lossy plates in two dimensions.

An electric field integral equation is formulated which has as its unknown the electric current flowing in a single unit cell of the structure. The periodicity of the structure is accounted for by using an efficiently calculated periodic Green's function. The loss is modeled by the resistive boundary condition. The integral equation is solved by the method of moments using subdomain basis functions. The generalized scattering matrix is calculated and the propagating reflection coefficients are plotted as a function of frequency for various structures.

The oblique scattering from one-dimensional arrays of strips is examined for various configurations of unit cells and various resistances. A depolarizing effect of the structure is found to be a function of incident angle and symmetry in the unit cell. The reflection from two-dimensional arrays of plates connected to form slabs of zigzag plates and honeycombs is also examined. The symmetry of the honeycomb unit cell minimizes the coupling between the TE and TM polarizations.

The structured slab is usually very thick in terms of wavelengths so that the incident electromagnetic energy can be absorbed effectively. To solve a thick structure in a straightforward manner requires too many unknowns; therefore, the final subject discussed in this thesis is how to extrapolate the scattering characteristics of a thick slab from the solution of a thin slab. Three methods are examined: cascading the generalized scattering matrix of a thin slab, which cannot account for currents flowing between the thin slabs; finding the modes in a lossy structure and mode matching, which is numerically intensive; using a few basis functions to model the interior current in a thick slab. The basis functions are constructed through the application of Prony's method.

TABLE OF CONTENTS

	Page
1. INTRODUCTION	1
2. PRELIMINARY CONCEPTS	15
2.1 Introduction	15
2.2 One-dimensional Periodicity	16
2.2.1 Definitions of terms	16
2.2.2 Formulation of the periodic Green's function	20
2.2.3 Convergence characteristics of G_p	23
2.2.4 Smoothness of basis/test functions to help convergence	25
2.2.5 Acceleration of convergence	32
2.2.6 Numerical implementation of the spatial domain acceleration	39
2.3 Two-dimensional Periodicity	53
2.3.1 Definitions of terms	53
2.3.2 Formulation of G_p	59
2.3.3 Acceleration of convergence in spatial domain	63
2.3.4 Numerical implementation of the spatial domain acceleration	64
2.4 Conclusions for Convergence	67
2.5 The Resistive Boundary Condition	70
3. PERIODICITY IN ONE DIMENSION — PROBLEMS BASED ON STRIP ARRAYS	84
3.1 Introduction	84
3.2 Integral Equation Formulation	87

	Page
3.3 Results	98
3.4 Conclusions	110
4. PERIODICITY IN TWO DIMENSIONS -- PROBLEMS BASED ON PLATE ARRAYS	118
4.1 Introduction	118
4.2 Integral Equation Formulation	119
4.3 Results	137
4.4 Conclusions	157
5. THICK PERIODIC PROBLEMS	162
5.1 Introduction	162
5.2 Cascading the Generalized Scattering Matrix	163
5.2.1 Definition of the scattering matrix	163
5.2.2 Cascading procedure	167
5.2.3 Results of cascading	178
5.2.4 Continuity problems with the S matrix	184
5.3 The Modal Method	189
5.3.1 Introduction	189
5.3.2 Parallel-plate waveguide array	191
5.3.3 One-dimensional array of rectangular waveguides	203

5.4 Large Basis Functions	209
5.4.1 Introduction	209
5.4.2 Description of the method	211
5.4.3 Results	222
6. CONCLUSIONS	234
APPENDIX A. CODE VALIDATION	242
A.1 Introduction	242
A.2 Assumptions and Approximations	243
A.3 Validation	245
REFERENCES	261

1. INTRODUCTION

This thesis examines numerically how an electromagnetic plane wave interacts with an infinite, artificial dielectric slab. The slab is constructed by arranging unit cells, composed of thin, lossy, dielectric cards, on a one-dimensional or two-dimensional lattice. Some examples of the resulting structures, as shown in Figure 1.1, are honeycombs, corrugated surfaces, egg-crate-type structures and strip gratings. The size of the unit cell across the face of the slab is on the order of fractions of a wavelength, but the slab may be many wavelengths thick. Before going into the details of analysis, two topics will be discussed in order to show how these structures are used and why the interaction of an electromagnetic plane wave with these structures is of such importance.

In 1909, Victor Loughheed wrote the book "Vehicles of the Air" which documents the then state-of-the-art in aircraft design [1]. In the chapter on materials and construction he states:

The questions of structural materials and methods of construction are among the most vital of all that the aeronautical engineer has to face. Every matter of safety and success depends directly upon the quality and reliability of the materials of which the machines are built, and the ways in which these materials are put together....It is becoming more and more established that successful flying machines require the use of comparatively little metal...Not without considerable basis of fact it has been asserted that the flying machines of the future will be built in the carpenter shops of the future, for wood is by far the most utilized material in all successful fliers...Veneered, bent and built-up wooden structures are usually the strongest, because of the many opportunities they present of eliminating flaws, of crossing grains to prevent splitting and of building hollow members to combine the maximum of strength with the minimum of weight.

In the years that followed, the construction techniques using laminations and hollow supports fell out of favor, being replaced by welded steel and aluminum. Today, however, the principles stated three-quarters of a century ago are again valid except that

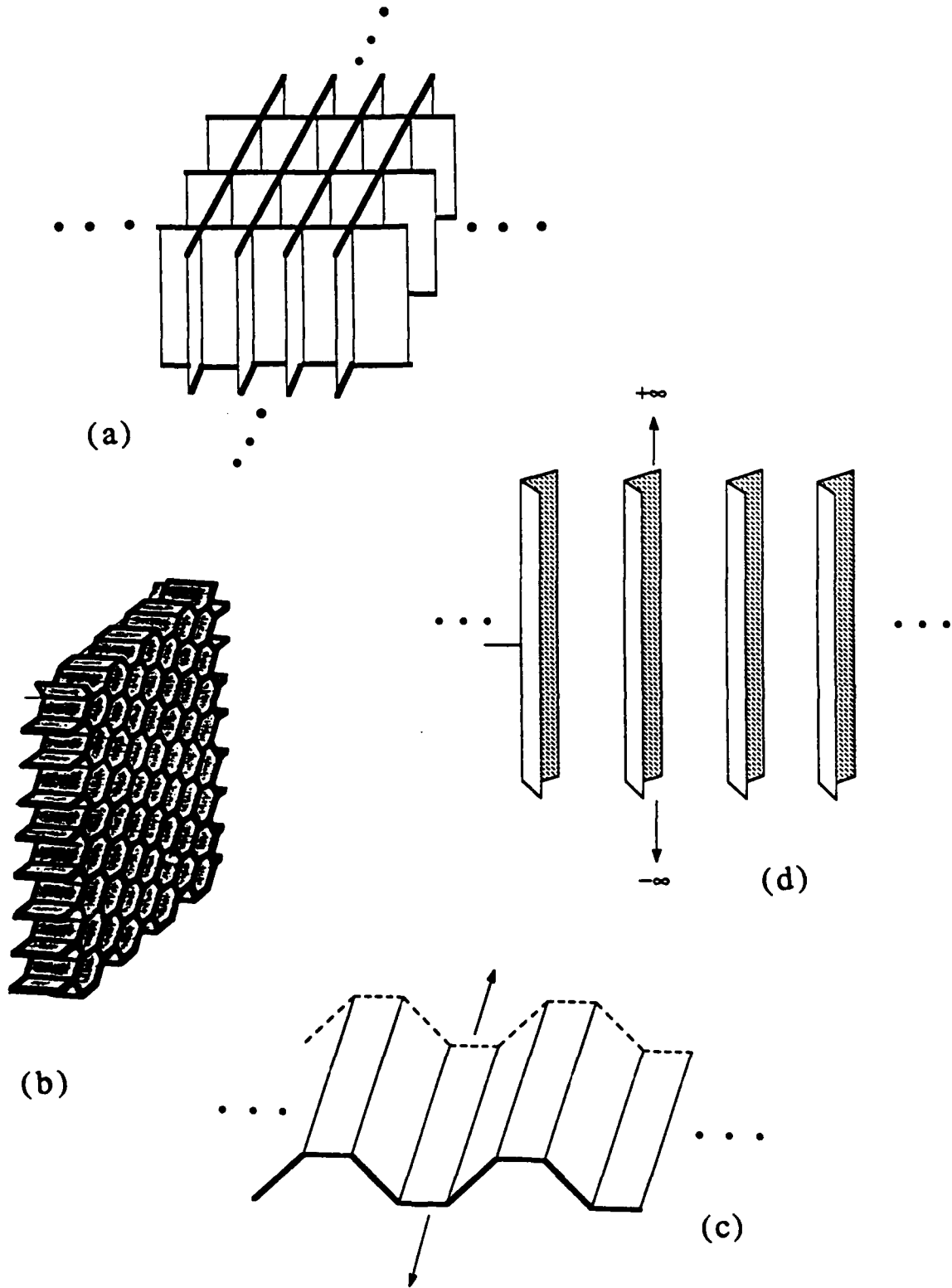


Figure 1.1 Examples of structured slab geometries. Plates are joined along a two-dimensional lattice to form the egg-crate structure (a) and the honeycomb (b). Strips are joined along a one-dimensional lattice to form a corrugated sheet (c) and a complex grating (d).

the naturally fibrous wood has been replaced with man-made materials that have a higher strength-to-weight ratio and whose properties may be controlled more consistently. The first widely publicized laboratory production of boron fibers was reported in 1959 by C.P. Talley of Texaco [2]. Graphite and Kevlar fiber production followed in the late 1960s. These fibers are laminated to make strong composite airplane parts such as ribs, spars and skin as was done with the natural material in 1910. The principle of using hollow beams in construction has been further exploited by decreasing the density of the supporting ribs and filling the volume between the ribs with honeycomb, which can be thought of as thin, hollow beams glued together. The honeycomb is bonded to the aircraft skin for structural integrity. The overall result is a lighter but stronger structure.

Initially, the honeycomb was considered to be an esoteric material. It was constructed by brazing thin, stainless steel strips individually to locate the elements; machining the slab to the contour of the finished part; placing the honeycomb between preformed inner and outer sheets of metal for stability and lightly brazing the finished product. The entire structure was then placed on a large graphite block, which was machined to the contour of the finished part and heated in an inert gas until the brazed joints were satisfactory. This process was very expensive and the resulting honeycomb cost over 1200 dollars per square foot. At that time, the honeycomb structure was only used for high-performance aircraft such as the supersonic Convair B-28 [3]. With the advent of composites and advances in manufacturing technology, the honeycomb became cheap to construct and shape for specific applications.

The honeycomb today is manufactured by two processes: expansion and corrugation as shown in Figure 1.2 [4]. In the expansion process, the sheets of material are fed into machines where continuous ribbons of adhesive are applied. The sheets are stacked layer

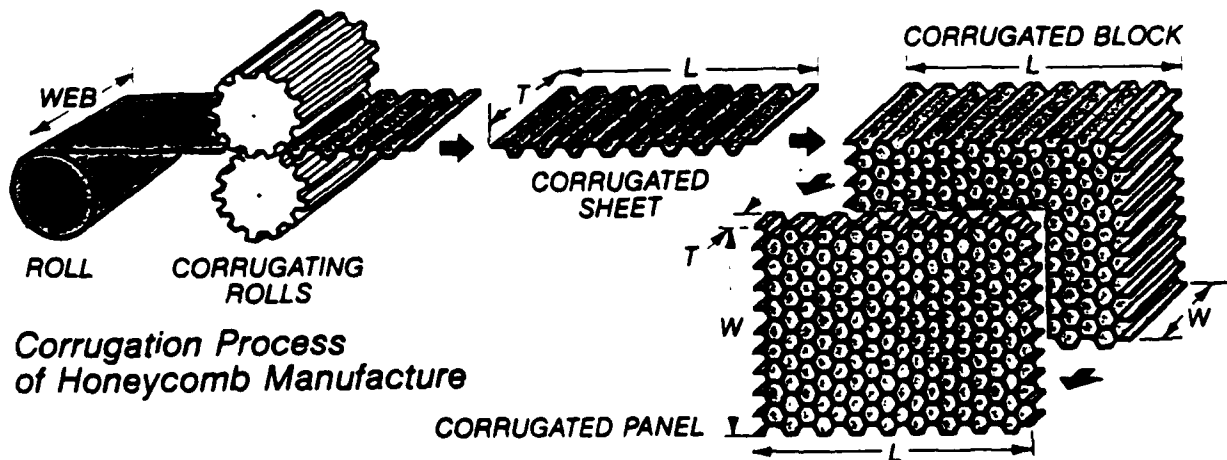
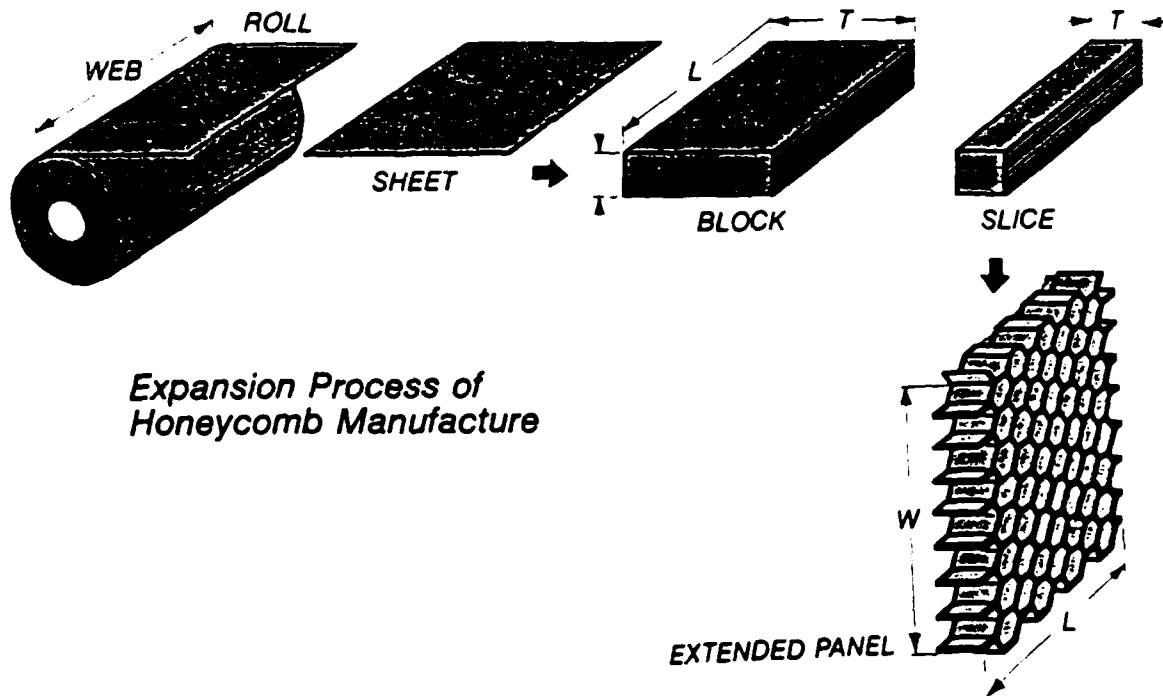


Figure 1.2 Manufacturing technology for honeycomb production. Both the expansion and corrugation processes are shown [4].

upon layer to form a block. The desired slab thickness is sliced off of the block and expanded into a honeycomb slab. Corrugation is used for constructing a honeycomb of higher density than that made by the expansion method. A sheet of material is fed through corrugating rollers to form a corrugated sheet, several of which are then bonded together to form a slab of honeycomb.

The honeycomb alone does not have an inordinate amount of strength or stiffness. To enhance these qualities, the honeycomb is bonded to two sheets of material which could be, for example, the skin of the airplane, to form a sandwich. The facings of the sandwich behave similarly to the flanges of an I beam by taking the bending loads--one in tension, the other in compression. The honeycomb core corresponds to the web of the I beam giving continuous support to the facings. The core resists the shear loads and increases the stiffness of the structure by spreading the facings apart. The honeycomb sandwich has the highest strength-to-weight ratio and highest stiffness-to-weight ratio of all slabs of the same material. For example, a metal honeycomb sandwich twice as thick as a solid metal laminate is seven times more rigid and 3.5 times as strong as the laminate for a 5% increase in weight [4].

The availability and structural qualities of the honeycomb sandwich cause it to be a primary construction material in the aerospace industry. Some applications are in radome construction for the AWACS radar surveillance plane or as supports for frequency selective surfaces (FSSs) on communication satellites. These applications exploit the lightness and strength of the composite honeycomb and the ability of the honeycomb to be heat formed and machined to close tolerances. The honeycomb can also be used in the construction of control surfaces and leading edges of wings in high performance aircraft due to its superior strength and stiffness-to-weight ratio [5]. Finally, the honeycomb is

being used in the construction of composite helicopter main rotor blades because the plastic nature of the materials permits molding of a precise aerodynamic shape, stiffness and mass distribution. The blade can be shaped to maximize performance and to move the blade's natural frequency in order to avoid resonance with the harmonics of the rotational speed. The high strength and high resistance to fatigue capability of the honeycomb result in blades with long service lives needing little maintenance [6].

When using composites as construction materials, the electromagnetic compatibility of the new materials with the surrounding environment must also be considered. When used in radomes or as supports for FSSs, the role of the honeycomb is obvious: it must interact with the electromagnetic wave as little as possible. The honeycomb is a strong candidate to fulfill this specification since most of its volume is free space and its walls are a Kevlar/Epoxy composite ($\epsilon_r = 3.29 - j 0.023$). In spite of this, it has been found experimentally, as shown in Figure 1.3 [7], that the honeycomb support does affect the characteristics of the FSS, for example; therefore, its electromagnetic behavior must be studied.

When airplanes were made of metal, the internal electronics were shielded from the effects of lightning and electromagnetic pulse. With an ever-increasing percentage of the aircraft being constructed of composites, the effect of pulsed waves on the aircraft becomes a concern [8],[9]. Although pulsed waves will not be considered in this thesis, this reaffirms the need for the study of electromagnetic interaction with classes of structures such as the honeycomb.

In the case of military aircraft, observability is a factor that arises where the interaction of the aircraft construction with electromagnetic waves is of crucial importance. It has long been an axiom of air combat that if an aircraft can complete an

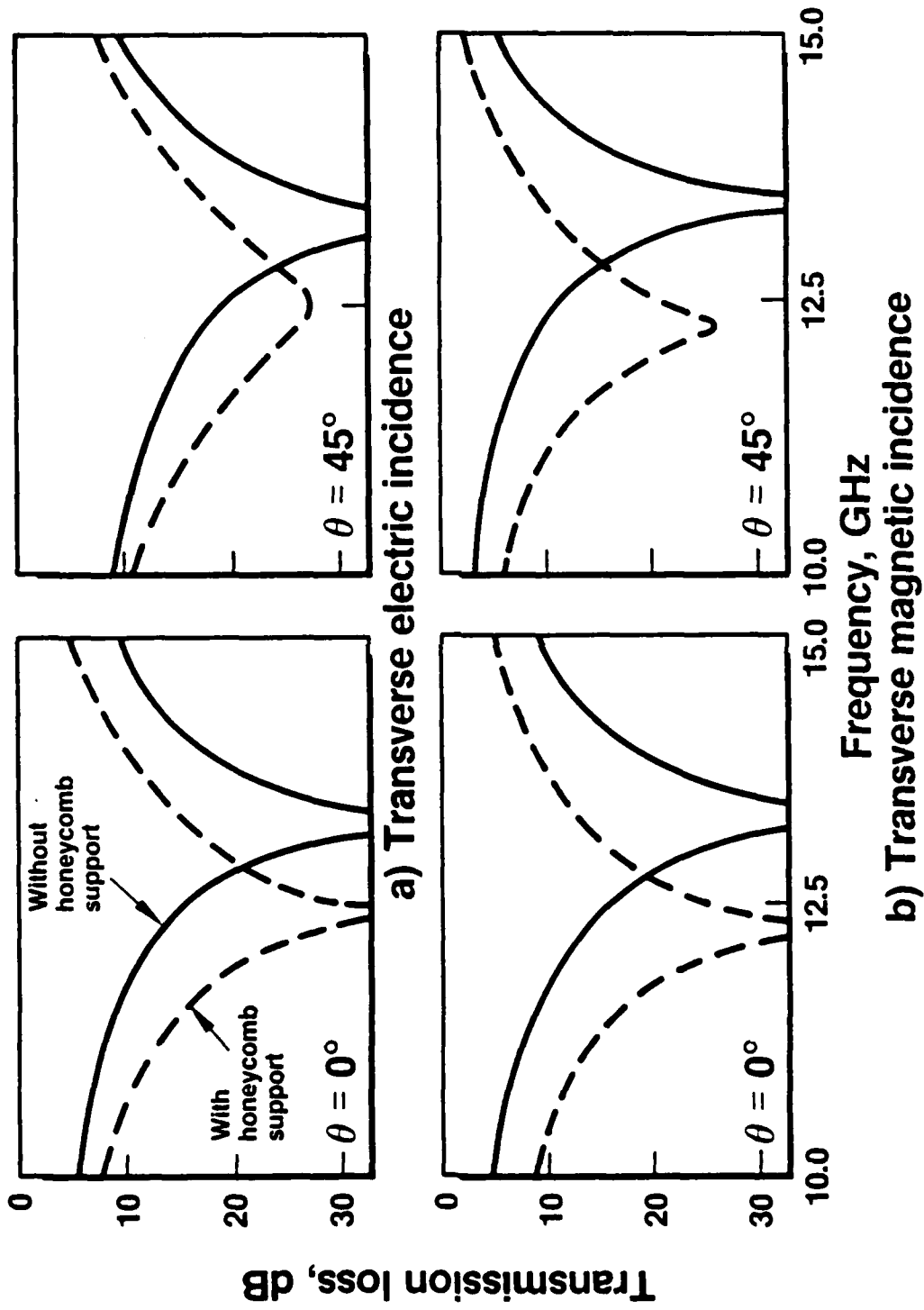


Figure 1.3 Measured transmission loss vs. frequency for an FSS with and without honeycomb backing [7].

attack without being observed, the chances for success are dramatically increased. In keeping with this concept, during the early years of air warfare, airplanes dove from the sun or hid in clouds prior to attacking. In 1917, the Axis Powers, building on the concept of invisibility, tested the Fokker E.1 fighter which had a wooden frame covered in heavy, clear cellophane. This effort was unsuccessful because the cellophane could not structurally handle the wing loading of air maneuvers or the outdoor environment [10]. Generally, however, the notion of reducing the observability of an aircraft was ignored since the main detector available--the eye--was hard to fool except by making the aircraft smaller.

In the 1930's, aircraft were able to fly higher and faster, out of range of the human senses. To counter this new capability, RADAR, an acronym for RADio Detection And Ranging, was developed to pierce through cloud cover and illuminate night operations. Unlike the human eye, however, radar could be fooled. Initially, strips of foil called chaff cut to the radar's resonant frequency were dropped ahead of an attacking air force giving a large radar return and providing a screen behind which the attackers could hide. Later, the radar signals themselves were received, modified and re-transmitted or simply saturated to fool the radar operators and decrease their effectiveness. This was the beginning of electronic warfare.

As always, every technique developed to decrease the effectiveness of radar was countered by a technique to increase its effectiveness. As a result, the electronic warfare equipment became increasingly sophisticated and expensive. Additionally, in the 1950's, because of the need for the higher-power but less-efficient jet engine, airplanes became larger and more detectable by radar. Therefore, even though the jets were faster than the propeller planes, they could be picked up farther away on radar and much of the

advantage of surprise was lost. In the mid-1950's, attention was finally turned to reducing the amount of radar power reflected by the aircraft, known as its radar cross section (RCS), without reducing its physical size. This was done for the reconnaissance aircraft designed to replace the U2—the SR-71. The RCS reduction was achieved by shaping the fuselage and wings, integrating the engines within the body and putting radar absorbing material (RAM) on the leading edges of the wings and the control surfaces [10].

In the years following the introduction of the SR-71, up to the present, RCS reduction concepts are being applied to more types of military aircraft to increase their chances of survivability. The goal is not necessarily to make the airplane totally invisible, but rather to lessen the visibility so that traditional procedures such as electronic counter measures and chaff have a greater chance of success. Unfortunately, the range of detection varies as the fourth root of the radar cross section; therefore, the RCS must be reduced significantly before any advantage can be realized. On the positive side, since the attention to RCS reduction is relatively recent, reductions by a factor of 100 to 1000 can be achieved. For example, the B-1B bomber, upon which RCS techniques were applied almost as an afterthought, has an RCS of 1/100 that of the B-52 bomber [11].

Reduction of the RCS is a hierarchical process in which each level of contribution must be taken care of by a different technique. For example, application of Radar Absorbing Material (RAM) to a conventional aircraft would require so much material in order to reduce the RCS significantly that the plane would not be able to fly. Reduction of RCS begins at the aircraft design stage by modifying the aircraft's shape. The RCS can be reduced in the direction of the probing radar at the expense of increasing the RCS in other directions. These techniques, which include eliminating vertical sections, blending

the wings into the body, eliminating external structures, and making the engine inlets flush with the body, reduce the major portion of RCS [10],[12]. After the major contributions to the RCS are reduced by changing the shape of the aircraft, the smaller contributions are reduced by use of materials.

The first defensive use of RAM was in the period 1944-45 when the conning towers of some German submarines were covered with absorbent material to reduce the risk of detection by radar-carrying Allied patrol aircraft [10]. Early RAM was heavy, bulky and would disintegrate at operational airspeed. It was, therefore, unsuitable for use in an aircraft. Today, however, the new composite materials may be used as a structure around which the radar absorbing materials are applied. For example, an absorber made from carbon impregnated foam can be covered with a Kevlar skin for support, or the honeycomb, which is already being used as a construction material, may be made lossy and shaped to distort the incoming wave and reduce the size of the reflected signal. With the strength and lightness of the new materials, the RAM may be used as needed on the leading edges of wings, on control surfaces, in cavity inlets, on material transitions etc., to reduce the RCS as shown in Figure 1.4 [11]. Because the honeycomb is such an integral part of aircraft construction, it is important to characterize such structures in the presence of the radar wave.

The numerical analysis of a plane wave incident on a slab of artificial dielectric, such as the honeycomb, has its roots in past analysis done on FSSs where vanishingly thin, perfect conductors, lying flat in the plane of periodicity are repeated along a one-dimensional or two-dimensional lattice. Strip gratings were among the first periodic structures to be analyzed by treating the strips as a thin sheet of dielectric with a modulated impedance along the direction of periodicity [13]-[16]. The impedance was zero

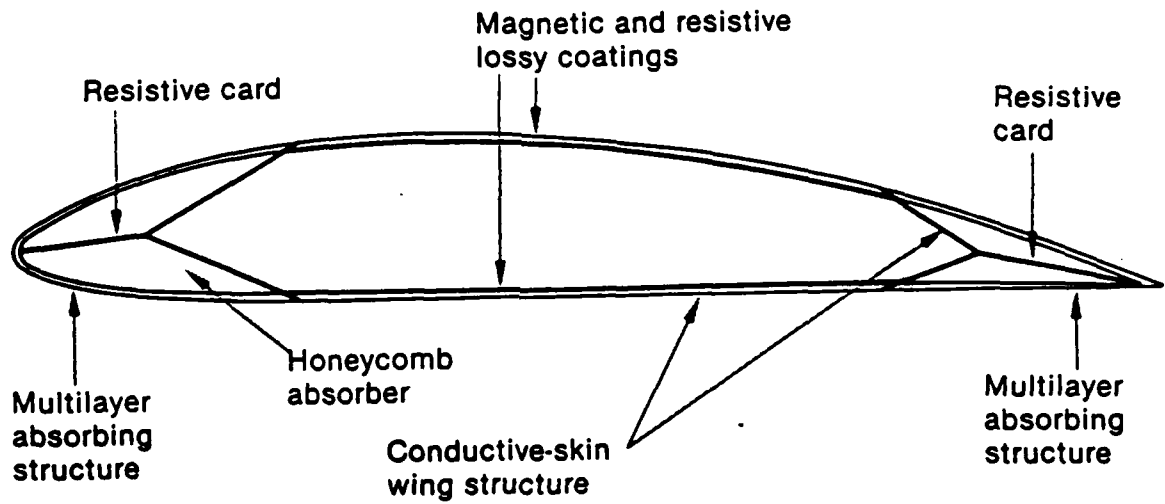


Figure 1.4 Use of radar absorbing structures on a wing to absorb radar waves incident from head on. The honeycomb cells, located on the leading edge of the wing, are as long as possible to absorb low-frequency radar. Resistive cards minimize edge diffraction [11].

on the strip and infinity in the aperture. The entire unit cell was discretized by the method of moments using Floquet harmonics as basis and testing functions. This led to large, but diagonally dominant matrices to invert. Later, because of convergence problems with the Floquet basis functions, the practice became to use basis functions that modeled the physical quantity more precisely. Entire domain basis functions and subdomain basis functions that discretized only the metal or only the aperture were applied to the strip [17],[18]. The same type of approach was used to model FSSs composed of apertures or rectangular plates arranged periodically on a two-dimensional lattice [19],[20]. As experience was gained, more complex unit cells were attempted using both entire domain basis functions and subdomain basis functions [21]-[24]. The ability to model the thickness of an FSS element was added by using subdomain basis functions to discretize the element in the direction perpendicular to the plane of periodicity [18],[24].

The structures of interest in this thesis also have a thickness parameter; however, the thickness is not due to the elements themselves being thick, rather, it arises due to having a unit cell comprised of thin, lossy cards which do not lie flat in the plane of periodicity. To model the loss, a resistive boundary condition is used [25]-[29]. The problem of a plane wave normally incident on a non-flat, lossy strip array was handled by a modified spectral Galerkin method with entire domain basis functions [30]. The solution method is similar to that of the FSS problem, but a convolution must be performed in \hat{z} in order to account for the thickness dimension of the structure.

Very thick structures, those that cannot be handled conveniently by straightforward application of the method of moments, have been approached in FSS problems by cascading a generalized scattering matrix [31-33]. Special cases, similar to the lossy honeycomb, have been solved using mode matching. These cases include arrays of lossless

waveguides where the modes of the waveguide are known analytically [34-36] or a lossy, parallel-plate waveguide array [37].

The numerical solution of all periodic problems hinges on finding a way to efficiently compute the periodic Green's function. Therefore, a thorough study of the periodic Green's function is found in Chapter 2, which discusses how the periodic Green's function arises and how it may be computed efficiently for one-dimensional and two-dimensional periodicities. Since the problem formulation involves the use of the resistive boundary condition, it is also discussed in Chapter 2.

In Chapter 3, various slab geometries whose unit cells are composed of lossy strips and are periodic in one dimension are examined. The oblique incidence case is solved where the waves polarized Transverse Magnetic (TM) and Transverse Electric (TE) with respect to the strip axis are coupled to one another. The case in which the propagation vector of the incident wave lies in the plane normal to the strip axis is treated as a special case.

In Chapter 4, slabs are composed of unit cells repeated on a two-dimensional lattice. The unit cells are composed of thin, lossy plates, set on edge in the periodic plane. Slabs of isolated plates, or plates attached together to form lossy waveguide structures, such as the honeycomb, are examined.

The straightforward application of the method of moments to structured slabs that are many wavelengths thick leads to large impedance matrices that are difficult, if not impossible, to fill and solve using today's computers. It is, therefore, desirable to find a procedure where the results from a thin slab solved rigorously by the method of moments could be used to extrapolate the solution of a thick slab. The study of these procedures is the subject of Chapter 5. First, a method used successfully to solve the multilayer FSS problem is examined—the generalized scattering matrix. Problems associated with the

application of the scattering matrix to continuous structures necessitated the search for alternate methods. The first alternative was to find the modes of the lossy waveguide structure and to mode match at the aperture. This was found to be numerically intractable. The final method, and the one that was ultimately successful, was to construct large basis functions that accurately model the currents within the thick structure and use these functions in a method of moments solution. Conclusions are drawn in Chapter 6. An appendix is included in the thesis which compares the results of the computer codes used in this thesis with exact solutions or solutions obtained by other numerical methods in order to validate the codes.

2. PRELIMINARY CONCEPTS

2.1 Introduction

All the structures considered in this thesis have two features in common: they are periodic with an incident field that is a plane wave and they are composed of thin-shell, lossy material. Consequently, prior to the formulation of a specific problem, the efficient solution of periodic problems in general will be discussed followed by an investigation of the resistive boundary condition used to model the loss of the problem.

A periodic structure is formed by arranging identical cells, known as unit cells, on a periodic lattice in space. The case where the incident field is a plane wave is the basis for analyzing all problems involving scattering from a periodic structure. If an arbitrary field (not a plane wave) is incident upon a periodic structure, no relationship exists between the currents of different unit cells; the currents on the entire structure must be treated as unknowns in a moment method solution. On the other hand, if the incident field is a plane wave, then a relationship may be found between currents of different unit cells based on Floquet's theorem and only the currents in a single unit cell must be treated as unknowns. The solution of an arbitrary field incident on a periodic structure is found by decomposing the field into plane waves, finding the response to each plane wave and adding the responses.

One fruitful approach toward solving periodic problems involves the formulation of an integral equation and its numerical solution via the method of moments. The integral equation has as its kernel a periodic Green's function, which is, unfortunately, a slowly convergent summation. Consequently, the computer time required to solve the problem by the method of moments is dominated by the time needed to compute the impedance matrix elements. In the past, investigators have used various techniques to speed

convergence of the summation. For example, functions with a wide support in the spatial domain have been used as basis and testing functions to make the summations in the spectral domain more convergent [17],[21],[30]. Poisson's summation formula [38] has been applied to speed convergence using a spatial domain approach [39],[40] or a spectral domain approach [41]-[43].

The following three sections discuss how to efficiently compute the periodic Green's functions. Two examples of periodic problems are used for illustration. The first example, discussed in Section 2.2, is that of plane-wave scattering from the strip grating shown in Figure 2.1. In Section 2.3, extensions of the techniques developed in Section 2.2 are applied to a two-dimensional array of plates arranged on a skewed lattice as shown in Figure 2.16. The main points of the study are summarized in Section 2.4. The final section discusses the formulation of the resistive boundary condition and the guidelines for its application.

2.2 One-dimensional Periodicity

2.2.1 Definitions of terms

In this section, the integral equation formulation of plane-wave scattering from the strip grating shown in Figure 2.1 will be examined. The strips, whose axes are aligned with \hat{z} , are each rotated, making an angle θ with respect to \hat{x} . They are perfect electric conductors and are spaced b meters apart along the \hat{x} axis. The propagation vector of the incident plane wave lies in the xy plane making an angle of θ_i with the \hat{y} axis. The plane wave is polarized either transverse magnetic (TM) or transverse electric (TE) with respect to \hat{z} . The periodic Green's function derived for this simple geometry is applicable to the more complex, singly-periodic structures of Chapter 3.

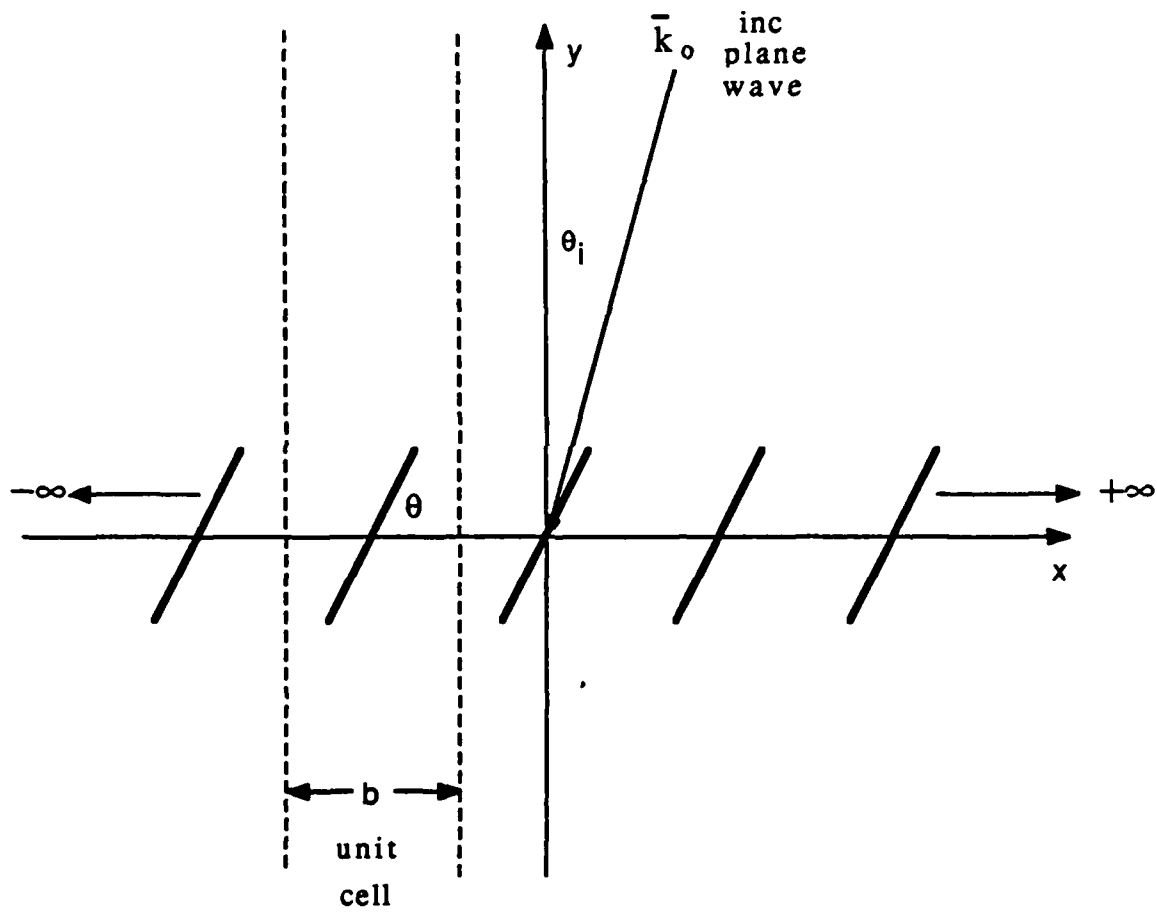


Figure 2.1 One-dimensional strip array geometry showing the incident plane wave and the unit cell. The strips are rotated out of the plane of periodicity by θ .

In the remainder of this chapter, the Fourier transform is used extensively. The Fourier transform pair for the one-dimensional case is defined as

$$\tilde{F}(\beta_x) = \int_{-\infty}^{+\infty} f(x) e^{-j\beta_x x} dx \quad (2.1a)$$

$$f(x) = \frac{1}{2\pi} \int_{-\infty}^{+\infty} \tilde{F}(\beta_x) e^{+j\beta_x x} d\beta_x \quad (2.1b)$$

where $f(x)$ is a function in the space domain and $\tilde{F}(\beta_x)$ is its Fourier transform into the spectral domain.

The Fourier transform is used in this thesis to transform periodic functions in the space domain into their equivalent representations in the spectral domain. A periodic function may be viewed as the function truncated to one period convolved with a comb function in space [44], i.e.,

$$f_p(x) = f(x) * \sum_{m=-\infty}^{\infty} \delta(x - mb) \quad (2.2)$$

where

$$f(x) = \begin{cases} f_p(x) & \text{for } -b/2 < x < +b/2 \\ 0 & \text{otherwise} \end{cases}$$

b is the period of $f_p(x)$ and $*$ denotes the convolution operation defined as

$$f(x) * g(x) = \int_{-\infty}^{\infty} f(x') g(x - x') dx' \quad (2.3)$$

Since the Fourier transform of a comb function is also a comb function, albeit with a different period, and the transform of a convolution is the product of the transforms, the Fourier transform of Equation (2.2) is a function sampled at discrete values in the spectral domain.

$$\tilde{F}_p(\beta_x) = \tilde{F}(\beta_x) \frac{2\pi}{b} \sum_{m=-\infty}^{\infty} \delta\left(\beta_x - \frac{2\pi m}{b}\right) \quad (2.4)$$

A concise way to predict the location of the spectral domain comb components in Equation (2.4) given the location of the spatial domain comb components in Equation (2.2) is through the use of a reciprocal lattice.

A periodic geometry has associated with it a spatial lattice and a reciprocal lattice [45]. The spatial lattice is a periodic arrangement of points in space and is formed by adding an integer number (m) of primitive vectors (\hat{S}_1) to a location \vec{r} . For the one-dimensional case under consideration, $\hat{S}_1 = b\hat{x}$.

$$\begin{aligned} \vec{r}' &= \vec{r} + m\hat{S}_1 \\ &= \vec{r} + mb\hat{x} \end{aligned} \quad (2.5)$$

The overall periodic structure is formed when the unit cell, shown in Figure 2.1, is attached to each lattice point.

The reciprocal lattice is associated with the spectral domain just as the spatial lattice is associated with the spatial domain. The reciprocal lattice predicts where the discrete components of $\tilde{F}_p(\beta_x)$ are located in the spectral domain. In the one-dimensional case under consideration, the reciprocal lattice is defined by adding an integer number (n) of primitive reciprocal vectors (\tilde{S}_1) to a location in the spectral domain (\vec{k})

$$\vec{k}' = \vec{k} + n\tilde{S}_1 \quad (2.6)$$

where the primitive reciprocal vector is related to the primitive spatial vector by

$$\hat{S}_1 \cdot \tilde{S}_1 = 2\pi \quad (2.7)$$

Therefore,

$$\tilde{S}_1 = \frac{2\pi}{b} \hat{x} \quad (2.8)$$

2.2.2 Formulation of the periodic Green's function

The electric field integral equation is used to solve the one-dimensional strip array problem. Using the fact that the tangential E field is zero on the strip, the following equation is obtained:

$$\hat{n} \times \left[-j \omega \mu \int \vec{J}(s') G_p(s, s') ds' + \frac{1}{j \omega \epsilon} \nabla \int \nabla \cdot \vec{J}(s') G_p(s, s') ds' \right] = -\hat{n} \times \vec{E}_{inc}(s) \quad (2.9)$$

where ω is the radian frequency of the incident wave, \hat{n} is the normal to the strip surface, and μ and ϵ are, respectively, the magnetic permeability and the electric permittivity of the surrounding medium. The integral in the equation is performed over the strip in the unit cell and represents the periodic Green's function (G_p) convolved with either the surface electric current density (\vec{J}) or the surface electric charge density ($-\nabla \cdot \vec{J} / j \omega$) in a single unit cell.

The periodic Green's function arises from Floquet's theorem which says, given a plane wave incident upon a periodic structure, all observable quantities will have the same periodicity as the structure and have a cell-to-cell phase shift equal to the cell-to-cell phase shift of the incident plane wave. For example, the current at a point \vec{r} within cell m is related to the current at a corresponding position within cell 0 by

$$J(\vec{r} + mb\hat{x}) = J(\vec{r}) e^{-j\vec{k}_0 \cdot mb\hat{x}} \quad (2.10)$$

where \vec{k}_0 is the propagation constant of the incident wave. It is not necessary, therefore, to consider the entire structure in a periodic geometry. Rather, a single unit cell may be considered along with a Green's function which reflects the relationship of Equation (2.10). The Green's function in this section is defined as the vector potential response at

(x_0, y_0) due to an array of line sources located at (x', y') within each unit cell and having a cell-to-cell phase shift of $\vec{k}_0 \cdot \hat{x}b = k_x b$ due to the incident plane wave as shown in Figure 2.2.

The response to an array of line sources may be obtained in two ways. In the spatial domain, an array of line sources located at x', y' in each unit cell may be represented as

$$J_a(x, y) = \sum_{m=-\infty}^{\infty} \delta(x - x' - mb) e^{-jk_x mb} \delta(y - y') \quad (2.11)$$

Summing the response at (x_0, y_0) due to each line source [46], the following expression is obtained which is a function periodic in x with a phase shift due to the incident wave.

$$G_p(x_0, y_0 | x', y') = \frac{1}{4j} \sum_{m=-\infty}^{\infty} e^{-jk_x mb} H_0^2 \left(k_0 \sqrt{(x_0 - x' - mb)^2 + (y_0 - y')^2} \right) \quad (2.12)$$

If the phase shift is extracted from Equation (2.12), the resulting periodic function could be interpreted in terms of the convolution in Equation (2.2). H_0^2 is the Hankel function of the second kind, zeroth order.

In the spectral domain, the Fourier transform is used to express the line array of Equation (2.11) as a series of current sheets. Each current sheet has a period dictated by the reciprocal lattice and a cell-to-cell phase shift dictated by the incident field (Equation (2.6)).

$$J_a(x, y) = \frac{1}{b} \sum_{m=-\infty}^{\infty} e^{+j\beta_{xm}(x-x')} \delta(y - y') \quad (2.13)$$

where

$$\beta_{xm} = \frac{2\pi m}{b} - k_x$$

Adding the response at (x_0, y_0) due to each current sheet, the spectral domain Green's function is obtained

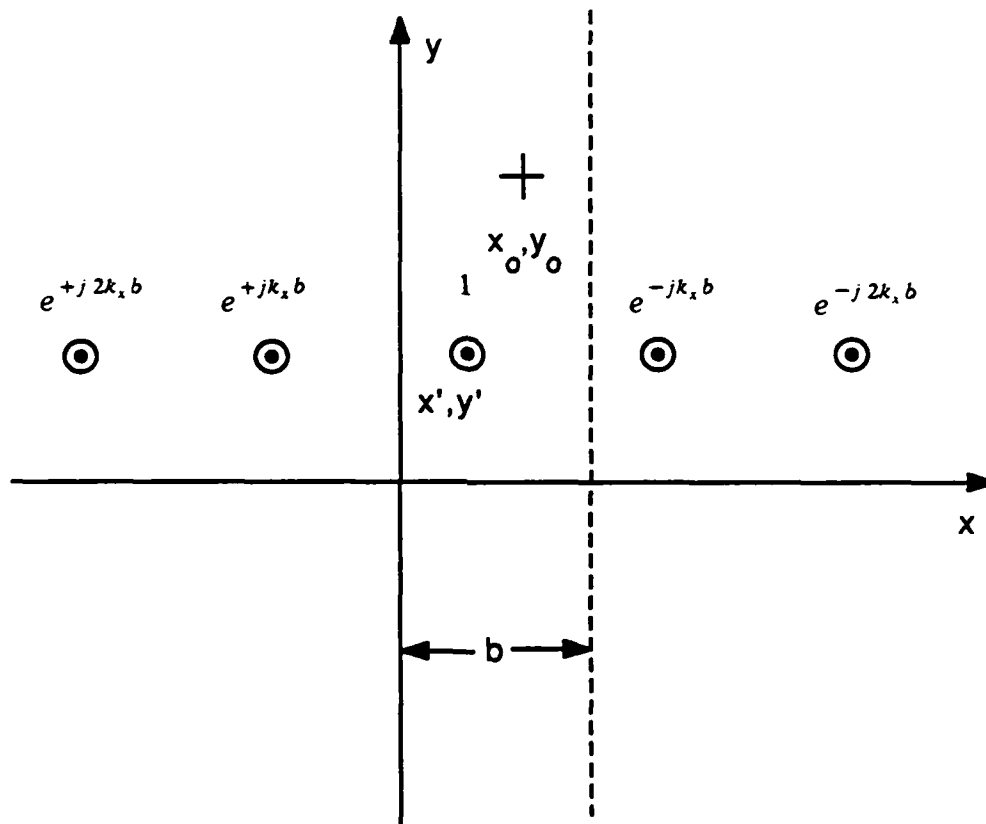


Figure 2.2 Array of line sources with a cell-to-cell phase shift caused by the incident plane wave. The sources are located at x', y' within each unit cell. The observation point is at x_0, y_0 .

$$G_p(x_0, y_0 | x', y') = \frac{1}{b} \sum_{m=-\infty}^{\infty} \frac{e^{-j\beta_y |y_0 - y'|}}{2j\beta_y} e^{+j\beta_{xm}(x_0 - x')} \quad (2.14)$$

where application of the radiation condition yields

$$\beta_y = \begin{cases} \sqrt{k_0^2 - \beta_{xm}^2} & \text{if } k_0^2 > \beta_{xm}^2 \\ -j\sqrt{\beta_{xm}^2 - k_0^2} & \text{if } \beta_{xm}^2 > k_0^2 \end{cases} \quad (2.14a)$$

The spectral domain Green's function could have been obtained directly by applying Equation (2.4) to the periodic portion of Equation (2.12) and taking the inverse Fourier transform, which is a summation. This means that the two representations of the Green's function are a Fourier transform pair sampled with a comb function. In the spatial domain, the sampling falls on the spatial lattice, while in the spectral domain, the sampling falls on the reciprocal lattice. This concept will be expanded further in Section 2.2.5.

2.2.3 Convergence characteristics of G_p

In this section, the convergence characteristics of the periodic Green's function are examined for both the spatial domain (Equation (2.12)) and the spectral domain (Equation (2.14)). Using the asymptotic approximation for the Hankel function in Equation (2.12), the spatial domain summation is found to behave as

$$G_p(x_0, y_0 | x', y') \approx \sum_{m=-\infty}^{\infty} \frac{e^{-jk_x mb} e^{-jk_0 \sqrt{(x_0 - x' - mb)^2 + (y_0 - y')^2}}}{k_0^{1/2} \left| (x_0 - x' - mb)^2 + (y_0 - y')^2 \right|^{1/4}} \quad (2.15)$$

for large values of m . This expression is convergent [38] only because of the phase variation in the numerator of the summand. For certain array spacings it doesn't converge at all, and for all positions of the source and observation points, it converges slowly.

The spectral domain formulation of Equation (2.14) converges rapidly as long as $y_0 \neq y'$, which in this thesis is called the "off-plane" case since the observation point is located off the plane of the current sheet. The rapid convergence in the "off-plane" case occurs because as m increases, the plane-wave responses to the current sheets change from waves propagating in \hat{y} to waves evanescent in \hat{y} ; therefore, the summand decays exponentially with increasing m .

For the "on-plane" case, meaning that $y_0 = y'$, the summand no longer has the exponential decay to aid convergence. For large m , the summand behaves like the function $e^{jm\Delta x}/m$ so the sum converges slowly in most cases, and for some spacings of the source and observation points (i.e., when $\Delta x = 0$), doesn't converge at all. Unfortunately, the "on-plane" case inevitably occurs. For example, it occurs in the self term when the strips are rotated with respect to \hat{x} ($\theta \neq 0^\circ$) or in all terms when the strips lie flat in the plane of periodicity ($\theta = 0^\circ$).

A further problem in the spectral formulation is that for certain combinations of array spacing, incidence angle and summation index, the denominator of the summand, β_y , equals zero which causes isolated terms of the summation to go to infinity. However, since the function is sampled at discrete points, these singularities may be avoided by changing the angle of incidence slightly.

The reason that the different domains exhibit the convergence behavior outlined above can be traced to the existence of singularities in each of the domains. Recall that the periodic Green's functions are a Fourier transform pair sampled by the comb function in each domain. In the spectral domain (Equation (2.14)), the function is singular when β_y equals zero which is unavoidable in a continuous function representation. This implies

that the Fourier transform (the spatial domain Green's function) is always a function with a wide support and is, therefore, slowly convergent. Conversely, the spatial domain representation of the Green's function (Equation (2.12)) has a singularity when the argument of the Hankel function goes to zero. This singularity is inevitable for the continuous function only when $y_0 = y'$ — the "on-plane" case. For this case, the Fourier transform (the spectral domain Green's function) has a wide support and is slowly convergent. As the $(y_0 - y')$ portion of the argument becomes larger, moving the observation point off the plane of the current sheet, the continuous representation of the Hankel function loses its singular behavior and the convergence in the spectral domain becomes more rapid.

2.2.4 Smoothness of basis/test functions to help convergence

The pure spatial formulation will be abandoned at this point due to its convergence problems that occur regardless of the location of the source and observation point. The pure spectral formulation, which has a convergence problem only in the "on-plane" case, will be considered further. It is common, in the pure spectral formulation, to speed convergence for the "on-plane" case by analytically performing the convolution operation of the Green's function with the basis and test functions to exploit the combined degree of smoothness of the basis and testing functions. To demonstrate this technique, consider a TM to \hat{z} plane wave incident on an array of flat strips ($\theta = 0^\circ$). The equation for an element of the impedance matrix is

$$\begin{aligned} \langle \vec{T}, -\vec{E}^{scat} \rangle &= \int \vec{T}(x) \cdot \frac{j\omega\mu}{b} \int \vec{J}(x') \sum_{m=-\infty}^{\infty} \frac{e^{+j\beta_{zm}(x-x')}}{2j\beta_y} dx' dx \\ &= \frac{j\omega\mu}{b} \sum_{m=-\infty}^{\infty} \frac{1}{2j\beta_y} \int T(x) e^{+j\beta_{zm}x} dx \int J(x') e^{-j\beta_{zm}x'} dx' \end{aligned} \quad (2.16)$$

$$= \frac{j \omega \mu}{b} \sum_{m=-\infty}^{\infty} \tilde{T}^*(\beta_{xm}) \tilde{J}(\beta_{xm}) \frac{1}{2j \beta_y}$$

\tilde{J} is the Fourier transform of the basis function in the \hat{x} direction performed analytically and sampled at β_{xm} . \tilde{T}^* is the complex conjugate of the Fourier transform of the test function also taken analytically and sampled at β_{xm} . β_{xm} is defined in Equation (2.13) and β_y is defined in Equation (2.14a). Since the strips are lying flat in the plane of periodicity, the positions of the basis and testing functions are always the same in the \hat{y} direction.

If the basis function is a pulse of width Δ located at the origin, and the test function is a delta function located at x_0 , then

$$\tilde{J}(\beta_{xm}) = \Delta \operatorname{sinc} \left(\frac{\beta_{xm} \Delta}{2} \right) \quad (2.17a)$$

and

$$\tilde{T}^*(\beta_{xm}) = e^{+j \beta_{xm} x_0} \quad (2.17b)$$

The summand now asymptotically behaves as $1/m^2$ which converges regardless of spacing and quicker than the $1/m$ convergence of the Green's function alone.

Symbolically, the linearity of the Fourier transform has been used to change

$$T^R * J * F^{-1} \left[\tilde{G}_p \right] \quad (2.18)$$

into

$$F^{-1} \left[\tilde{T}^* \tilde{J} \tilde{G}_p \right] \quad (2.19)$$

In Equation (2.18), $T^R(x) = T(-x)$ is needed to get the testing function inner product into convolutional form. F^{-1} is the inverse Fourier transform and takes the form of a summation since β_{xm} is discrete.

The smoothness of the basis and testing functions becomes essential for convergence when differential operators arise in the integral equation, such as when a TE to \hat{z} plane wave is incident on an array of flat strips ($\theta = 0^\circ$). In this case, the impedance matrix element for the integral equation (Equation (2.9)) becomes

$$\begin{aligned} \langle \vec{T}, -\vec{E}^{scat} \rangle = & -\frac{1}{j\omega\epsilon b} \left[k_0^2 \int T(x) \int J(x') \sum_{m=-\infty}^{\infty} \frac{e^{+j\beta_{xm}(x-x')}}{2j\beta_y} dx' dx \right. \\ & \left. + \int T(x) \frac{d}{dx} \int \frac{d}{dx'} J(x') \sum_{m=-\infty}^{\infty} \frac{e^{+j\beta_{xm}(x-x')}}{2j\beta_y} dx' dx \right] \end{aligned} \quad (2.20)$$

In order to transfer the derivatives of the scalar potential term onto the basis and test functions, the functions must have a combined degree of smoothness of at least a triangle basis and a pulse test in order for the convolution integrals to make sense. The transfer of a derivative onto the test function converts the pulse into a set of two delta functions while the transfer of a derivative onto the basis function converts the triangle into a pulse doublet as shown in Figure 2.3. Performing the convolution of the basis, test and Green's functions analytically leads to a Fourier transform of a delta function, which behaves as 1, and a Fourier transform of the pulse doublet, which behaves as $1/\beta_{xm}$. These terms, together with the $1/\beta_y$ behavior of the Green's function, yield the same $1/m^2$ speed of convergence for the scalar potential term as for the vector potential term in the TM case discussed above. The TE vector potential term will converge much faster ($1/m^4$) since it has no derivatives associated with it and the functions to be convolved are, therefore, smoother.

If the derivatives are first transferred onto the Green's function in Equation (2.20), the following equation results:

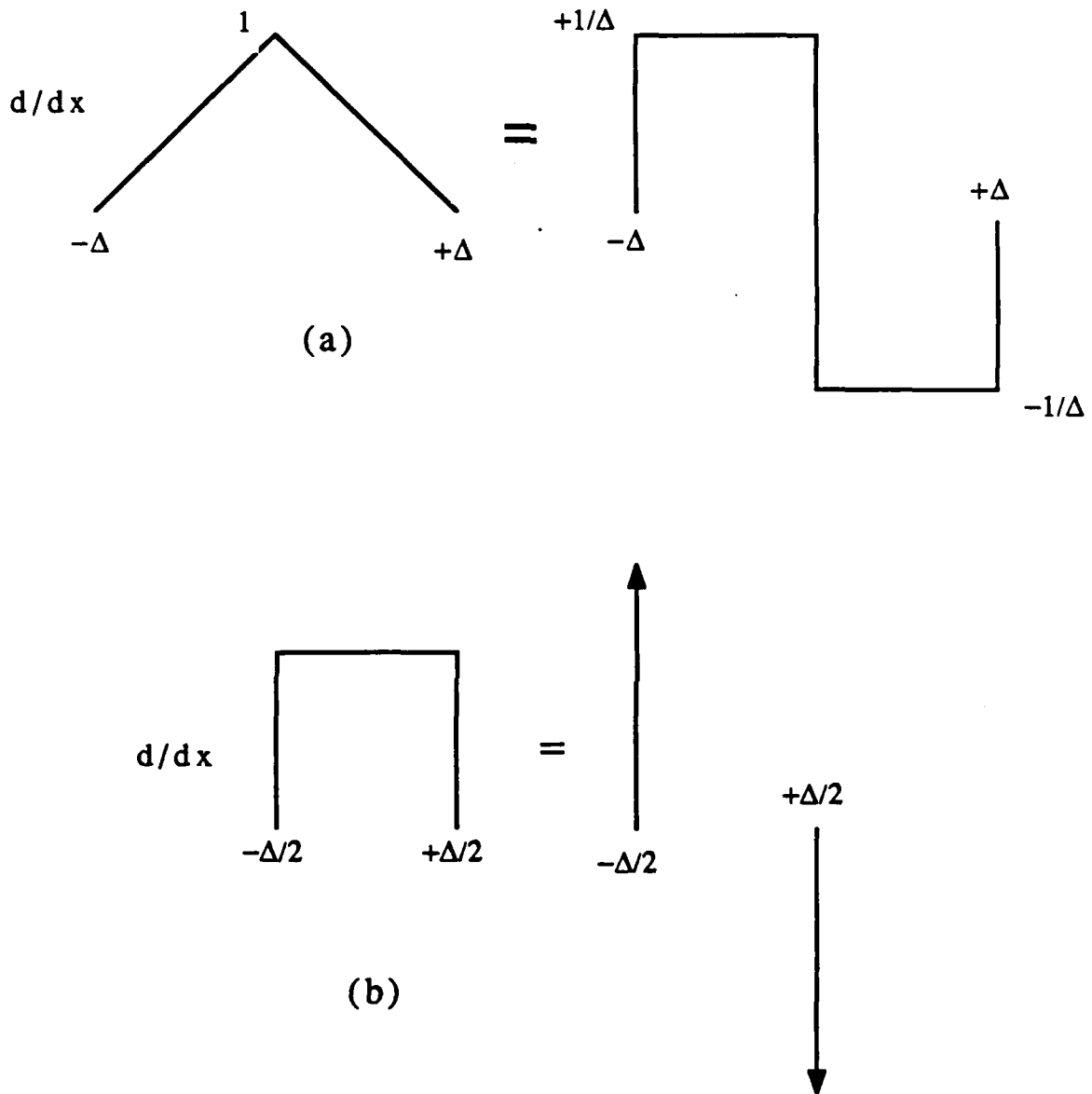


Figure 2.3 Result of applying a derivative to a triangle basis function (a) and to a pulse testing function (b).

$$\langle \vec{T}, -\vec{E}^{scat} \rangle = -\frac{1}{j\omega\epsilon b} \sum_{m=-\infty}^{\infty} \frac{k_0^2 - \beta_{xm}^2}{2j\beta_y} \tilde{T}^*(\beta_{xm}) \tilde{J}(\beta_{xm}) \quad (2.21)$$

The level of smoothness needed for the above sum to be convergent is again at least that exhibited by triangle basis and pulse test functions. In the flat case, therefore, it makes no difference if the derivatives are transferred onto the Green's function, and the smoothness of the basis and testing functions is used to help convergence, or if the derivatives are transferred onto the basis and testing functions explicitly, and then the convolution is performed. In either case, the speed of convergence and the level of smoothness required are the same.

In contrast to the flat case, if the strips are rotated ($\theta \neq 0^\circ$) with respect to the \hat{x} axis, the order of operations does matter. If the derivatives are first transferred to the Green's function, the resulting sum will not converge regardless of the level of smoothness in the basis and test functions. This is best illustrated by examining the case in which the strips are rotated 90 degrees to the \hat{x} axis. With the derivatives transferred to the Green's function, the expression for the the matrix elements becomes

$$\langle T, -E^{scat} \rangle = -\frac{1}{j\omega\epsilon b} \sum_{m=-\infty}^{\infty} \frac{(k_0^2 - \beta_y^2)}{2j\beta_y} \int_y \int_{y'} \tilde{J}(\beta_{xm}, y') \tilde{T}^*(\beta_{xm}, y) e^{-j\beta_y |y - y'|} dy' dy \quad (2.22)$$

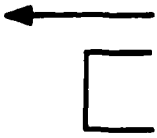


In order for the sum to converge, the integration over y and y' must yield a factor of at least $1/\beta_y^3$ in order to mitigate the β_y^2 factor that arises due to the derivatives in the scalar potential term.

In Table 2.1, the results of the integration

$$\int \tilde{T}^*(\beta_{xm}, y) \int \tilde{J}(\beta_{xm}, y') e^{-j\beta_y |y - y'|} dy' dy \quad (2.23)$$

are shown for when basis and testing functions of varying degrees of smoothness are overlapping as shown in Figure 2.4(a) and when they are non-overlapping as shown in

Table 2.1 Results of integration performed in Equation (2.23) for overlapping and non-overlapping basis and testing functions.

Basis/Test Functions	Overlap Case	Non-Overlap Case
	$\frac{2}{j\beta_y} - \frac{2}{j\beta_y} e^{-j\frac{\beta_y \Delta}{2}}$	$\Delta \text{sinc} \left[\frac{\beta_y \Delta}{2} \right] e^{-j\beta_y \gamma_0}$
	$\frac{2\Delta}{j\beta_y} - \frac{4}{j\beta_y^2} \sin \left[\frac{\beta_y \Delta}{2} \right] e^{-j\frac{\beta_y \Delta}{2}}$	$\Delta^2 \text{sinc}^2 \left[\frac{\beta_y \Delta}{2} \right] e^{-j\beta_y \gamma_0}$
	$\frac{3\Delta}{2j\beta_y} + \frac{2e^{-j\beta_y \Delta}}{j\beta_y^3 \Delta} \left[1 - e^{+j\frac{\beta_y \Delta}{2}} \right] + \left[\frac{4}{j\beta_y^3 \Delta} - \frac{2e^{-j\beta_y \Delta}}{j\beta_y^3 \Delta} \right] \left[1 - e^{-j\frac{\beta_y \Delta}{2}} \right]$	$\Delta \text{sinc}^2 \left[\frac{\beta_y \Delta}{2} \right] \Delta \text{sinc} \left[\frac{\beta_y \Delta}{2} \right] e^{-j\beta_y \gamma_0}$

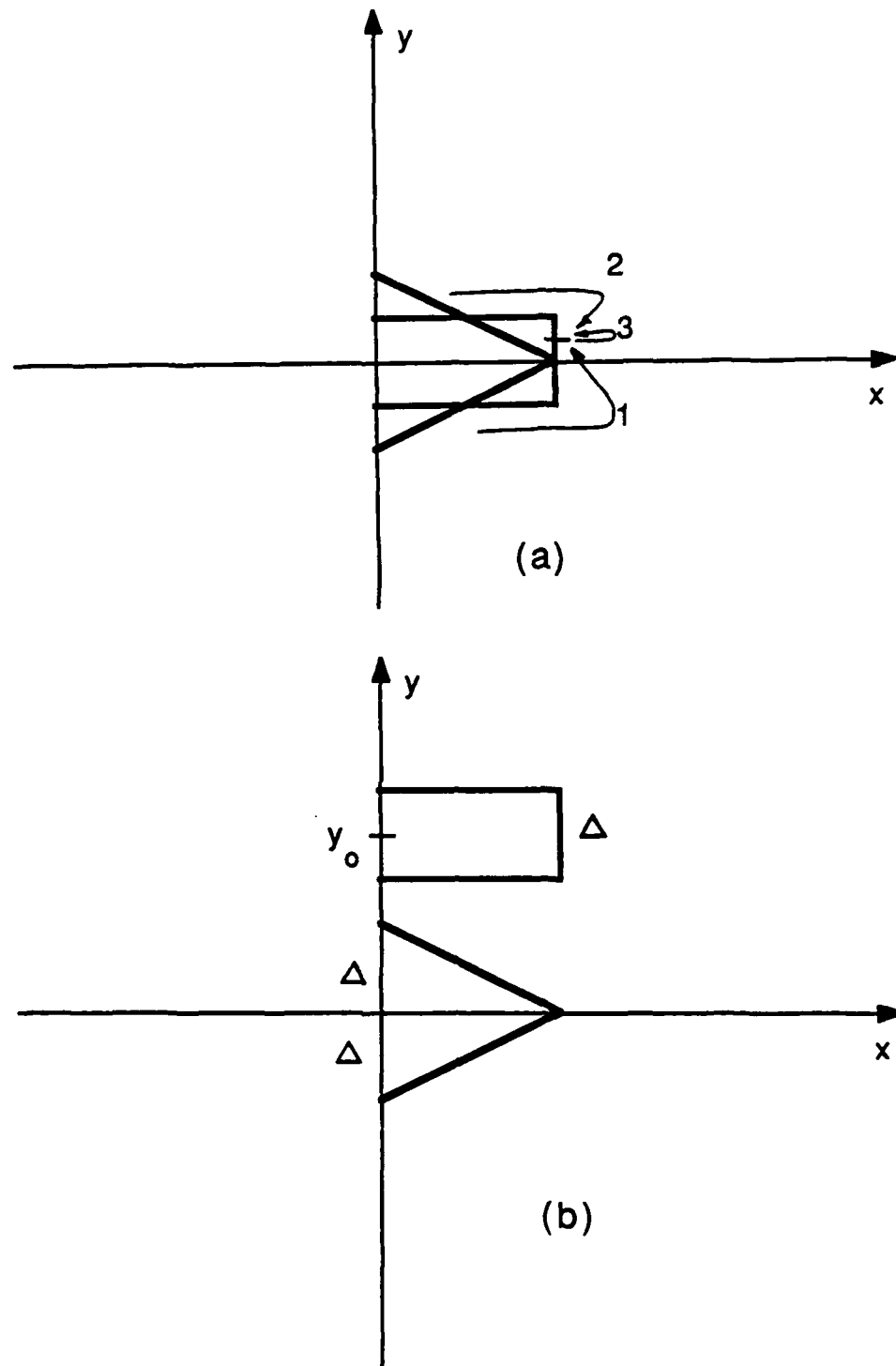


Figure 2.4 Relative positions of the basis and testing functions for the overlapping (a) and non-overlapping case (b). 1 and 2 in (a) are the "off-plane" contributions while 3 represents the "on-plane" contribution.

Figure 2.4(b). The pattern that emerges is as follows: when there is no overlap between basis and testing functions, both exponential decay and degree of smoothness contribute to rapid convergence. In this case, the derivatives may be transferred to the Green's function. For the case in which there is overlap between the basis and test functions (even touching at one point), one term arises which behaves as $1/\beta_y$ regardless of the combined level of smoothness of the basis and testing functions. This term represents the "on-plane" contribution of the basis to the testing function (contribution 3 of Figure 2.4(a)) and, therefore, has no exponential decay. For this case, the derivatives may not be transferred to the Green's function to obtain a convergent summation. Rather, basis and testing functions must be chosen with a level of smoothness to accept the derivatives, and the derivatives must be explicitly transferred onto the basis and testing functions.

To ensure that the above problem is not unique to the $\theta = 90^\circ$ case, a strip of arbitrary rotation θ is examined for completely overlapping pulse basis and pulse test functions. For this case, the "on-plane" contribution term of Equation (2.23) becomes

$$\left| \frac{\Delta}{j(\beta_x \cos\theta + \beta_y \sin\theta)} - \frac{\Delta}{j(\beta_x \cos\theta - \beta_y \sin\theta)} \right| \quad (2.24)$$

When $\theta = 0^\circ$ (the flat case), the terms in the braces cancel, but for all other cases, the terms in the braces remain, leading to nonconvergence of the sum.

2.2.5 Acceleration of convergence

Section 2.2.4 showed that it is necessary to transfer all derivatives in the scalar potential term explicitly onto the basis and testing functions when computing the impedance matrix elements for strips of arbitrary rotation. The derivative operations reduce triangle basis and pulse testing functions to combinations of pulse basis and delta testing functions if the basis and testing functions each take a derivative. The vector

potential term calculation will be simplified by approximating the triangle basis function by a pulse with the same moment and approximating the pulse testing function by a delta function weighted by the support of the pulse [47]. This approximation can be justified by observing that when the testing function is near the basis function, the scalar potential term is the dominant contributor to the impedance matrix element and the the vector potential term is insignificant. As the distance between the basis and testing functions is increased, making the vector potential more important, the moment of the current is the quantity that determines the value of the vector potential. The moments are the same for the triangle basis and the approximate pulse basis. Through the above approximations, all of the calculations required to fill the matrix are reduced to the same form: finding the vector potential response at the test location x_0, y_0 due to an array of current pulses, each rotated with respect to the direction of periodicity.

In order to accelerate the convergence of the summation in the periodic Green's function, the Poisson summation formula will be used. This method makes use of the fact that a smooth, nonsingular function with a wide support in one domain (either spatial or spectral) has a narrow support in the reciprocal domain. It also employs Parseval's theorem.

$$\int h(x) f(x) dx = \frac{1}{2\pi} \int \tilde{H}(-\beta) \tilde{F}(\beta) d\beta \quad (2.25)$$

If $h(x)$ is chosen to be a phase-shifted comb function whose elements fall on the spatial lattice

$$h(x) = \sum_{m=-\infty}^{\infty} e^{-jk_x mb} \delta(x - mb) \quad (2.26a)$$

then its Fourier transform $\tilde{H}(\beta)$ is also a comb function whose elements fall on the reciprocal lattice.

$$\tilde{H}(\beta) = \frac{2\pi}{b} \sum_{m=-\infty}^{\infty} \delta \left| \beta - \left(\frac{2\pi m}{b} - k_x \right) \right| \quad (2.26b)$$

Thus, using Parseval's theorem, a series may be represented in either domain by

$$\begin{aligned} \sum_{m=-\infty}^{\infty} e^{-jk_x mb} f(mb) &= \int \sum_{m=-\infty}^{\infty} e^{-jk_x mb} \delta(x - mb) f(x) dx \\ &= \frac{1}{b} \int \sum_{m=-\infty}^{\infty} \delta \left| \beta + \left(\frac{2\pi m}{b} - k_x \right) \right| \tilde{F}(\beta) d\beta \\ &= \sum_{m=-\infty}^{\infty} \tilde{F} \left(-\frac{2\pi m}{b} + k_x \right) \end{aligned} \quad (2.27)$$

If $f(x)$ has a wide support and is nonsingular, which implies slow convergence, then $\tilde{F}(\beta)$ will have a narrow support and be nonsingular, which implies rapid convergence. The converse is also true since the Fourier transform is a symmetric operation.

To demonstrate a fundamental problem with this straightforward approach, Equation (2.27) is applied to the slowly convergent "on-plane" case of the pure spectral domain (Equation (2.14)).

$$\frac{1}{b} \sum_{m=-\infty}^{\infty} \frac{e^{+j\beta_{xm}(x_0-x')}}{2j\sqrt{k_0^2 - \beta_{xm}^2}} = \frac{1}{b} \int \sum_{m=-\infty}^{\infty} \delta \left| \beta + \left(\frac{2\pi m}{b} - k_x \right) \right| \frac{1}{2j} \frac{e^{-j\beta(x_0-x')}}{\sqrt{k_0^2 - \beta^2}} \quad (2.28)$$

In terms of Parseval's theorem, $\tilde{H}(\beta)$ is the comb function in Equation (2.26b), while $\tilde{F}(\beta)$ is given by

$$\tilde{F}(\beta) = \frac{e^{-j\beta(x_0-x')}}{2j\sqrt{k_0^2 - \beta^2}} \quad (2.29a)$$

$$f(x) = \frac{1}{2\pi} \int \frac{e^{-j\beta(x_0-x')}}{2j\sqrt{k_0^2 - \beta^2}} e^{+j\beta x} d\beta \quad (2.29b)$$

As discussed previously, the summand in Equation (2.28) is singular when $\beta_{xm}^2 = k_0^2$, but

Since β_{xm} is discrete in m , the singularity is avoidable. In Equation (2.29b), however, β is continuous and the singularity cannot be avoided. The integrand is sharply peaked, so it is expected that application of Poisson acceleration will not help convergence. In spite of this, if the integration in Equation (2.29b) is performed,

$$f(x) = \frac{1}{4j} H_0^2(k_0 |x_0 - x - x'|) \quad (2.30)$$

is obtained. Applying Parseval's theorem using $h(x)$ as defined by Equation (2.26a) yields

$$\int f(x)h(x)dx = \frac{1}{4j} \sum_{m=-\infty}^{\infty} e^{-jk_x mb} H_0^2(k_0 |x_0 - x' - mb|) \quad (2.31)$$

This is the pure spatial formulation of the periodic Green's function, shown earlier in Equation (2.12), which is slowly convergent. If the Poisson summation formula were to be applied to Equation (2.31), the result would be the pure spectral domain formulation of the Green's function for an observation point located "on-plane." The unavoidable singularity of the Hankel function as the argument approaches zero leads to the slow convergence of the "on-plane" sum in the pure spectral domain.

In both the spectral and spatial domains, application of the Poisson summation formula did not speed convergence because it was applied to a peaked function with an unavoidable singularity. Thus, a better strategy is to subtract from the singular function, an auxiliary, nonsingular function that is asymptotically equal to the singular function for large m , then add the nonsingular asymptotic function back in. The Poisson summation formula may be successfully applied to this smooth, wide, asymptotic function. First, working with the spectral domain:

$$\begin{aligned}
& \frac{1}{b} \sum_{m=-\infty}^{\infty} \frac{1}{2j} \frac{e^{+j\beta_{xm}(x_0-x')}}{\sqrt{k_0^2 - \beta_{xm}^2}} = \\
& \frac{1}{b} \sum_{m=-\infty}^{\infty} \frac{e^{+j\beta_{xm}(x_0-x')}}{2j} \left[\frac{1}{\sqrt{k_0^2 - \beta_{xm}^2}} - \frac{1}{-j\sqrt{u^2 + \beta_{xm}^2}} \right] \\
& + \frac{1}{b} \sum_{m=-\infty}^{\infty} \frac{1}{2} \frac{e^{+j\beta_{xm}(x_0-x')}}{\sqrt{u^2 + \beta_{xm}^2}}
\end{aligned} \tag{2.32}$$

The first summation is done in the spectral domain and converges as $1/\beta_{xm}^3$. The second summation is never singular so the Poisson summation formula can be successfully applied. The second sum becomes

$$\frac{1}{2\pi} \sum_{m=-\infty}^{\infty} e^{-jk_x mb} K_0(u |x_0 - x' - mb|) \tag{2.33}$$

where K_0 is the modified Bessel function which exponentially decreases with increasing argument.

The operations of Equation (2.18) may be rewritten using the concepts in Equation (2.32) as

$$T^R * J * F^{-1}(\tilde{G}) = T^R * J * \left[F^{-1}(\tilde{G} - \tilde{G}^a) + G^a \right] \tag{2.34}$$

The inverse Fourier transform, symbolized by F^{-1} , is a summation. The smooth auxiliary function, \tilde{G}^a , has the same asymptotic behavior as the desired function \tilde{G} . It is subtracted from \tilde{G} and added in the spatial domain through use of the Poisson summation formula. In Equation (2.34), the operations in brackets may be viewed as a way to accelerate a slowly convergent summation by breaking it up into two rapidly convergent summations.

The convolution operation of Equation (2.34) may be distributed onto each domain and performed analytically in the spectral domain, according to

$$F^{-1} \left[\tilde{T}^* \tilde{J} (\tilde{G} - \tilde{G}^a) \right] + T^R * J * G^a \quad (2.35)$$

This is equivalent to computing the impedance matrix elements by adding the elements of two impedance matrices: one computed in the spectral domain and the other computed in the spatial domain.

To accelerate the spatial domain summation successfully for the "on-plane" case ($y_0 - y' = 0$), the asymptotic behavior of the Hankel function is removed by moving the observation point of the auxiliary term off the plane, cb units.

$$\begin{aligned} & \frac{1}{4j} \sum_{m=-\infty}^{\infty} e^{-jk_x mb} H_0^2 \left(k_0 \sqrt{(x_0 - x' - mb)^2} \right) = \\ & \frac{1}{4j} \sum_{m=-\infty}^{\infty} e^{-jk_x mb} \left[H_0^2 \left(k_0 \sqrt{(x_0 - x' - mb)^2} \right) - H_0^2 \left(k_0 \sqrt{(x_0 - x' - mb)^2 + cb^2} \right) \right] \\ & + \frac{1}{4j} \sum_{m=-\infty}^{\infty} e^{-jk_x mb} H_0^2 \left(k_0 \sqrt{(x_0 - x' - mb)^2 + cb^2} \right) \end{aligned} \quad (2.36)$$

The first summation remains in the spatial domain and converges rapidly because the asymptotic behavior of the summand is being subtracted out. The second summation is brought into the spectral domain using the Poisson summation formula. To apply Parseval's theorem to the second sum, the following expressions are needed in addition to the transform of the comb function, given in Equation (2.26):

$$f(x) = \frac{1}{4j} H_0^2 \left(k_0 \sqrt{(x_0 - x' - x)^2 + cb^2} \right) \quad (2.37a)$$

$$\begin{aligned} \tilde{F}(\beta) &= \int \frac{1}{4j} H_0^2 \left(k_0 \sqrt{\xi^2 + cb^2} \right) e^{-j\beta\xi d} \xi e^{-j\beta(x_0 - x')} \\ &= e^{-j\beta(x_0 - x')} \frac{e^{-jcb\sqrt{k_0^2 - \beta^2}}}{2j\sqrt{k_0^2 - \beta^2}} \end{aligned} \quad (2.37b)$$

Application of Parseval's theorem yields

$$\frac{1}{2\pi} \int \tilde{F}(\beta) \tilde{H}(-\beta) d\beta = \frac{1}{b} \sum_{m=-\infty}^{\infty} \frac{e^{-jcb\beta_y}}{2j\beta_y} e^{+j\beta_{xm}(x_0-x')} \quad (2.38)$$

where β_{xm} and β_y , defined previously in Equations (2.13) and (2.14), are repeated below for convenience.

$$\beta_{xm} = \frac{2\pi m}{b} - k_x$$

$$\beta_y = \begin{cases} \sqrt{k_0^2 - \beta_{xm}^2} & \text{if } k_0^2 > \beta_{xm}^2 \\ -j\sqrt{\beta_{xm}^2 - k_0^2} & \text{if } \beta_{xm}^2 > k_0^2 \end{cases}$$

Since this summation is performed in the spectral domain for an "off-plane" observation point, it is rapidly convergent.

In a view similar to that taken for the spectral domain acceleration, the above procedure may be looked upon either as a way to quickly perform the summation of the spatial periodic Green's function,

$$T^R * J * G = T^R * J * \left[(G - G^a) + F^{-1}(\tilde{G}^a) \right] \quad (2.39)$$

or by distributing the convolution operation of Equation (2.39) onto the different domains and performing the convolutions analytically in the spectral domain, the following is obtained.

$$T^R * J * (G - G^a) + F^{-1}(\tilde{T} * \tilde{J} \tilde{G}^a) \quad (2.40)$$

If cb is allowed to equal zero, the asymptotic testing point is moved "on-plane." The first term of Equations (2.39) and (2.40) goes to zero, and the Green's function is summed entirely in the spectral domain. Since the test point of the asymptotic term is now "on-plane," the summation is the slowly convergent pure spectral domain approach. The next section will discuss the details of implementing Equations (2.39) and (2.40).

2.2.6 Numerical implementation of the spatial domain acceleration

In this section, the details of implementing the spatial domain acceleration procedure will be examined. The accelerated periodic Green's function, shown in Equation (2.36) with $y_0 - y' \neq 0$, is expressed as a weighted combination of the spatial domain and spectral domain.

$$G_p(x_0, y_0 | x', y') = \frac{1}{4j} \sum_{m=-\infty}^{\infty} e^{-jk_x mb} \quad (2.41)$$

$$\left[H_0^2 \left\{ k_0 \sqrt{(x_0 - x' - mb)^2 + (y_0 - y')^2} \right\} - H_0^2 \left\{ k_0 \sqrt{(x_0 - x' - mb)^2 + (|y_0 - y'| + cb)^2} \right\} \right]$$

$$+ \frac{1}{b} \sum_{m=-\infty}^{\infty} \frac{e^{-j(|y_0 - y'| + cb)\beta_y}}{2j\beta_y} e^{j\beta_{xm}(x_0 - x')}$$

The factor that determines the weighting given to each domain is c , which is a measure of how far "off-plane" the testing point of the asymptotic term in the Green's function is located. In this thesis, c is always multiplied by the cell size (b), for example, $c=0.1$ and cell size = 0.7 m moves the test point of the asymptotic Green's function (cb) 0.07 m "off-plane."

As c increases, the contribution of each domain shifts in importance from the spectral to the spatial domain. This is seen in Figures 2.5 and 2.6 where the value of the sum in each domain is plotted as the limits of the summation are increased from $m=-1:1$ to $m=-100:100$. As the asymptotic observation point is moved farther "off-plane," i.e., from $c=0.01$ to 0.1, the spectral domain sum converges in a fewer number of terms and becomes smaller while the spatial domain sum requires more terms to converge and makes a larger contribution.

The question that arises is: Can the parameter c be chosen to minimize the time needed to do the two summations in the spatial and spectral domains? In order to answer

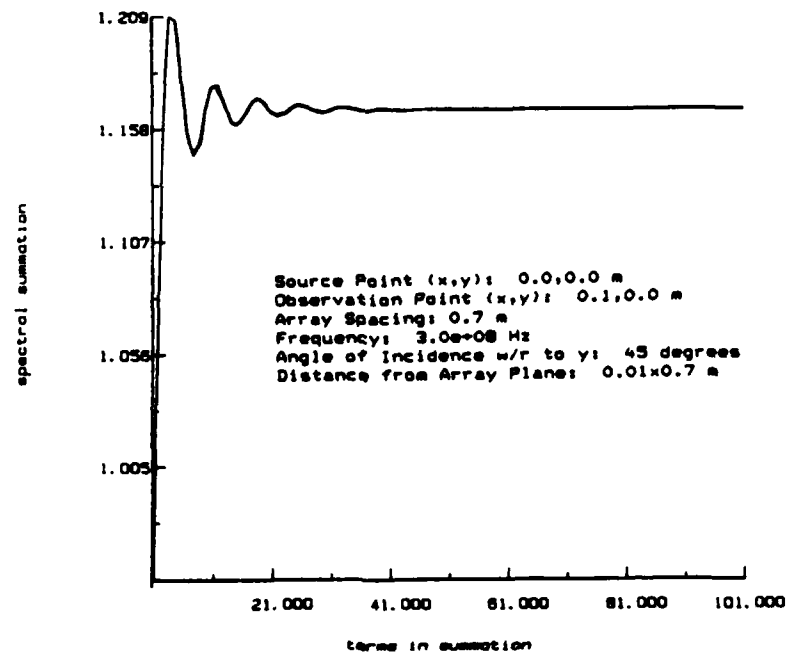
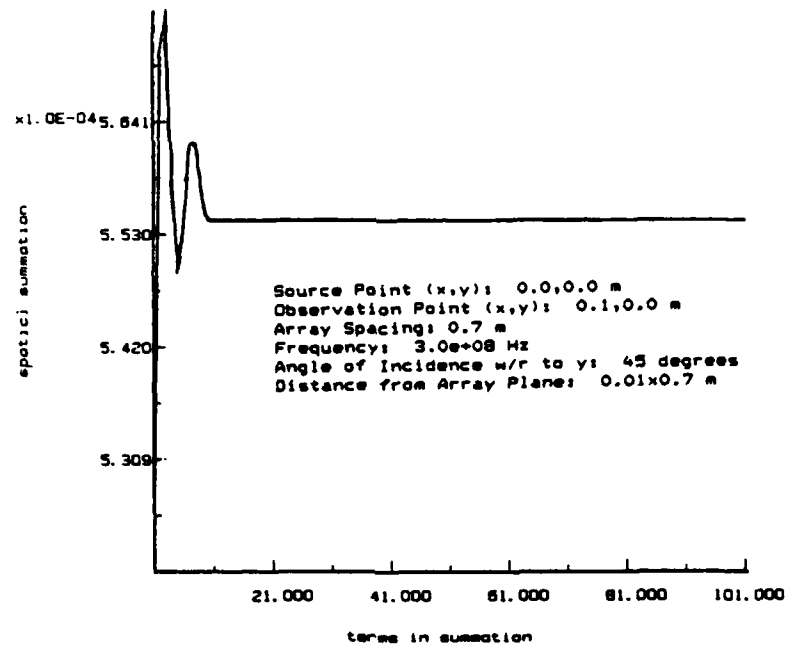


Figure 2.5 Contributions to the periodic Green's function from the spatial domain (top) and the spectral domain (bottom) plotted as a function of the limits of the summation in each domain for $c=0.01$.

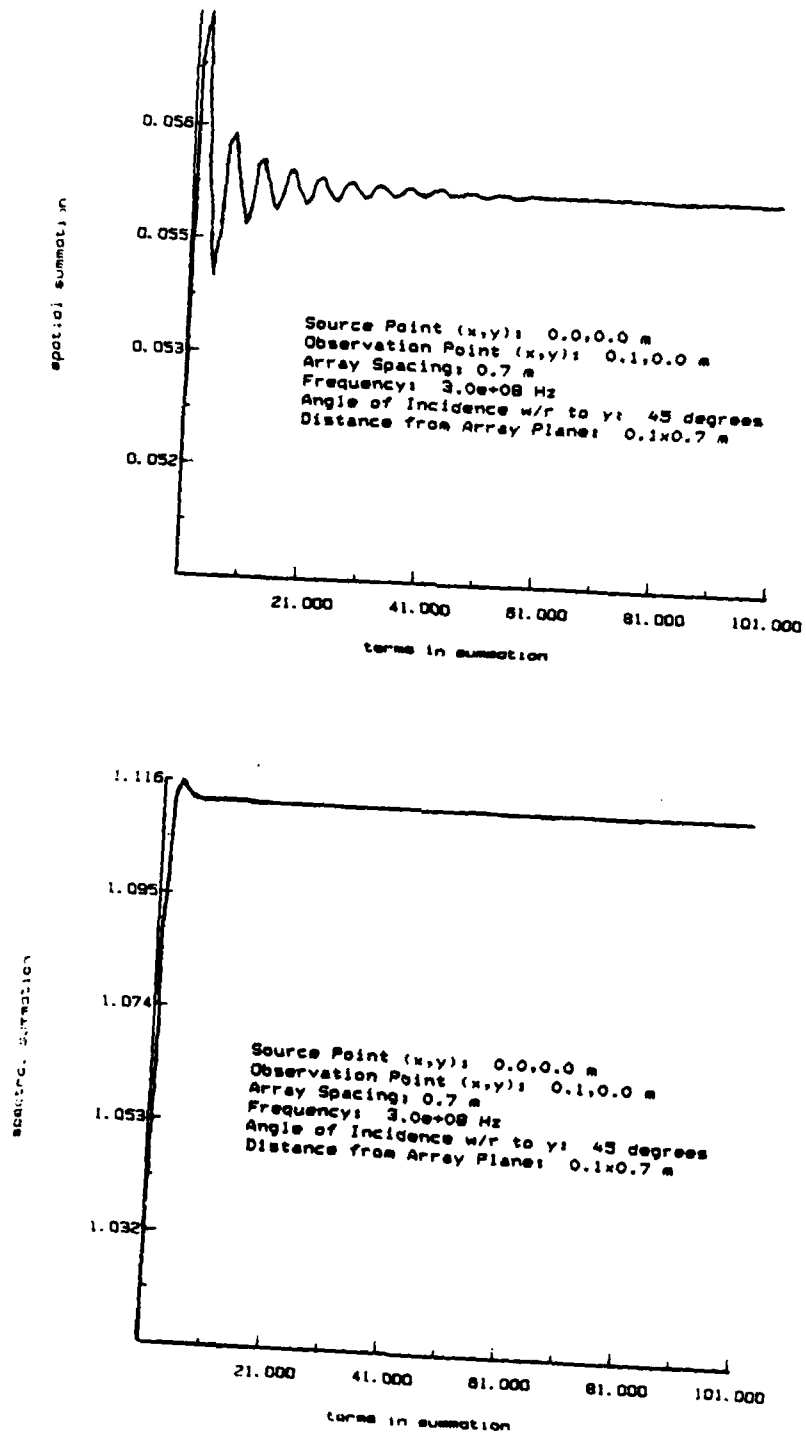


Figure 2.6 Contributions to the periodic Green's function from the spatial domain (top) and the spectral domain (bottom) plotted as a function of the limits of the summation in each domain for $c=0.1$.

this question, a parameter study was performed where the sum limit needed for convergence to a given accuracy in both domains was plotted versus c for various combinations of cell size, frequency, incident angle and test position. What emerged from this study is that although the number of terms needed for convergence changes with the parameters, the general nature of these curves remains essentially constant. An example is shown in Figure 2.7. When c is small, the spectral domain needs many terms to converge and the spatial domain converges immediately. As c increases, the number of spectral terms needed decreases while the number of spatial terms needed increases until at around $c=0.05$, the graphs cross over. The area of cross-over is relatively flat so c can be picked from the range 0.02-0.1 and both domains will be weighted approximately the same.

The true test of optimization, however, is not to minimize the total number of terms needed to perform the spectral and spatial summations, but rather to minimize the computer time needed to perform the calculation in Equation (2.39) or (2.40). The implementation of Equation (2.39) using a pulse basis function of support Δ , located at the origin, and a delta testing function, located at (x_0, y_0) , is subsequently called Method 1. This particular combination of basis and testing functions is used because, as discussed in Section 2.2.4, all calculations involving the periodic Green's function in the electric field integral equation can, through approximation and manipulation of the derivatives, be reduced to using this combination of functions. A numerical Romberg integration routine is used to integrate the prime coordinates of G_p over the one-dimensional pulse in the unit cell. Since the test is a delta function, the integration of the unprimed coordinates becomes an evaluation at the point x_0, y_0 . For each s' chosen by the integration routine along the strip, the spectral and spatial domains of (2.41) are summed to a specified accuracy. When the test is coincident with the basis function, the singularity is removed from the G_p

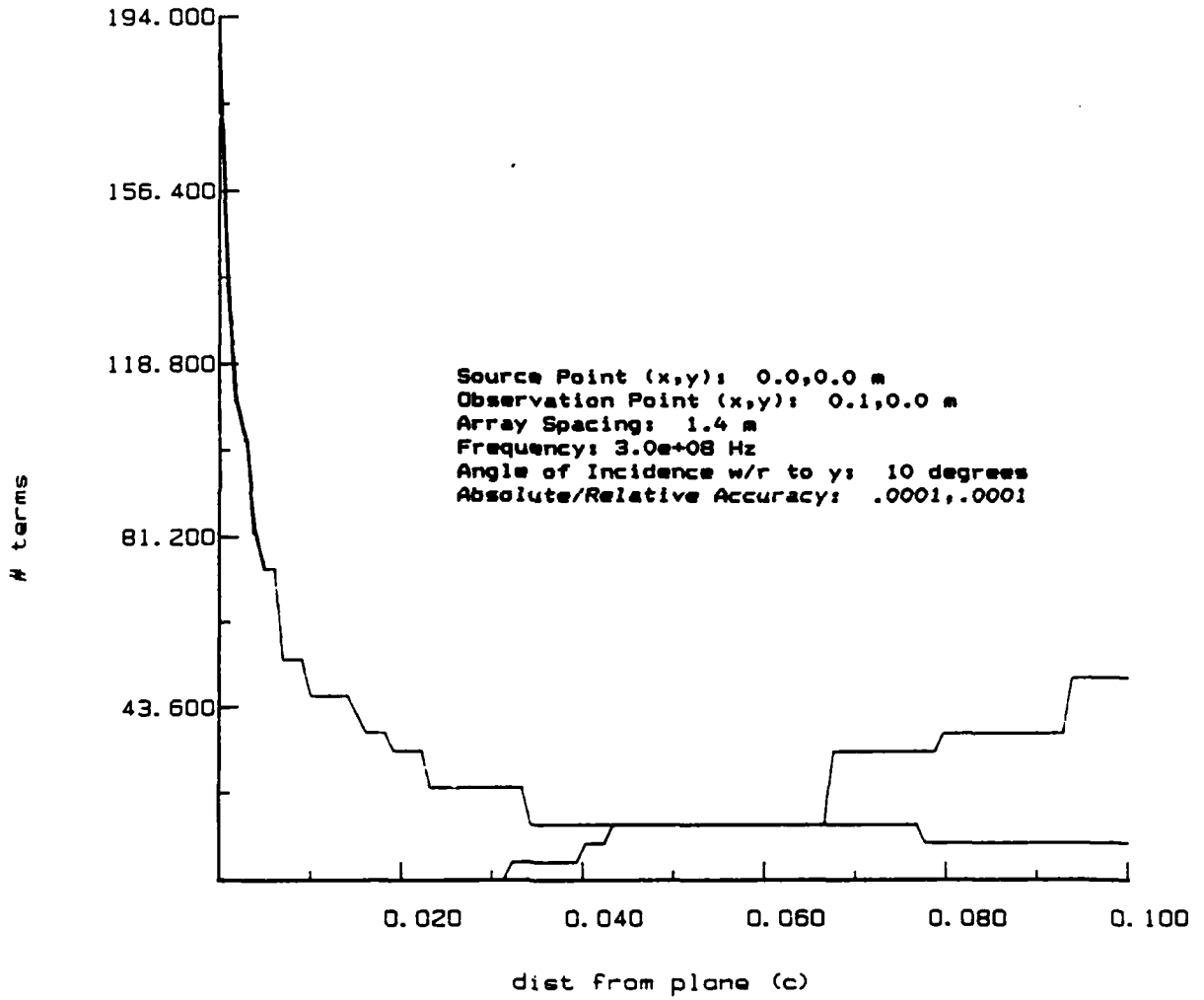


Figure 2.7 Number of terms needed for convergence in the spatial and spectral domains plotted as a function of the parameter c.

term and added back in after being computed analytically. The singularity does not occur in the asymptotic term since the fact that c is greater than zero ensures that the argument of the Hankel function is never zero.

The implementation of Equation (2.40) using pulse basis and delta testing functions is subsequently termed Method 2. In this method, the basis and testing functions are distributed onto the spatial and spectral domains, i.e.,

$$\int T(s) \int J(s') \frac{1}{4j} \sum_{m=-\infty}^{\infty} e^{-jk_x mb} \quad (2.42)$$

$$\left[H_0^2 \left(k_0 \sqrt{(x_0 - x' - mb)^2 + (y_0 - y')^2} \right) - H_0^2 \left(k_0 \sqrt{(x_0 - x' - mb)^2 + (|y_0 - y'| + cb)^2} \right) \right] ds' ds$$

$$+ \frac{1}{b} \sum_{m=-\infty}^{\infty} \int \tilde{T}(\beta_{xm}, y) \int \tilde{J}(\beta_{xm}, y') \frac{e^{-j(|y_0 - y'| + cb)\beta_y}}{2j\beta_y} dy' dy$$

The spatial domain integrations are done numerically, as was done in Method 1, while the spectral domain integrations are calculated analytically. When no overlap exists between \tilde{J} and \tilde{T}^* in y (see Figure 2.8), the spectral domain sum (the last term in Equation (2.42)) becomes

$$\frac{1}{b} \sum_{m=-\infty}^{\infty} \frac{1}{j\beta_y} \frac{\sin(\beta_{xm} \cos\theta \pm \beta_y \sin\theta) \frac{\Delta}{2}}{(\beta_{xm} \cos\theta \pm \beta_y \sin\theta)} e^{+j(\beta_{xm} x_0 - \beta_y |y_0|)} y_0 \begin{cases} < -\Delta/2 \sin\theta \\ > +\Delta/2 \sin\theta \end{cases} \quad (2.43)$$

When \tilde{J} and \tilde{T}^* do overlap in y , the spectral domain summation becomes

$$\frac{1}{b} \sum_{m=-\infty}^{\infty} \left[e^{-j\beta_y y_0} \left| \frac{e^{+jA_1 \frac{\Delta}{2}} - e^{-jA_1 \frac{y_0}{\sin\theta}}}{jA_1} \right| + e^{+j\beta_y y_0} \left| \frac{e^{-jA_2 \frac{y_0}{\sin\theta}} - e^{-jA_2 \frac{\Delta}{2}}}{jA_2} \right| \right] \frac{e^{+j\beta_{xm} x_0}}{2j\beta_y} \quad (2.44)$$

$$A_1 = \beta_{xm} \cos\theta - \beta_y \sin\theta$$

$$A_2 = \beta_{xm} \cos\theta + \beta_y \sin\theta$$

Note that when overlap exists between the basis and test functions, certain terms of

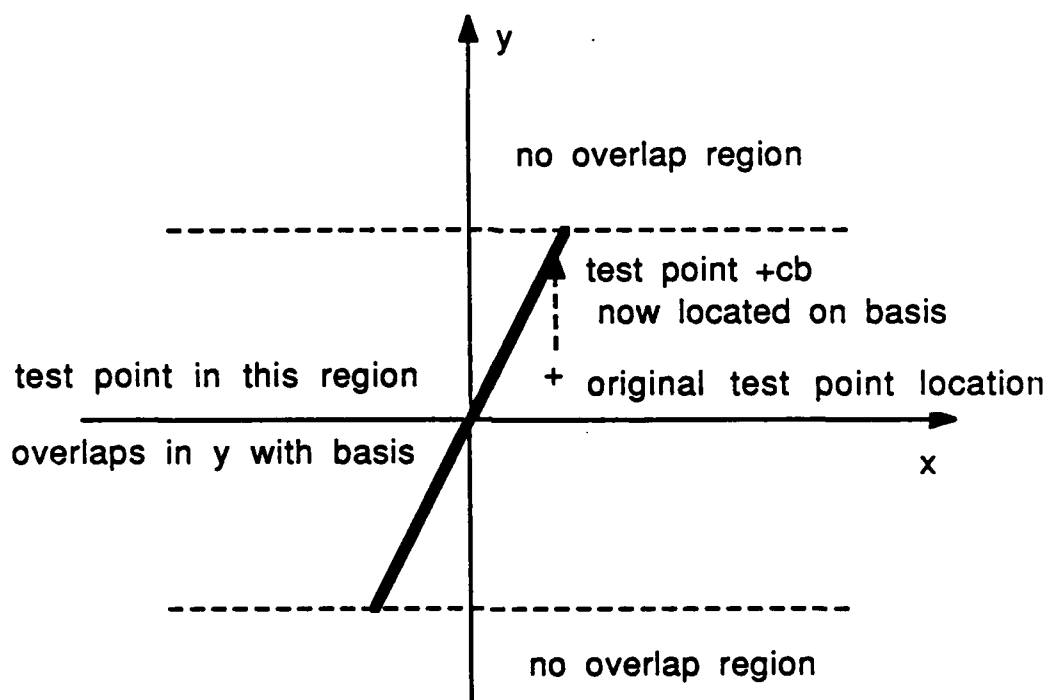


Figure 2.8 Overlapping and non-overlapping regions in y for the basis and testing functions when the basis function is rotated. The undesirable situation where the asymptotic test point is located on the basis function is also shown.

Equation (2.44) decay as $1/\beta_y^2$ but have no exponential decay. In order to obtain exponential convergence, therefore, it is necessary to move the test point of the asymptotic term "off-plane" enough so that no overlap occurs between the basis and test functions. In Method 1, the asymptotic test point $(|y_0 - y'| + cb)$ could be re-chosen for every point called by the integration routine because the spectral and spatial contributions were calculated together. In Method 2, the asymptotic test point must be fixed for the entire calculation because the spectral and spatial contributions are calculated in separate subroutines. This means that in Method 2, it is possible for the asymptotic terms to be singular if c is chosen such that $\sqrt{(x_0 - x' - mb)^2 + (|y_0 - y'| + cb)^2}$ falls on the basis function as shown in Figure 2.8.

Method 3 is similar to Method 2 except that outside a core region ($m = -1:1$) in the summation, the numerical integration is performed by a one-point approximation. Inside the core, where the integrand varies quickly, the integration is performed more accurately.

Figure 2.9 shows the time needed to compute the convolution of pulse basis, delta test and periodic Green's functions using Methods 1, 2, and 3 when the strips lie flat in the plane of periodicity ($\theta = 0^\circ$). Although the calculation time changes with parameters such as test location, frequency, array spacing and incident angle, the shape of the curves remains essentially the same. Method 3 is the fastest method regardless of the parameters, but since it involves an approximation in the spatial domain, it is not as accurate as Methods 1 and 2. This inaccuracy becomes more pronounced as the parameter c increases and the spatial domain gets more weight. In Method 1, if c is too small ($c < 0.01$), too much time is spent summing the spectral domain and the required time for the calculation increases. As c increases ($0.01 < c < 0.08$), the time goes to a minimum then slowly increases as the spatial domain becomes over-weighted.

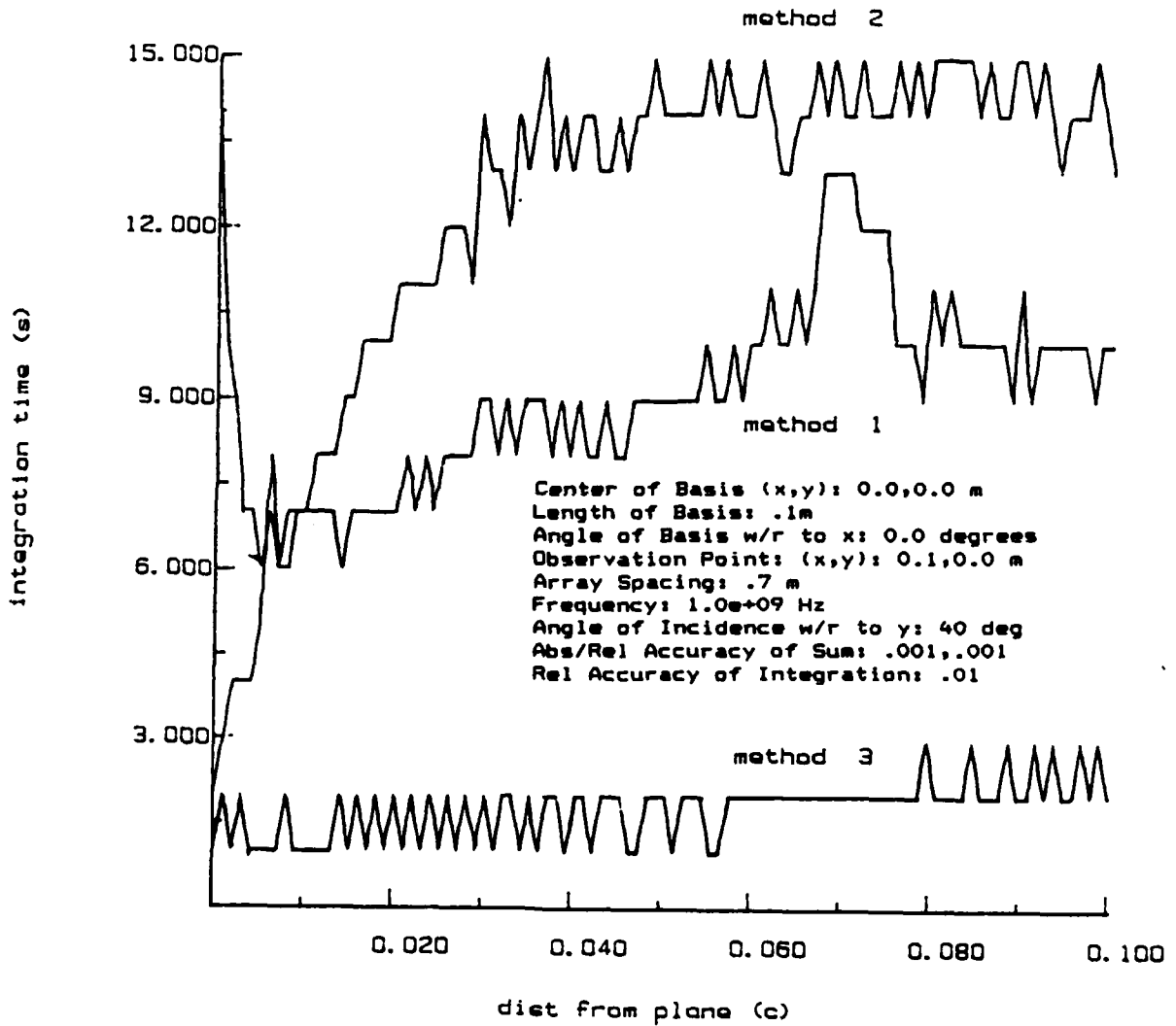


Figure 2.9 Time required to calculate $T^R * J * G_p$ by Methods 1, 2 and 3 as a function of the parameter c for the flat strip case ($\theta = 0^\circ$).

The time requirements for Method 2 are similar to the requirements for Method 3 for small c but increase with increasing c , crossing over Method 1 at around $c=0.02$. Method 2 time is dominated by the time needed to integrate numerically in the spatial domain. Although Method 2 has a simpler integrand than Method 1, it is difficult to specify correctly a consistent accuracy parameter for the summations occurring in the different subroutines of Method 2, and consequently, it requires more time.

In Figure 2.10, the calculation of the self term by Method 1 takes far more time for $c < 0.01$ than could be explained by saying that the spectral sum is overweighted. The explanation for this behavior comes from an examination of the integrand. When c is close to the strip, the integrand is ill-behaved, as shown in Figure 2.11. The singularity has been subtracted only from the nonasymptotic term in the Green's function. When c is small, however, the asymptotic terms are also tending to be singular. Moving the test point of the asymptotic term a larger distance away from the plane of periodicity by increasing c , causes the integrand to become better behaved (Figure 2.12).

When the strip is rotated with respect to the plane of periodicity ($\theta = 45^\circ$), the results, as shown in Figure 2.13, have essentially the same behavior as in the flat case with the exception of two features. The first feature is that Method 1 no longer increases in time when $c < 0.01$ because, since the strip is rotated, most of the points called by the integration routine are farther "off-plane" than the specified "off-plane" factor. The second feature is the drop in time exhibited by both Methods 2 and 3 at $c=0.05$. This occurs because c has moved from the overlap region of the basis function, where the spectral convergence behaves as $1/\beta_y^2$, to the non-overlap region ($c \times .7 > .05 \sin(45^\circ)$), where the convergence is exponential.

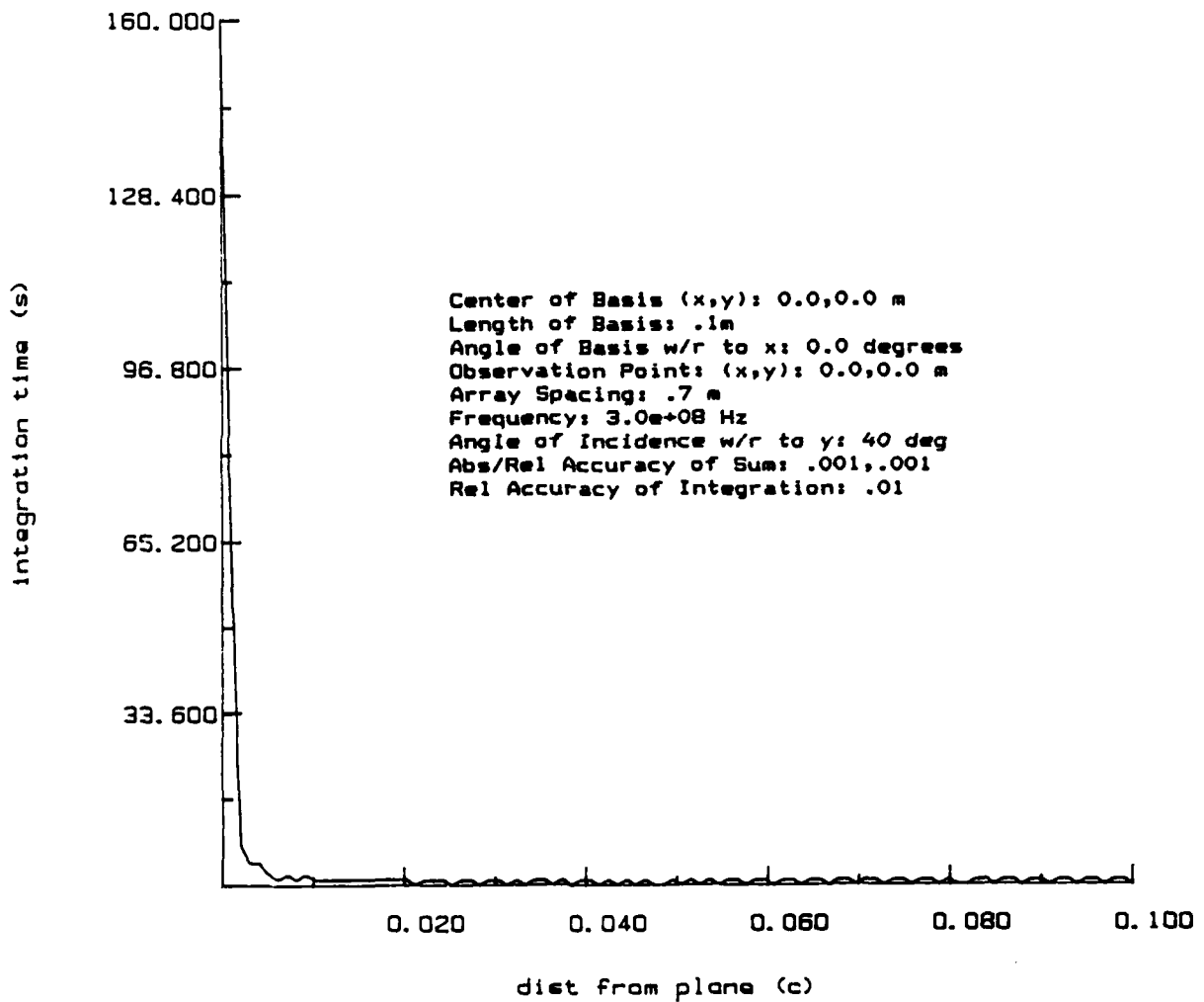


Figure 2.10 Time required to calculate $T^R * J * G_p$ by Method 1 for the self term as a function of c for the flat strip case. Note the time spike when c is small.

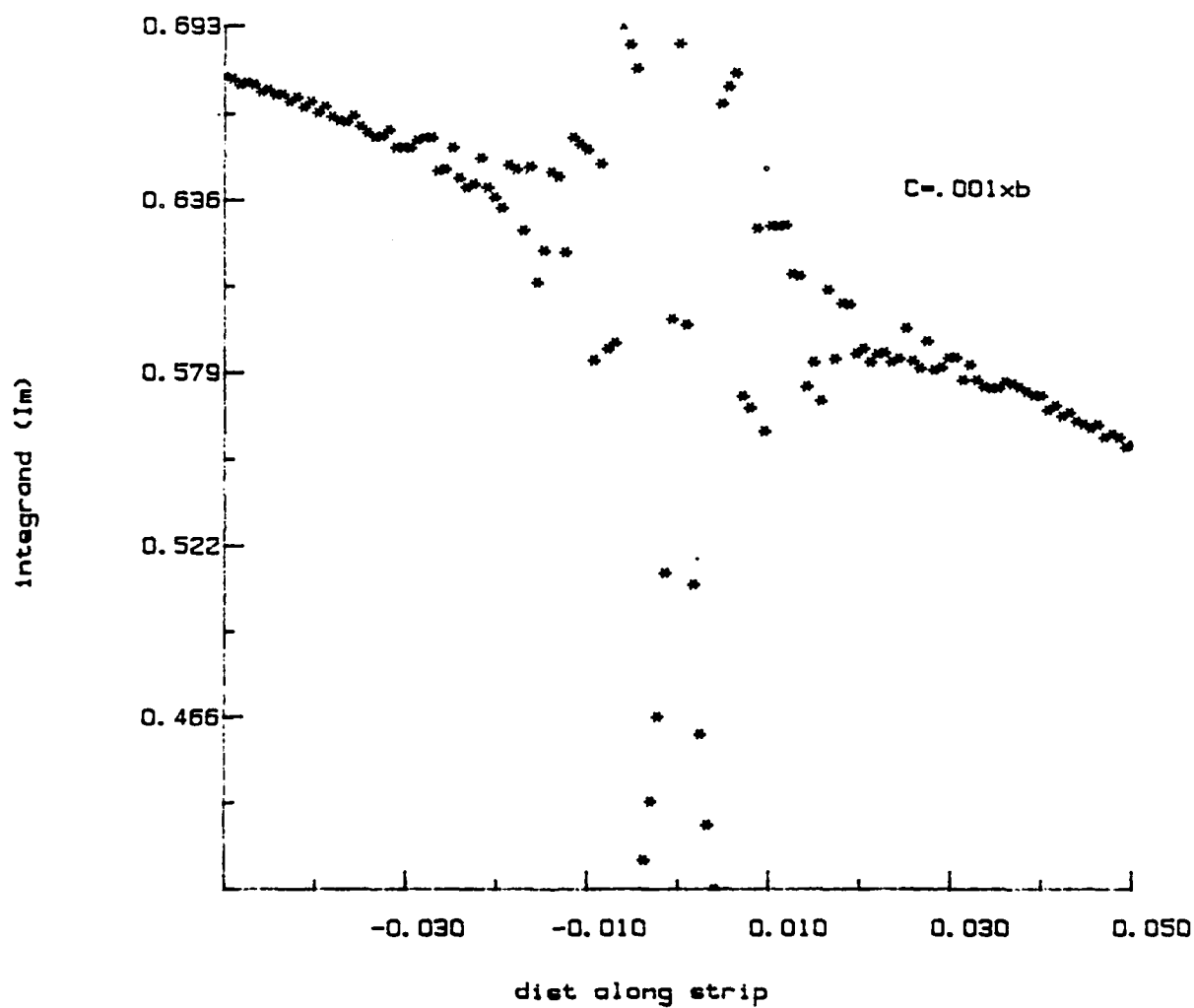


Figure 2.11 Poorly-behaved, imaginary portion of the integrand when $c=0.001$ in Figure 2.10. Integrating this function numerically accounts for the large time required to calculate $T^R * J * G_p$ when c is small.

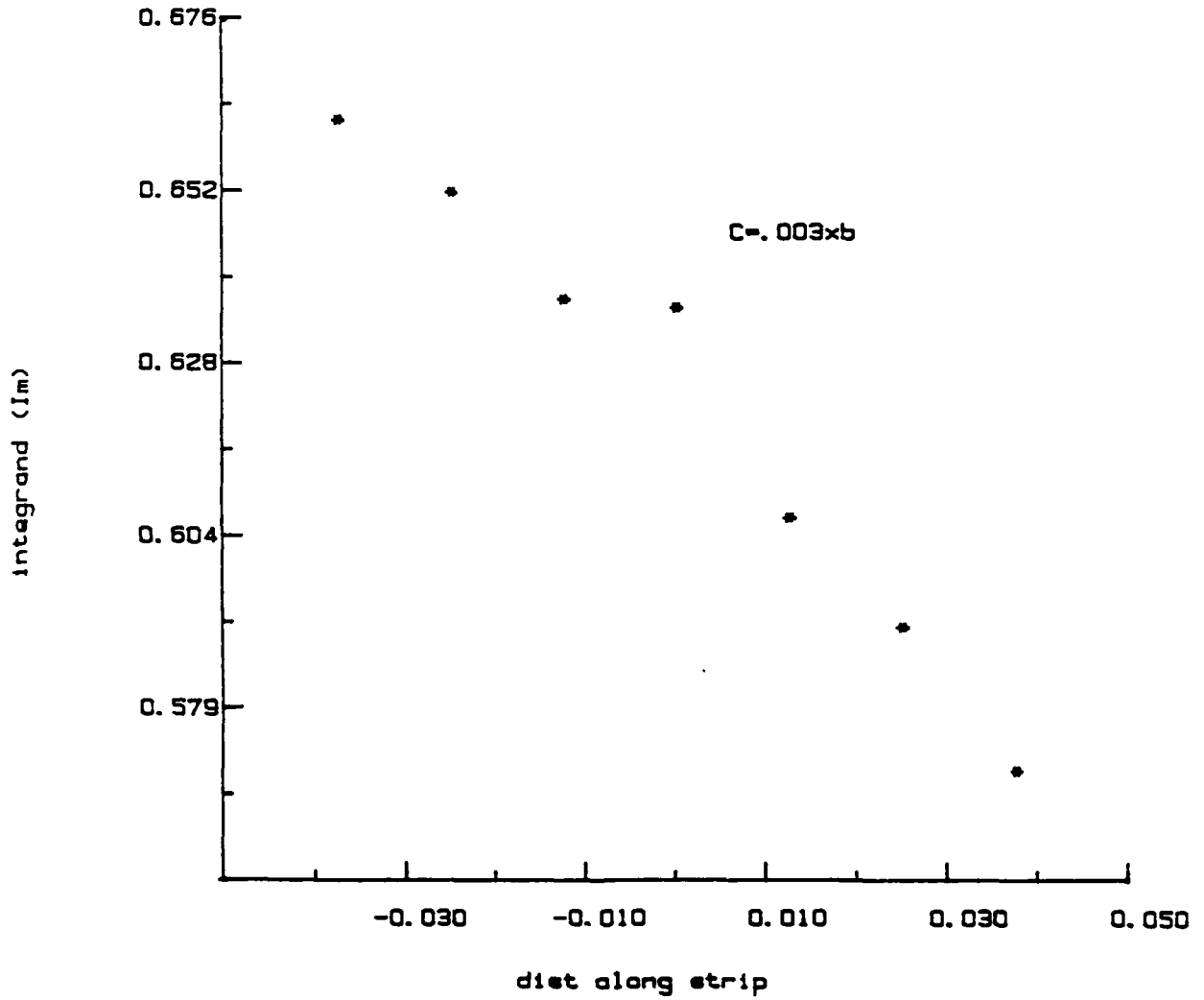


Figure 2.12 Smoother, improved behavior of the imaginary portion of the integrand when c is increased to 0.003 in Figure 2.10.

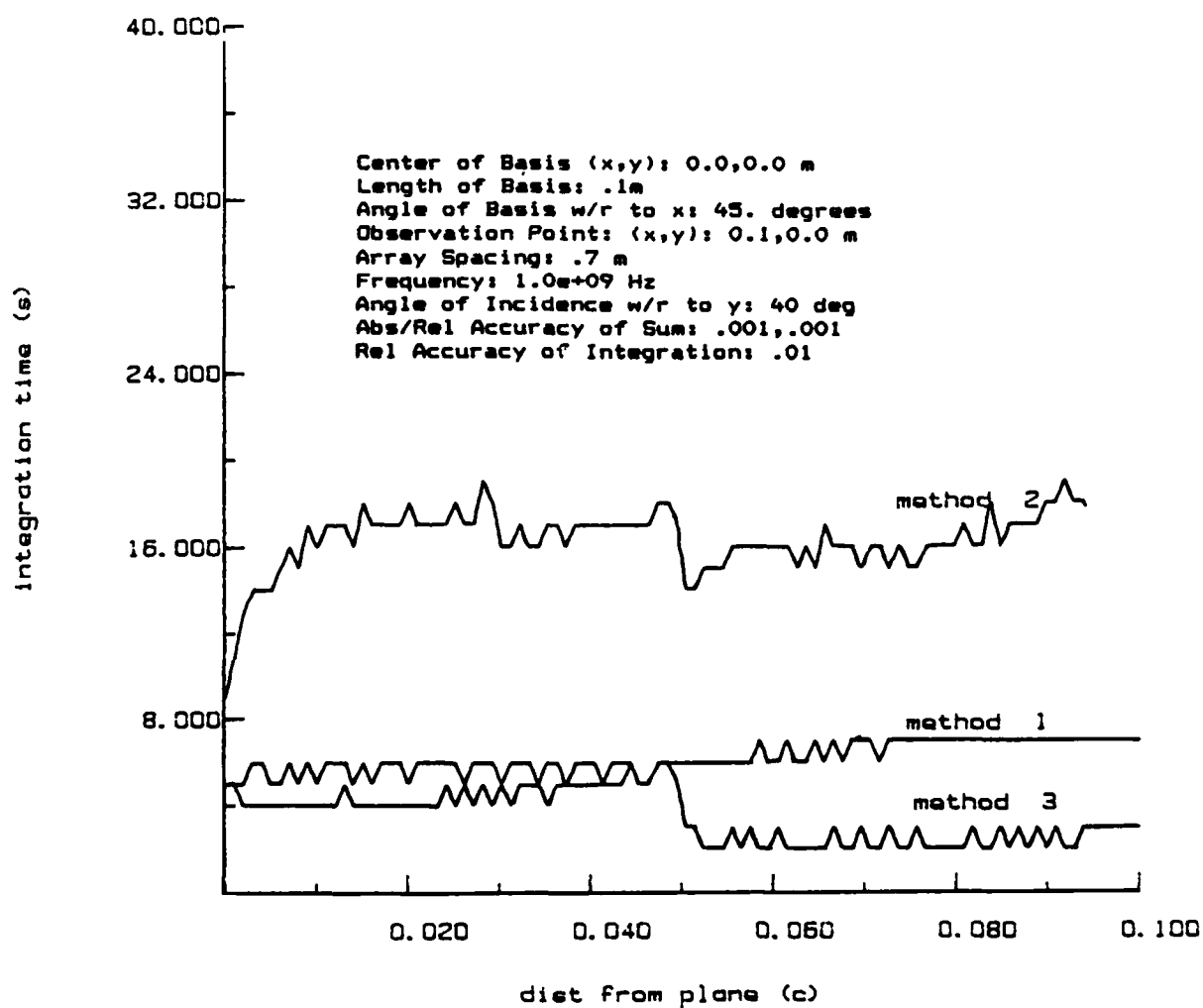


Figure 2.13 Time required to calculate $T^R * J * G_p$ by Methods 1, 2 and 3 as a function of the parameter c for the rotated strip case ($\theta = 45^\circ$).

As c approaches zero in Method 2, the accuracy of the sum must be specified more precisely because the sum is behaving as $1/m^2$ with no exponential decay. To study the region when c approaches zero, Method 2 was summed until four digits of accuracy were obtained in the final answer for all c . The result is shown for a flat strip ($\theta = 0^\circ$) case in Figure 2.14 and for a rotated ($\theta = 45^\circ$) case in Figure 2.15. For the flat case, the best choice for c was found to be $c=0$ for the given size of basis and testing functions. No weighting in the spatial domain is necessary for Method 2, because the smoothness of the basis and testing functions helps convergence for all combinations of these functions. Since the convolution is done analytically in the spectral domain, there is no numerical integration involved. When $c \neq 0$, a numerical integration must be performed which dominates the calculation in time even though the contribution from the integration is small. In the rotated case, the best choice for c is $0.05 < c < 0.15$. Here, smoothness of basis and testing functions does not help convergence in the spectral domain. In order to get exponential convergence, c must be large enough to move the test point "off-plane" (for this to occur for these parameters, $c > 0.05$). In this case, the time needed for numerical integration does not outweigh the time needed to sum in the spectral domain accurately.

2.3 Two-dimensional Periodicity

2.3.1 Definitions of terms

In this section, the concepts developed in Section 2.2 will be extended to examine the formulation of scattering from the two-dimensional array of rectangular plates shown in Figure 2.16. The plates are set on edge and are perpendicular to the plane of periodicity which, in this case, is the xy plane. They are then rotated about the \hat{z} axis to make an angle θ with respect to the \hat{x} axis. The plates are repeated periodically along the skewed axes \hat{S}_1 and \hat{S}_2 . The incident field is a plane wave with a propagation vector making an

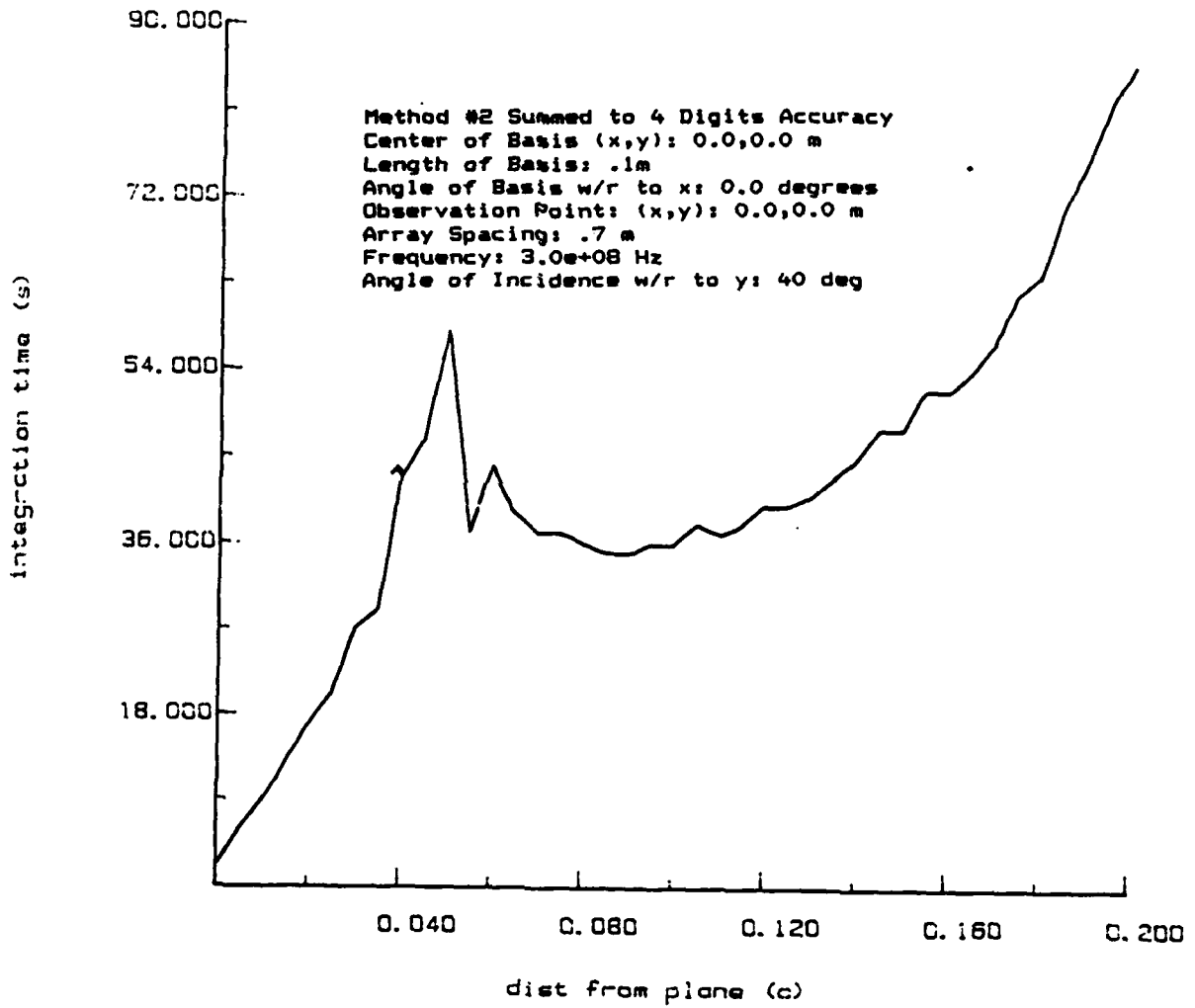


Figure 2.14 Time required to calculate $T^R * J * G_p$ by Method 2 as a function of the parameter c for the flat strip case ($\theta = 0^\circ$) when 4 digit accuracy is specified. Note that the calculation is optimal when $c=0$.

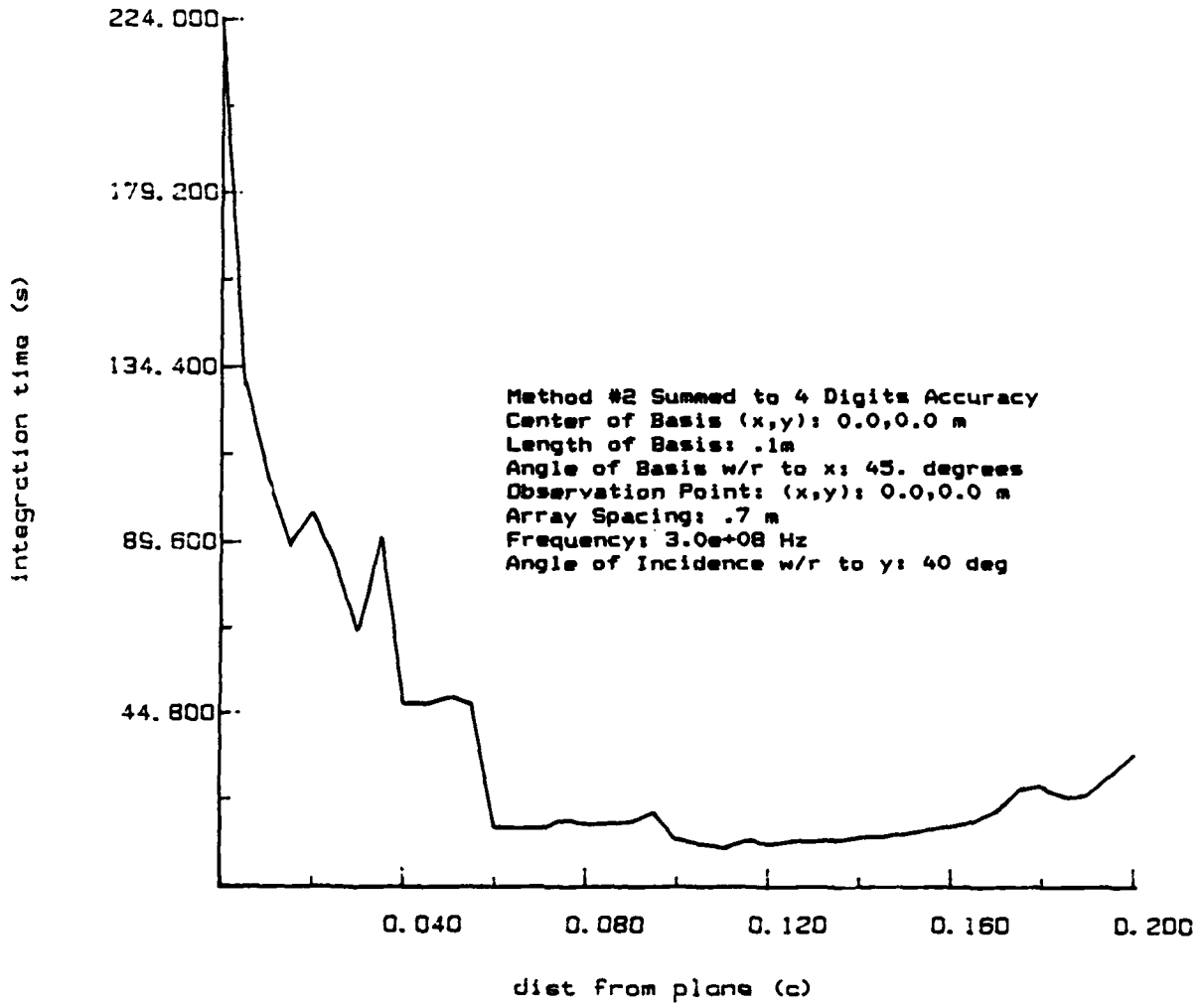


Figure 2.15 Time required to calculate $T^R * J * G_p$ by Method 2 as a function of the parameter c for the rotated strip case ($\theta = 45^\circ$) when 4 digit accuracy is specified.

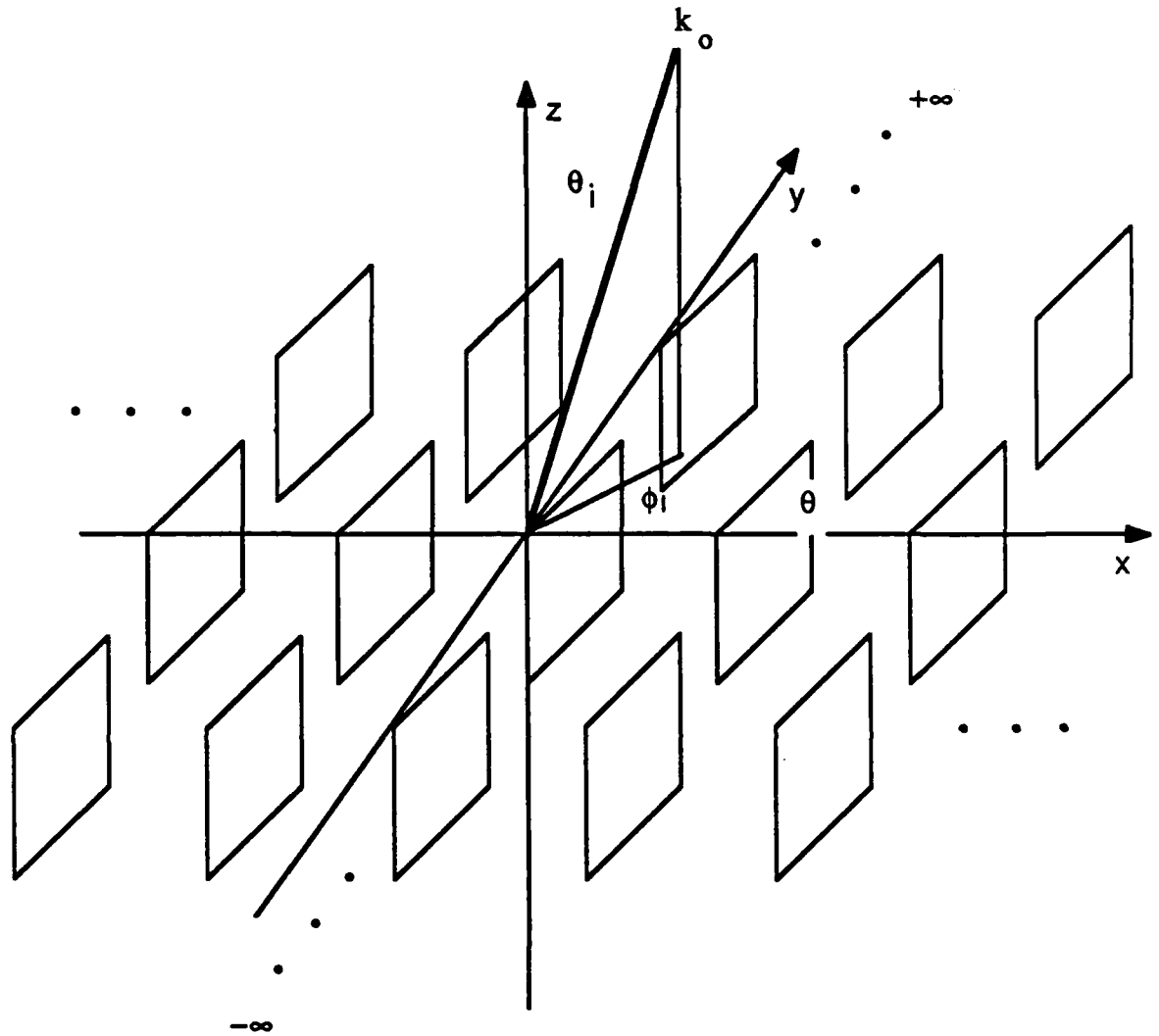


Figure 2.16 Two-dimensional plate array geometry. The rectangular plates are set on edge, perpendicular to the xy plane and rotated θ degrees with respect to \hat{x} . The incident plane wave is also shown.

angle of θ_i with respect to \hat{z} and ϕ_i with respect to \hat{x} . The incident field is polarized TE or TM to \hat{z} .

The Fourier transform needed for the two-dimension array is

$$\tilde{F}(\beta_x, \beta_y) = \iint f(x, y) e^{-j(\beta_x x + \beta_y y)} dx dy \quad (2.45a)$$

$$f(x, y) = \frac{1}{(2\pi)^2} \iint \tilde{F}(\beta_x, \beta_y) e^{+j(\beta_x x + \beta_y y)} d\beta_x d\beta_y \quad (2.45b)$$

where $f(x, y)$ is a function in the space domain and $\tilde{F}(\beta_x, \beta_y)$ is its Fourier transform representation in the spectral domain.

The spatial lattice for this problem, as shown in Figure 2.17, is defined by use of a translation vector $\vec{\rho}_{mn}$.

$$\begin{aligned} \vec{\rho} &= \vec{\rho} + \vec{\rho}_{mn} \\ &= \vec{\rho} + m\hat{S}_1 + n\hat{S}_2 \end{aligned} \quad (2.46)$$

where \hat{S}_1 and \hat{S}_2 are the primitive vectors defined as

$$\hat{S}_1 = c\hat{y} \quad (2.47a)$$

$$\hat{S}_2 = d \cos \Omega \hat{x} + d \sin \Omega \hat{y} \quad (2.47b)$$

Therefore, the translation vector in Cartesian coordinates is

$$\vec{\rho}_{mn} = (nd \cos \Omega) \hat{x} + (mc + nd \sin \Omega) \hat{y} \quad (2.48)$$

The reciprocal lattice is defined through the use of a reciprocal translation vector \vec{K}_{mn} .

$$\begin{aligned} \vec{K}' &= \vec{K} + \vec{K}_{mn} \\ &= \vec{K} + m\tilde{S}_1 + n\tilde{S}_2 \end{aligned} \quad (2.49)$$

The reciprocal primitive lattice vectors, \tilde{S}_1 and \tilde{S}_2 , are defined such that the relations

$$\hat{S}_1 \cdot \tilde{S}_1 = 2\pi \quad \hat{S}_2 \cdot \tilde{S}_1 = 0 \quad (2.50)$$

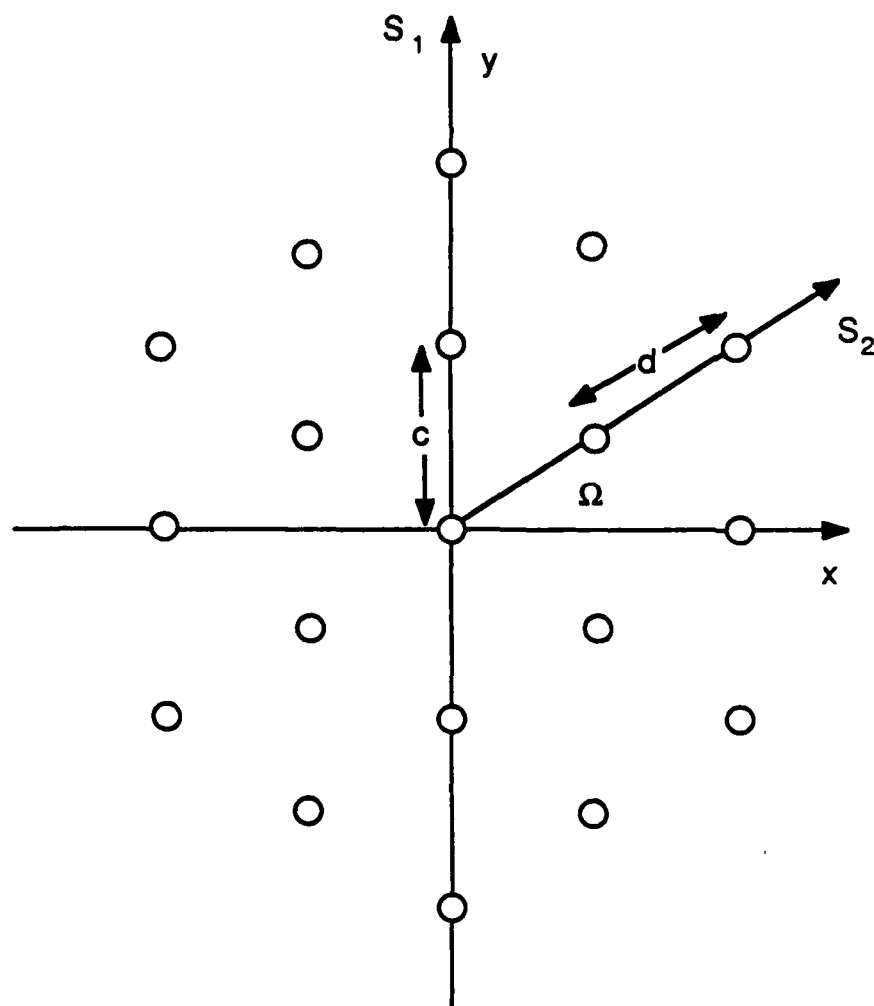


Figure 2.17 Two-dimensional spatial lattice showing the periodicity along the skewed axes S_1 and S_2 . S_1 is parallel to \hat{y} . S_2 makes an angle of Ω with respect to \hat{x} .

$$\hat{S}_1 \cdot \tilde{S}_2 = 0 \quad \hat{S}_2 \cdot \tilde{S}_2 = 2\pi$$

are true. Therefore,

$$\tilde{S}_1 = \frac{2\pi}{c \cos \Omega} \left[\hat{y} \cos \Omega - \hat{x} \sin \Omega \right] \quad (2.51a)$$

$$\hat{S}_2 = \frac{2\pi}{d \cos \Omega} \hat{x} \quad (2.51b)$$

and the reciprocal translation vector in Cartesian coordinates becomes

$$\vec{K}_{mn} = 2\pi \left[\frac{n}{d \cos \Omega} - \frac{m \sin \Omega}{c \cos \Omega} \right] \hat{x} + \frac{2\pi m}{c} \hat{y} \quad (2.52)$$

The reciprocal primitive lattice vectors are shown in relation to the spatial primitive lattice vectors in Figure 2.18.

2.3.2 Formulation of G_p

The electric field integral equation (Equation (2.9)) is used to analyze the doubly periodic array of plates. As with the strip case, the Green's function is defined as the vector potential response to an array of point sources. In the spatial domain, an array of point sources located at x', y', z' in each unit cell may be represented as

$$J_a(x, y, z) = \sum_{m=-\infty}^{\infty} \sum_{n=-\infty}^{\infty} \delta(\vec{\rho} - \vec{\rho}' - \vec{\rho}_{mn}) e^{-j\vec{k}_0 \cdot \vec{\rho}_{mn}} \delta(z - z') \quad (2.53)$$

The response at x_0, y_0, z_0 due to each point source may be summed to obtain

$$G_p(\vec{r}_0 | \vec{r}') = \sum_{m=-\infty}^{\infty} \sum_{n=-\infty}^{\infty} e^{-j\vec{k}_0 \cdot \vec{\rho}_{mn}} \frac{e^{-jk_0 \sqrt{|\vec{\rho}_0 - \vec{\rho}' - \vec{\rho}_{mn}|^2 + (z_0 - z')^2}}}{4\pi \sqrt{|\vec{\rho}_0 - \vec{\rho}' - \vec{\rho}_{mn}|^2 + (z_0 - z')^2}} \quad (2.54)$$

In the spectral domain, a point source array may be expressed as a double summation of current sheets through the use of the Fourier transform pair (Equation (2.45)). Each of the current sheets has a period dictated by the reciprocal lattice and a cell-to-cell phase shift dictated by the incident field.

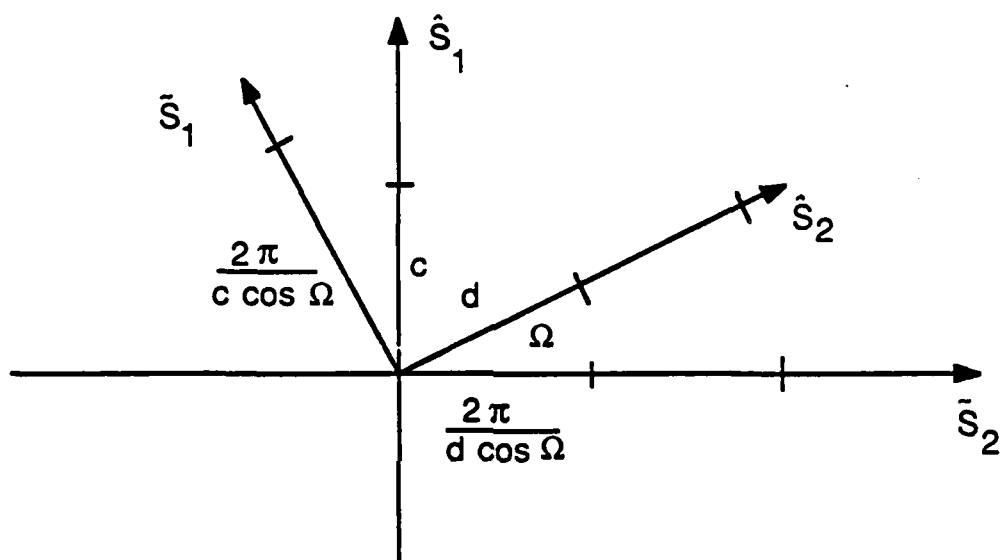


Figure 2.18 Spatial (\hat{S}) and reciprocal (\tilde{S}) primitive lattice vectors showing the period and orientation of each.

$$J_a(x, y, z) = \frac{1}{C.A.} \sum_{m=-\infty}^{\infty} \sum_{n=-\infty}^{\infty} e^{+j(\vec{K}_{mn} - \vec{k}_0) \cdot (\vec{r} - \vec{r}')} \delta(z - z') \quad (2.55)$$

C.A. is the area of the unit cell, \vec{K}_{mn} is defined in Equation (2.52) above and \vec{k}_0 is the propagation constant of the incident wave. Adding the response at x_0, y_0, z_0 to each current sheet, the following equation is obtained:

$$G_p(\vec{r}_0 | \vec{r}') = \frac{1}{C.A.} \sum_{m=-\infty}^{\infty} \sum_{n=-\infty}^{\infty} \frac{e^{-j\gamma|z_0 - z'|} e^{+j(\vec{K}_{mn} - \vec{k}_0) \cdot (\vec{r}_0 - \vec{r}')}}{2j\gamma} \quad (2.56)$$

where application of the radiation condition yields

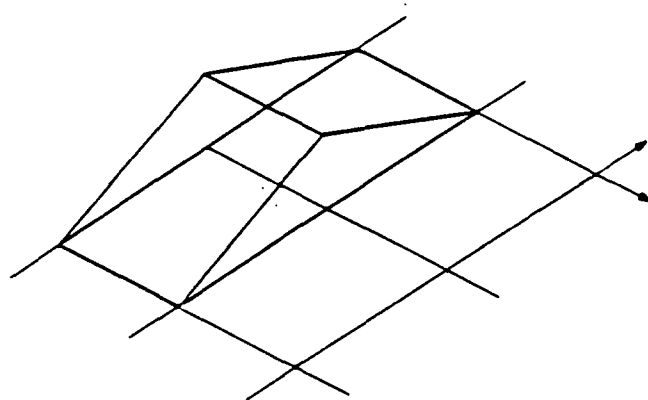
$$\gamma = \begin{cases} \sqrt{k_0^2 - \beta_{xmn}^2 - \beta_{ym}^2} & \text{if } k_0^2 > \beta_{xmn}^2 + \beta_{ym}^2 \\ -j \sqrt{\beta_{xmn}^2 + \beta_{ym}^2 - k_0^2} & \text{if } \beta_{xmn}^2 + \beta_{ym}^2 > k_0^2 \end{cases} \quad (2.57)$$

$$\beta_{xmn} = (\vec{K}_{mn} - \vec{k}_0) \cdot \hat{x} = 2\pi \left| \frac{n}{d \cos \Omega} - \frac{m \sin \Omega}{c \cos \Omega} \right| - k_x$$

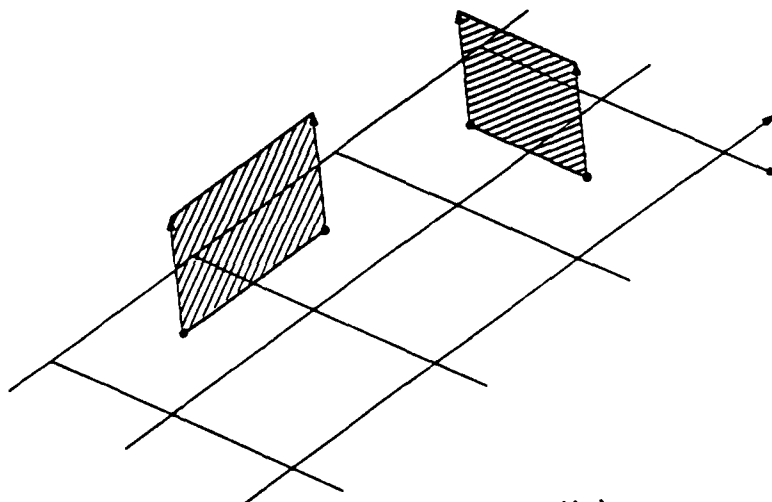
$$\beta_{ym} = (\vec{K}_{mn} - \vec{k}_0) \cdot \hat{y} = \frac{2\pi m}{c} - k_y$$

The spatial domain formulation of G_p converges slowly for the same reasons given previously for the strip array in Section 2.2.3. The spectral formulation converges rapidly when $z_0 \neq z'$, the "off-plane" case, and converges slowly when $z_0 = z'$, the "on-plane" case. As with the strip array, since the plates do not lie flat in the xy plane, the derivatives of the scalar potential term may not be transferred onto the Green's function, rather the derivatives must be transferred explicitly onto the basis and testing functions.

In order for the subsequent integrations to make sense, rooftop basis and razor testing functions, shown in Figure 2.19, are chosen to discretize the problem. Making the same approximations and transfer of derivatives as in the previous section [47], all of the impedance matrix calculations are reduced to the same form: finding the response at a



(a)



(b)

Figure 2.19 Rooftop basis functions (a) and razor testing functions (b).

point x_0, y_0, z_0 due to a two-dimensional array of two-dimensional current pulses located on the spatial lattice.

2.3.3 Acceleration of convergence in spatial domain

In order to accelerate the convergence of the spatial domain sum (Equation (2.54)), the asymptotic behavior of e^{-jkR}/R is subtracted from and added to the periodic Green's function by moving off the xy plane, cCA units.

$$\sum_{m=-\infty}^{\infty} \sum_{n=-\infty}^{\infty} e^{-j\vec{k}_0 \cdot \vec{\rho}_{mn}} \frac{e^{-jk_0 \sqrt{|\vec{\rho}_0 - \vec{\rho}' - \vec{\rho}_{mn}|^2 + (z_0 - z')^2}}}{4\pi \sqrt{|\vec{\rho}_0 - \vec{\rho}' - \vec{\rho}_{mn}|^2 + (z_0 - z')^2}} = \sum_{m=-\infty}^{\infty} \sum_{n=-\infty}^{\infty} e^{-j\vec{k}_0 \cdot \vec{\rho}_{mn}} \quad (2.58)$$

$$\left[\frac{e^{-jk_0 \sqrt{|\vec{\rho}_0 - \vec{\rho}' - \vec{\rho}_{mn}|^2 + (z_0 - z')^2}}}{4\pi \sqrt{|\vec{\rho}_0 - \vec{\rho}' - \vec{\rho}_{mn}|^2 + (z_0 - z')^2}} - \frac{e^{-jk_0 \sqrt{|\vec{\rho}_0 - \vec{\rho}' - \vec{\rho}_{mn}|^2 + (|z_0 - z'| + cCA)^2}}}{4\pi \sqrt{|\vec{\rho}_0 - \vec{\rho}' - \vec{\rho}_{mn}|^2 + (|z_0 - z'| + cCA)^2}} \right]$$

$$+ \sum_{m=-\infty}^{\infty} \sum_{n=-\infty}^{\infty} e^{-j\vec{k}_0 \cdot \vec{\rho}_{mn}} \frac{e^{-jk_0 \sqrt{|\vec{\rho}_0 - \vec{\rho}' - \vec{\rho}_{mn}|^2 + (|z_0 - z'| + cCA)^2}}}{4\pi \sqrt{|\vec{\rho}_0 - \vec{\rho}' - \vec{\rho}_{mn}|^2 + (|z_0 - z'| + cCA)^2}}$$

The first summation remains in the spatial domain and converges rapidly because the asymptotic behavior is subtracted out. The second summation is smooth, nonsingular and slowly converging. It is brought into the spectral domain by means of the Poisson summation formula.

For a two-dimensional space, Parseval's theorem is

$$\iint h(x, y) f(x, y) dx, dy = \frac{1}{4\pi^2} \iint \tilde{H}(-\beta_x, -\beta_y) \tilde{F}(\beta_x, \beta_y) d\beta_x d\beta_y \quad (2.59)$$

If $h(x, y)$ is a comb function distributed along the spatial lattice with a cell-to-cell phase shift,

$$h(x, y) = \sum_{m=-\infty}^{\infty} \sum_{n=-\infty}^{\infty} \delta(\vec{\rho} - \vec{\rho}_{mn}) e^{-j\vec{k}_0 \cdot \vec{\rho}_{mn}}, \quad (2.60a)$$

then $\tilde{H}(\beta_x, \beta_y)$ is also a comb function distributed along the reciprocal lattice.

$$\tilde{H}(\beta_x, \beta_y) = \frac{4\pi^2}{C.A.} \sum_{m=-\infty}^{\infty} \sum_{n=-\infty}^{\infty} \delta(\vec{K} - (\vec{K}_{mn} - \vec{k}_0)) \quad (2.60b)$$

Application of Parseval's theorem to the second sum of Equation (2.58) yields

$$\frac{1}{C.A.} \sum_{m=-\infty}^{\infty} \sum_{n=-\infty}^{\infty} \frac{e^{-j\gamma(|z-z'|+cCA)}}{2j\gamma} e^{+j(\vec{K}_{mn}-\vec{k}_0)\cdot(\vec{p}_0-\vec{p})} \quad (2.61)$$

where γ is defined by Equation (2.57).

2.3.4 Numerical implementation of the spatial domain acceleration

As with the strip problem, the time needed to calculate the convolution of a two-dimensional current pulse with the periodic Green's function tested with a delta function was plotted for three different methods. In this section, c is multiplied by the unit cell area (C.A.).

Method 1 integrates the periodic Green's function (Equation (2.58)) over a two-dimensional patch numerically using a Romberg integration routine. The patch has dimensions Δ_x by Δ_y , is centered at the origin and makes an angle of θ with respect to \hat{x} . For every x', y', z' chosen by the routine, the spectral and spatial domains are summed to accuracy. When the test is coincident with the basis function, the singularity is removed from the non-asymptotic term and added back in analytically. The singularity does not occur in the asymptotic terms since c is greater than zero. Figure 2.20 shows the time behavior of Method 1 for a 0.1m x 0.1m basis arranged on a regular hexagonal lattice. The time required to calculate the matrix element for a plate array is similar to the time required for a strip array. If c is too small ($c < 0.02$), the spectral domain is overweighted, and if c is too large ($c > 0.12$), the spatial domain is overweighted. The time needed to calculate the matrix element for the plate array is approximately the time needed to calculate the strip array matrix element raised to the fourth power.

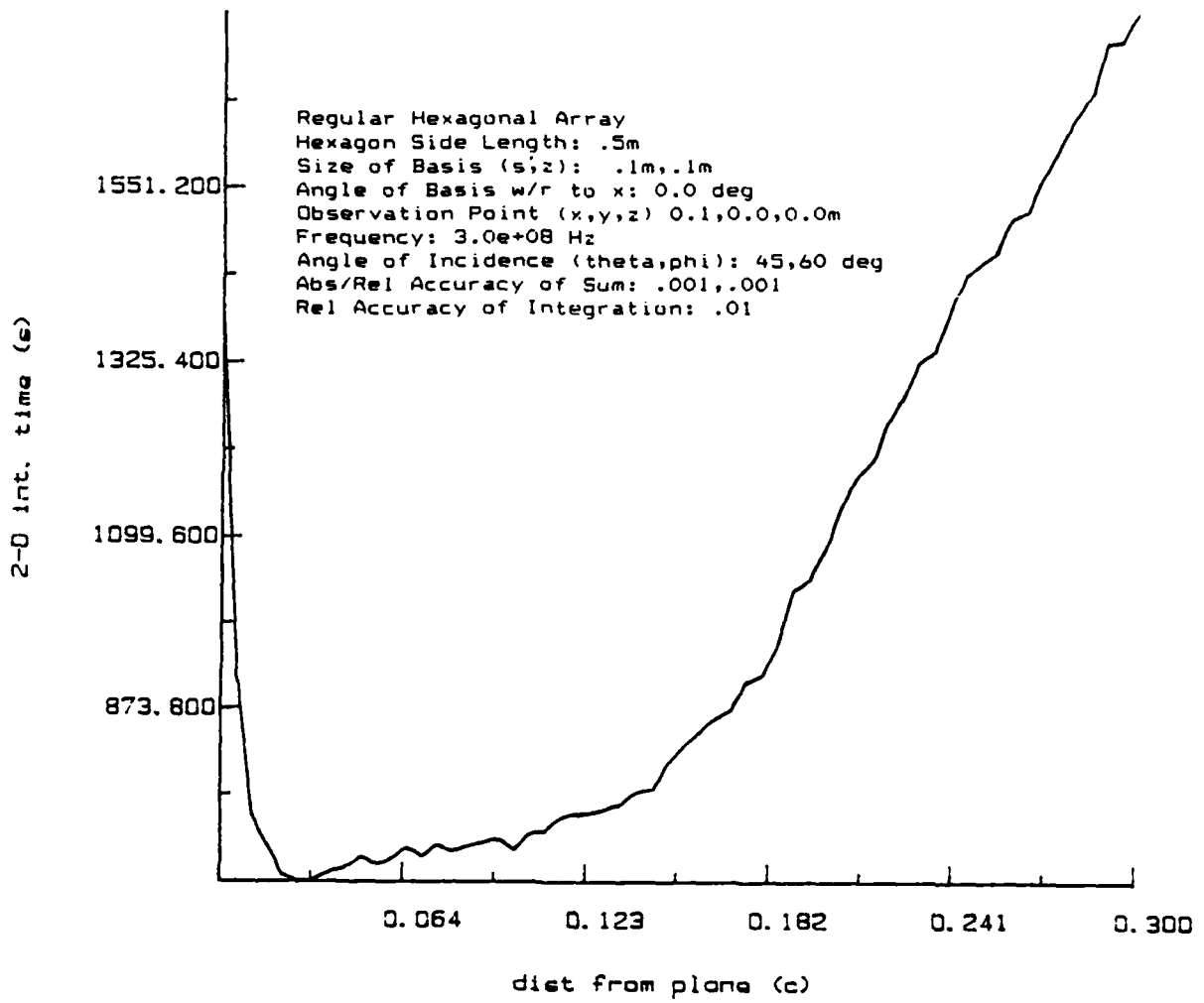


Figure 2.20 Time required to calculate $T^R * J * G_p$ by Method 1 as a function of the parameter c for plates arranged on a hexagonal array.

Method 2 distributes the basis and testing functions onto the spatial and spectral domains.

$$\int \int T(\rho, z) \int \int J(\rho', z') \sum_{m=-\infty}^{\infty} \sum_{n=-\infty}^{\infty} e^{-jk_0 \vec{\rho}_{mn}} \quad (2.62)$$

$$\left[\frac{e^{-jk_0 \sqrt{|\vec{\rho}_0 - \vec{\rho}' - \vec{\rho}_{mn}|^2 + (z_0 - z')^2}}}{4\pi \sqrt{|\vec{\rho}_0 - \vec{\rho}' - \vec{\rho}_{mn}|^2 + (z_0 - z')^2}} - \frac{e^{-jk_0 \sqrt{|\vec{\rho}_0 - \vec{\rho}' - \vec{\rho}_{mn}|^2 + (|z_0 - z'| + cCA)^2}}}{4\pi \sqrt{|\vec{\rho}_0 - \vec{\rho}' - \vec{\rho}_{mn}|^2 + (|z_0 - z'| + cCA)^2}} \right] \frac{d\rho' dz'}{d\rho dz}$$

$$+ \frac{1}{C.A.} \sum_{m=-\infty}^{\infty} \sum_{n=-\infty}^{\infty} \int \tilde{T}^*(\beta_x, \beta_y, z) \int \tilde{J}(\beta_x, \beta_y, z') \frac{e^{-j\gamma(|z_0 - z'| + cCA)}}{2j\gamma} dz' dz$$

The spatial domain integration is performed numerically, while the spectral domain integration is performed analytically. When there is no overlap in \hat{z} between \tilde{J} and \tilde{T}^* , the spectral domain contribution becomes

$$\frac{1}{C.A.} \sum_{m=-\infty}^{\infty} \sum_{n=-\infty}^{\infty} \left| \frac{e^{-jA_1 \frac{\Delta_z}{2}} - e^{+jA_1 \frac{\Delta_z}{2}}}{-jA_1} \right| \left| \frac{e^{+j(\beta_{xmn} x_0 + \beta_{ym} y_0)}}{2j\gamma} \right| \quad (2.63a)$$

$$\left| \frac{e^{+j\gamma \left(\frac{\Delta_z}{2} - |z_0| \right)} - e^{-j\gamma \left(\frac{\Delta_z}{2} + |z_0| \right)}}{j\gamma} \right|$$

With overlap the spectral domain contribution becomes

$$\frac{1}{C.A.} \sum_{m=-\infty}^{\infty} \sum_{n=-\infty}^{\infty} \left| \frac{e^{-jA_1 \frac{\Delta_z}{2}} - e^{+jA_1 \frac{\Delta_z}{2}}}{-jA_1} \right| \left| \frac{e^{+j(\beta_{xmn} x_0 + \beta_{ym} y_0)}}{2j\gamma} \right| \quad (2.63b)$$

$$\left| \frac{2 - e^{-j \left(\frac{\Delta_z}{2} + z_0 \right)} - e^{-j \left(\frac{\Delta_z}{2} - z_0 \right)}}{j\gamma} \right|$$

where

$$A_1 = \beta_{xmn} \cos\theta + \beta_{ym} \sin\theta$$

Since the spectral and spatial domain contributions are integrated separately, the test point of the asymptotic terms must be fixed for the entire calculation. The asymptotic

test point must not fall on the basis function since the singularity of the asymptotic term is not taken into account. Method 3 is the same as Method 2 with a point approximation for the spatial domain integral outside the core region $(m-1:1, n-1:1)$ of the summation.

Figure 2.21 shows the typical calculation time needed for all three methods. In all cases, Method 3 is fastest at the cost of accuracy. Method 1 is most accurate for all values of c . Method 1 shows optimum time behavior in the $0.01 < c < 0.1$ range where the weighting of the spectral and spatial domain is approximately equal. Methods 2 and 3 show a drop in time at $c = .08$ where the spectral domain test point moves out of the overlap region with the basis function and gets exponential convergence.

2.4 Conclusions for Convergence

The periodic problem may be formulated in terms of responses to line/point sources (spatial domain) or in terms of responses to current sheets (spectral domain). The spatial domain is slowly convergent everywhere, while the spectral domain is only slowly convergent in the "on-plane" case, when the testing function is located in the array plane. The slow convergence in one domain stems from an unavoidable singularity in the reciprocal domain.

If the basis function is located entirely in the array plane (flat case), the derivatives may be transferred onto the Green's function and the smoothness of the basis and testing functions may be used to help convergence. If, on the other hand, the basis function is rotated out of the array plane, then all derivatives in the expression must be transferred explicitly onto the basis and testing functions.

In order to compute the periodic Green's function efficiently, a combination of both the spectral and spatial domains must be used. Numerical experiments were performed to determine the value of c required to minimize the time needed to calculate G_p . Three

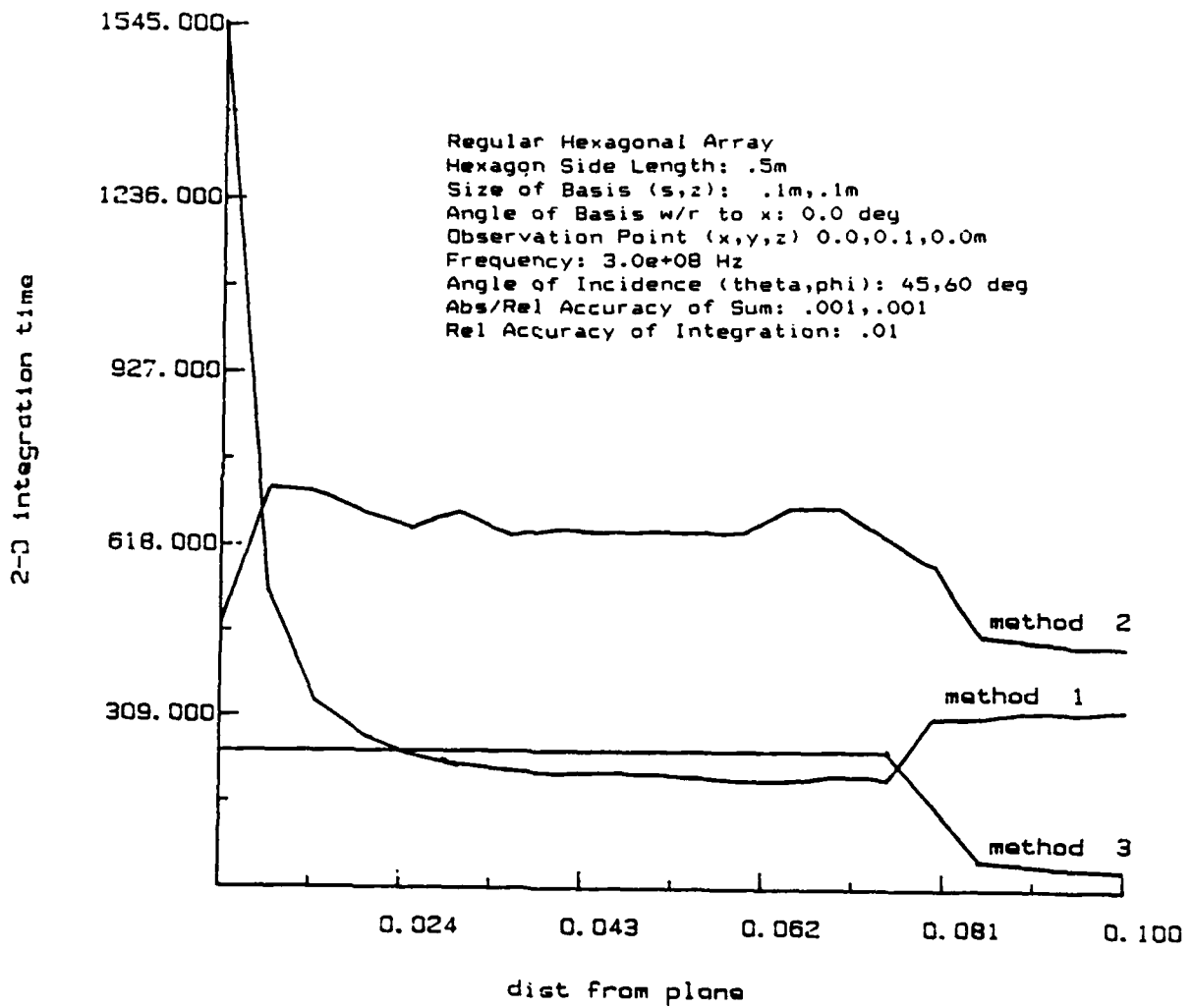


Figure 2.21 Time required to calculate $T^R * J * G_p$ by Methods 1, 2 and 3 as a function of the parameter c for plates arranged on a hexagonal array.

methods were studied: Using the spectral and spatial domain combination to efficiently sum the periodic Green's function and performing the convolution operations numerically (Method 1); distributing the basis and test convolutions onto each domain and performing the convolution analytically in the spectral domain (Method 2); finally, calculating the out-of-core terms in the spatial summation of Method 2 using a point approximation to the integrals (Method 3).

Method 1 is the most accurate of all the methods for all values of c chosen. The optimum value of c for Method 1 is in the range $0.01 < c < 0.1$. For this range, the spatial and spectral domains are weighted approximately evenly. Method 3 is the least accurate of the methods and its accuracy decreases as c is increased, due to the approximation in the spatial domain. Method 3 is also the fastest method of the three for a wide range of c . The optimum value of c for Method 3 due to the accuracy is $0.001 < c < 0.03$. Method 2 has accuracy problems whenever the "on-plane" case occurs. It is also the slowest of all the methods due to problems in specifying the absolute accuracy of the summations consistently between the different domains.

In summary, Method 1 is recommended when accuracy is the prime concern while Method 3 is recommended when speed is desired. In all cases, the choice of c must be made to ensure that the asymptotic term test point does not fall on the basis function since the singularity of the asymptotic term has not been taken into account.

In general, it was found that when the strips or plates are flat in the array plane, the smoothness and width of the basis and testing functions help the convergence of the spectral domain so much that the spectral domain should get the entire weighting. Acceleration techniques need not be applied. In the cases where the strips or plates are rotated with respect to the array plane, acceleration techniques can be applied resulting in a substantial time saving.

2.5 The Resistive Boundary Condition

The structures being considered in this thesis are made of thin, lossy dielectric cards that have a high relative permittivity. In general, the modeling of a penetrable body, such as a dielectric, involves either discretizing the volume of the body and considering the electric polarization currents as unknowns in a volume integral equation, or discretizing only the surface of the body and having both magnetic and electric currents as unknowns in a surface integral equation. Both of these methods can lead to a large number of unknowns.

An alternative approach is to use one of the family of approximate boundary conditions known as the Impedance Boundary Condition (IBC), which, like the surface integral equation, requires discretizing the surface of the body. Unlike the surface integral equation, however, the IBC provides a relationship between the electric and magnetic currents on the surface so that only the electric current needs to be regarded as unknown. This procedure cuts the number of unknowns in half making it a very popular condition to be applied [26],[27],[48],[49]. Because the IBC is approximate, it only holds for a specific range of material and geometric parameters. The resistive boundary condition, used in this thesis to model loss, is a further approximation of the IBC and subject to even more restrictions. It is the purpose of this section to show how the resistive boundary condition arises and quantify the conditions under which it may be applied.

The Impedance Boundary Condition in its simplest form [26],[27] states that the tangential E field is perpendicular to the tangential H field on the surface of the scatterer and that the fields are related by the intrinsic impedance of the scatterer.

$$\vec{E} \times \hat{n} = -Z_c \hat{n} \times \hat{n} \times \vec{H} \quad (2.64)$$

where \hat{n} is the outward normal to the surface of the scatterer and Z_c is the intrinsic

impedance of the scattering material. This relationship occurs regardless of the local geometry of the body and the form of the external field. The IBC basically transforms the three-dimensional interior problem into a one-dimensional transmission line that has a characteristic impedance Z_c and an infinite length (see Figure 2.22(a)). Mitzner [27],[28] took into account the local curvature of the body, but this aspect will not be considered here.

The material and geometric restrictions under which Equation (2.64) is valid serve mainly to ensure that the field internal to the scatterer behaves as a plane wave propagating normally into the body and that the wave "sees" only an infinite medium. The first restriction is that the complex refractive index of the scatterer $N = \sqrt{\mu_r \epsilon_r}$ must have a magnitude much greater than one. The fields external to a scatterer always may be decomposed into a series of plane waves. The first restriction ensures that all incident plane waves bend sufficiently towards the surface normal interior to the scatterer so that they can be approximated as waves transverse electric and magnetic (TEM) to the surface normal. The impedance, therefore, looking into the scatterer is the intrinsic impedance of the material. Along the interface, the field varies slowly. The second restriction occurs if the surface is curved. The smallest radius of curvature on the surface must be much larger than the wavelength inside the scatterer, i.e., the surface must appear planar to the wave inside the scatterer. The final restriction occurs if the scatterer is a closed body. The penetration depth of the wave in the scatterer must be small compared to the smallest radius of curvature so that a wave entering from one surface does not interfere with the wave from another surface.

If the general scatterer considered above is flattened to form a curved shell of thickness (Δ), then the IBC may be applied to both faces of the shell taking into account

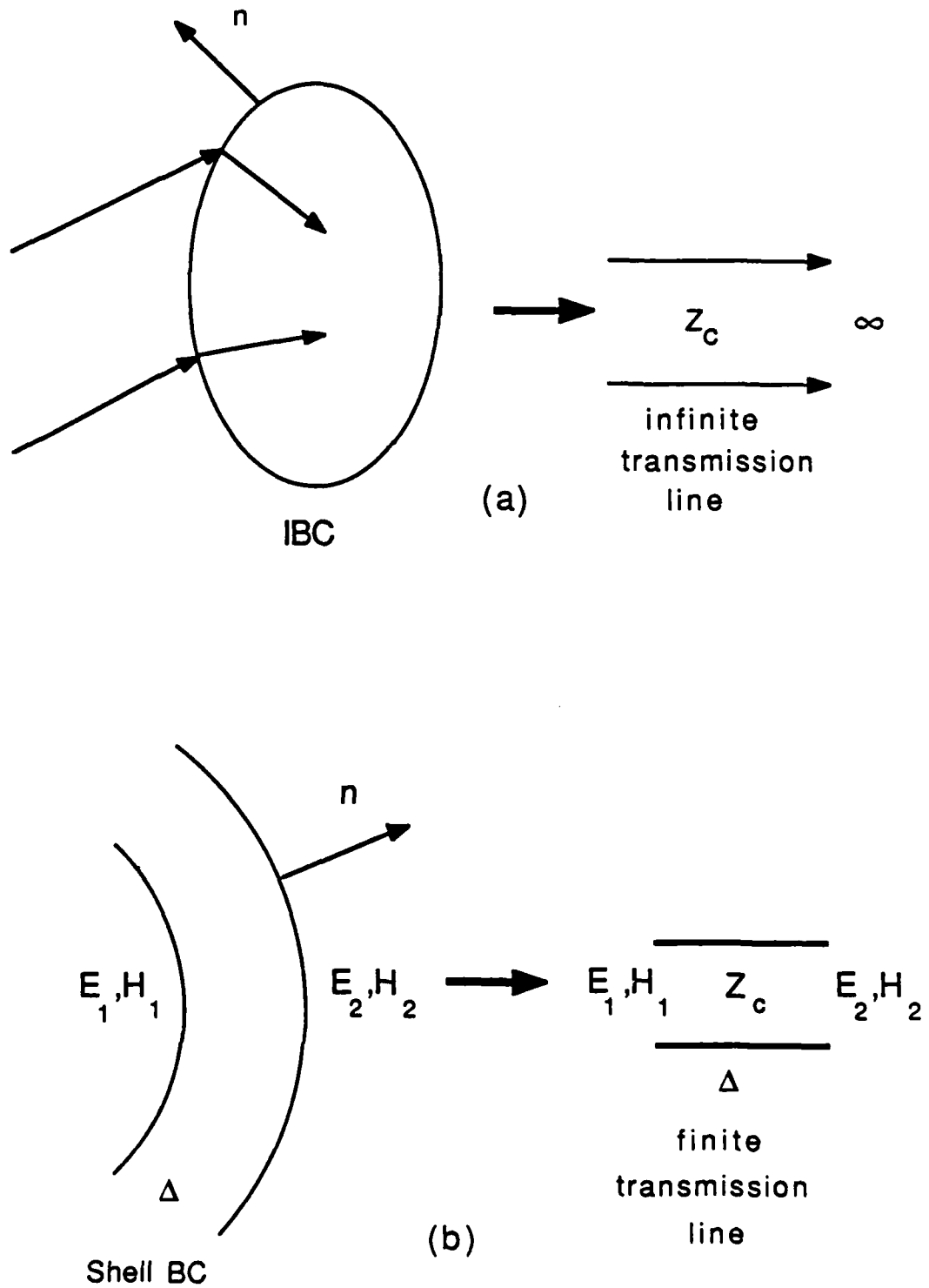


Figure 2.22 Transmission line models corresponding to the Impedance Boundary Condition (a) and the Shell Boundary Condition (b).

the interaction between them [28]. The IBC restrictions discussed in the above paragraph are required to make the approximation valid except that the penetration depth in the final restriction doesn't have to be small compared to the shell thickness since the face-to-face interactions are specifically accounted for. The three-dimensional shell is modeled as a transmission line of length Δ , propagation constant γ and characteristic impedance Z_c as shown in Figure 2.22(b). The tangential E and H fields on each side of the shell are considered as unknowns.

The transmission line equation for impedance

$$Z_1 = Z_c \left[\frac{Z_2 \cosh(\gamma\Delta) + Z_c \sinh(\gamma\Delta)}{Z_c \cosh(\gamma\Delta) + Z_2 \sinh(\gamma\Delta)} \right] \quad (2.65)$$

where the input and output impedances are defined as

$$Z_1 = \frac{\vec{E}_1 \times \hat{n}}{\hat{n} \times \hat{n} \times \vec{H}_1}$$

$$Z_2 = \frac{\vec{E}_2 \times \hat{n}}{\hat{n} \times \hat{n} \times \vec{H}_2}$$

leads directly to a set of two equations which relate two of the four unknown quantities.

These equations can be written in several different forms:

$$\vec{E}_2 \times \hat{n} + Z_c \hat{n} \times \hat{n} \times \vec{H}_2 - e^{-\alpha} \vec{E}_1 \times \hat{n} - Z_c e^{-\alpha} \hat{n} \times \hat{n} \times \vec{H}_1 = 0 \quad (2.66a)$$

$$e^{-\alpha} \vec{E}_2 \times \hat{n} - Z_c e^{-\alpha} \hat{n} \times \hat{n} \times \vec{H}_2 - \vec{E}_1 \times \hat{n} + Z_c \hat{n} \times \hat{n} \times \vec{H}_1 = 0 \quad (2.66b)$$

$$\vec{E}_2 \times \hat{n} = \vec{E}_1 \times \hat{n} \cosh \alpha - Z_c \hat{n} \times \hat{n} \times \vec{H}_1 \sinh \alpha \quad (2.67a)$$

$$\hat{n} \times \vec{H}_2 = \hat{n} \times \vec{H}_1 \cosh \alpha + 1/Z_c \hat{n} \times \vec{E}_1 \times \hat{n} \sinh \alpha \quad (2.67b)$$

$$\vec{E}_1 \times \hat{n} = \vec{E}_2 \times \hat{n} \cosh \alpha + Z_c \hat{n} \times \hat{n} \times \vec{H}_2 \sinh \alpha \quad (2.68a)$$

$$\hat{n} \times \vec{H}_1 = \hat{n} \times \vec{H}_2 \cosh \alpha - 1/Z_c \hat{n} \times \vec{E}_2 \times \hat{n} \sinh \alpha \quad (2.68b)$$

where $\alpha = \gamma\Delta$ in the above equations.

The fact that the geometry under consideration is a shell adds several restrictions in addition to those already imposed by the IBC. The first restriction is that the shell must be thin compared to its radius of curvature; the shell may have no kinks. Additionally, the normals to the inside and outside faces of the shell must be in the same direction, i.e., the shell must be uniform in thickness. Finally, the shell should not double back on itself or change its curvature suddenly so that it loses its locally planar character. In the structures under consideration, the additional restrictions imposed by the shell are no problem except possibly near the junctions of the honeycombs. It is the initial restrictions, imposed by the IBC, that need to be monitored.

If the thickness of the shell is reduced such that $e^{-\alpha}$ in Equation (2.66) can be approximated by $1-\alpha$, then $\sinh(\alpha)$ and $\cosh(\alpha)$ in Equations (2.67) and (2.68) can be approximated by α and 1, respectively. Applying these approximations to Equations (2.67a) and (2.68a) and subtracting Equation (2.68a) from (2.67a) yield

$$\left(\vec{E}_2 - \vec{E}_1\right) \times \hat{n} = -Z_c \alpha \hat{n} \times \hat{n} \times \frac{\left(\vec{H}_1 + \vec{H}_2\right)}{2} \quad (2.69a)$$

Combining Equations (2.67b) and (2.68b) in the same manner yields

$$\hat{n} \times \left(\vec{H}_2 - \vec{H}_1\right) = -\frac{\alpha}{Z_c} \hat{n} \times \hat{n} \times \frac{\left(\vec{E}_2 + \vec{E}_1\right)}{2} \quad (2.69b)$$

Equation (2.69a) states that a jump in the tangential E field across the thin shell is related to the average value of the tangential H field on the two interfaces by the factor $Z_c \alpha$. Equation (2.69b) states that a jump in the tangential H field across the thin shell is related to the average value of the tangential E field on the two interfaces by the factor α/Z_c . Note that although the equations have simplified in form, there are still two equations relating four unknowns.

The possibility of further simplification depends on whether the jumps in the tangential E field (δE) or H field (δH) are significant compared to the value of the E or H field outside the shell. Normalizing the equations of (2.69) to the outside field yields

$$\frac{\delta \vec{E}}{E} = -\frac{Z_c \alpha}{Z_0} \quad (2.70a)$$

$$\frac{\delta \vec{H}}{H} = -\frac{\alpha Z_0}{Z_c} \quad (2.70b)$$

If $Z_c \alpha / Z_0$ is approximately equal to $\alpha Z_0 / Z_c$, then the discontinuities of both E and H are significant and both equations of Equation (2.69) are needed to describe the shell.

If $Z_c \alpha / Z_0 \gg \alpha Z_0 / Z_c$, then the magnetic field discontinuity is insignificant compared to the electric field discontinuity. Since the H field may be approximated as being the same on both sides of the shell, $\vec{H}_2 = \vec{H}_1 = \vec{H}$ in Equations (2.69). Equation (2.69a) now becomes

$$\hat{n} \times \hat{n} \times \vec{H} = -\frac{1}{Z_c \alpha} \vec{K} \quad (2.71)$$

where $\vec{K} = \delta \vec{E} \times \hat{n}$ is the magnetic current caused by the jump of the E field across the shell. Since this shell can be described by the magnetic current alone, this condition is known as the magnetic thin-shell condition.

The converse to the above case is the electric thin-shell condition. It is this case that ultimately gives rise to the resistive boundary condition. The electric thin-shell condition occurs if $\alpha Z_0 / Z_c \gg Z_c \alpha / Z_0$. For this case, since the E field is approximately the same on both sides of the shell, $\vec{E}_2 = \vec{E}_1 = \vec{E}$ in Equations (2.69). Equation (2.69b) becomes

$$\hat{n} \times \hat{n} \times \vec{E} = -\frac{Z_c}{\alpha} \vec{J} \quad (2.72)$$

where \vec{J} is the electric current caused by the jump of the H field across the shell. The multiplying factor Z_c/α can be re-expressed as $[j\omega\epsilon\Delta]^{-1}$. If the conducting portion of the current outweighs the displacement current, the displacement current can be ignored and the factor becomes $1/\sigma\Delta$ which Senior defines as the resistance of the card in ohms [29].

The above discussion focussed on how the resistive boundary condition arises from considering the surface integral equation. The same results can be found from specializing a volume integral equation [25] to a thin, dielectric shell. The volume integral equation is

$$\frac{\vec{J}_{vol}}{j\omega(\epsilon-\epsilon_0)} - E^{scat}(\vec{J}_{vol}) = E^{inc} \quad (2.73)$$

where E^{scat} is the scattered field caused by the electric polarization currents flowing in the dielectric volume. E^{inc} is the incident E field and the total field has been expressed in terms of the polarization currents. If the shell is thin and the permittivity is high, the polarization currents flowing normally to the shell surface are negligible compared to the tangentially flowing currents. Further, the tangential currents may be considered constant across the shell thickness, so that the integrals over the shell volume can be replaced by surface integrals multiplied by the thickness of the shell. Equation (2.73) becomes

$$\frac{\vec{J}_{sur}}{j\omega(\epsilon-\epsilon_0)\Delta} - E^{scat}(\vec{J}_{sur}) = E^{inc} \quad (2.74)$$

If $\epsilon \gg \epsilon_0$, this procedure yields the same factor as was found by using the surface integral equation and making all the IBC approximations.

Figures 2.23-2.27 illustrate the above surface and volume approaches to the resistive boundary condition as applied to an infinite, dielectric slab. Figure 2.23(a) shows the angle made with respect to the surface normal for the interior plane-wave propagation

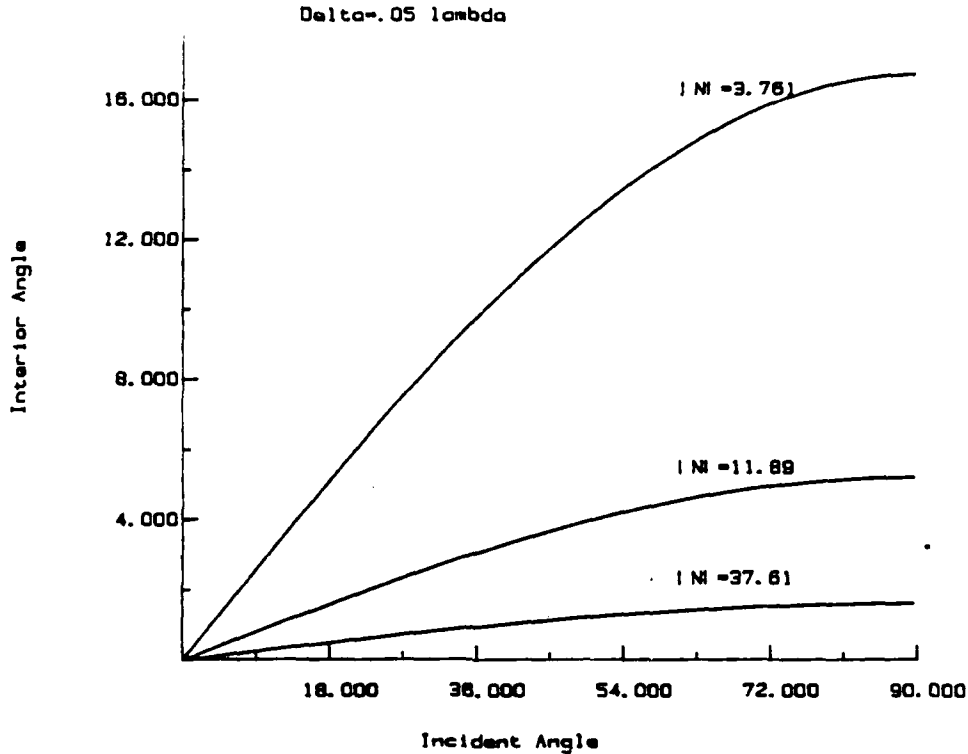


Figure 2.23a Angle of the interior wave propagation vector plotted as a function of the exterior wave propagation vector angle for various refractive indices (N). The angle is with respect to the slab normal. As N increases the interior wave becomes increasingly TEM-like with respect to the normal.

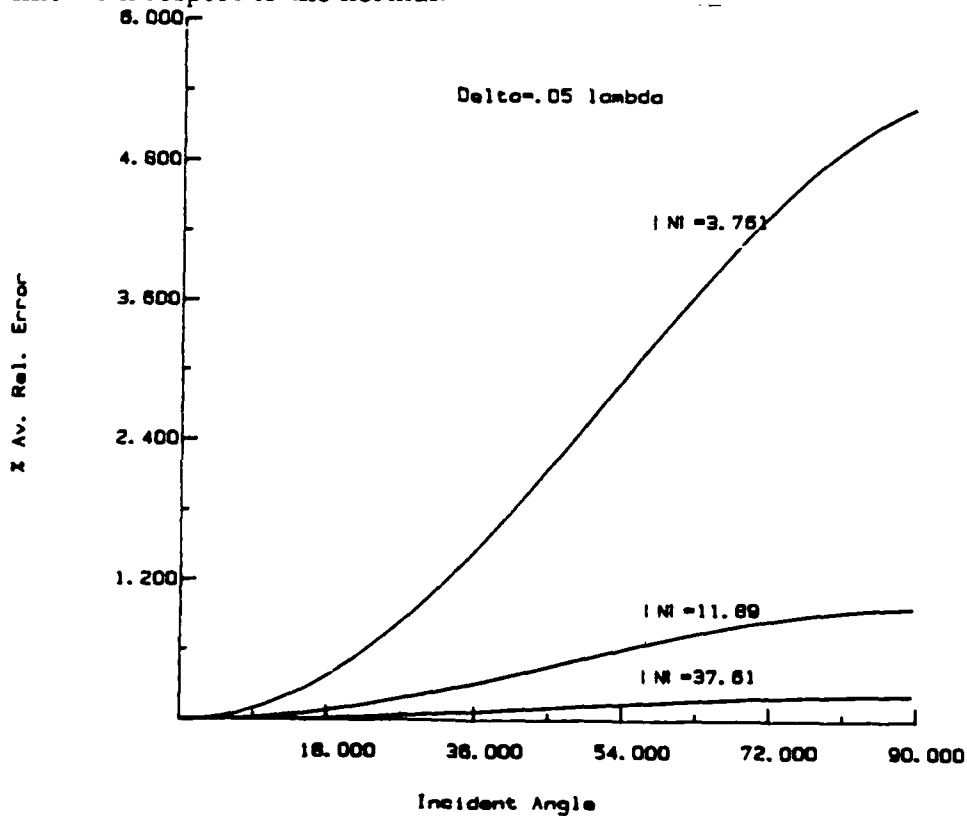


Figure 2.23b Error in thick-shell boundary condition as a function of the incident angle for the same refractive indices plotted in Figure 2.23a. As the interior wave becomes more TEM-like, the error between the approximation and the exact fields decreases.

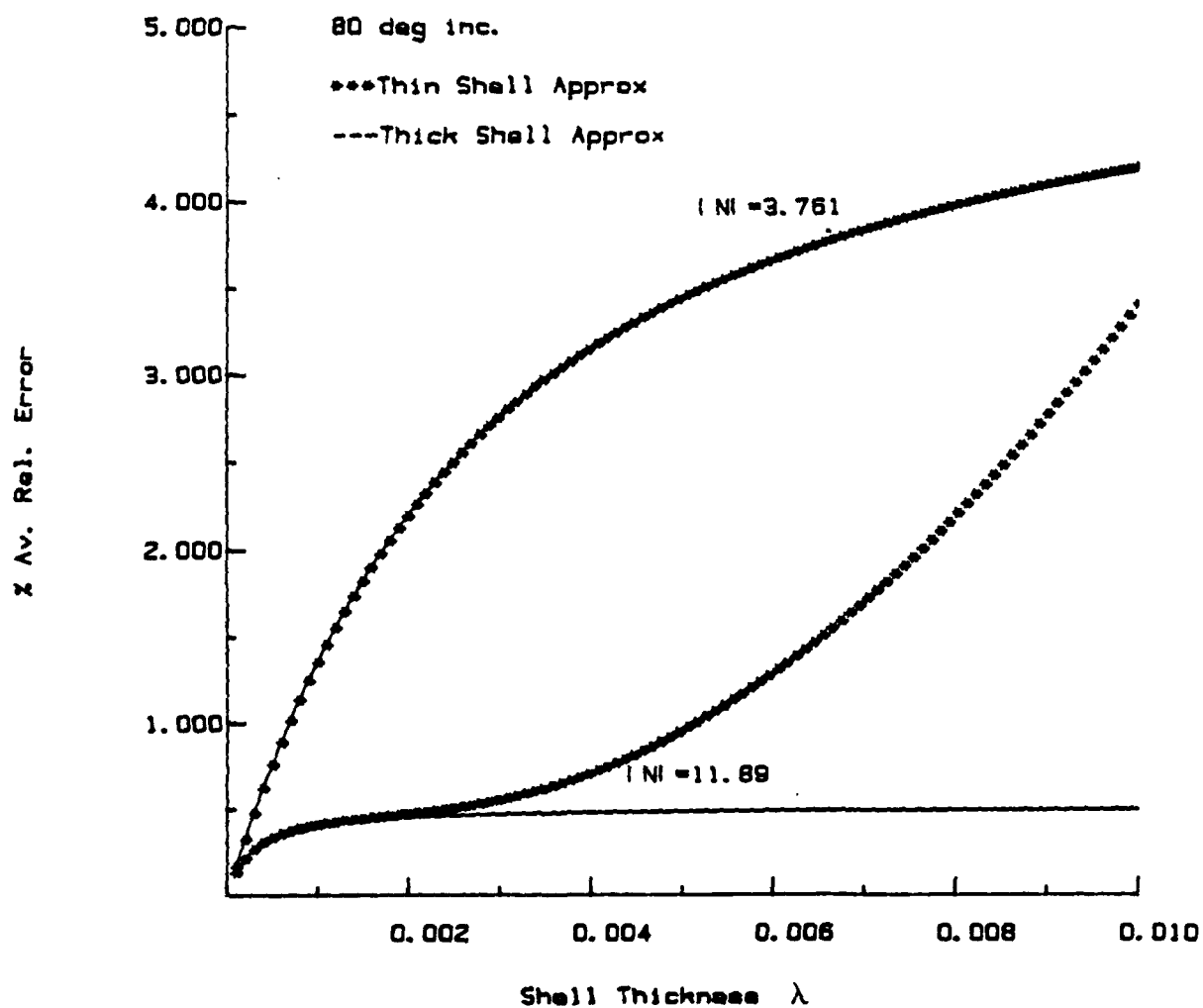


Figure 2.24 Comparison of the error caused by applying thin and thick-shell boundary conditions as the shell thickness is increased. For $N=3.761$, the thin and thick-shell approximations overlay each other, but both deviate from the exact solution. For $N=11.89$, the thin-shell approximation deviates from the thick-shell as the shell becomes thicker, but both approximate the exact solution better.

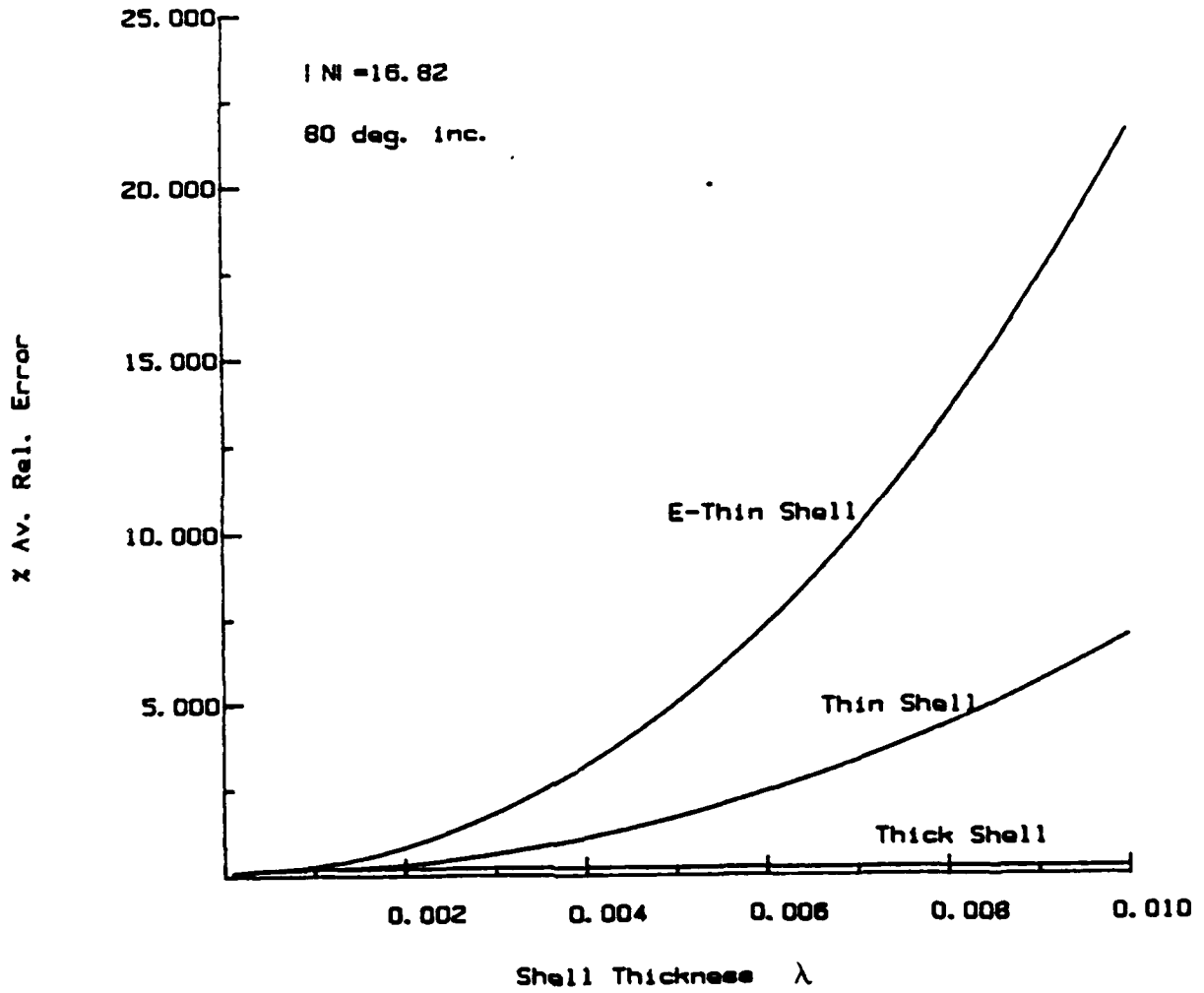


Figure 2.25 Comparison of the error caused by applying thin, thick and electric thin-shell conditions as the shell thickness is increased.

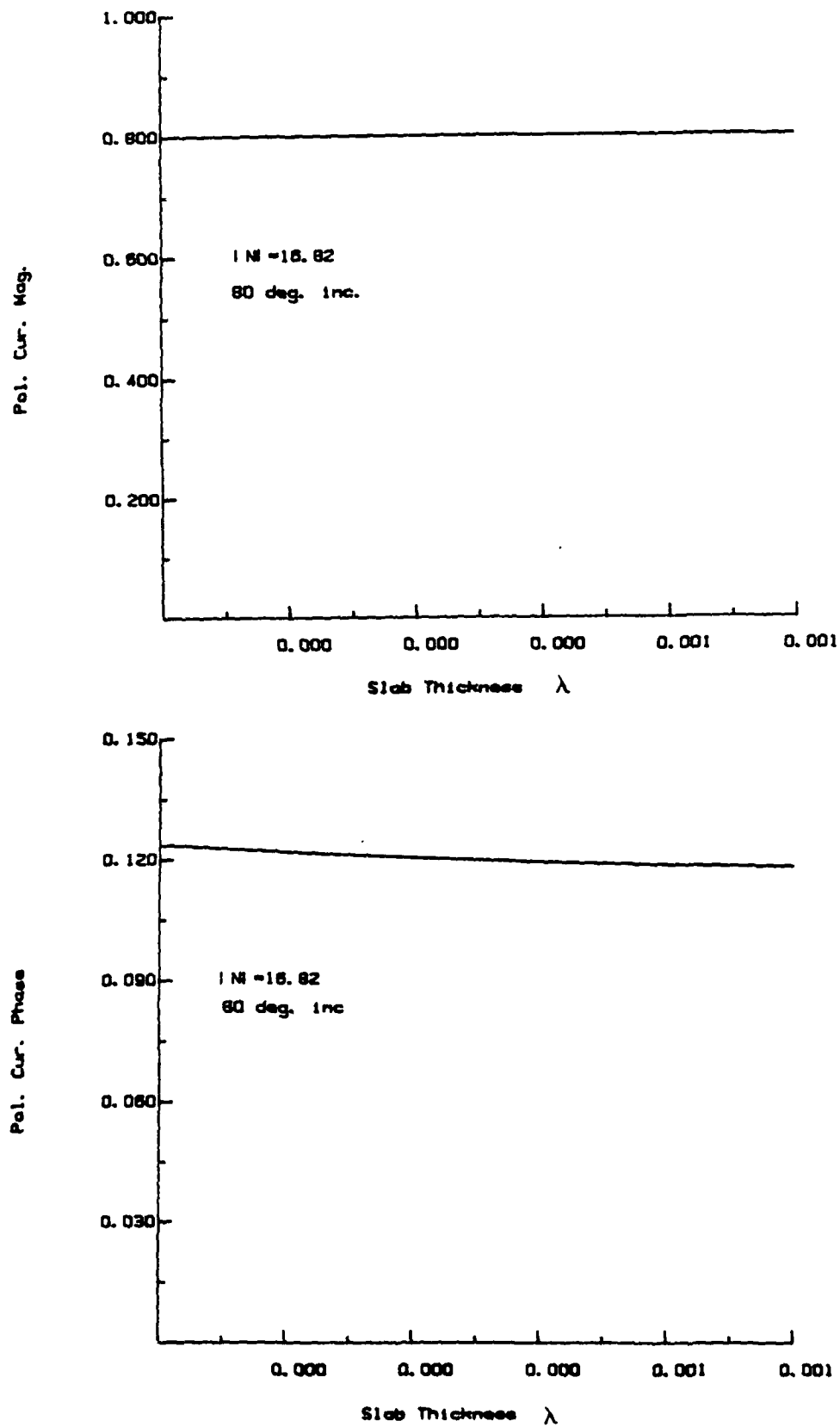


Figure 2.26 Polarization current magnitude (top) and phase (bottom) across the slab for a 0.001λ thick slab of Figure 2.25. Both phase and magnitude are constant across the shell meaning that the electric thin-shell boundary condition is valid.

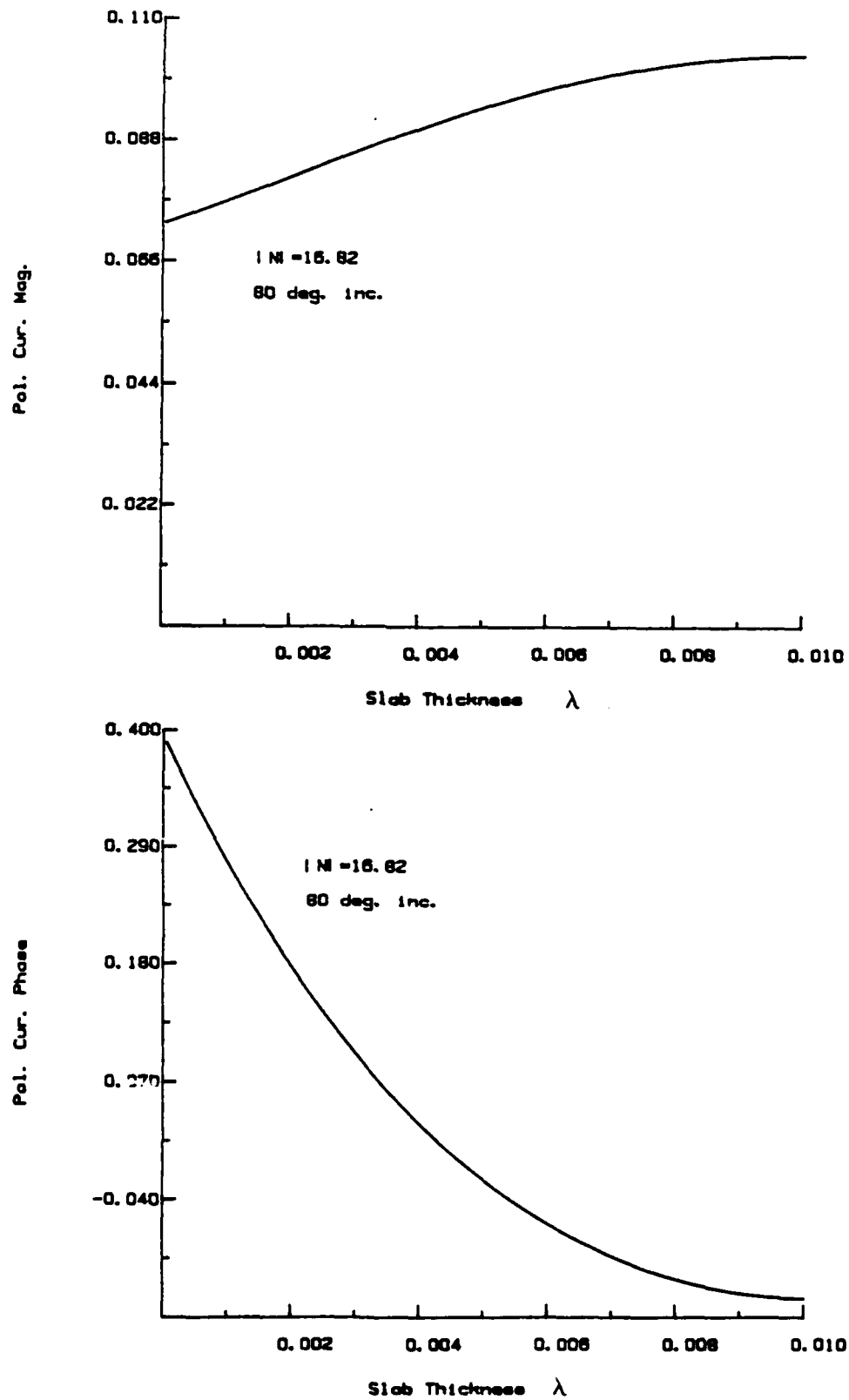


Figure 2.27 Polarization current magnitude (top) and phase (bottom) across the slab for a 0.01λ thick slab of Figure 2.25. Phase and magnitude are no longer constant across the shell so the electric thin-shell boundary condition is invalid.

vector versus the incident angle with respect to the surface normal for different values of the refractive index. The thickness of the slab is fixed at 0.05λ in free space. The plot shows how increasing the magnitude of the complex refractive index causes an incident plane wave to bend toward the surface normal interior to the slab—the first requirement for the IBC to work. Consequently, as shown for the same set of slabs in Figure 2.23(b), the fields found by the thick-shell boundary condition (Equation (2.66)) better approximate the exact fields calculated for the slab as the refractive index becomes larger. Figure 2.23(b) is a plot of the average relative error versus incident angle for various refractive indices. The average error is found by computing the relative error for the E and H fields on each side of the slab and averaging the result.

Figure 2.24 compares the error for the thin-shell approximation with the error for the thick-shell approximation as the shell is increased in thickness from 0.0001λ to 0.01λ . The error is plotted for two refractive indices. The incident angle is fixed at a worst case of 80° . Since the accuracy of the thin-shell approximation with respect to the thick-shell approximation is a function of γ as well as shell thickness, the approximation deviates from the thick-shell approximation more when the refractive index is high. On the other hand, both thick and thin-shell approximations compare to the exact solution better for higher refractive index because of the bending phenomenon discussed above.

Figure 2.25 compares the relative error for the thick-shell, thin-shell and electric thin-shell approximations as the shell thickness is increased. Both thin-shell and electric thin-shell curves deviate from the thick-shell curve as the thickness is increased. The electric thin-shell approximation is valid when $\Delta < 0.001 \lambda$. For this case, $\alpha Z_0/Z_c \approx 300 \alpha Z_c/Z_0$. The jump in the electric field is, therefore, insignificant compared to the value of the E field itself. Indeed, the exact fields are calculated to be

$E_1 = (0.135, -0.104)$ on one side of the shell and $E_2 = (0.135, -0.105)$ on the other. The exact jump in the tangential H field multiplied by Z_c/α calculates the E field to be equal to $(0.133, -0.104)$. The electric polarization current for this case is shown in Figure 2.26. It is constant in both phase and magnitude and can, therefore, be approximated as a delta function weighted by Δ as required by the volume integral approach to the resistive boundary condition. When $\Delta = 0.01 \lambda$, the shell is too thick to be approximated by the electric thin-shell approximation. Correspondingly, as shown in Figure 2.27, the polarization current is no longer a constant.

It has been shown in this section that through the proper use of approximations the resistive boundary condition may be derived. These approximations may be summarized as follows: first, the IBC eliminates the need to consider both magnetic and electric surface currents as unknowns; second, shell conditions are invoked to account for the interactions between the shell faces; third, thin-shell conditions simplify the equations; and finally, electric thin-shell conditions eliminate one of the equations and one of the unknowns. More complex shells, such as two layers bonded by a glue layer, may also be handled by the resistive boundary condition provided that the layers together satisfy all the required restrictions. It must be stressed that the resistive boundary condition only handles thin electric shells, not lossy structures in general. If the shells become thick, or backed by metal, or surrounded by a medium so that the jump in the E field becomes important, the condition fails and a formulation based on the IBC or the surface integral equation must be used.

3. PERIODICITY IN ONE DIMENSION -- PROBLEMS BASED ON STRIP ARRAYS

3.1 Introduction

Electromagnetic scattering from a one-dimensional array of unit cells that are composed of strips has long been of interest. In 1969, for example, Weinstein [50] obtained an analytical solution for a plane wave incident on an array of perfectly conducting strips lying flat in the plane of periodicity and filling half of the unit cell. Later, investigators were able to relax the strip-width restriction by applying numerical techniques to the above strip-grating problem [14]-[16].

Rubin and Bertoni [18] examined the case of scattering from an array of lossy bars, in which the bar thickness was accounted for. Subdomain basis functions were used to discretize not only the width of the bars (in the direction of periodicity), but also the thickness of the bars (perpendicular to the direction of periodicity). Periodic arrays with a thickness were also studied by Kent and Lee [51] and Montgomery [52], who used the modified residue calculus method to analytically solve a one-dimensional array of thin, parallel strips; each strip was rotated 90° with respect to the direction of periodicity. The thickness in this case was caused, not by making the strip itself thick, as was done by Rubin, but by rotating the thin strips out of the plane of periodicity. Hall [30], using entire domain basis functions, examined more general unit cells than Kent and Montgomery. The cells were composed of several thin, resistive strips which were translated in the unit cell and rotated with respect to the direction of periodicity, such as the example shown in Figure 3.2 (p. 87).

In all of the above problems, the incident field was a plane wave with a propagation vector lying in the plane normal to the strip axis. The wave was polarized either TM or TE with respect to the strip axis. In general, the problem of scattering from an array of

strips must be solved numerically using an extended version of the Spectral Galerkin method; the convolution with the Green's function is performed in the spectral domain along the direction of periodicity and in the spatial domain perpendicular to the direction of periodicity.

This chapter considers an oblique plane wave incident on structures similar to those solved by Hall; that is, the arrangement of the thin strips in the unit cell gives the array its thickness. Two coupled electric field integral equations (EFIEs) are derived in Section 3.2 and discretized by the method of moments [53]. The scattered field is represented as a truncated series of Floquet harmonics. The interactions of the strip array with the surrounding medium are described by a generalized scattering matrix. The coupling of reflected power between the TE and TM polarized waves is observed in Section 3.3 as a function of frequency for various strip resistances, angles of incidence, and cell geometries. Conclusions are drawn in Section 3.4.

3.2 Integral Equation Formulation

The problem under consideration consists of a plane wave, obliquely incident on an infinite, one-dimensional array of two-dimensional, lossy structures as shown in Figure 3.1. The array is formed by repeating a unit cell every b units along \hat{x} . Each unit cell is described in terms of several lossy strips, the axes of which are parallel to \hat{z} . The strips may be as narrow in width as one subdomain basis function and may be isolated, connected to each other within the unit cell, or connected to strips in neighboring unit cells in order to form the example unit cell shown in Figure 3.2. The strips are not constrained to lie flat in the xz plane—they can make an angle with \hat{x} to give the structure thickness in \hat{y} .

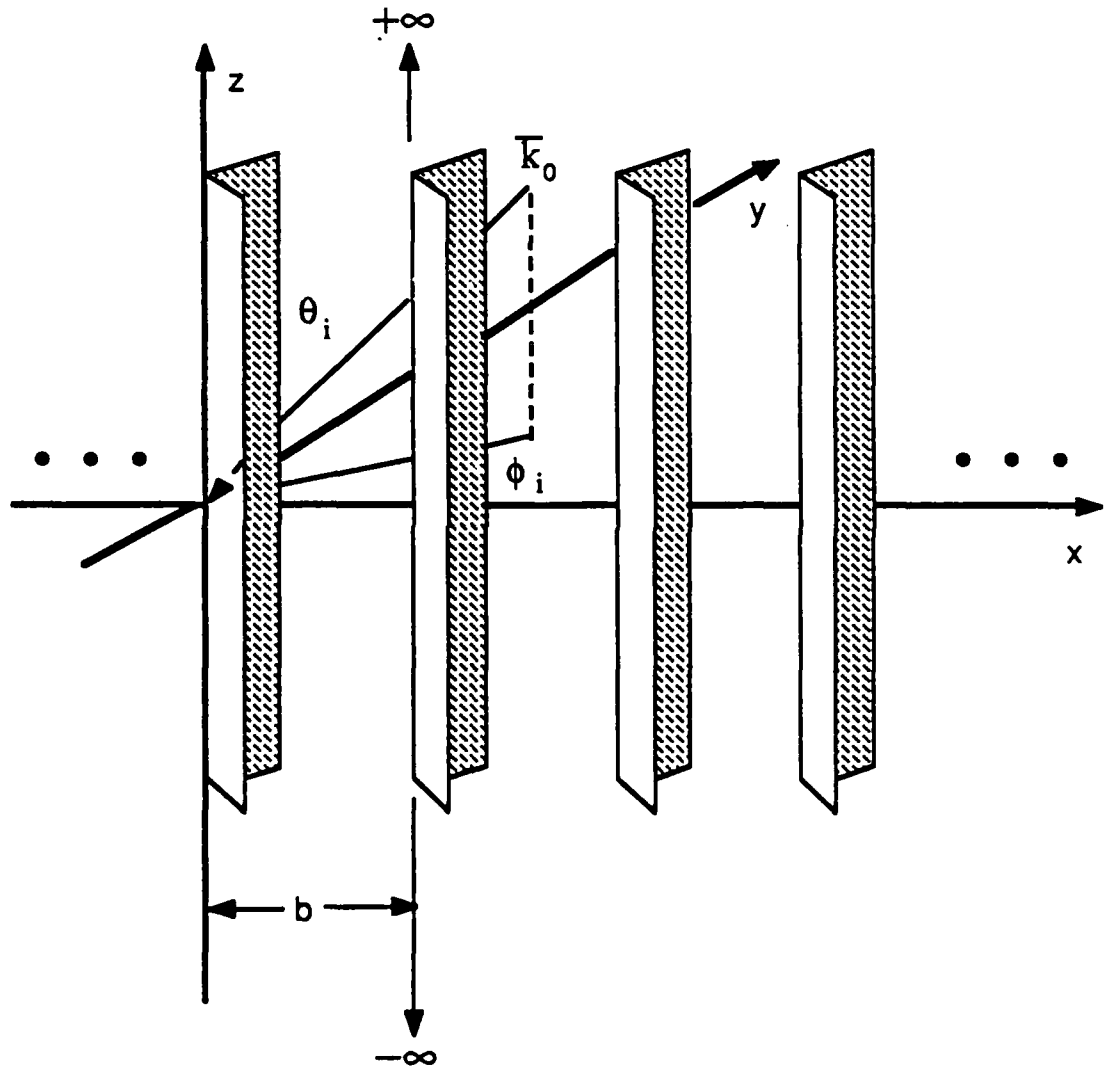


Figure 3.1 Geometry of a typical one-dimensional strip array with unit cells spaced b units apart along the \hat{x} axis. A plane wave is obliquely incident, making an angle of θ_i with respect to \hat{z} and ϕ_i with respect to \hat{x} .

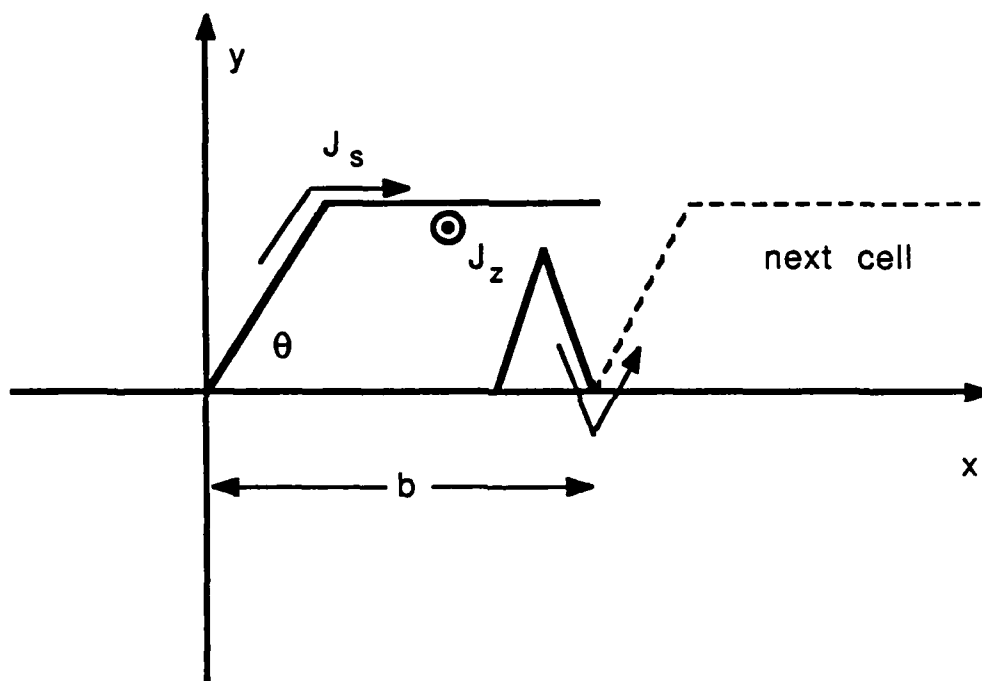


Figure 3.2 Example unit cell looking along the \hat{z} axis. Resistive strips can make an angle of θ with the \hat{x} axis and can connect to each other using overlapping triangle basis functions. The surface currents flow along the strip in the \hat{s} or \hat{z} direction.

An obliquely incident plane wave means that in addition to making an angle ϕ_i with respect to \hat{x} , the propagation vector makes an angle of θ_i with respect to \hat{z} . The wave is defined as being either TM or TE to the \hat{z} axis by expressing all field components in terms of a scalar function [46].

$$\begin{cases} \Psi_{TE} \\ \Psi_{TM} \end{cases} = e^{-j(k_x x + k_y y - k_z z)} \quad (3.1a)$$

where

$$k_x = -k_0 \sin\theta_i \cos\phi_i \quad (3.1b)$$

$$k_y = -k_0 \sin\theta_i \sin\phi_i$$

$$k_z = +k_0 \cos\theta_i$$

k_0 is the wavenumber in the surrounding medium, which is usually taken to be free space, and the time dependence ($e^{+j\omega t}$) is suppressed.

If the vector electric potential (\vec{F}) equals zero and the vector magnetic potential (\vec{A}) equals $\hat{z} \Psi_{TM}$, then the substitution of Equation (3.1a) into Equation (3.86) of [46] gives the components of the \vec{E} field for the TM case as

$$E_x = \frac{1}{j \omega \epsilon} k_x k_z \Psi_{TM} \quad (3.2a)$$

$$E_y = \frac{1}{j \omega \epsilon} k_y k_z \Psi_{TM} \quad (3.2b)$$

$$E_z = \frac{k_0^2 - k_z^2}{j \omega \epsilon} \Psi_{TM} \quad (3.2c)$$

where ϵ is the electric permittivity of the surrounding medium. By duality, if $\vec{A} = 0$ and $\vec{F} = \hat{z} \Psi_{TE}$, substituting Equation (3.1a) into Equation (3.89) of [46] yields the \vec{E} field components for the TE case.

$$E_x = +j^l{}_y \Psi_{TE} \quad (3.3a)$$

$$E_y = -jk_x \Psi_{TE} \quad (3.3b)$$

$$E_z = 0 \quad (3.3c)$$

Two integral equations will be derived which have as their unknown the equivalent electric surface current density on the resistive strips in a single unit cell. The surface current, as shown in Figure 3.2, has two orthogonal components: J_z , which is the current along the \hat{z} axis of the strip, and J_s , which is the current in the xy plane flowing tangent to the strip. If the strips are lossless, the equations for J_s and J_z are decoupled. The two components may be solved for separately by using the formulation for normal plane incidence with the wavenumber transverse to \hat{z} substituted for k_0 . When the strips are lossy, however, the currents only decouple when the propagation vector of the incident plane wave lies in the plane normal to the axis of the strips, i.e., when $\theta_i = 90^\circ$ [54]. For general oblique incidence, the integral equations must account for this coupling which exists between J_z and J_s .

Since the problem geometry is composed of thin strips, the EFIE approach must be used for stability. Two EFIEs will be derived by applying boundary conditions on the strip to the \hat{z} and \hat{s} components of the total electric field. The \hat{z} component of the total electric field (E_z^{tot}) may be expressed as a sum of the \hat{z} components of the incident (E_z^{inc}) and scattered fields (E_z^{scat}).

$$E_z^{tot} = E_z^{inc} + E_z^{scat} \quad (3.4)$$

E_z^{inc} is obtained from Equation (3.2c) for the TM case or Equation (3.3c) for the TE case. E_z^{scat} is the field due to the equivalent surface current, $\vec{J} = \hat{s}J_s + \hat{z}J_z$, on the strips in the unit cell.

AD-A210 145

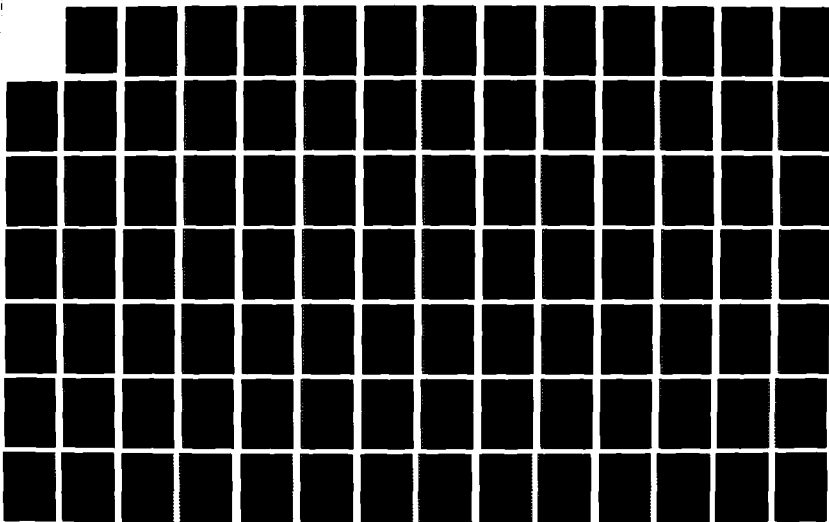
ELECTROMAGNETIC SCATTERING FROM A STRUCTURED SLAB
COMPRSED OF PERIODICAL (U) ILLINOIS UNIV AT URBANA
COORDINATED SCIENCE LAB R E JORGENSEN ET AL MAY 89

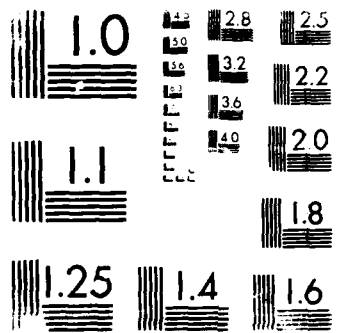
UNCLASSIFIED

UILU-ENG-89-2218 N00014-84-C-0149

F/G 20/14

NL





E_z^{scat} may be written in terms of the vector magnetic potential \vec{A} and the scalar electric potential Φ .

$$E_z^{scat} = \hat{z} \cdot \left[-j \omega \vec{A} - \nabla \Phi \right] \quad (3.5)$$

Both \vec{A} and Φ satisfy the wave equation. \vec{A} is due to the surface electric current density

$$\nabla^2 \vec{A} + k_0^2 \vec{A} = -\mu \vec{J} \quad (3.6a)$$

where μ is the magnetic permeability of the surrounding medium and Φ is due to the surface electric charge density (q).

$$\nabla^2 \Phi + k_0^2 \Phi = -\frac{q}{\epsilon} \quad (3.6b)$$

Since the strip geometry is invariant in the \hat{z} direction, the incident field dictates the functional form of all quantities in z as $e^{+jk_z z}$. Consequently, the second derivative with respect to z in Equation (3.6) can be replaced by $(-k_z^2)$, and Equation (3.6a), for example, becomes

$$\nabla_t^2 \vec{A} + \kappa \vec{A} = -\mu \vec{J} \quad (3.7a)$$

where ∇_t^2 is the Laplacian in the coordinates transverse to \hat{z} , and κ , the transverse propagation constant, is related to k_0 and k_z by

$$\kappa = \sqrt{k_0^2 - k_z^2} \quad (3.7b)$$

Equation (3.6b) is similarly transformed.

Since the unknown quantities are confined to a single unit cell, the Green's function must account for the fact that the unknowns are actually distributed on an infinite array. The vector magnetic potential, therefore, is expressed as a convolution of current in the unit cell with a periodic Green's function (G_p), while Φ is expressed as a convolution of charge with G_p .

$$\vec{A} = \mu \vec{J} * G_p \quad (3.8a)$$

$$\Phi = \frac{1}{\epsilon} q * G_p \quad (3.8b)$$

The periodic Green's function, $G_p(\rho, \rho')$, which satisfies the equation

$$\nabla_t^2 G_p(\rho, \rho') + \kappa^2 G_p(\rho, \rho') = - \sum_{m=-\infty}^{\infty} e^{-jk_x mb} \delta(\vec{\rho} - \vec{\rho}' - mb\hat{x}) \quad (3.9)$$

is a scalar function defined as the A/μ response at the observation point ρ due to an infinite array of unit amplitude line sources spaced b units apart along \hat{x} and located at ρ' in each cell. The line sources are shifted in phase from cell-to-cell by $e^{-jk_x b}$ due to the incident field in accordance with Floquet's theorem as discussed in Chapter 2. The response is

$$G_p(\rho', \rho) = \frac{1}{4j} \sum_{m=-\infty}^{\infty} e^{-jk_x mb} H_0^2(\kappa[(x-x'-mb)^2 + (y-y')^2]^{1/2}) \quad (3.10)$$

where H_0^2 is the Hankel function of the second kind, zero order representing the outgoing cylindrical waves due to each line source.

Using Equations (3.8a) and (3.8b) and invoking the continuity condition ($\nabla \cdot \vec{J} = -j\omega q$) to relate charge and current, Equation (3.5) becomes

$$E_z^{scat} = \frac{k_o^2}{j\omega\epsilon} \left[J_z * G_p \right] + \frac{1}{j\omega\epsilon} \frac{\partial}{\partial z} \left[\frac{\partial J_{s'}}{\partial s'} + \frac{\partial J_z}{\partial z} \right] * G_p \quad (3.11)$$

where unprimed variables denote observation coordinates and primed variables denote source coordinates. The divergence has been expressed as derivatives along \hat{s} and along \hat{z} . Replacing all derivatives in z by $+jk_z$ in Equation (3.11) and substituting the result into Equation (3.4) yield

$$E_z^{inc} = E_z^{tot} - \frac{k_o^2 - k_z^2}{j \omega \epsilon} \left[J_z * G_p \right] - \frac{jk_z}{j \omega \epsilon} \left[\frac{\partial J_{s'}}{\partial s'} * G_p \right] \quad (3.12)$$

In a similar manner, the \hat{s} component of the total E field can be related to the incident and scattered fields by

$$E_s^{tot} = E_s^{inc} + E_s^{scat} \quad (3.13)$$

E_s^{inc} is the incident electric field component along the direction tangent to the strip and perpendicular to the \hat{z} direction. It can be obtained by forming the inner product between \hat{s} and Equation (3.2) for the TM polarization, or between \hat{s} and Equation (3.3) for the TE polarization. The scattered field is obtained by

$$E_s^{scat} = \hat{s} \cdot \left[-j \omega \vec{A} - \nabla \Phi \right] \quad (3.14)$$

where \vec{A} and Φ are defined by Equation (3.8). Invoking the continuity equation and using the periodic Green's function, the expression for the \hat{s} component of the scattered field becomes

$$E_s^{scat} = \frac{k_o^2}{j \omega \epsilon} \hat{s} \cdot \left[J_{s'} * G_p \right] + \frac{1}{j \omega \epsilon} \hat{s} \cdot \nabla \left[\frac{\partial J_{s'}}{\partial s'} + \frac{\partial J_z}{\partial z} \right] * G_p \quad (3.15)$$

which, after utilizing the known z dependency, can be substituted into Equation (3.13) to derive the integral equation for the \hat{s} component of the electric field:

$$E_s^{inc} = E_s^{tot} - \frac{k_o^2}{j \omega \epsilon} \hat{s} \cdot \left[J_{s'} * G_p \right] - \frac{1}{j \omega \epsilon} \frac{\partial}{\partial s} \left[\frac{\partial J_{s'}}{\partial s'} * G_p \right] - \frac{jk_z}{j \omega \epsilon} \frac{\partial}{\partial s} \left[J_z * G_p \right] \quad (3.16)$$

The total E field on the surface of the strip can be expressed in terms of the surface currents through the use of the resistive boundary condition discussed in Chapter 2. The total E field in the shell volume is, therefore, related to the surface polarization current, the electric permittivity and the thickness of the shell (Δ) by

$$E_{s/z}^{tot} = RJ_{s/z} \quad (3.17a)$$

where

$$R = \frac{1}{j \omega \epsilon \Delta} \quad (3.17b)$$

Applying the boundary condition to (3.12) and (3.16) on the strips in the unit cell yields the two integral equations to be solved.

$$E_z^{inc} = RJ_z - \frac{k_o^2 - k_z^2}{j \omega \epsilon} \left[J_z * G_p \right] - \frac{jk_z}{j \omega \epsilon} \left[\frac{\partial J_{s'}}{\partial s'} * G_p \right] \quad (3.18a)$$

$$E_s^{inc} = RJ_s - \frac{k_o^2}{j \omega \epsilon} \hat{s} \cdot \left[J_{s'} * G_p \right] - \frac{1}{j \omega \epsilon} \frac{\partial}{\partial s} \left[\frac{\partial J_{s'}}{\partial s'} * G_p \right] - \frac{jk_z}{j \omega \epsilon} \frac{\partial}{\partial s} \left[J_z * G_p \right] \quad (3.18b)$$

Note that the last terms on the right-hand side of Equations (3.18a) and (3.18b) provide the coupling between the two equations. When the propagation constant of the incident plane is in the xy plane, namely, when k_z equals zero, the equations are the decoupled TE and TM equations used previously by Hall [30].

The integral equations are discretized by the method of moments. Pulse basis functions are used to model J_z and triangle basis functions are used to model J_s . Both functions adequately model the behavior of the current near edges of the structure. If the strips in the unit cell of the structure are physically connected to each other or to strips in neighboring unit cells, the triangle functions overlap the connecting portions of the structure to explicitly enforce the current continuity of J_s . The electric field is tested in the \hat{z} direction with a delta function and tested in the \hat{s} direction with a pulse. The discretization of a typical unit cell is shown in Figure 3.3. In order to simplify computation, the transfer of the derivatives and the function approximations discussed previously in Section 2.2.5 are applied to Equations (3.18a) and (3.18b) to reduce all calculations involving the periodic Green's function to the same form: integrating G_p over

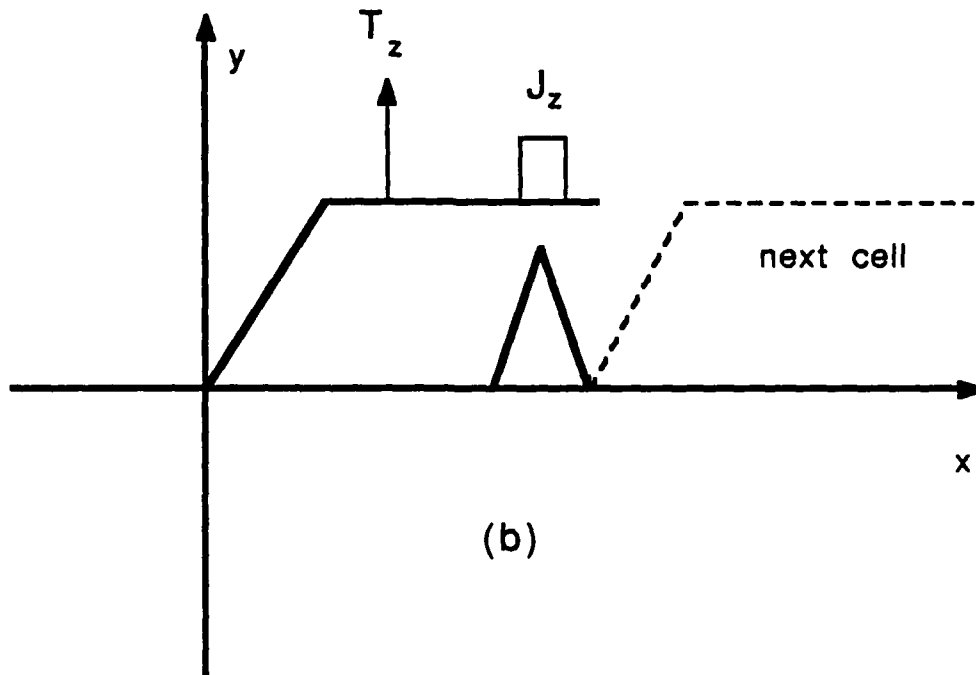
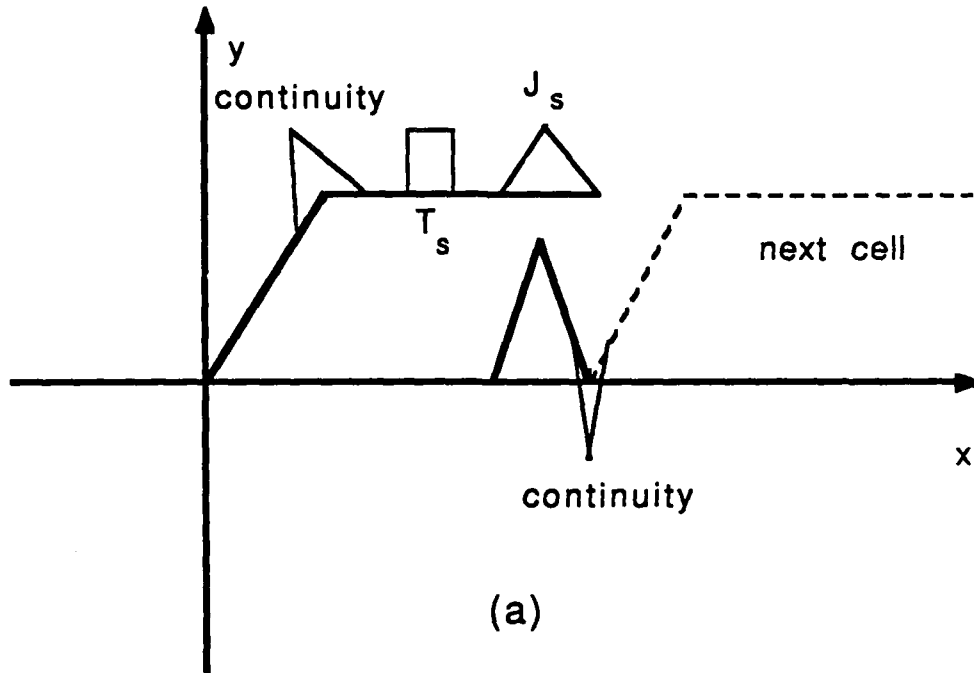


Figure 3.3 Discretization of the unit cell showing the \hat{s} directed (a) and the \hat{z} directed (b) basis and testing functions.

a basis pulse and testing the result at a point. The formulas derived in Chapter 2 are applied to these calculations making them as efficient as possible.

A generalized scattering matrix, which will be discussed in more detail in Chapter 5, is used to describe the interaction of the structure with the surrounding environment [31]. A brief description of the scattering matrix as applied to the problems of this chapter is given here to clarify the results given in Section 3.3. Two terminal planes enclosing the entire array structure are defined by $y = Y_{top}$ and $y = Y_{bot}$. Due to the periodic nature of the array, the scattered fields at the terminal planes may be described as a sum of outgoing, plane waves based on Floquet harmonics. Each plane wave is, in turn, divided into a combination of two plane waves polarized TE or TM to \hat{z} . The generalized scattering matrix catalogues the power, phase and polarization of each outgoing plane wave due to an incoming plane wave of defined power, phase and polarization. All outgoing/incoming combinations are listed.

The cataloguing method hinges on the fact that the components of each polarized plane wave can be expressed in terms of a scalar function as was done for the incident wave in Equations (3.2) and (3.3).

$$\Psi_{m \text{ TM/TE}} = a_{m \text{ TM/TE}} e^{+j(\beta_{xm}x + k_z z)} e^{\pm j\beta_y y} \quad (3.19)$$

where β_{xm} is the Floquet propagation constant in \hat{x} defined by Equation (2.13) (p. 21); β_y is defined by Equation (2.14) (p. 23) with k_0 replaced by κ ; and k_z is defined by Equation (3.1b). Equation (3.19) represents plane waves, either propagating or attenuating in the \hat{y} direction, going away from the array. The two weighting coefficients $a_{m \text{ TM/TE}}$ are determined from two outwardly traveling total \vec{E} field components for each Floquet harmonic (m) on the terminal planes. Remember that for the incident field, $a_{m \text{ TM/TE}}$ is equal to 1.

For the class of problems in this chapter, the \vec{E} field components in the \hat{z} and \hat{x} directions were chosen to define the weighting coefficients. E_z only contributes to the TM polarization; by invoking Equation (3.3c), the TM coefficient is obtained.

$$a_{m \text{ TM}} = \frac{j \omega \epsilon}{k_0^2 - k_z^2} E_{zm} \quad (3.20a)$$

Using $a_{m \text{ TM}}$ in Equation (3.2a) (with $-jk_x$ replaced by $+j\beta_{xm}$), the TM wave contribution to E_{xm} is obtained. If this contribution is subtracted from the total E_{xm} component, the TE contribution to E_{xm} remains, which is used in Equation (3.3a) (with $-jk_y$ replaced by $\pm j\beta_y$) to calculate the TE coefficient.

$$a_{m \text{ TE}} = \pm \frac{1}{j\beta_y} \left[E_{xm} + \frac{\beta_{xm} k_z}{k_0^2 - k_z^2} E_{zm} \right] \text{ for } \pm y \text{ traveling wave} \quad (3.20b)$$

In order to obtain the total \hat{x} and \hat{z} \vec{E} field components required in the calculations above, the scattered field for a given harmonic must be calculated using Equations (3.11) and (3.15).

$$E_{zm}^{\text{scat}} = \frac{k_0^2 - k_z^2}{j\omega\epsilon} \left[\tilde{J}_{zm} \tilde{G}_m \right] + \frac{jk_z}{j\omega\epsilon} \left[\frac{\partial \tilde{J}_{s'm}}{\partial s'} \tilde{G}_m \right] \quad (3.21a)$$

$$E_{xm}^{\text{scat}} = \frac{k_0^2}{j\omega\epsilon} \hat{x} \cdot \left[\tilde{J}_{s'm} \tilde{G}_m \right] + \frac{j\beta_{xm}}{j\omega\epsilon} \left[\frac{\partial \tilde{J}_{s'm}}{\partial s'} \tilde{G}_m \right] - \frac{k_z \beta_{xm}}{j\omega\epsilon} \left[\tilde{J}_{zm} \tilde{G}_m \right] \quad (3.21b)$$

where

$$\tilde{G}_m = \frac{1}{b} \frac{e^{-j|y-y'|\beta_y}}{2j\beta_y} e^{j\beta_{xm}(x-x')} \quad (3.22)$$

is a single Floquet harmonic of the spectral portion of the periodic Green's function shown in Equation (2.14a). The derivatives in the z direction are represented by $+jk_z$, while the derivatives in \hat{x} have been replaced by $+j\beta_{xm}$ for each harmonic. The total E field is found by adding the incident E field to the scattered field if the incident and scattered fields have the same harmonic and are propagating in the same direction.

The power carried by each plane wave in \hat{y} may be written in terms of Ψ as

$$P_{m \text{ TM}} = \pm \frac{\beta_y^*}{\omega \epsilon} (k_0^2 - k_z^2) |\Psi_{m \text{ TM}}|^2 \quad \pm y \text{ traveling} \quad (3.23a)$$

$$P_{m \text{ TE}} = \pm \frac{\beta_y}{\omega \mu} (k_0^2 - k_z^2) |\Psi_{m \text{ TE}}|^2 \quad \pm y \text{ traveling} \quad (3.23b)$$

β_y^* is the complex conjugate of β_y . The power is real for propagating waves and imaginary for attenuating waves.

The above calculations are used in the generalized scattering matrix to replace the physical structure by a multiport network, each port of which corresponds to one Floquet harmonic with a given polarization. The generalized scattering matrix is an extension of the ordinary S matrix [55], since instead of a simple two by two matrix, the elements of the S matrix

$$S = \begin{bmatrix} S_{11} & S_{12} \\ S_{21} & S_{22} \end{bmatrix} \quad (3.24)$$

are made of submatrices. For example,

$$S_{11} = \begin{bmatrix} \text{TE}|\text{TE} & \text{TE}|\text{TM} \\ \text{TM}|\text{TE} & \text{TM}|\text{TM} \end{bmatrix} \quad (3.25)$$

where TE/TM means the the TE polarization of the outgoing wave is catalogued given that the incoming wave is polarized TM.

Within each of the submatrices, a sub-submatrix describes the interaction between input and output Floquet harmonics m and n . Continuing with the above example, each element $S_{\text{TE}|\text{TM}}(m, n)$ is defined as

$$S_{TE/TM}(m,n) = \left[\frac{|P_{m TE}(out)|}{|P_{n TM}(in)|} \right]^{1/2} \text{Phase } \Psi_{m TE}(out) - \text{Phase } \Psi_{n TM}(in) \quad (3.26)$$

The magnitude of the matrix element is determined by the square root of the power magnitude ratios of the output and input waves in keeping with the units of the traditional S matrix definition. The phase of the element is determined by the difference between the phases of Ψ at the output and input planes. Note that the output and input planes are the same for the S_{11} and S_{22} calculations.

3.3 Results

In all of the following results, the magnitudes of the propagating S_{11} harmonics are plotted versus cell size (b) for various configurations of the unit cell. The cell size is normalized to the wavelength of the incident wave. Given a normally incident ($\theta_i = 90^\circ, \phi_i = 88^\circ$) TM wave on the two strip configuration of Figure 3.4, the 0 and ± 1 reflected TM harmonics are shown in Figure 3.5. Since $\theta_i = 90^\circ$ and $R = 0 \Omega$, no TM/TE cross-coupling exists. This compares to Hall's results [30] which are found using entire domain basis functions and are shown by points on the curves.

The effect of adding loss to the corrugated structure of Figure 3.6 is shown in Figure 3.7 for a normally incident TE wave ($\theta_i = 90^\circ, \phi_i = 88^\circ$). Continuity functions are added between strips and between unit cells in order to make the structure continuous. Added resistance attenuates the amount of power reflected and reduces the variation in the reflection curves as the cell size is changed. The 500Ω curve is compared to Hall's results. The form and level of the two results are the same. There is a slight shift in resonance between the two, which is attributable to the difference in basis functions. Since $\theta_i = 90^\circ$, no cross-coupling exists.

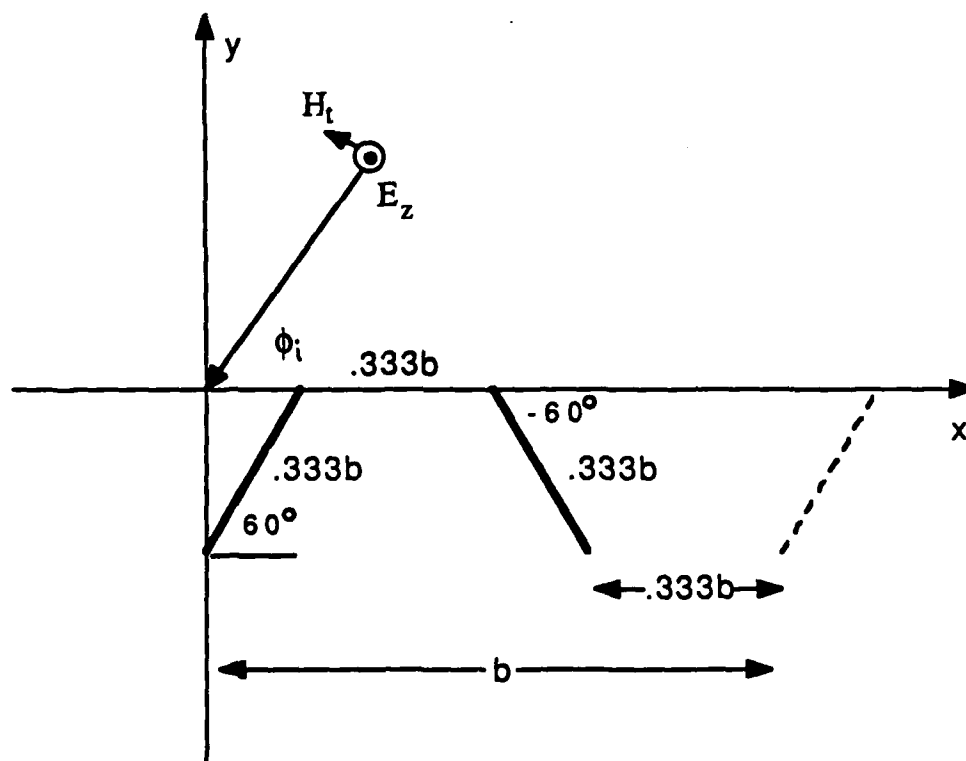


Figure 3.4 A unit cell composed of two lossless strips, each $b/3$ long and rotated 60° with respect to \hat{x} . The spacing between the strips is $b/3$. The incident wave lies in the xy plane and is polarized TM to \hat{z} .

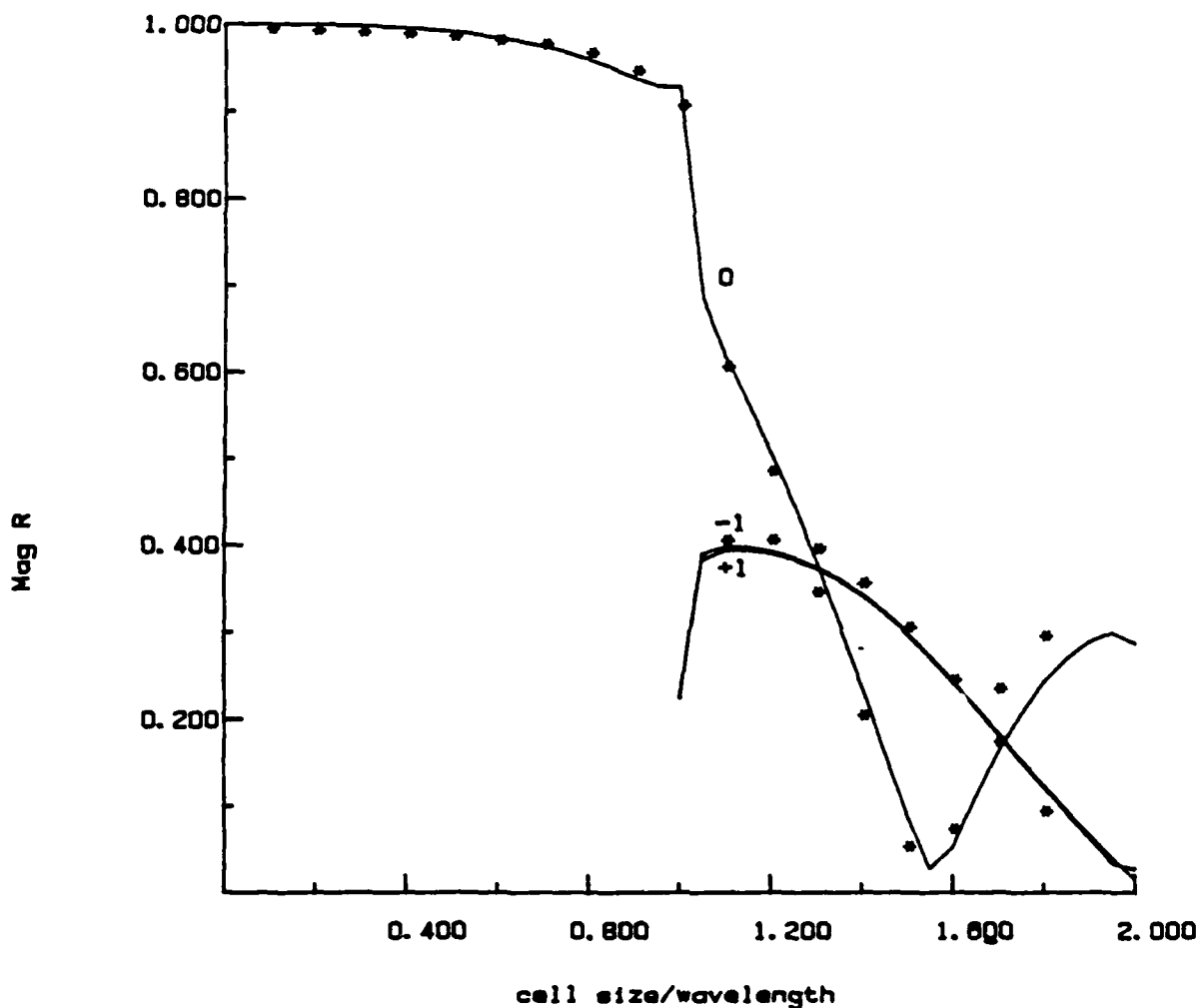


Figure 3.5 The magnitude of the TM reflection coefficient given that the incident field is TM polarized ($|S_{11TM/TM}|$) plotted versus the size of the unit cell which is normalized to the wavelength of the incident field (b/λ). The geometry is shown in Figure 3.4. The incident wave is almost normally incident on the array, i.e., $\theta_i = 90^\circ$, $\phi_i = 88^\circ$ and the strips are lossless ($R = 0 \Omega$). Only the harmonics propagating in \hat{y} ($0, \pm 1$) are shown. The results are compared to Hall's [30] results which are indicated by *.

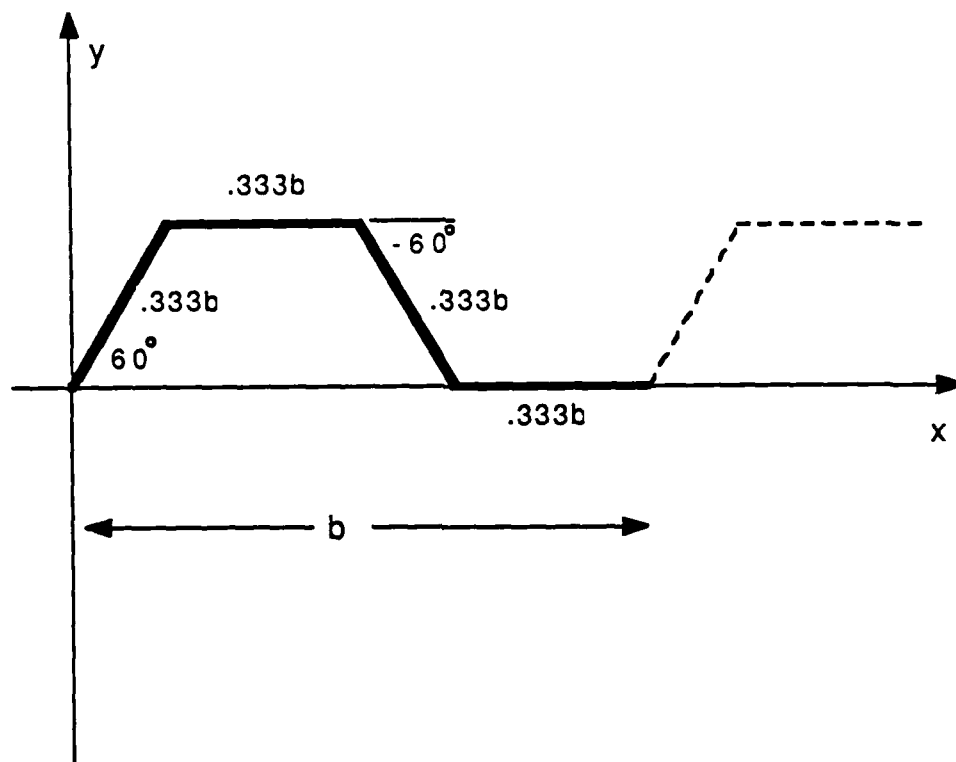


Figure 3.6 Corrugated structure made of four resistive strips each $b/3$ long. In the following results, the strips are either all connected to each other and to adjacent unit cells using overlapping triangles or all insulated from each other.

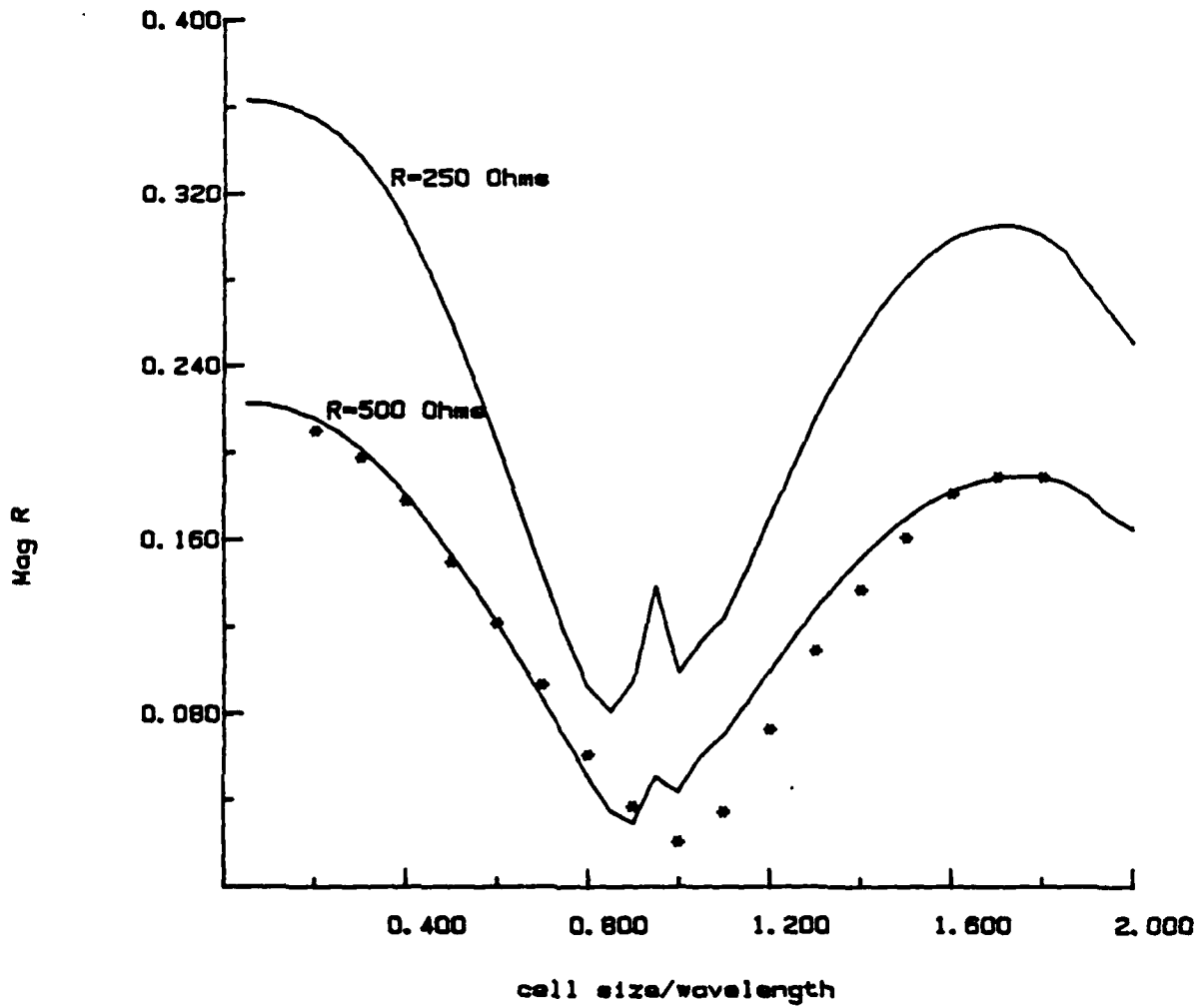


Figure 3.7 $|S_{11TE/TE}|$ versus b/λ for the continuous geometry of Figure 3.6. The incident field is almost normally incident, i.e., $\theta_i = 90^\circ$, $\phi_i = 88^\circ$. The lossy strips are modeled by $R=250 \Omega$ and $R=500 \Omega$. Only the zeroth-order harmonic is shown although the ± 1 harmonics also propagate at around $b/\lambda = 1.0$. This is the cause of the Wood's anomaly shown. The points * are from Hall [30] for 500Ω .

Figures 3.8-3.11 show the reflection due to an oblique ($\theta_i=45^\circ, \phi_i=88^\circ$) wave from two variations of the geometry shown in Figure 3.6. Resistance in this case was set at 100Ω . The curves labeled "continuous" are for the geometry in which current continuity is imposed between strips and between unit cells. Insulating the strips from one another produces the curves labeled "discontinuous." Making the structure discontinuous affects mostly the TE/TE reflection as shown in Figure 3.8. At low frequencies, the TE/TE harmonic for the continuous structure behaves similarly to a TM/TM harmonic in that the reflection coefficient is large. For the discontinuous structure, however, the TE wave travels through the structure with very little reflection at low frequencies. The TM/TM case, shown in Figure 3.9, shows little difference between the reflection from a continuous or discontinuous structure because the main contributor to the TM reflection is J_z which is not affected by the discontinuity of the structure in the \hat{s} direction. The TM/TE coupling (Figure 3.10) and the TE/TM coupling (Figure 3.11) show little difference between the continuous and discontinuous geometries.

The TE/TM and TM/TE cross-coupling for Figure 3.6 and $\phi_i \approx 90^\circ$ angle of incidence is very weak for the zeroth harmonic as shown in Figure 3.12. If the incident wave is scanned off the direction normal to \hat{x} , the cross-coupling becomes stronger. This is shown in Figure 3.13 for $\theta_i=45^\circ, \phi_i=45^\circ$, where the zeroth harmonic of TM/TE actually becomes stronger than that for TE/TE for some cases of cell size. It was found that if the unit cell has even symmetry in an x -constant plane, then for $\phi_i=90^\circ$, little cross-coupling in the zeroth harmonic is produced. Cross-coupling is increased as ϕ_i is scanned away from normal. If the unit cell has no symmetry in an x -constant plane, then there is strong coupling in the zeroth harmonic regardless of the value of ϕ_i .

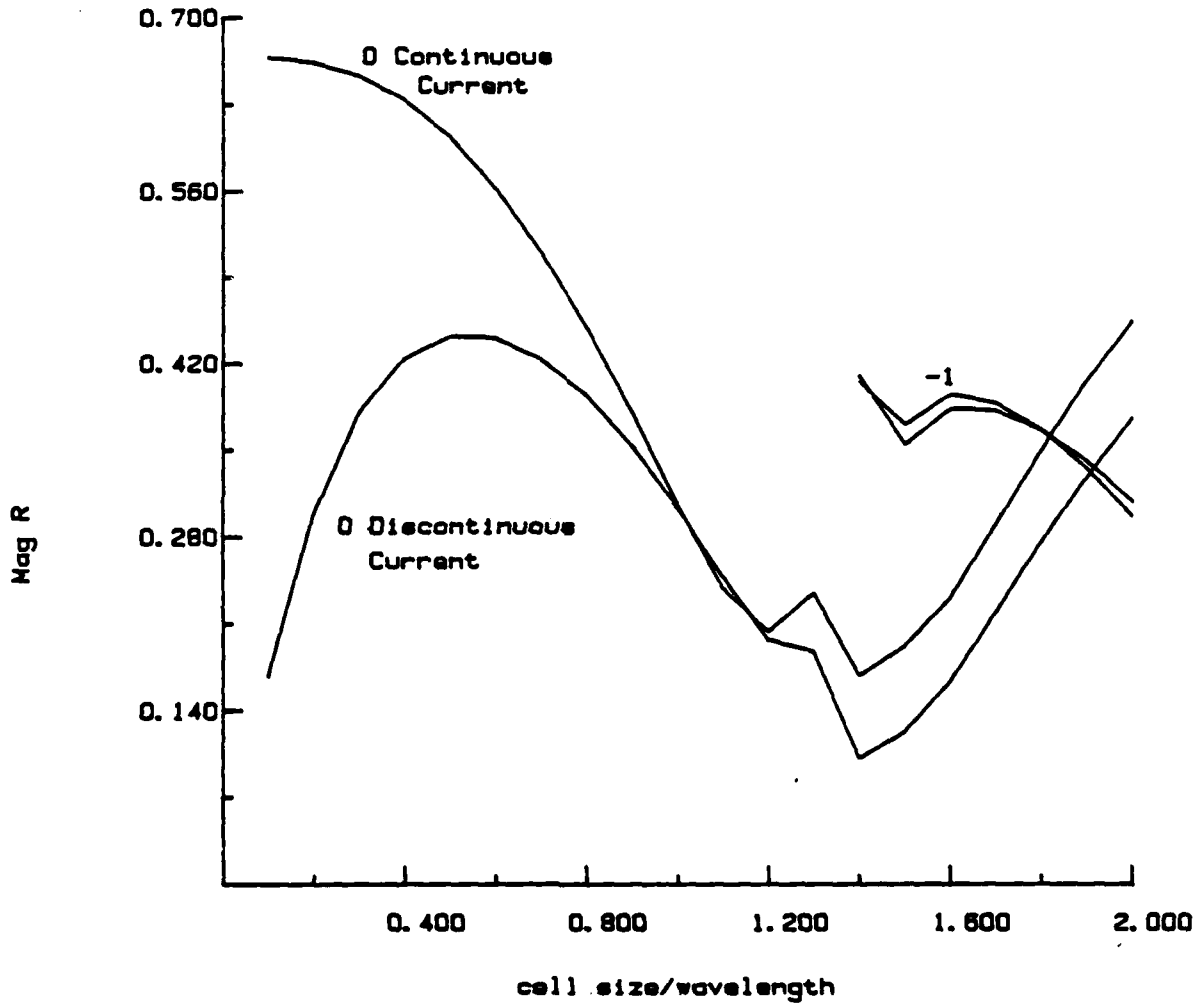


Figure 3.8 $|S_{11TE/TE}|$ versus b/λ for the continuous and discontinuous geometries of Figure 3.6. The strips all have the resistance $R = 100 \Omega$. The incident wave is obliquely incident, $\theta_i = 45^\circ$, $\phi_i = 88^\circ$.

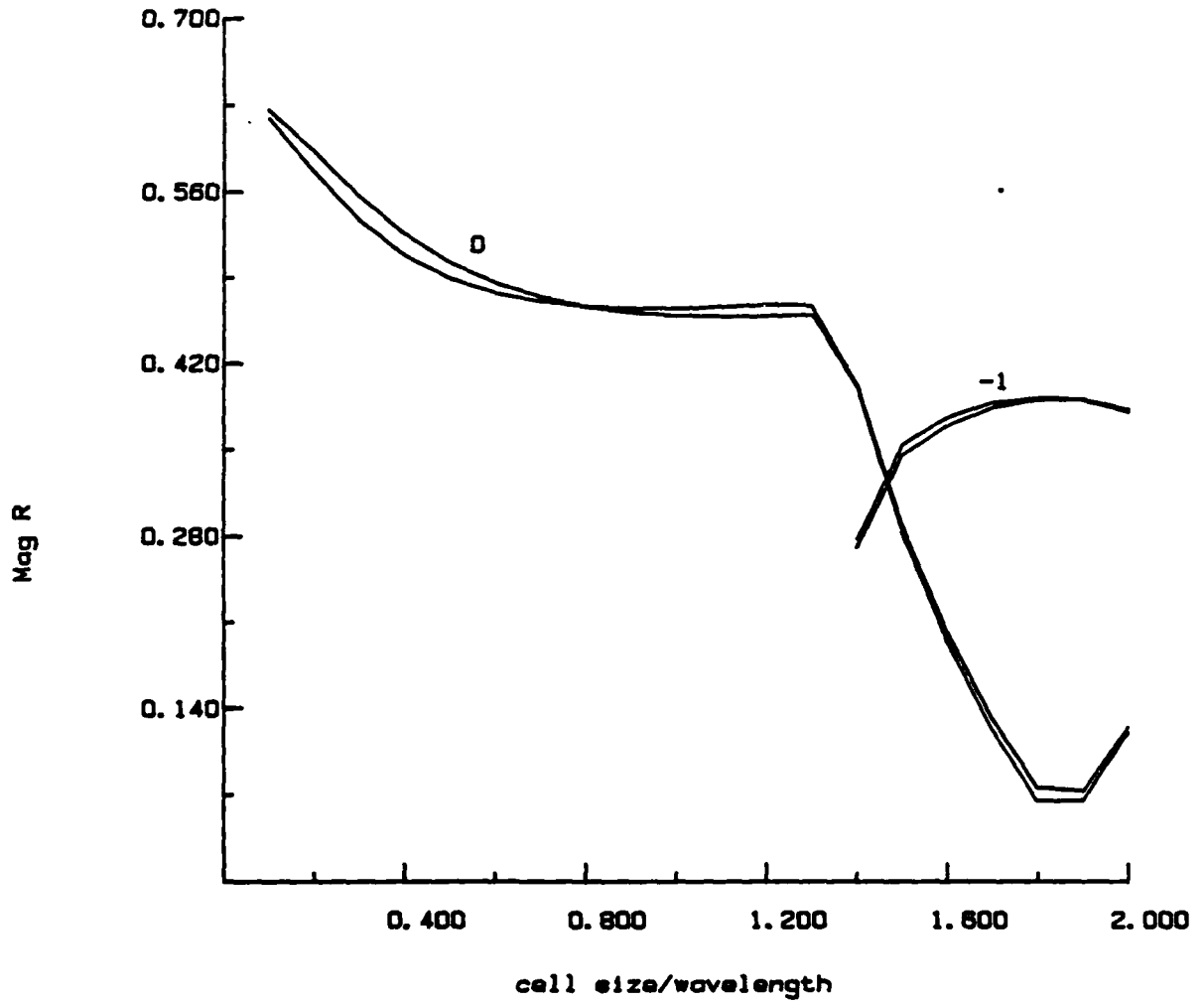


Figure 3.9 $|S_{11TM/TM}|$ versus b/λ for the continuous and discontinuous geometries of Figure 3.6. The strips all have the resistance $R = 100 \Omega$. The incident wave is obliquely incident, $\theta_i = 45^\circ$, $\phi_i = 88^\circ$.

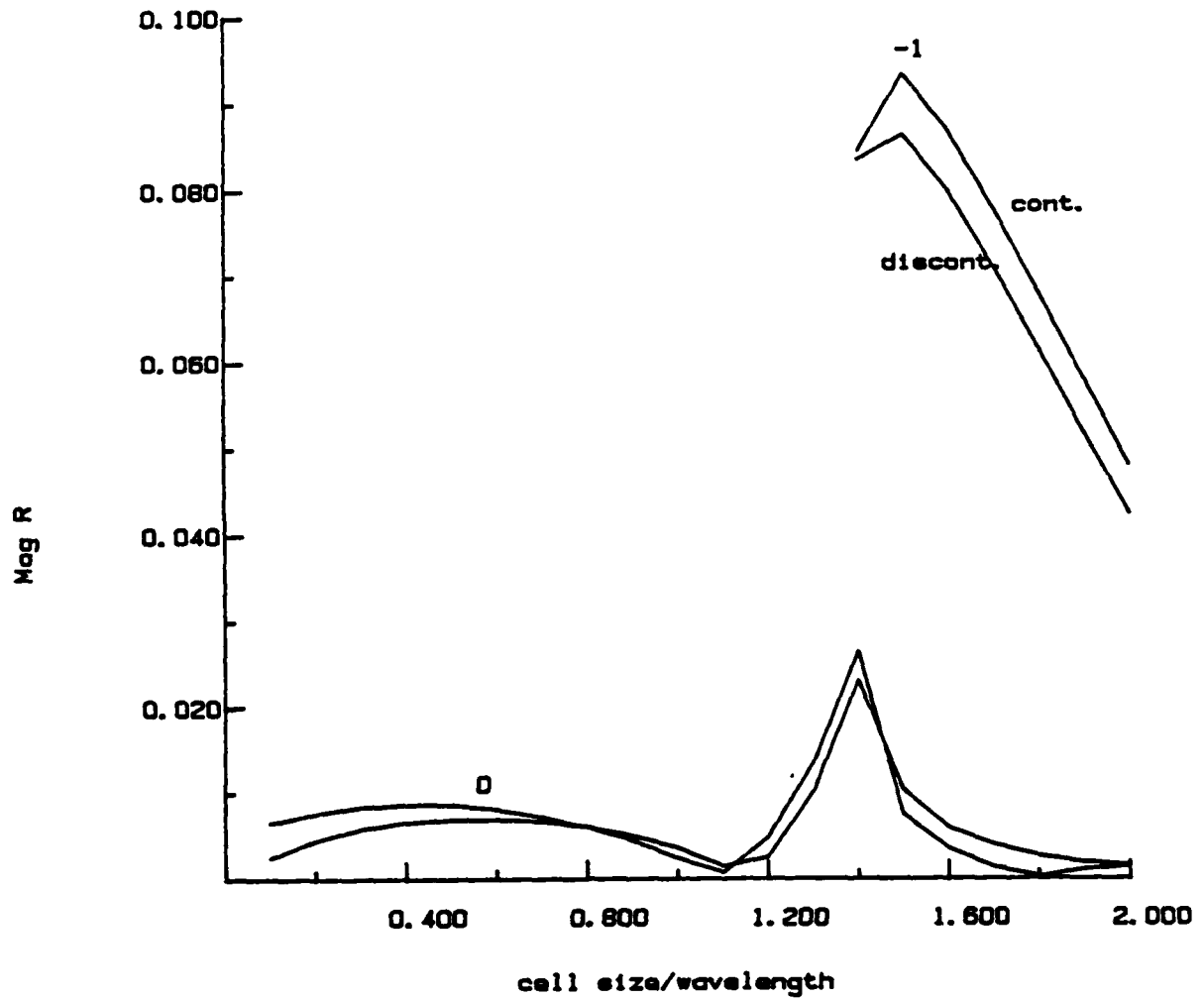


Figure 3.10 $|S_{11TM/TE}|$ versus b/λ for the continuous and discontinuous geometries of Figure 3.6. The strips all have the resistance $R = 100 \Omega$. The incident wave is obliquely incident, $\theta_i = 45^\circ$, $\phi_i = 88^\circ$.

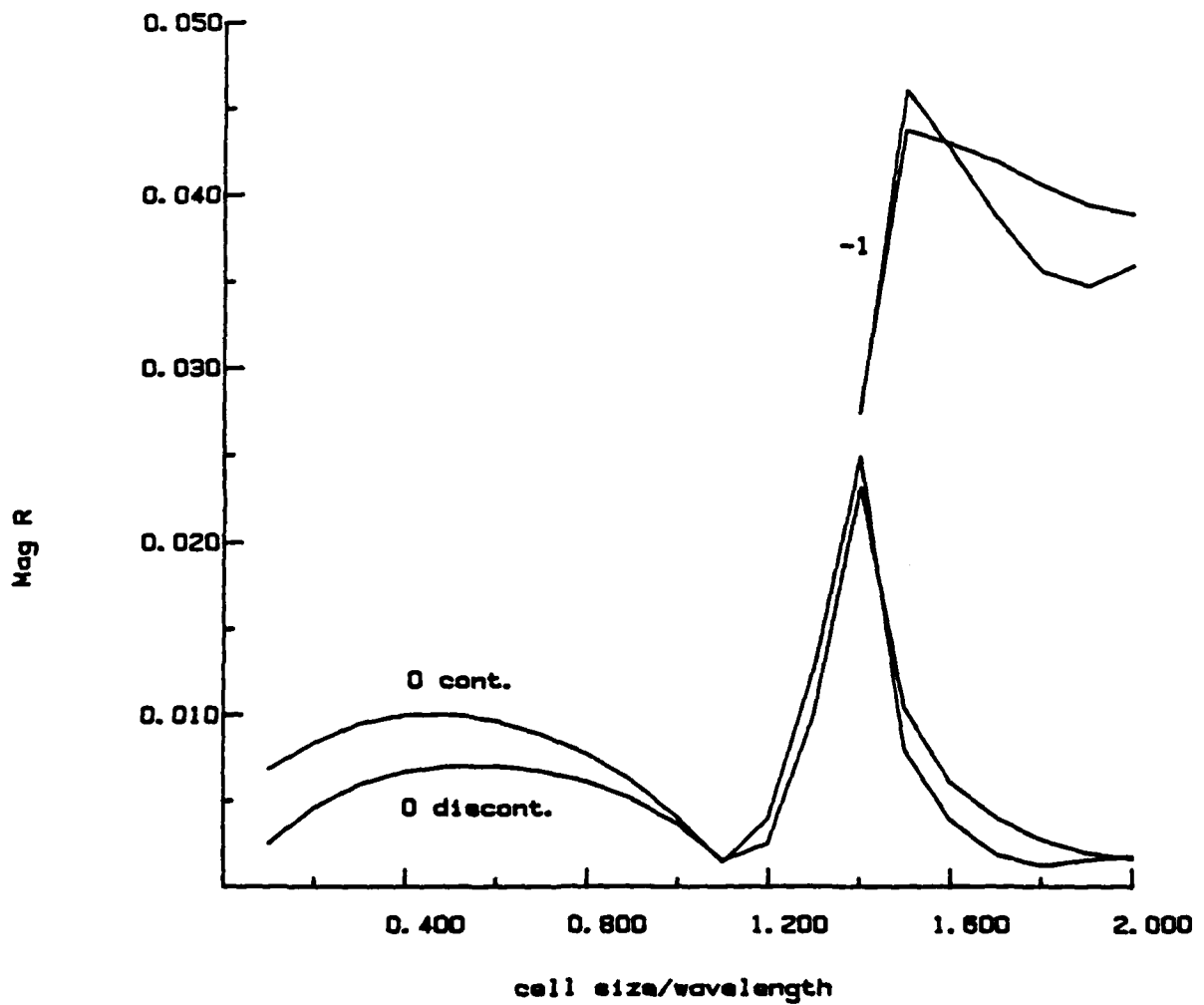


Figure 3.11 $|S_{11TE/TM}|$ versus b/λ for the continuous and discontinuous geometries of Figure 3.6. The strips all have the resistance $R = 100 \Omega$. The incident wave is obliquely incident, $\theta_i = 45^\circ$, $\phi_i = 88^\circ$.

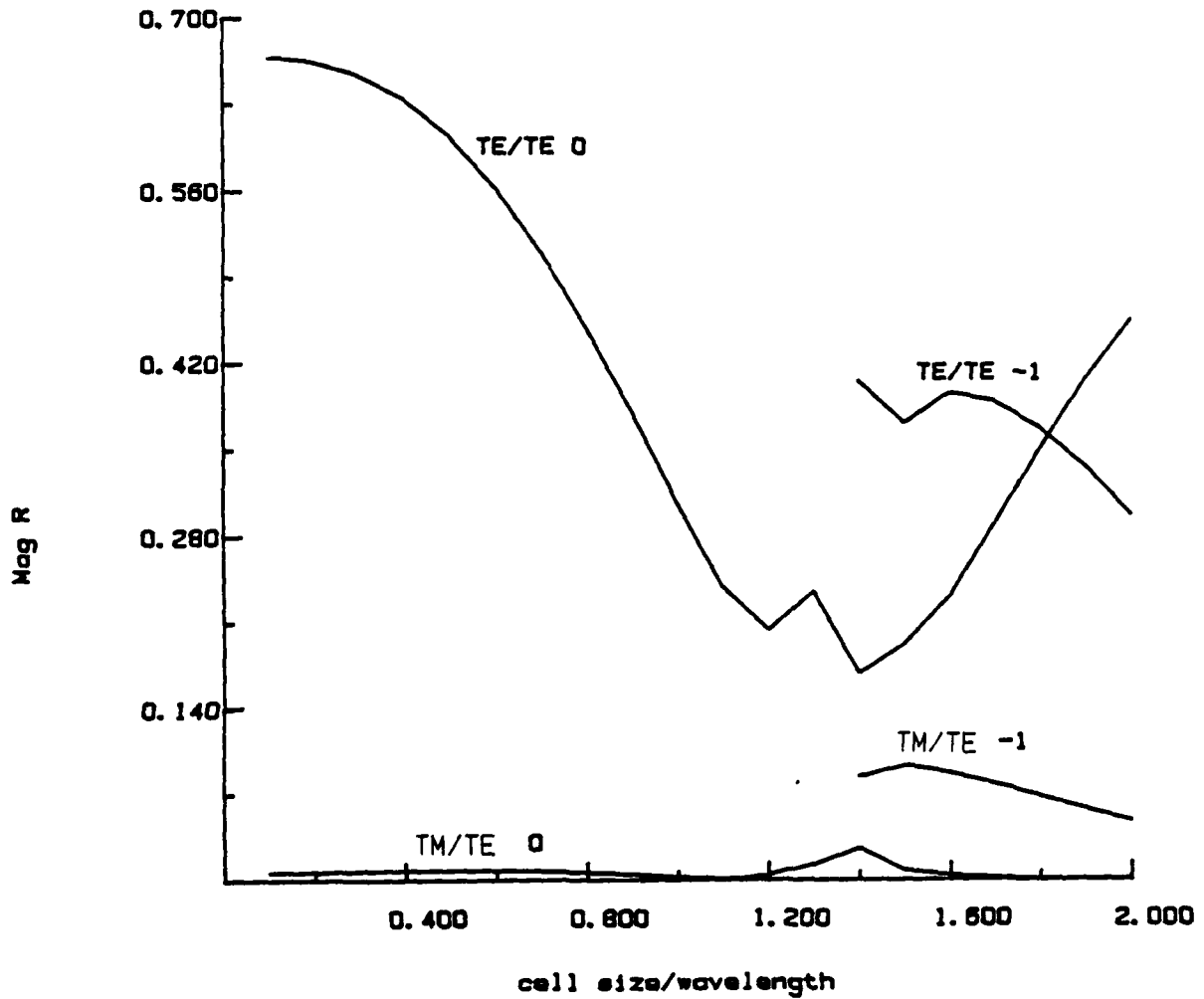


Figure 3.12 $|S_{11TE/TE}|$ and $|S_{11TM/TE}|$ versus b/λ for the geometry of Figure 3.6 with the strips connected to each other and to neighboring unit cells. The strip resistance is set at $R=100 \Omega$. The Floquet harmonics 0 and -1 are plotted for an incident angle of $\theta_i = 45^\circ$, $\phi_i = 88^\circ$. Note that the zeroth-order cross-coupled harmonics are small compared to the co-coupled harmonics.

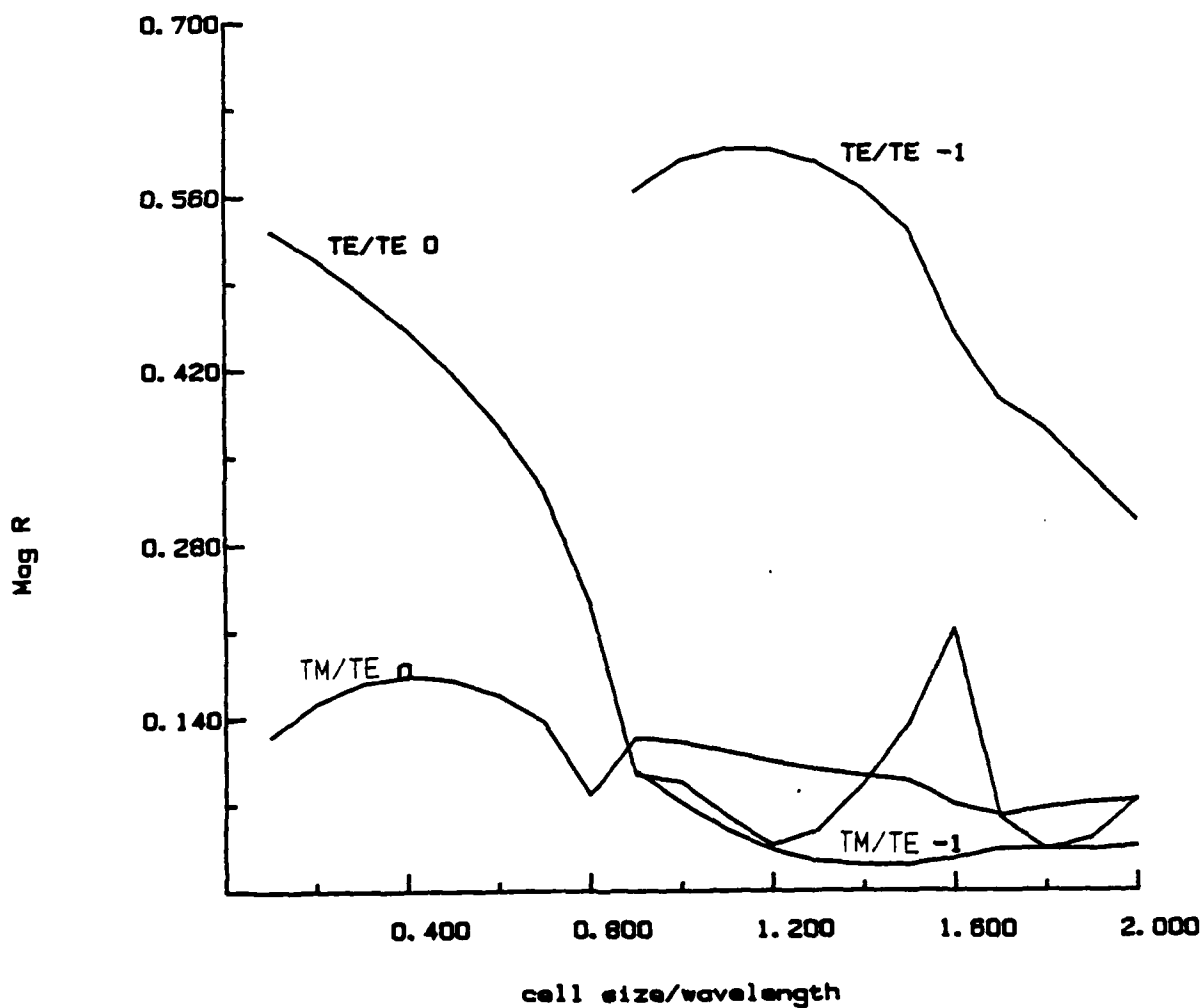


Figure 3.13 $|S_{11TE/TE}|$ and $|S_{11TM/TE}|$ versus b/λ for the geometry of Figure 3.6 with the strips connected to each other and to neighboring unit cells. The strip resistance is set at $R=100 \Omega$. The Floquet harmonics 0 and -1 are plotted for an incident angle of $\theta_i = 45^\circ$, $\phi_i = 45^\circ$. Note that the zeroth-order cross-coupled harmonics are comparable to the co-coupled harmonics.

The effect on the coefficient S_{11} of adding resistance to the unit cell described in Figure 3.14 is shown in Figures 3.15-3.18. The incident plane wave is obliquely incident ($\theta_i=45^\circ, \phi_i=45^\circ$) and the strips of the unit cell are connected to each other where they touch. Figures 3.15 and 3.16 show the co-coupled and cross-coupled harmonics for a strip resistance of 250Ω . The cross-coupled harmonics have increased from a value of zero for $R=0 \Omega$ to values comparable to that for the co-coupled harmonics. The co-coupled harmonics decrease as the resistance is increased. The zeroth harmonic is shown as resistance increases to 500Ω (Figure 3.17) and 1000Ω (Figure 3.18). Both co-coupled and cross-coupled reflection characteristics decrease and flatten as resistance increases. This behavior as a function of resistance is shown more clearly in Figure 3.19, in which the magnitude of S_{11} is plotted versus resistance for a plane wave obliquely incident ($\theta_i=45^\circ, \phi_i=45^\circ$) on the geometry of Figure 3.14. The cell size is fixed at 0.6λ .

The small peaks in the curves that occur, for example, in Figures 3.15-3.18 at around $b/\lambda = 0.8$ and $b/\lambda = 1.6$ are due to a type of Wood's anomaly associated with Rayleigh wavelengths [13]. These anomalies occur when the higher-order harmonics (in this case the -1,-2 harmonics) change from waves that are nonpropagating to waves that are propagating in \hat{y} . At this point, the power distribution in the various harmonics is rearranged. Note that the -2 harmonic is not plotted in these figures to avoid graph clutter which makes it seem as if the peaks around $b/\lambda = 1.6$ occur without reason.

3.4 Conclusions

This chapter has shown the reflection behavior of an oblique plane wave incident on a one-dimensional array of unit cells composed of resistive strips. It was shown that coupling exists between the TE and TM components of the waves. The coupling for the zeroth harmonic is very weak if the plane wave is incident normally ($\phi_i=90^\circ$) on a

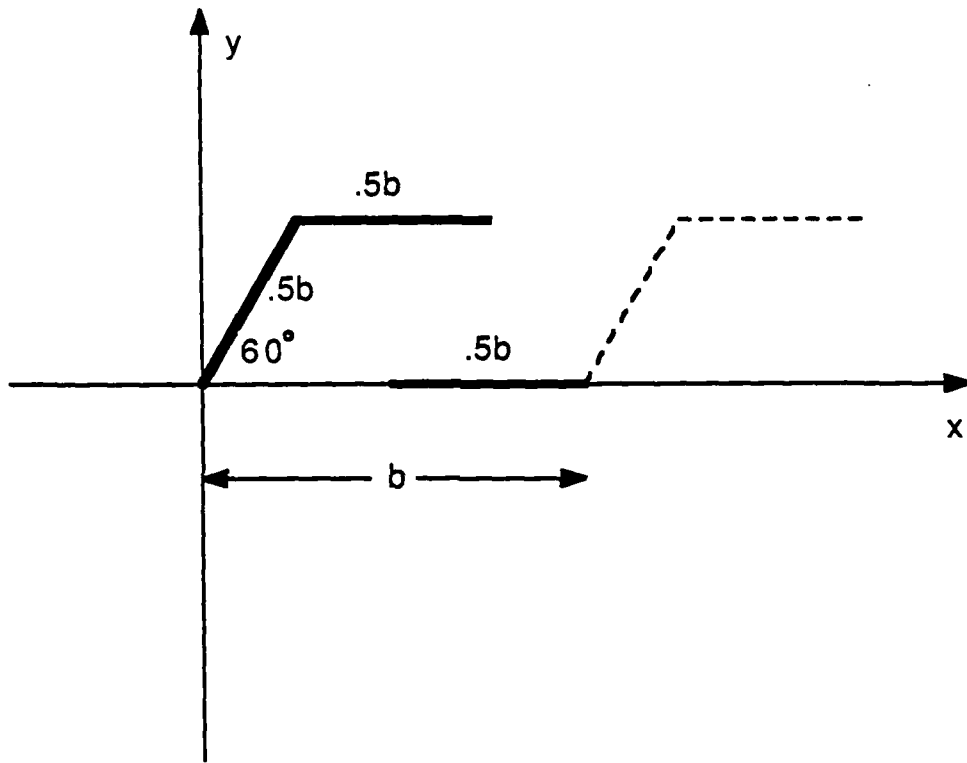


Figure 3.14 Overlapping structure made of three strips each $b/2$ long. The strips are connected to each other where they touch.

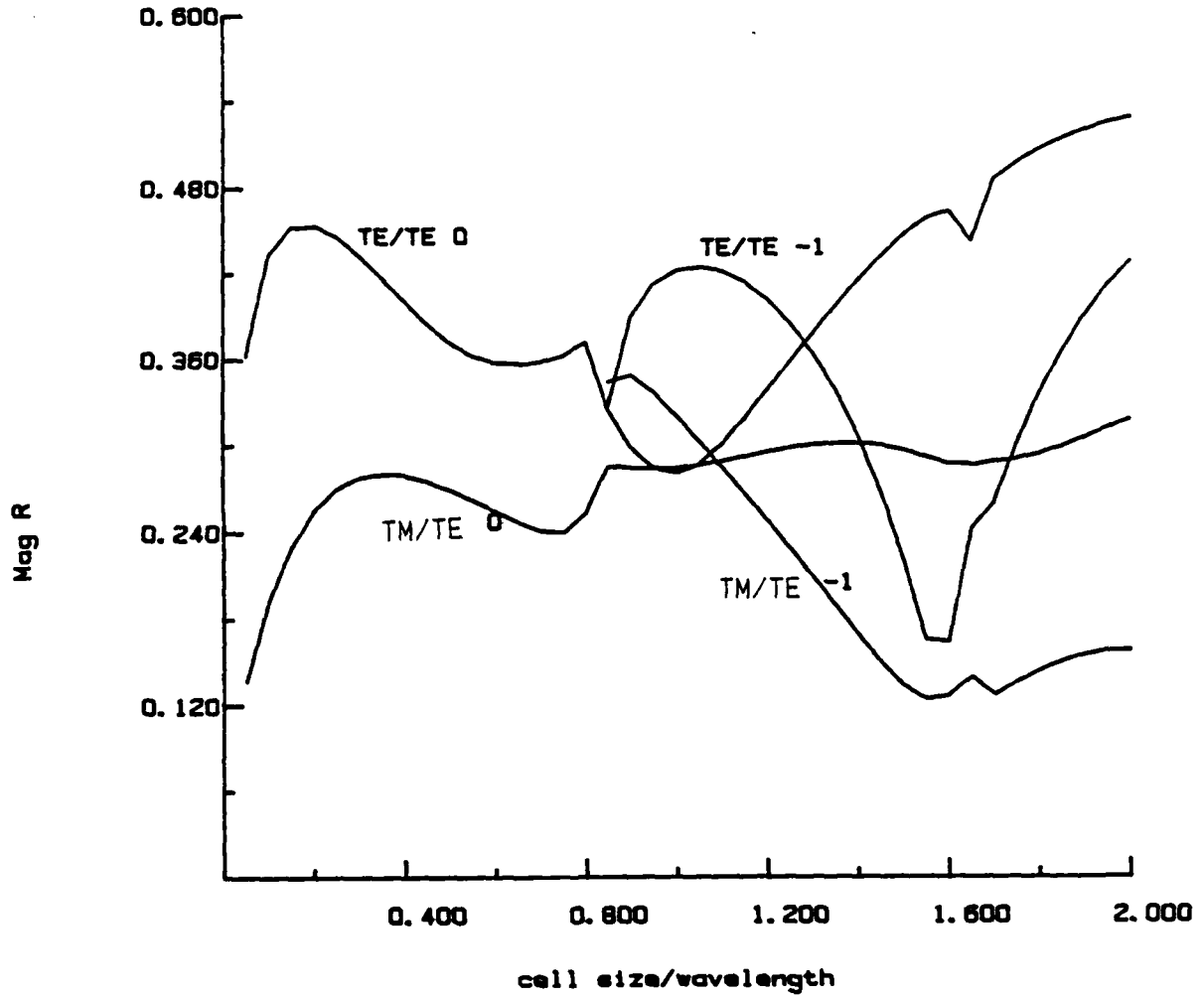


Figure 3.15 $|S_{11}|$ versus b/λ for the geometry of Figure 3.14. A wave is obliquely incident ($\theta_i = 45^\circ, \phi_i = 45^\circ$) on a structure with $R = 250 \Omega$. The 0 and -1 harmonics are shown for the TE/TE and TM/TE responses. The -2 harmonic begins propagating at around $b/\lambda = 1.6$ but is not shown to prevent graph clutter.

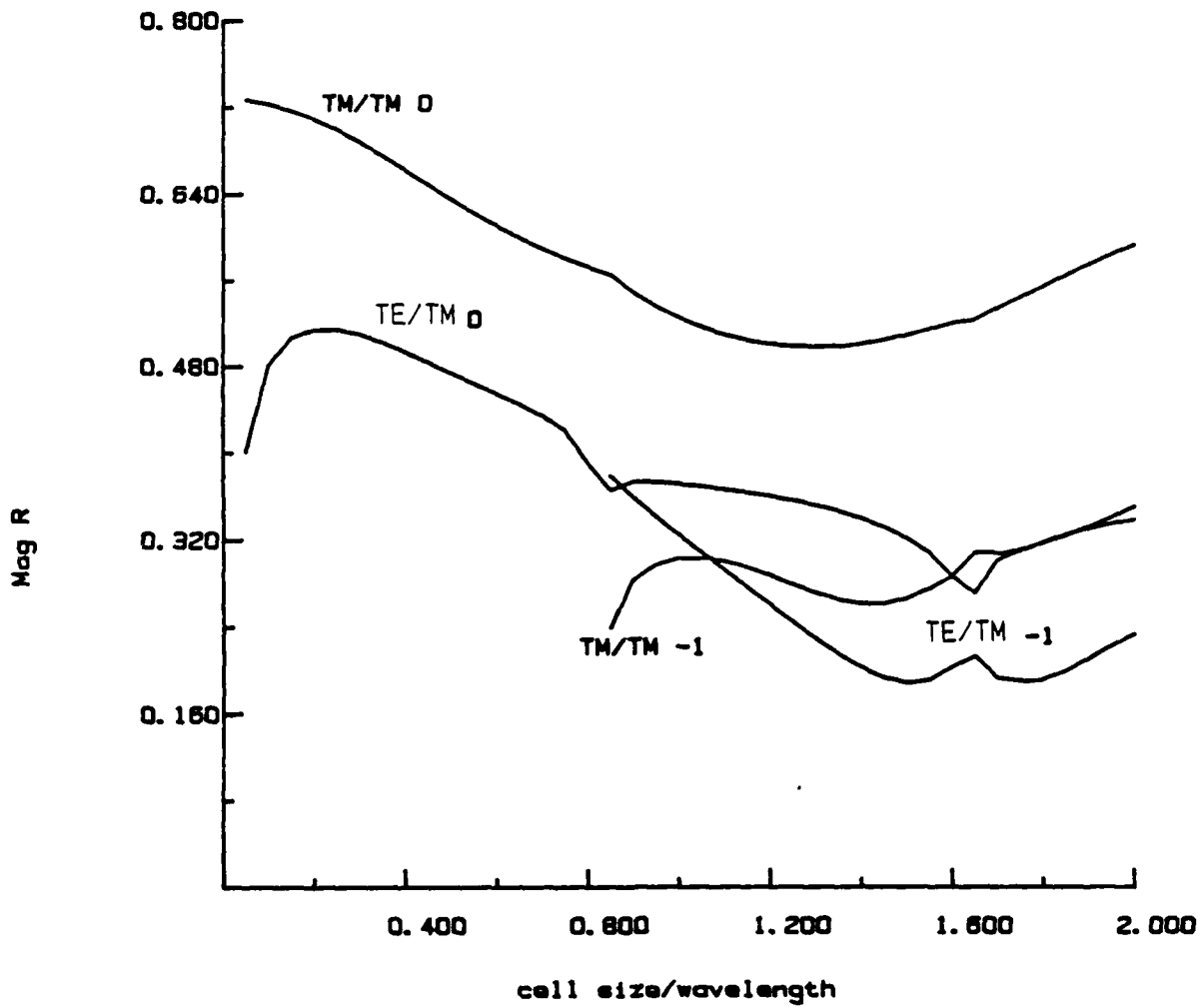


Figure 3.16 $|S_{11}|$ versus b/λ for the geometry of Figure 3.14. A wave is obliquely incident ($\theta_i = 45^\circ, \phi_i = 45^\circ$) on a structure with $R=250 \Omega$. The 0 and -1 harmonics are shown for the TM/TM and TE/TM responses. The -2 harmonic begins propagating at around $b/\lambda = 1.6$ but is not shown to prevent graph clutter.

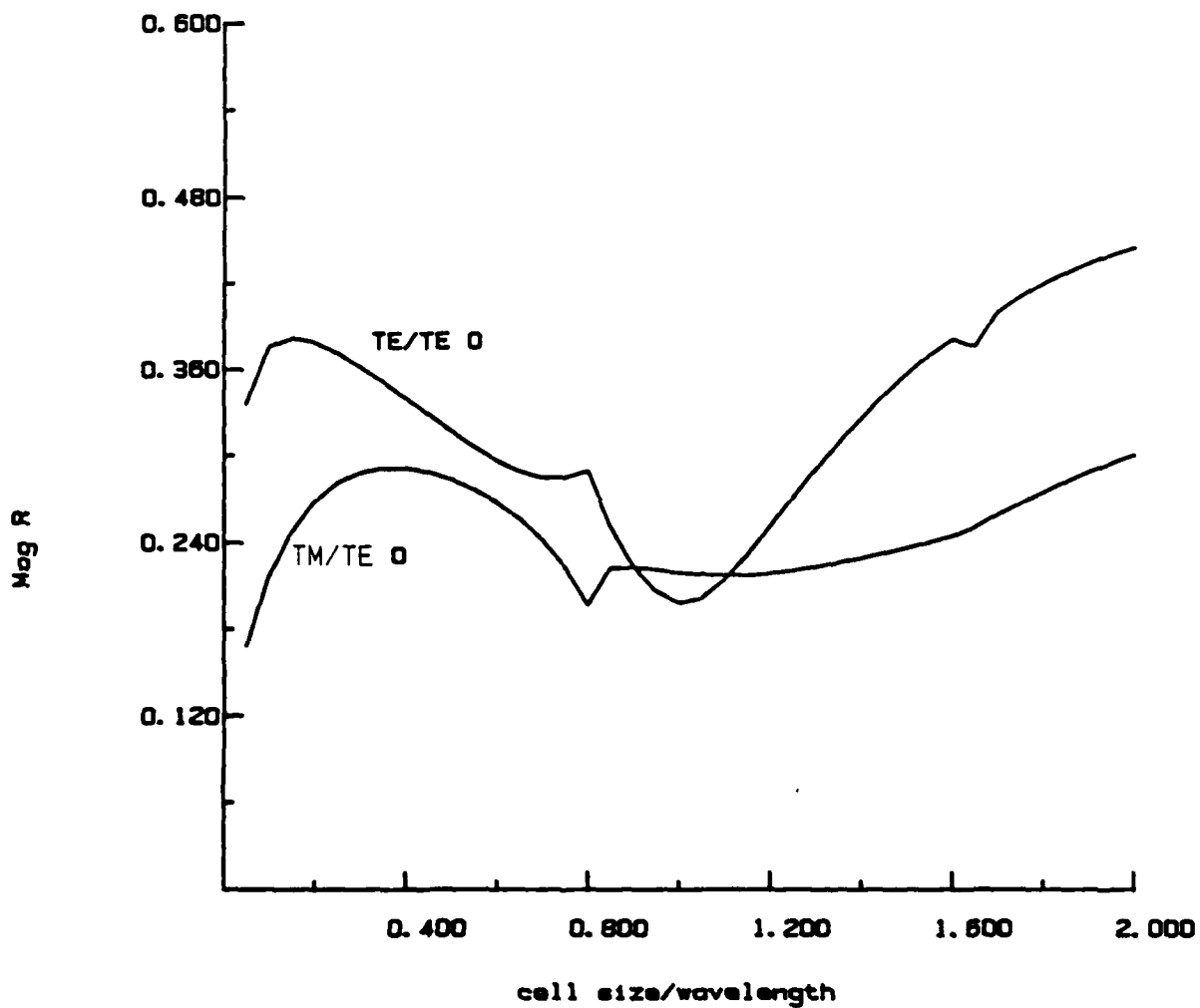


Figure 3.17 $|S_{11}|$ versus b/λ for the geometry of Figure 3.14. A wave is obliquely incident ($\theta_i = 45^\circ, \phi_i = 45^\circ$) on a structure with $R=500 \Omega$. The zeroth harmonic is shown for the TE/TE and TM/TE responses. The -1 and -2 harmonics also propagate but are not shown.

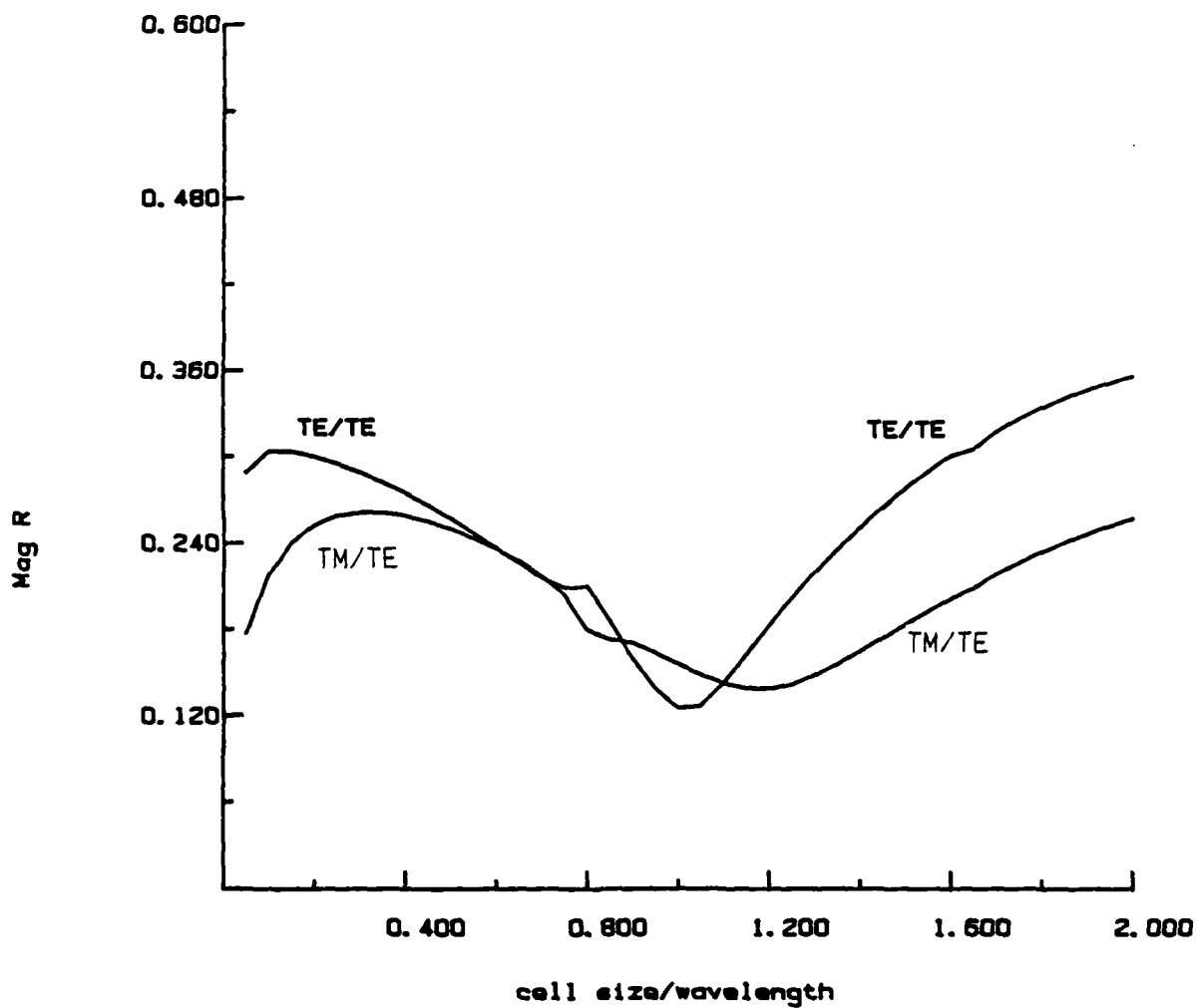


Figure 3.18 $|S_{11}|$ versus b/λ for the geometry of Figure 3.14. A wave is obliquely incident ($\theta_i = 45^\circ, \phi_i = 45^\circ$) on a structure with $R = 1000 \Omega$. The zeroth harmonic is shown for the TE/TE and TM/TE responses. The -1 and -2 harmonics also propagate but are not shown.

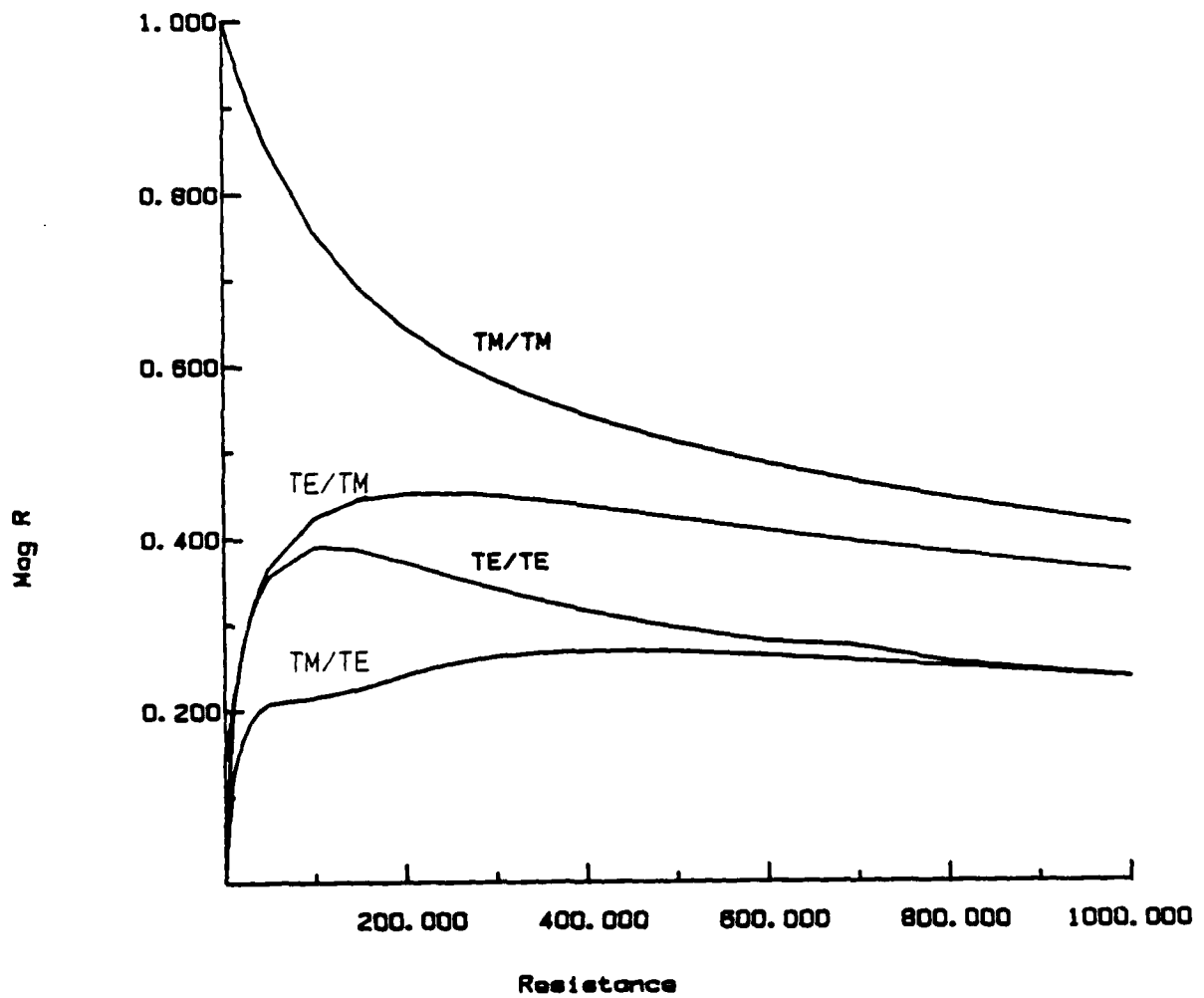


Figure 3.19 The zeroth harmonic of $|S_{11}|$ versus strip resistance for geometry of Figure 3.14. All polarization combinations are plotted. The incident wave is $\theta_i = 45^\circ$, $\phi_i = 45^\circ$. The frequency is fixed so that $b = 0.6\lambda$.

structure of even symmetry with respect to an x -constant plane. The cross-coupling for the zeroth harmonic is comparable to the co-coupled harmonic if $\phi_i \neq 90^\circ$ or if no even symmetry exists in the unit cell with respect to the x -constant plane. As resistance increases, the cross-coupling between TE and TM increases and the co-coupling decreases until $R > 500 \Omega$; then all reflection coefficients decrease.

4. PERIODICITY IN TWO DIMENSIONS – PROBLEMS BASED ON PLATE ARRAYS

4.1 Introduction

The method applied in the previous chapter to solve one-dimensional arrays of unit cells composed of resistive strips naturally extends to two-dimensional arrays of unit cells composed of resistive plates. The plate unit cell is more difficult to solve than the strip because the geometry is no longer invariant in one of the directions. The functional variation of quantities in that direction is, therefore, no longer solely dependent on the known incident field, rather it is an additional unknown which must be solved for. Consequently, the moment method solution of a relatively thin slab of honeycomb-like material can easily require a number of unknowns which can overload a computer system.

Most of the past analyses in the area of scattering from a two-dimensional array have been applied to Frequency Selective Surfaces (FSSs). An FSS is formed by repeating an infinitesimally thin, perfectly conducting patch periodically along a two-dimensional lattice. The patches lie flat in the plane of periodicity. This problem was initially solved by applying Babinet's principle to the complementary aperture problem which was, in turn, solved by mode matching the Floquet harmonics on either side of the screen to the modes of a waveguide having a cross-section identical to the shape of the aperture [19]. Later, investigators bypassed the use of the aperture as a conceptual aid by discretizing the patch directly [20]. The currents on simple patches were also modeled more accurately using basis functions that incorporated the edge condition, rather than basis functions that modeled the waveguide modes [56]. Patches with a more complex geometry were solved by putting entire domain basis functions over portions of the patch [21] or by using subdomain basis functions [22],[23],[57],[58].

Although the unit cell had evolved into a complicated structure over the years, it was, up to this point, still regarded as a thin, lossless structure. A few investigators [57],[58] added loss to the structure through the use of the resistive boundary condition in order to apply the FSS to the problem of RCS reduction. In 1986, Rubin [24], in a method analogous to the one he used for thick bars [18], examined the behavior of a thick, periodic structure. The patch still lay flat in the plane of periodicity; however, along with discretization in the major dimensions of the patch, the thickness was discretized with subdomain basis functions. The case in which the slab thickness is due to rotating thin resistive plates out of the plane of periodicity in a manner analogous to Hall's work with rotated strips [30] is yet to be analyzed.

This chapter analyzes the scattering from periodic slabs built from plates rotated ninety degrees out of the periodic plane. Section 4.2 begins with the formulation of an integral equation similar to the one derived in Chapter 3. This integral equation, however, does not simplify due to the known \hat{z} dependence of the current. The scattered fields are calculated and catalogued by using the generalized scattering matrix. The reflected power is plotted as a function of frequency for various structures in Section 4.3. Starting with the plates connected to each other in a row to form an array of strips, the link is shown between the problems of Chapters 3 and 4. Next, the plates are bent with respect to one another to form zigzag structures. Finally, a third plate is added to the bent plates to form a honeycomb slab. Throughout the study, the resistance on the plates in the unit cell is varied to see the effect of this parameter. Conclusions are drawn in Section 4.4.

4.2 Integral Equation Formulation

The problem under consideration consists of a plane wave incident on a structured, lossy slab; an example of this structure is shown in Figure 4.1. The structure is a two-

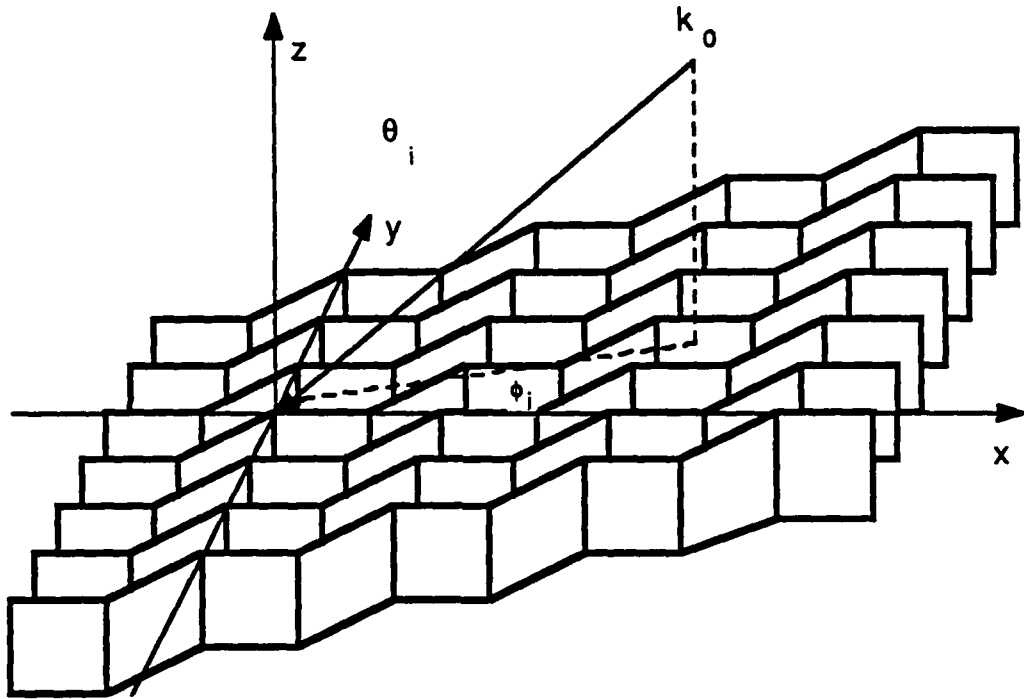


Figure 4.1 Oblique view of a structured slab made by repeating unit cells along a two-dimensional lattice. The unit cells are composed of resistive plates which are perpendicular to the xy plane. The size of the plates in \hat{z} causes the structured slab to have thickness. A plane wave is incident on this structure with an angle of θ_i, ϕ_i .

dimensional, infinite array in the xy plane and is formed by repeating a unit cell parallel to two skewed axes \hat{S}_1 and \hat{S}_2 as shown in Figure 4.2. The unit cell is composed of a number of lossy, thin plates each of which is set on its edge, perpendicular to the xy plane. The plates are either isolated, connected to each other within the cell, or connected to plates in neighboring cells to form the example unit cell shown in Figure 4.3. The plates are rotated by the angle θ with respect to the \hat{x} axis. The size of the plates in the \hat{z} direction gives the slab its thickness.

The incident plane wave has a propagation vector making an angle of θ_i with respect to \hat{z} and ϕ_i with respect to \hat{x} . As in Chapter 3, the wave is defined as being either TM or TE to the \hat{z} axis by defining all field components in terms of a scalar function [46].

$$\begin{cases} \Psi_{TE} \\ \Psi_{TM} \end{cases} = e^{-j\vec{k}_0 \cdot \vec{r}} = e^{-j(k_x x + k_y y - k_z z)} \quad (4.1a)$$

where $\vec{r} = x\hat{x} + y\hat{y} + z\hat{z}$, $\vec{k}_0 = k_x \hat{x} + k_y \hat{y} - k_z \hat{z}$ and

$$k_x = -k_0 \sin\theta_i \cos\phi_i \quad (4.1b)$$

$$k_y = -k_0 \sin\theta_i \sin\phi_i$$

$$k_z = +k_0 \cos\theta_i$$

k_0 is the wavenumber of the surrounding medium (usually free space) and the time dependency $e^{+j\omega t}$ is suppressed. Equation (3.2) of Chapter 3 gives the electric field components for an incident wave TM to \hat{z} , while Equation (3.3) gives the components for an incident wave TE to \hat{z} . Note that the \hat{z} direction in this chapter is perpendicular to the slab face, while for the problems of Chapter 3, the \hat{z} direction lies in the slab face.

A vector integral equation is derived which has as its unknown the equivalent electric surface current on the resistive plates in a single unit cell. The surface current, as shown in Figure 4.3, has two components: J_z , which is the current tangent to the plate

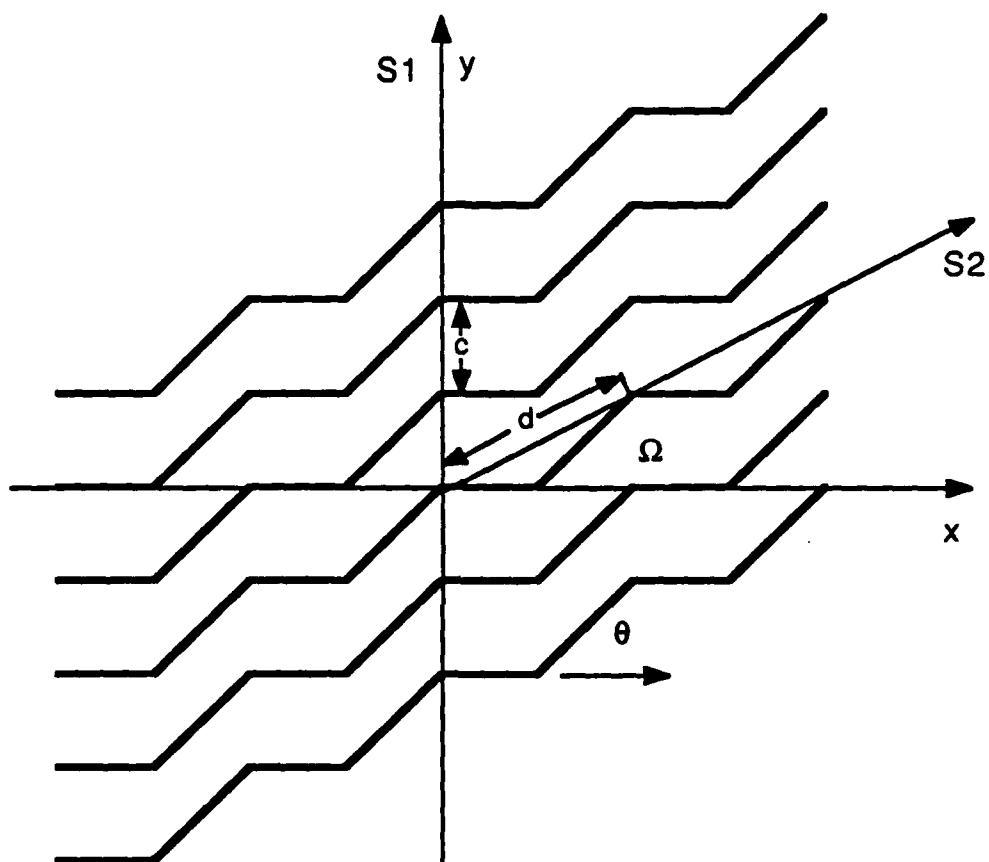


Figure 4.2 Top view of the structured slab shown in Figure 4.1. The skewed lattice axes S_1 and S_2 are shown along with the periodicity of the lattice along these axes (c, d). S_1 is parallel to \hat{y} and S_2 makes an angle of Ω with respect to \hat{x} . The resistive plates are rotated at an angle of θ with respect to \hat{x} .

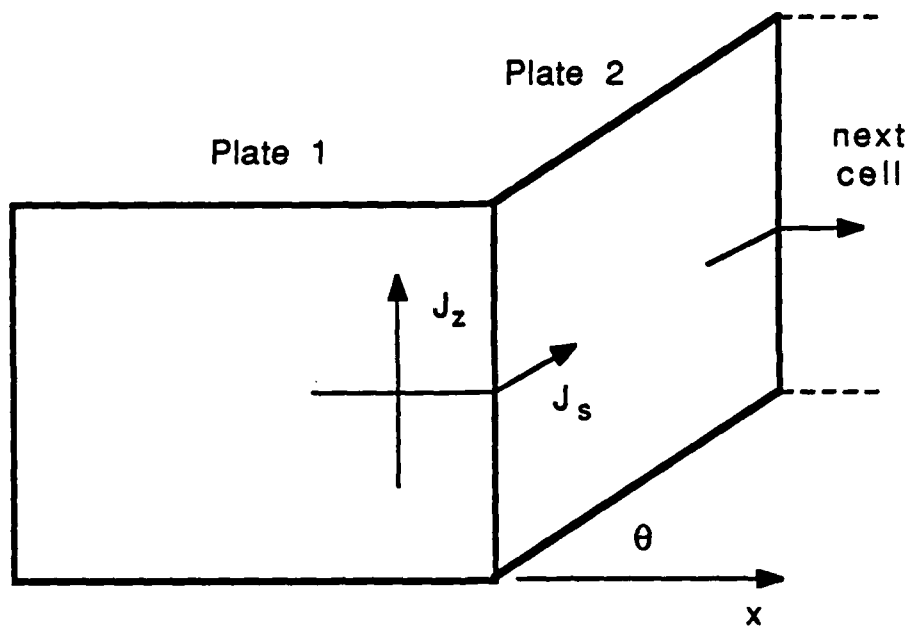


Figure 4.3 Typical unit cell for the slabs of Chapter 4. The direction of currents flowing in \hat{z} and \hat{s} is shown. The \hat{s} current may flow between plates within the unit cell and between plates into neighboring cells.

and flowing in the \hat{z} direction, and J_s , which is the current tangent to the plate and flowing perpendicular to the \hat{z} direction. Since the unit cell is composed of thin plates, the Electric Field Integral Equation (EFIE) approach must be used for stability. The boundary condition is applied on the plate to the tangential component (\hat{s} and \hat{z}) of the total electric field.

The total electric field is expressed as a sum of the incident and scattered fields.

$$\vec{E}^{tot} = \vec{E}^{inc} + \vec{E}^{scat} \quad (4.2)$$

\vec{E}^{inc} is obtained from Equation (3.2) for the TM case or (3.3) for the TE case. \vec{E}^{scat} is the scattered electric field due to the equivalent surface current $\vec{J} = \hat{s}J_s + \hat{z}J_z$. \vec{E}^{scat} may be written in terms of the vector magnetic potential \vec{A} and the scalar electric potential Φ , both of which satisfy the wave equation (Equation (3.6)).

$$\vec{E}^{scat} = -j\omega\vec{A} - \nabla\Phi \quad (4.3)$$

The vector magnetic potential is expressed as a convolution of surface electric current density in the unit cell with a periodic Green's function (G_p). Similarly, the scalar electric potential is expressed as a convolution of surface charge density with G_p , as was shown in Equation (3.8).

The periodic Green's function accounts for the fact that the unknowns are actually distributed on an infinite, two-dimensional lattice. In this chapter, the periodic Green's function, $G_p(\vec{r}, \vec{r}')$, which satisfies the equation

$$\nabla^2 G_p(\vec{r}, \vec{r}') + k_0^2 G_p(\vec{r}, \vec{r}') = - \sum_{m=-\infty}^{\infty} \sum_{n=-\infty}^{\infty} e^{-j\vec{k}_0 \cdot \vec{\rho}_{mn}} \delta(\vec{r} - \vec{r}' - \vec{\rho}_{mn}) \quad (4.4)$$

is defined as the scalar \vec{A}/μ response at the observation point $\vec{r} = x\hat{x} + y\hat{y} + z\hat{z}$ due to a doubly infinite array of point sources located at $\vec{r}' = x'\hat{x} + y'\hat{y} + z'\hat{z}$ within each cell. The

unit cells are distributed along a two-dimensional lattice defined by the vector $\vec{\rho}_{mn} = (nd \cos \Omega)\hat{x} + (mc + nd \sin \Omega)\hat{y}$ of Equation (2.48). The point sources are shifted in phase from cell-to-cell by $e^{-j\vec{k}_0 \cdot \vec{\rho}_{mn}}$ due to the incident field in accordance with Floquet's theorem as discussed in Chapter 2. The response is

$$G_p(\vec{r}', \vec{r}) = \frac{1}{4\pi} \sum_{m=-\infty}^{\infty} \sum_{n=-\infty}^{\infty} e^{-j\vec{k}_0 \cdot \vec{\rho}_{mn}} \frac{e^{-jk_0 |\vec{r} - \vec{r}' - \vec{\rho}_{mn}|}}{|\vec{r} - \vec{r}' - \vec{\rho}_{mn}|} \quad (4.5)$$

Using Equations (3.8a) and (3.8b) and invoking the continuity condition, $\nabla \cdot \vec{J} = -j\omega q$ to relate the charge and current density, Equation (4.3) becomes

$$\vec{E}^{scat} = -j\omega\mu \left[\vec{J} * G_p \right] + \frac{1}{j\omega\epsilon} \nabla \left[(\nabla \cdot \vec{J}') * G_p \right] \quad (4.6)$$

where the primed variables denote the source coordinates and unprimed variables denote the observation coordinates.

The total electric field on and tangent to the thin, lossy plate can be expressed in terms of the surface currents through the use of the resistive boundary condition discussed in Chapter 2. The total \vec{E} field in the shell volume is, therefore, related to the surface polarization current, the electric permittivity and the thickness of the shell Δ by

$$\hat{n} \times \hat{n} \times \vec{E}^{tot} = -R\vec{J} \quad (4.7a)$$

where \hat{n} is normal to the plate and

$$R = \frac{1}{j\omega\epsilon\Delta} \quad (4.7b)$$

Substituting Equations (4.6) and (4.7) into Equation (4.2) yields the vector integral equation to be solved on and tangent to the surface of the plate in the unit cell.

$$\vec{E}_{tan}^{inc} = R\vec{J} + j\omega\mu \left[\vec{J} * G_p \right]_{tan} - \frac{1}{j\omega\epsilon} \nabla \left[(\nabla \cdot \vec{J}') * G_p \right]_{tan} \quad (4.8)$$

where $[]_{tan}$ means the component of the quantity in the brackets in the direction of the

surface current. Equation (4.8) is discretized by the method of moments [53]. Rooftop basis functions, shown in Figure 2.19(a) (p. 62), are used to model the current. These functions have a triangular shape along the direction of the current flow and a pulse shape along the direction perpendicular to the current flow, which adequately represents the edge behavior of the current. If the plates of the structure are physically connected, the triangular direction of the rooftop function overlaps the connecting portion of the structure to explicitly enforce the current continuity of J_z . Discretization of a typical unit cell in \hat{s} and \hat{z} is shown in Figure 4.4.

The electric field is tested with a razor function, shown in Figure 2.19(b), in both \hat{s} and \hat{z} to yield the discretized form of the EFIE.

$$\langle \vec{T}, \vec{E}^{inc} \rangle = \langle \vec{T}, R\vec{J} \rangle + j\omega\mu \langle \vec{T}, \vec{J} * G_p \rangle - \frac{1}{j\omega\epsilon} \langle \vec{T}, \nabla[(\nabla \cdot \vec{J}) * G_p] \rangle \quad (4.9a)$$

The notation $\langle \rangle$ denotes the inner product.

$$\langle \vec{T}, \vec{F} \rangle = \iint \vec{T} \cdot \vec{F} \, dsdz \quad (4.9b)$$

In accordance with the discussion in Section 2.3.2, all calculations in Equation (4.9a) involving the periodic Green's function should be reduced to the same form for computational efficiency. The gradient operation on the scalar potential term in Equation (4.9a) is transferred to the testing function. Thus, all calculations involving the periodic Green's function in the scalar potential term reduce to integrating G_p over a two-dimensional pulse and testing at a point. With the same goal in mind for the vector potential term, the rooftop is approximated by a two-dimensional pulse with the same dipole moment [47], while the integration over the testing function is approximated by a single point evaluation at the center of the function weighted by the razor's support. The operations involving the incident field and the resistive term are unchanged. With the

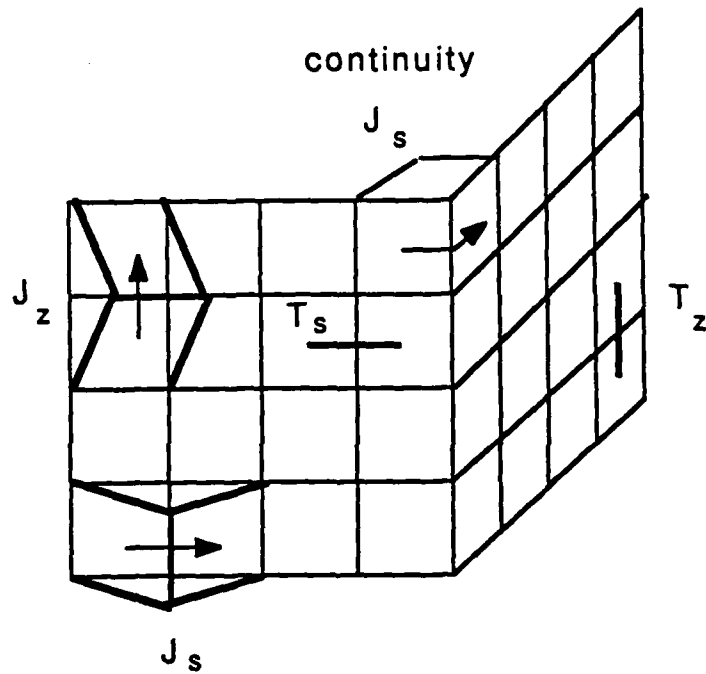


Figure 4.4 Discretizing the \hat{s} and \hat{z} directed currents with rooftop basis functions and testing with razor functions.

above changes, Equation (4.9a) becomes

$$\langle \vec{T} \cdot \vec{E}^{inc} \rangle = \langle \vec{T} \cdot R\vec{J} \rangle + j\omega\mu \langle \vec{T}_{pm} \cdot \vec{J} \rangle * G_p p l s \rangle - \frac{1}{j\omega\epsilon} \langle -\nabla \cdot \vec{T} \cdot (\nabla \cdot \vec{J}) \rangle * G_p \rangle \quad (4.10)$$

Expressing Equation (4.10) in terms of its components yields two sets of equations. Testing the \vec{E} field, which due to two components of current located at \vec{r}' , with an \hat{s} directed pulse located at \vec{r}_0 yields the following equation.

$$\begin{aligned} \int_{\Delta_s} E_s^{inc}(\vec{r}) ds &= R \int_{\Delta_s} J_s(s') ds' + j\omega\mu \Delta_s \hat{s}_0 \cdot \hat{s}' \int_{\Delta_z} \int_{\Delta_s} G_p(\vec{r}_0, \vec{r}') ds' dz' \\ &+ \frac{1}{j\omega\epsilon} \int \int \frac{\partial T_s}{\partial s} \int \int \frac{\partial J_s'}{\partial s'} G_p(\vec{r}, \vec{r}') ds' dz' ds dz \\ &+ \frac{1}{j\omega\epsilon} \int \int \frac{\partial T_s}{\partial s} \int \int \frac{\partial J_z'}{\partial z'} G_p(\vec{r}, \vec{r}') ds' dz' ds dz \end{aligned} \quad (4.11a)$$

The term on the left-hand side of the equal sign is the \hat{s} component of the incident \vec{E} field integrated over the pulse of the testing function. The resistive term, which is the first term on the right-hand side of the equal sign, has a contribution only if the basis and testing functions are in the same direction (in this case \hat{s}) and overlap. For efficiency, the practice is to first calculate and store the matrix elements due to the scattered fields for a given geometry and incident field direction. The tridiagonal matrix due to the resistance contribution is calculated separately and added to the scattered matrix. In this way, the scattering from many different configurations of resistance may be computed at little additional cost. The three types of elements in the tridiagonal resistance matrix are calculated in Figure 4.5.

The second term on the right-hand side is the vector magnetic potential contribution. The periodic Green's function is integrated over the two-dimensional current pulse approximation to the rooftop function. The integration over the test pulse is approximated by an evaluation at one point (\vec{r}_0) multiplied by the support of the pulse

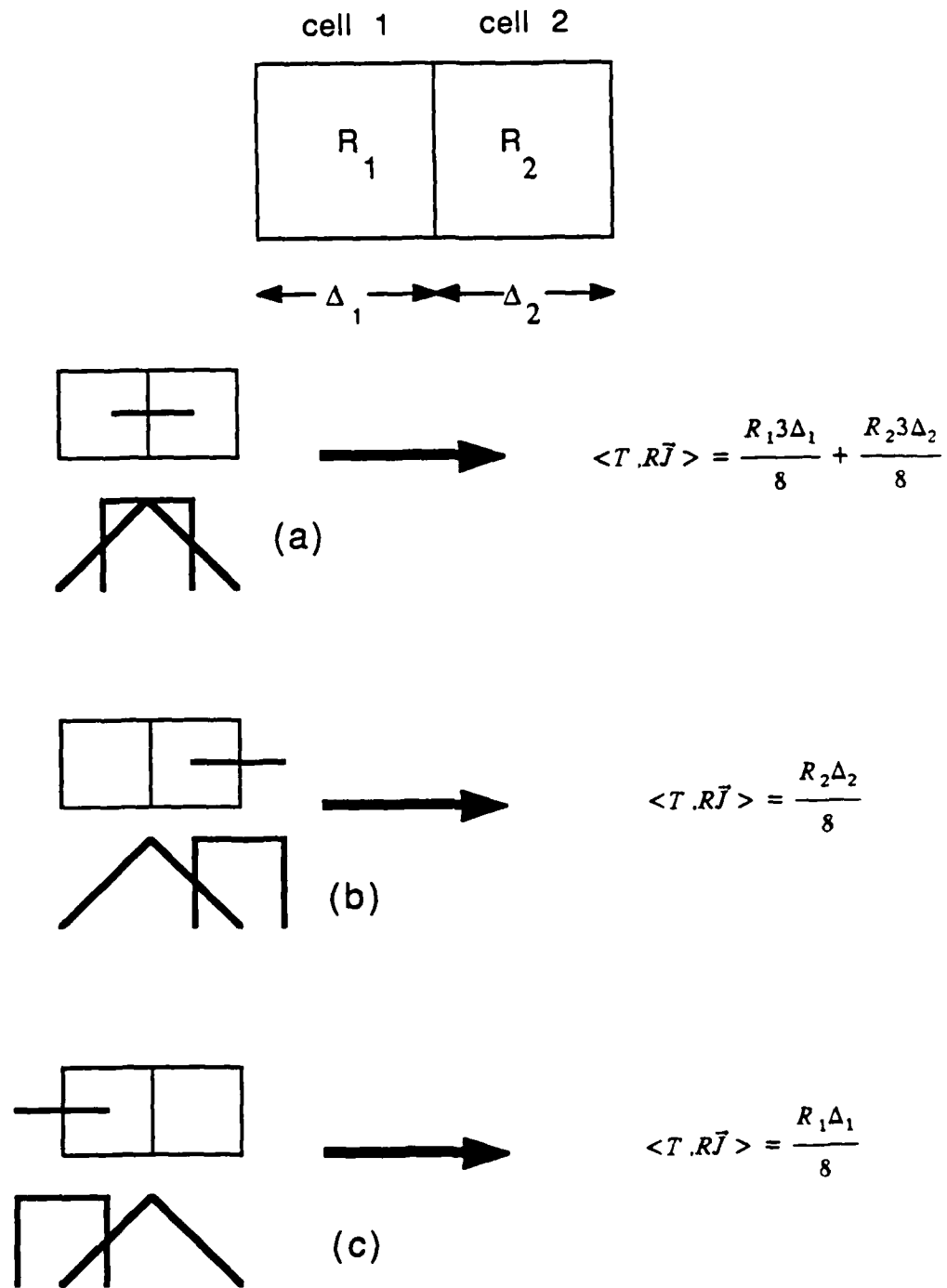


Figure 4.5 Calculation of the resistive term of the impedance matrix for (a) complete overlap (b) overlap with cell 2 (c) overlap with cell 1.

(Δ_z). The dot product accounts for the fact that the \hat{s} vector located at the basis and testing positions may be in different directions. The third and fourth terms on the right-hand side represent the scalar electric potential contribution. Because the derivative operation on the test pulse creates two delta functions, the double integration over the testing function becomes an evaluation at two points. The derivative operation on the basis function becomes a pulse doublet as discussed in Chapter 2. The scalar potential term gives rise to the coupling between the \hat{z} directed current and the \hat{s} directed field.

Applying a \hat{z} directed test pulse at \vec{r}_0 yields the following equation.

$$\begin{aligned} \int_{\Delta_z} E_z^{inc}(\vec{r}) ds &= R \int_{\Delta_z} J_z(z') dz' + j \omega \mu \Delta_z \int_{\Delta_z} \int_{\Delta_z} G_p(\vec{r}_0, \vec{r}') ds' dz' \\ &+ \frac{1}{j \omega \epsilon} \int \int \frac{\partial T_z}{\partial z} \int \int \frac{\partial J_s'}{\partial s'} G_p(\vec{r}, \vec{r}') ds' dz' ds dz \\ &+ \frac{1}{j \omega \epsilon} \int \int \frac{\partial T_z}{\partial z} \int \int \frac{\partial J_z'}{\partial z'} G_p(\vec{r}, \vec{r}') ds' dz' ds dz \end{aligned} \quad (4.11b)$$

The terms of Equation (4.11b) are calculated in the same manner as the terms of Equation (4.11a).

The computations involving the periodic Green's function are the major consumers of computer time in the solution of periodic problems, particularly for the problems in this chapter. Not only are there more unknowns to consider because the plates are finite in two dimensions, but each matrix element is more difficult to fill since the single integrations needed for the strip case become double integrations in the plate case and the single summations for the one-dimensional array become double summations for the two-dimensional array.

For the problems in this chapter, the acceleration techniques outlined in Chapter 2 are used to efficiently compute the periodic Green's function integrated over a two-

dimensional pulse and evaluated at a point. The basis and testing functions are distributed onto the spectral and spatial domains. The integrations in the spectral domain are done analytically while those in the spatial domain are done numerically. Outside a core region in the summation, the numerical integrations are computed using a single point approximation. This procedure was termed Method 3 in Chapter 2. When the basis and testing functions do not overlap in the \hat{z} direction, the computation is done entirely in the spectral domain to take advantage of the exponential convergence of the summand in the Green's function and the fact that the integration can be performed analytically.

The similarity of form for all Green's function calculations means that many of the operations needed to fill the impedance matrix are redundant from element to element, which can be exploited to save computer time. An example geometry, consisting of two plates attached to each other at an angle and attached to neighboring cells, will be used to show the effect of each time-saving technique applied. Each of the plates was discretized by six cells in the \hat{s} direction and five cells in the \hat{z} direction. The cells were all of the same size. There were, therefore, 60 basis functions to describe J_1 ((5 discretizations in \hat{s} per plate x 2 plates + 2 continuity functions) x 5 discretizations in \hat{z}) and 48 basis functions to describe J_2 (6 discretizations in \hat{s} per plate x 2 plates x 4 discretizations in \hat{z}) for a total of 108 unknowns. The total number of integrations without using redundancy—since each basis/test combination requires five integrations—is $108^2 \times 5 = 58,320$ which, even after using acceleration techniques, takes an unacceptable amount of time.

Since the Green's function depends only on the distance between the basis and testing functions in the \hat{z} direction, the impedance matrix is block Toeplitz. This means that once the rows of the impedance matrix are filled for the testing functions located at a constant

z value, the remaining rows of the impedance matrix may be filled using the block Toeplitz structure of the matrix. For our example structure, 12 rows must be calculated for the s -directed testing functions and 12 rows for the z -directed testing functions. The number of integrations is $5 \times 12 \times 108 + 5 \times 12 \times 108 = 12,960$. This is about one-fifth of the total integrations.

There is much redundancy for basis and testing function combinations in the \hat{x} and \hat{y} directions as well. Whenever an integral is calculated for a particular combination, the size of the basis pulse, rotation of the pulse with respect to the \hat{x} axis and the location of the test position with respect to the center of the pulse are stored in a lookup table along with the value of the integral. Before a new integration is performed, the lookup table is examined to see if the integral has already been calculated. If so, the value is taken from the table. If not, the integral is calculated and added to the table. The use of the lookup table reduces the number of integrations performed in the example to 1,111 which is about 9% of the number of integrations performed using the \hat{z} symmetry.

For a generally incident plane wave, the above redundancies are all that can be exploited. For special incident waves, however, additional redundancies can be exploited in the generation of the lookup table. These redundancies are shown in Figure 4.6. If the incident wave propagates normally to \hat{x} , then there is no phase shift imposed between cells in the \hat{x} direction by the incident wave. If the origin is shifted to the center of the basis function pulse, the impedance matrix element calculation is the same for x as for $-x$ when $y=0$. The size and rotation of the basis pulse are still differentiating factors in the construction of the lookup table. This symmetry helps the computational speed when all the plates lie in the xz plane, but in general, this symmetry further reduces the number of integrations by very little. For our example, the number of integrations was reduced to 1,086, which is only 98% of the previous reductions.

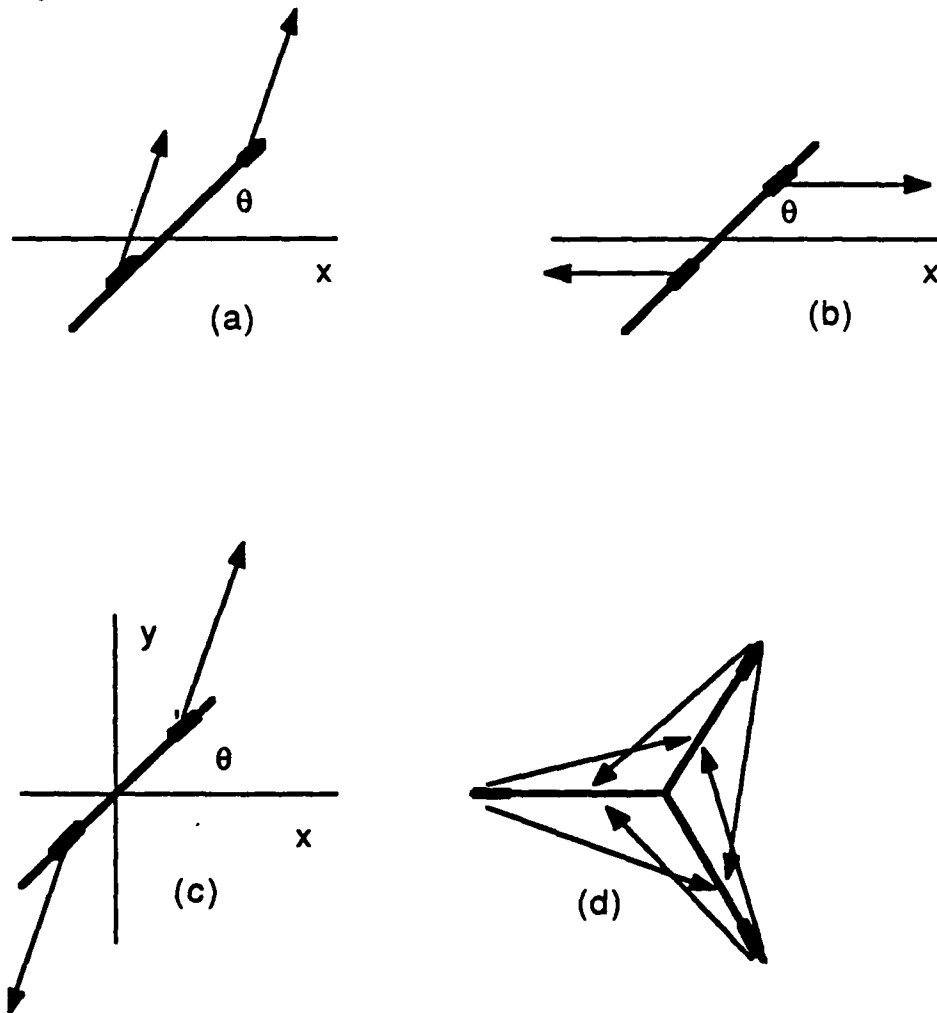


Figure 4.6 Exploitable symmetry for lookup tables. Arrows from the center of the basis function to the test point show identical results for impedance matrix elements given the following circumstances (a) general incidence (b) incidence normal to \hat{x} (c) incidence normal to \hat{x} and \hat{y} (d) normal incidence and 3-fold symmetry of array and unit cell geometry.

If the propagation vector of the incident wave is normal to both the \hat{x} and \hat{y} axes, then no phase shift is imposed between any of the cells by the incident wave. Again, upon shifting the origin to the center of the basis function, the impedance matrix calculation for the test point x,y is the same as that for the point $-x,-y$ and the point $-x,y$ is the same as for $x,-y$. This symmetry helps to reduce the calculations for interactions within a plate no matter what its orientation is in the array. It does not help for plate-to-plate interactions, unless the unit cell geometry has a special symmetry associated with it. Size and rotation of the basis function are still accounted for in the lookup table.

The honeycomb geometry has a three-fold symmetry in the lattice and the unit cell which may be exploited. With the incident plane wave normal to the slab interface, by using the symmetry of the geometry, the impedance matrix elements describing the interaction between two different plates in the unit cell can be used to generate the impedance matrix elements when the basis and testing function combination is rotated $\pm 120^\circ$. This symmetry, in addition to the symmetry of the above paragraphs, reduces the number of calculations significantly. If the example is made to conform to the honeycomb specifications, the number of integrations required is 496 which is 45% of the reduction achieved so far. If the integration over the basis function pulse can be reduced to a one-point approximation, then with a normally incident wave, the impedance matrix calculation no longer depends on the rotation of the basis pulse with respect to \hat{x} . In the example, the relaxation of the rotation requirement reduces the number of integrations to 566 which is approximately 50% of the reduction already achieved by exploiting normal incidence alone.

A generalized scattering matrix is used to describe the interaction of the structure with the surrounding environment [31]. Two terminal planes are defined at $z = Z_{top}$ and $z = Z_{bot}$ which contain the entire array structure between them. Due to the periodic nature of the array, the total fields at the terminal planes may be described in terms of a sum of plane waves based on Floquet harmonics. For two-dimensional periodicity, the Floquet harmonic is described by two indices (m,n) corresponding to the two sets of discrete propagation constants defined by Equation (2.57). The plane wave is broken into two polarized plane waves (TM to \hat{z} and TE to \hat{z}) which are expressed in terms of a scalar function as was done in Chapter 3.

$$\Psi_{mn \text{ TM/TE}} = a_{mn \text{ TM/TE}} e^{+j(\beta_{xmn}x + \beta_{ymn}y)} e^{\pm j\gamma z} \quad (4.12)$$

γ is the propagation constant in the \hat{z} direction defined by Equation (2.57). Equation (4.12) represents plane waves propagating or attenuating in \hat{z} going away from the slab.

The two weighting coefficients, $a_{mn \text{ TM/TE}}$, are calculated from two total electric field components for each Floquet harmonic (m,n) on the terminal planes. For this case, the components E_{zmn} and E_{xmn} are chosen.

$$a_{mn \text{ TM}} = \frac{j\omega\epsilon}{\beta_{xmn}^2 + \beta_{ymn}^2} E_{zmn} \quad (4.13a)$$

$$a_{mn \text{ TE}} = \frac{1}{j\beta_{ymn}} \left[-E_{xmn} \pm \frac{\beta_{xmn}\gamma}{\beta_{xmn}^2 + \beta_{ymn}^2} E_{zmn} \right] \quad \pm z \text{ traveling wave} \quad (4.13b)$$

E_{xmn} and E_{zmn} are found by first calculating a given harmonic of the scattered field by using Equation (4.6)

$$E_{zmn} = -j\omega\mu \hat{z} \cdot \left[\vec{J}_{mn} \tilde{G}_{mn} \right] + \frac{j\gamma}{j\omega\epsilon} \left[\nabla \cdot \vec{J}_{mn} \right] \tilde{G}_{mn} \quad \pm z \text{ traveling wave} \quad (4.14a)$$

$$E_{xmn} = -j\omega\mu \hat{x} \cdot \left[\vec{J}_{mn} \tilde{G}_{mn} \right] + \frac{j\beta_{xmn}}{j\omega\epsilon} \left[\nabla \cdot \vec{J}_{mn} \right] \tilde{G}_{mn} \quad (4.14b)$$

where

$$\tilde{G}_{mn} = \frac{1}{\text{cell area}} \frac{e^{-j\gamma|z_0-z'|} e^{j(\beta_{xmn}(x_0-x') + \beta_{ym}(y_0-y'))}}{2j\gamma} \quad (4.15)$$

is a single Floquet harmonic of the periodic Green's function written in the spectral domain (Equation (2.56)). In Equation (4.14), the derivatives in the \hat{z} direction have been replaced by $\pm j\gamma$, and the derivatives in the \hat{x} direction have been replaced by $j\beta_{xmn}$ for each harmonic. The notation $\vec{J}_{mn} G_{mn}$ is used to emphasize that only one harmonic at a time is being calculated for the scattered field due to all of the basis functions. Therefore, all operations in the brackets of Equation (4.14) involve evaluating the single-harmonic (m,n) response of an array of two-dimensional pulses for each basis function at the terminal planes $(x_0, y_0, z_0) = (0, 0, Z_{top})$ and $(0, 0, Z_{bot})$. This calculation can be done analytically using Equation (2.63a) (p.66). After the scattered electric field is calculated, the total \vec{E} field is found by adding the incident \vec{E} field to the scattered field if the incident and scattered fields have the same harmonic and are propagating in the same direction.

The power carried by each plane wave in \hat{z} may be written in terms of Ψ as

$$P_{mn \text{ TM}} = \pm \frac{\gamma}{\omega\epsilon} \left(\beta_{xmn}^2 + \beta_{ym}^2 \right) |\Psi_{mn \text{ TM}}|^2 \quad \pm z \text{ traveling} \quad (4.16a)$$

$$P_{mn \text{ TE}} = \pm \frac{\gamma^*}{\omega\mu} \left(\beta_{xmn}^2 + \beta_{ym}^2 \right) |\Psi_{mn \text{ TE}}|^2 \quad \pm z \text{ traveling} \quad (4.16b)$$

γ^* is the complex conjugate of γ . The power is real for propagating waves and imaginary for attenuating waves.

The generalized scattering matrix is filled exactly as the one-dimensional case in Chapter 3. The only difference is that the Floquet harmonics for the two-dimensional array are designated by two numbers rather than one. Therefore, within each of the

submatrices of Equation (3.25), a sub-submatrix describes the interaction between input Floquet harmonics m_i, n_i and output Floquet harmonics m_o, n_o . Equation (3.26) then becomes

$$S_{TE/TM}(m_o, n_o | m_i, n_i) = \left[\frac{|P_{m_o, n_o, TE}|}{|P_{m_i, n_i, TM}|} \right]^{1/2} \text{Phase } \Psi_{m_o, n_o, TE} - \text{Phase } \Psi_{m_i, n_i, TM} \quad (4.17)$$

Note that because of mirror symmetry of the slab in \hat{z} , $S_{11} = S_{22}$ and $S_{21} = S_{12}$.

4.3 Results

In this section, the reflection coefficient for the propagating Floquet harmonics will be plotted versus frequency for various configurations of unit cells composed of plates and for various resistance distributions. The frequency in each case is normalized by 3.0×10^8 . The reflection coefficients due to a plane wave incident on the unit cell shown in Figure 4.7 are plotted versus frequency in Figures 4.8 and 4.9. The unit cell for this problem is composed of a single plate, dimensioned 0.5 m by 0.5 m, which fills the entire cell. The plate is either insulated from or connected to the neighboring cells. The resulting striplike array has a periodicity in \hat{y} of 0.5 m. The propagation vector of the incident plane wave makes an angle of $\theta_i = 45^\circ$ with respect to \hat{z} and $\phi_i = 89.9^\circ$ with respect to \hat{x} . For this angle of incidence, the TE wave has its \vec{E} field parallel to the axes of the strips while the TM wave has its \vec{E} field perpendicular to the strip axes.

The TE wave induces its major current component along the axis of the strips. The connected plates allow this current to flow uninterrupted along the strips, while the disconnected plates clamp the current to zero at the breaks. At low frequencies, therefore, the axial current for the disconnected strips cannot build to the same value as for the connected strips and the scattered field is not as great. This is shown in Figure 4.8. The

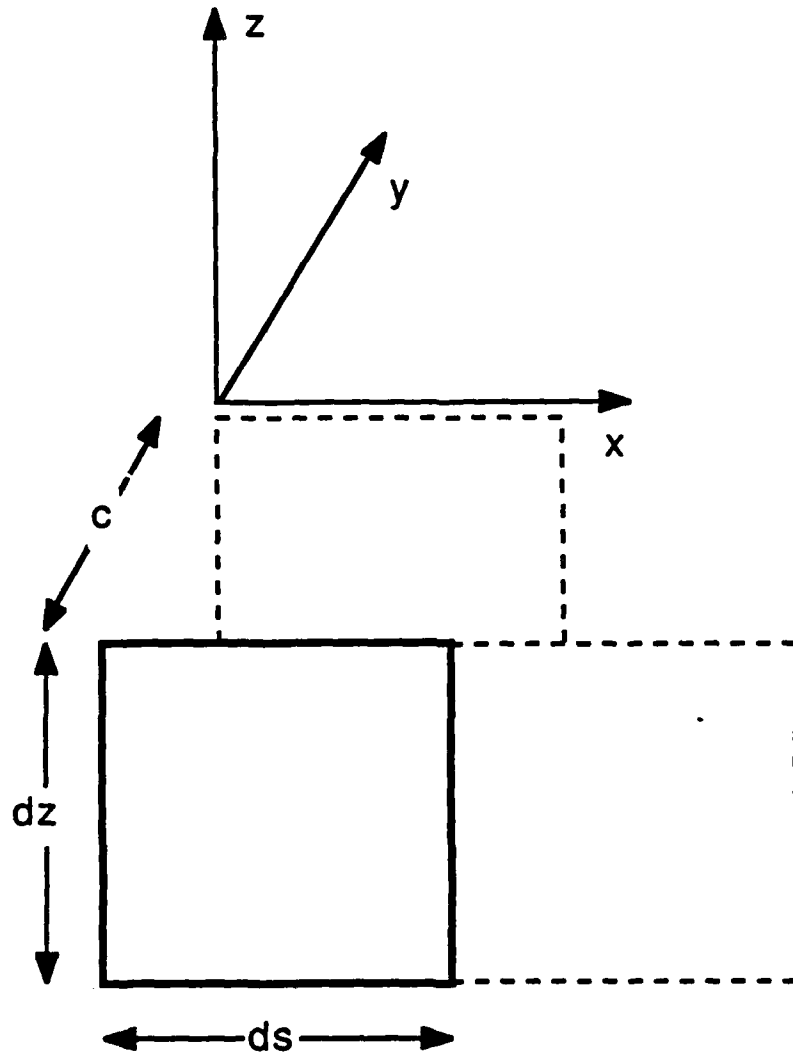


Figure 4.7 Unit cell for plates connected to form a one-dimensional strip array. Dimensions ds , dz and c are all 0.5 m.

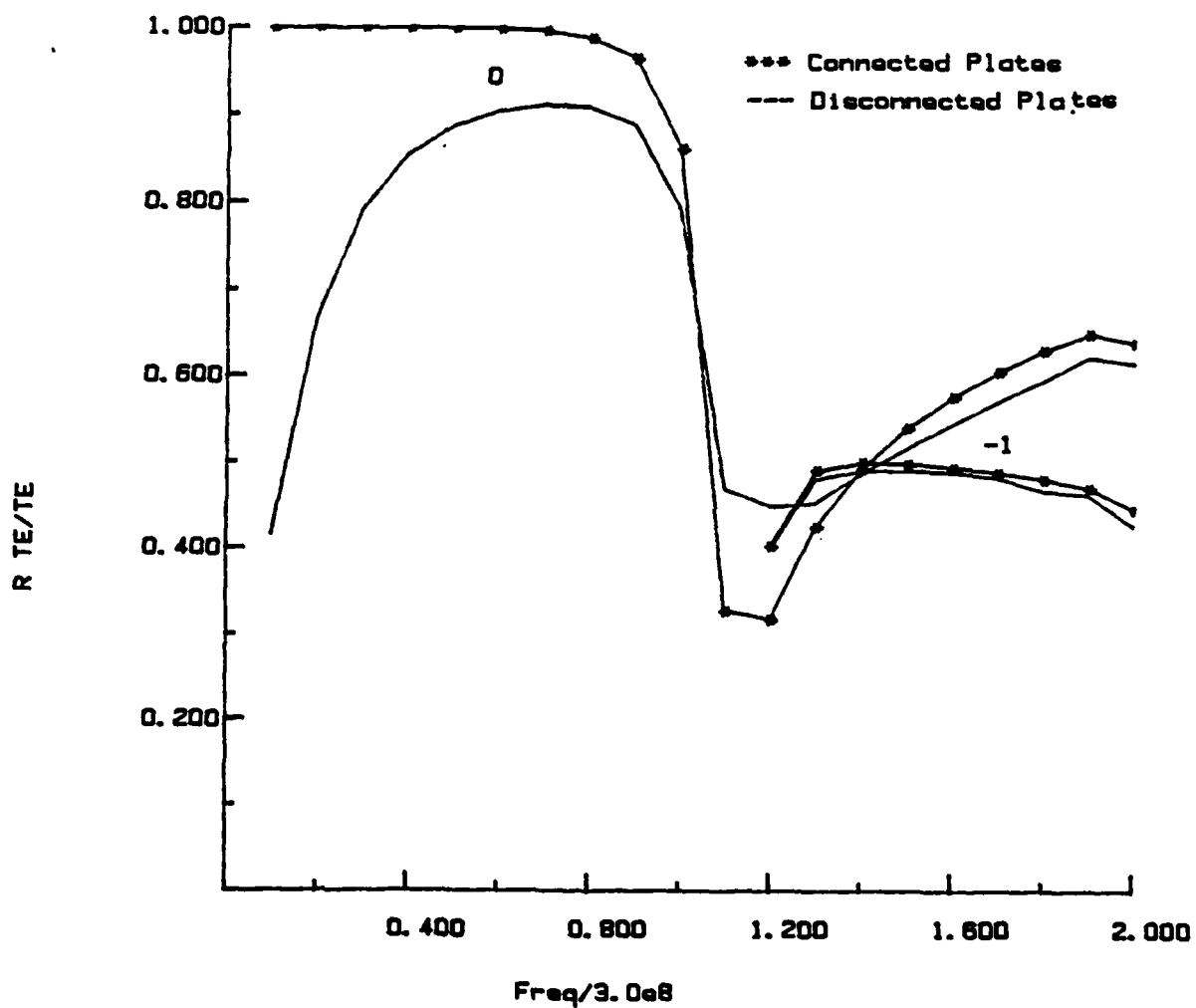


Figure 4.8 $|S_{11TE/TE}|$ versus normalized frequency for the lossless geometry of Figure 4.7. The reflection coefficient is plotted for plates connected to form strips and for plates insulated from each other. The angles of the incident wave are $\theta_i = 45^\circ$, $\phi_i = 89.9^\circ$.

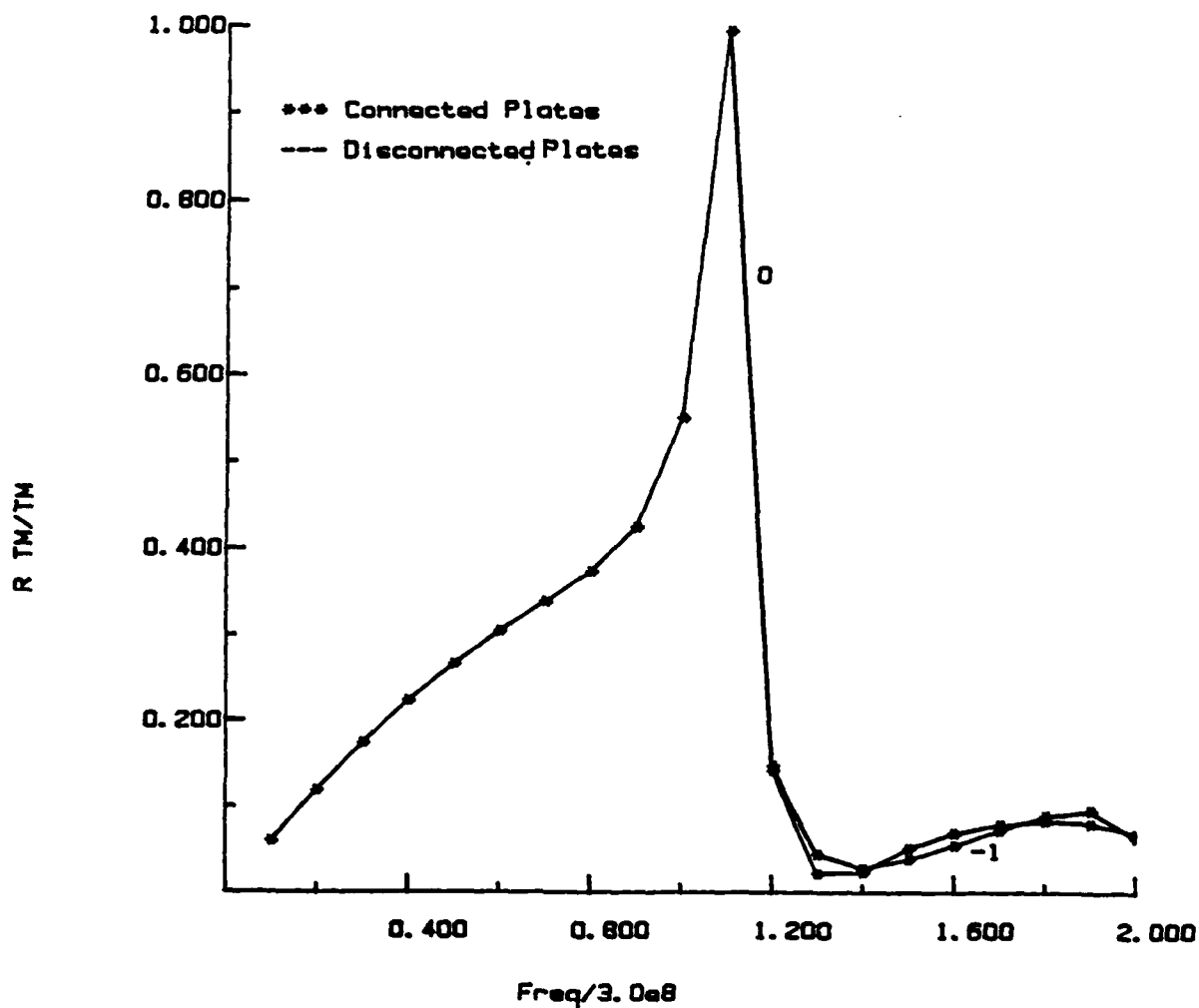


Figure 4.9 $|S_{11TM/TM}|$ versus normalized frequency for the lossless geometry of Figure 4.7. The reflection coefficient is plotted for plates connected to form strips and for plates insulated from each other. The angles of the incident wave are $\theta_i = 45^\circ$, $\phi_i = 89.9^\circ$.

TE wave is reflected totally at low frequencies by the connected plates, while it is only partially reflected by the disconnected plates.

As the frequency increases, the zeroth-order harmonic curves plotted for the connected and disconnected plates begin to track each other. This shows that at higher frequency, current discontinuity does not affect the characteristics as much as at lower frequencies. The disconnected plates do not have as sharp a resonance in the region about 3.0×10^8 Hz as the plates connected to form strips. The higher-order harmonics are unaffected by the presence or absence of current continuity. The TM wave induces its major current component along the \hat{z} direction which is unaffected by current discontinuity along the \hat{x} direction. Consequently, as seen in Figure 4.9, the reflection coefficients for the connected and disconnected plates lie on top of each other.

In the strip case, no coupling of TE to TM waves and vice versa exists when the incident wave lies in the plane normal to the strip axis. The disconnected plates should exhibit some cross-coupling, but for this angle of incidence, the coupling between polarizations is negligible. As loss is added to the plates— $R = 100\Omega$ —the reflection curves become smoother as seen in Figure 4.10. Although a difference still remains between the reflections from connected and disconnected plates, the difference has diminished.

The next set of curves shows the effect of putting bends in the unit cell. The geometry is shown in Figure 4.11. A strip structure 0.25 m (d_z) deep and separated along \hat{y} by 0.3 m (c dimension) is bent every 0.3 m by an angle θ so that the strip meanders back and forth in the xy plane. The reflection coefficient for the lossless cases are plotted in Figures 4.12-4.14. The incident plane wave has a propagation vector which makes an angle of $\theta_i = 45^\circ$ with respect to \hat{z} and $\phi_i = 89.9^\circ$ with respect to \hat{x} .

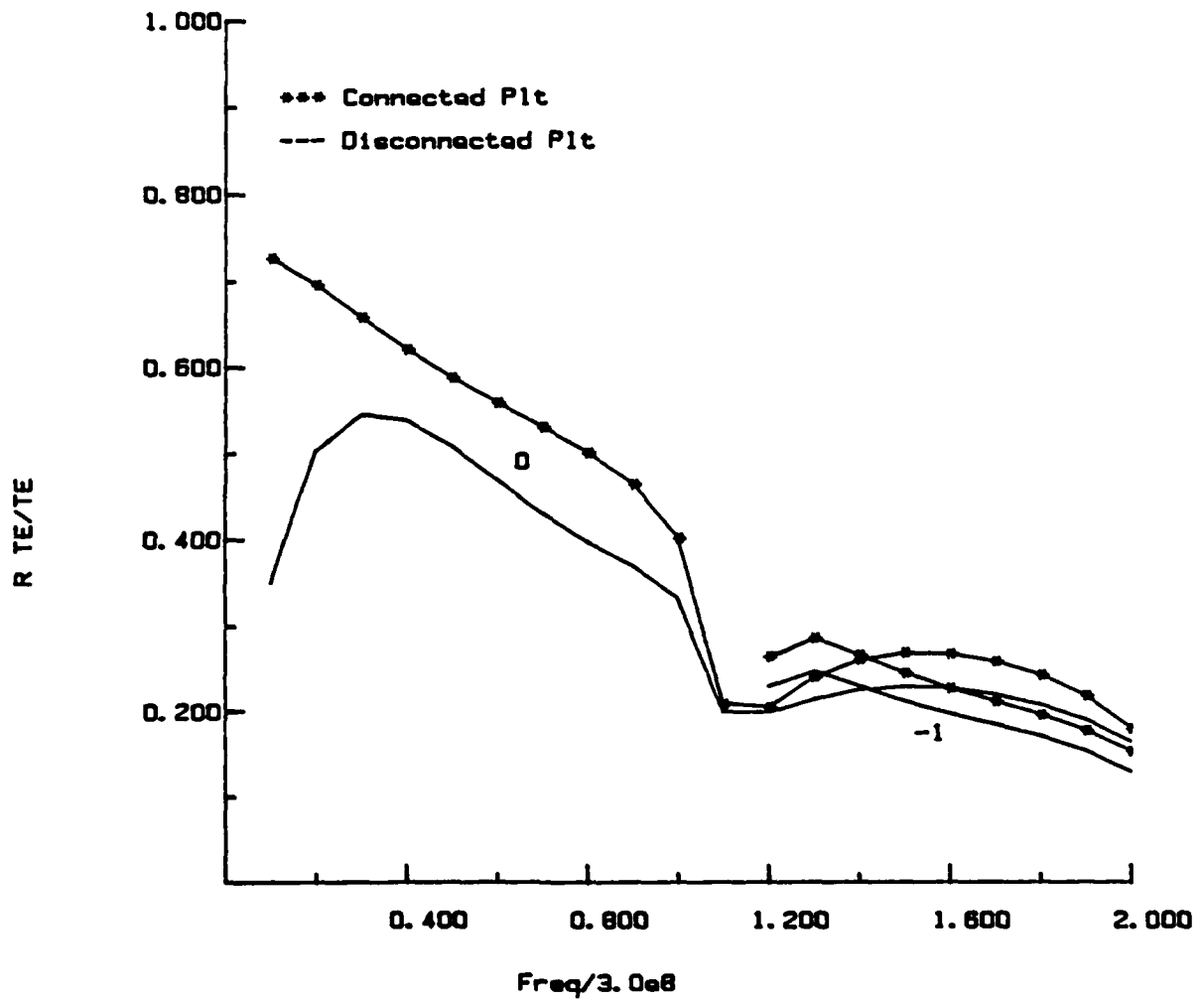


Figure 4.10 $|S_{11TE/TE}|$ versus normalized frequency for the geometry of Figure 4.7. The reflection coefficient is plotted for plates connected to form strips and for plates insulated from each other. The angles of the incident wave are $\theta_i = 45^\circ$, $\phi_i = 89.9^\circ$. The lossy plates are modeled by $R = 100 \Omega$.

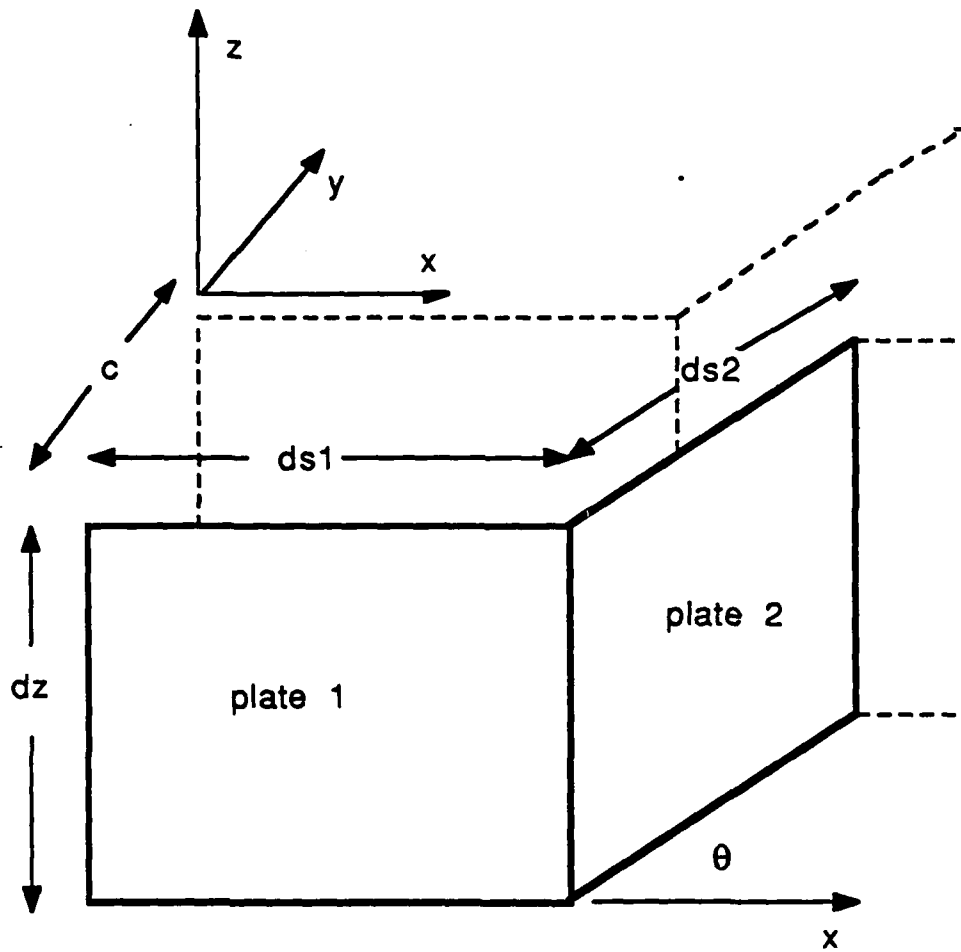


Figure 4.11 Unit cell for strips bent to form zigzag plate structures. Dimensions $ds1$, $ds2$ and c are all 0.3 m; dimension dz is 0.25 m.

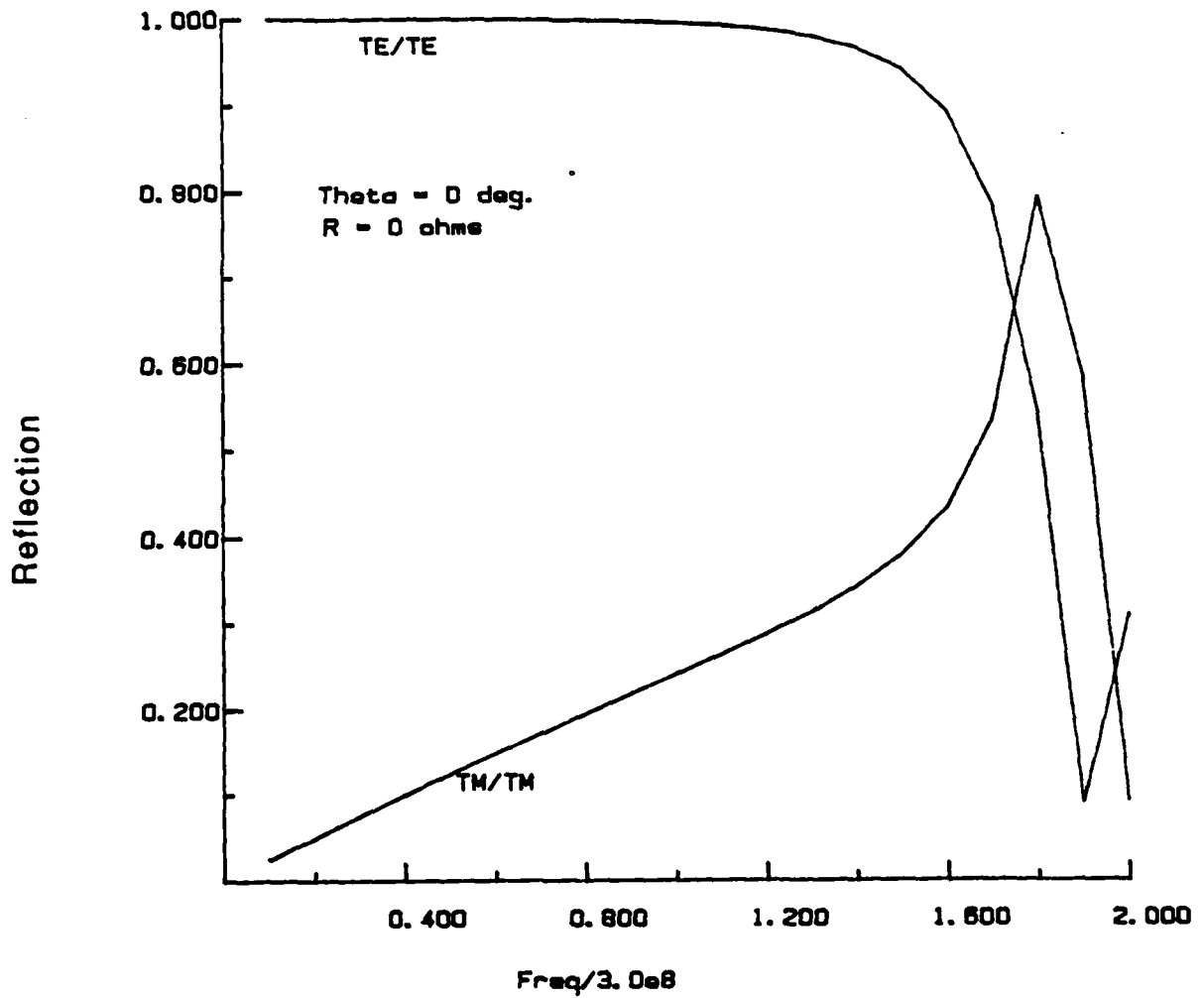


Figure 4.12 $|S_{11}|$ versus normalized frequency for the zigzag plates of Figure 4.11 with no bend. The angles of the incident wave are $\theta_i = 45^\circ$, $\phi_i = 89.9^\circ$. The plates are lossless ($R = 0 \Omega$). The zeroth harmonic is shown.

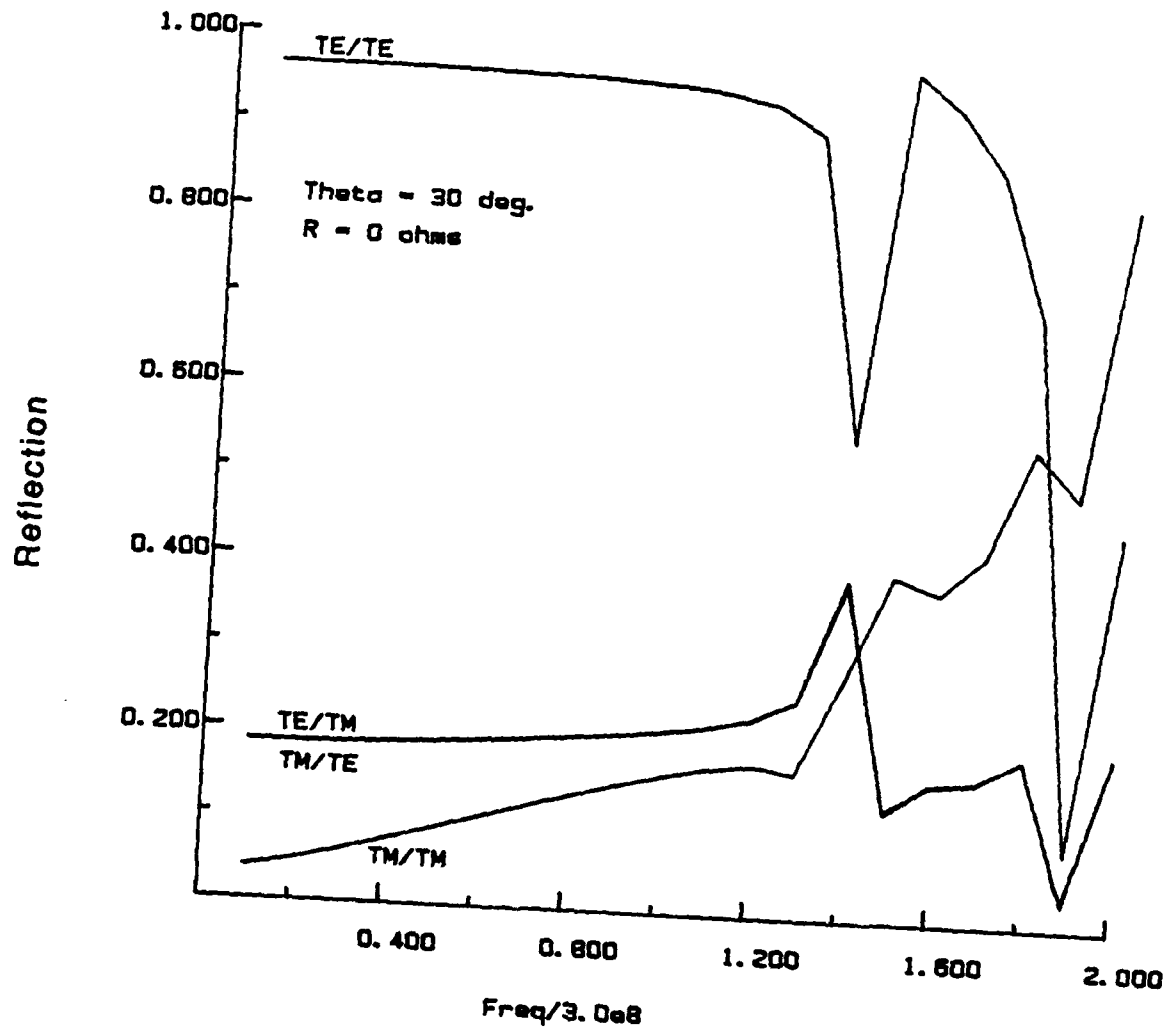


Figure 4.13 $|S_{11}|$ versus normalized frequency for zigzag plates of Figure 4.11 with a 30° bend. The angles of the incident wave are $\theta_i = 45^\circ$, $\phi_i = 89.9^\circ$. The plates are lossless ($R = 0 \Omega$). The zeroth harmonic is shown.

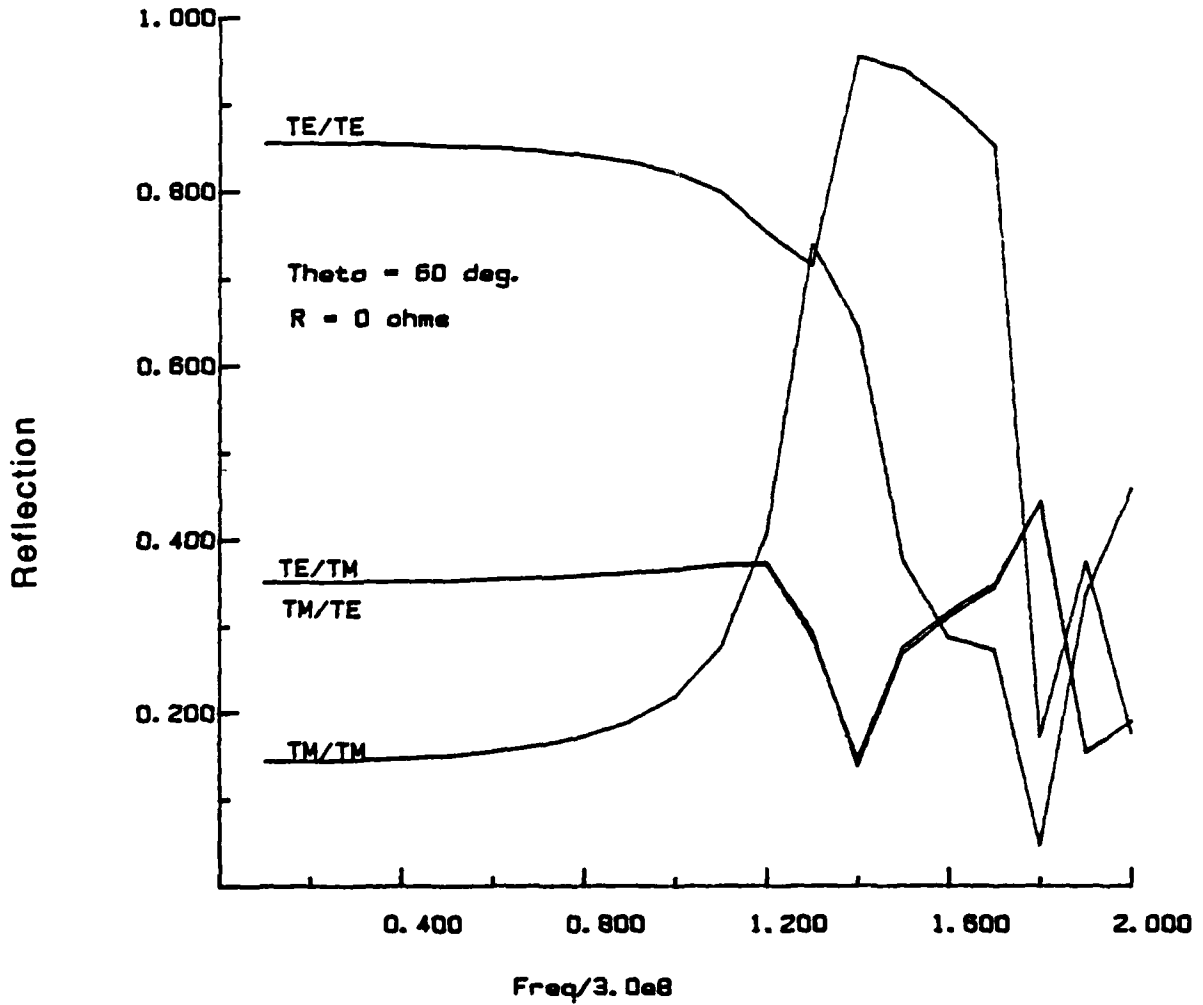


Figure 4.14 $|S_{11}|$ versus normalized frequency for zigzag plates of Figure 4.11 with a 60° bend. The angles of the incident wave are $\theta_i = 45^\circ$, $\phi_i = 89.9^\circ$. The plates are lossless ($R = 0 \Omega$). The zeroth harmonic is shown.

Figure 4.12 shows the case in which there is no bend between plates 1 and 2, i.e., the geometry is composed of parallel strips separated by 0.3 m. As expected, there is no cross-coupling between TE and TM polarizations. The TE wave with its E field parallel to \hat{x} (the axis of the strips) is totally reflected at the lower frequencies, while the TM wave with its E field in the plane perpendicular to the axis has a smaller reflection coefficient. As the frequency increases, a resonance is encountered where the TE wave is transmitted through the structure and the TM wave is reflected from the structure.

Figure 4.13 shows the effect of a 30° bend in the strips and Figure 4.14 shows the effect of a 60° bend. At low frequencies, as the angle of the bend increases, the \vec{E} field of the TE wave has less of a component along the second plate, so the second plate doesn't contribute as much directly to the reflection. The TE reflection coefficient decreases. The second plate does, however, contribute to the reflection by acting as a current path between the cells. In other words, the structure is not behaving as an array of unconnected plates.

For all bend angles, a resonance occurs at around 5.4×10^8 Hz due to the separation of the strips in the \hat{y} direction. For this angle of incidence, a second resonance occurs that is due to the bend itself. This resonance is absent for the straight strips, and occurs at around 4.2×10^8 Hz for the 30° bend and at around 3.9×10^8 Hz for the 60° bend. With increasing bend angle, the second resonance occurs for the TE and TM waves at ever lower frequencies. The disruptions in the \hat{s} current caused by the bends lead to an increased coupling between the two polarizations as the bend angle increases. Finally, adding resistance to the 60° bend case, as seen in Figures 4.15-4.17, causes the reflection coefficients to decrease and the resonance dips induced by the structure to flatten out.

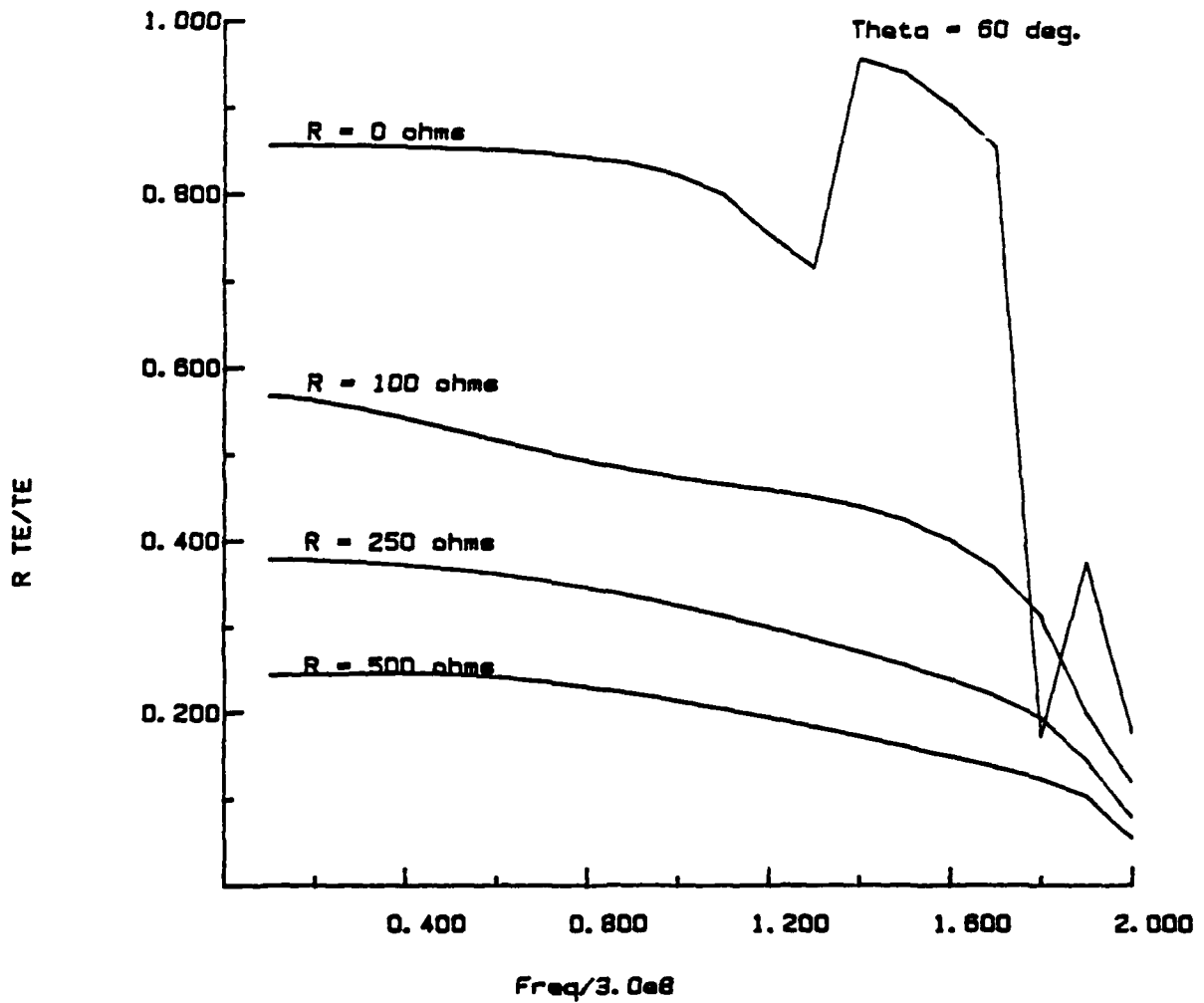


Figure 4.15 $|S_{11TE/TE}|$ versus normalized frequency for the zigzag plates of Figure 4.11 with a 60° bend. Plate resistance varies from lossless to $R = 500 \Omega$. The angles of the incident wave are $\theta_i = 45^\circ$, $\phi_i = 89.9^\circ$. The zeroth harmonic is shown.

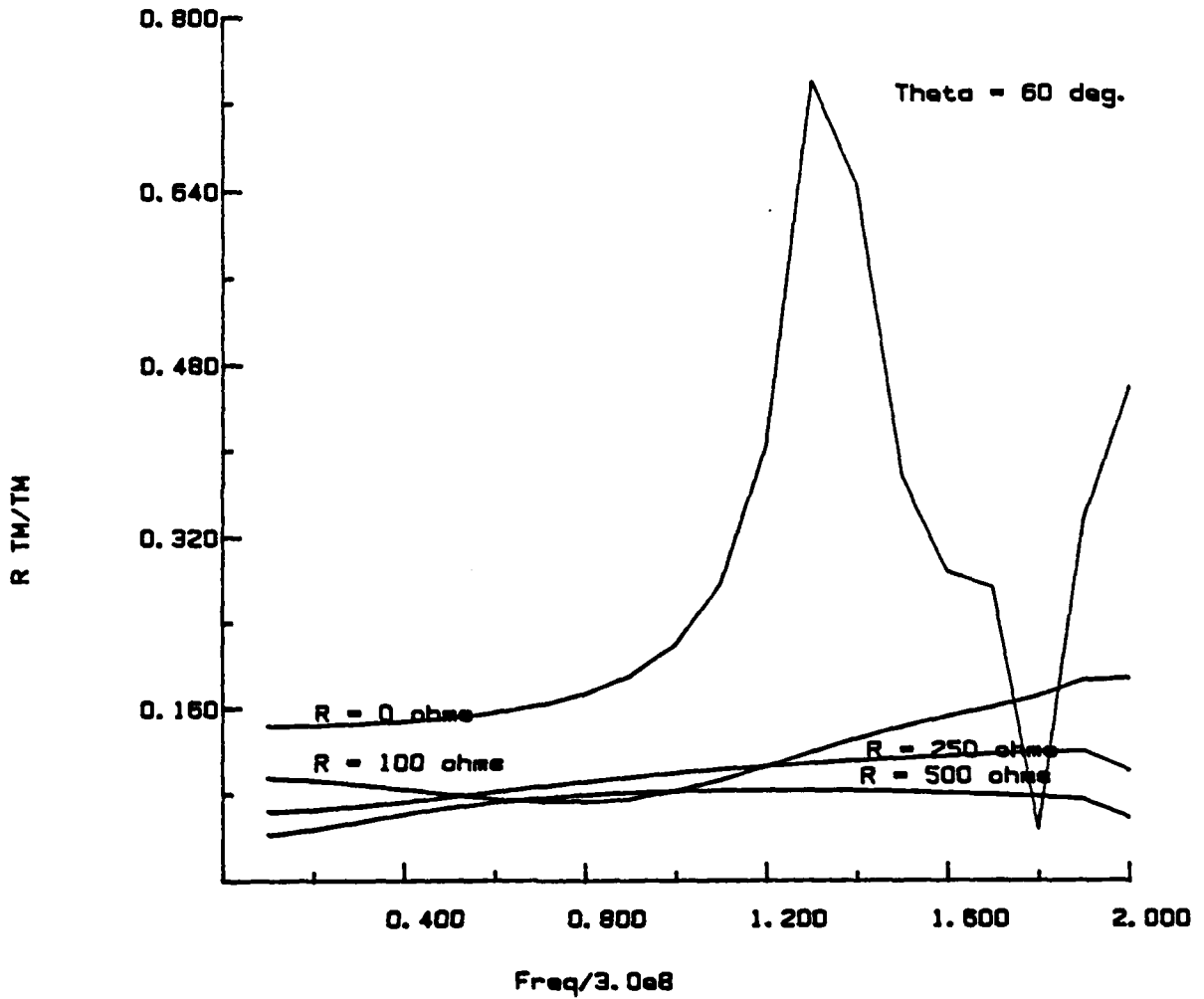


Figure 4.16 $|S_{11TM/TM}|$ versus normalized frequency for the zigzag plates of Figure 4.11 with a 60° bend. Plate resistance varies from lossless to $R = 500 \Omega$. The angles of the incident wave are $\theta_i = 45^\circ$, $\phi_i = 89.9^\circ$. The zeroth harmonic is shown.

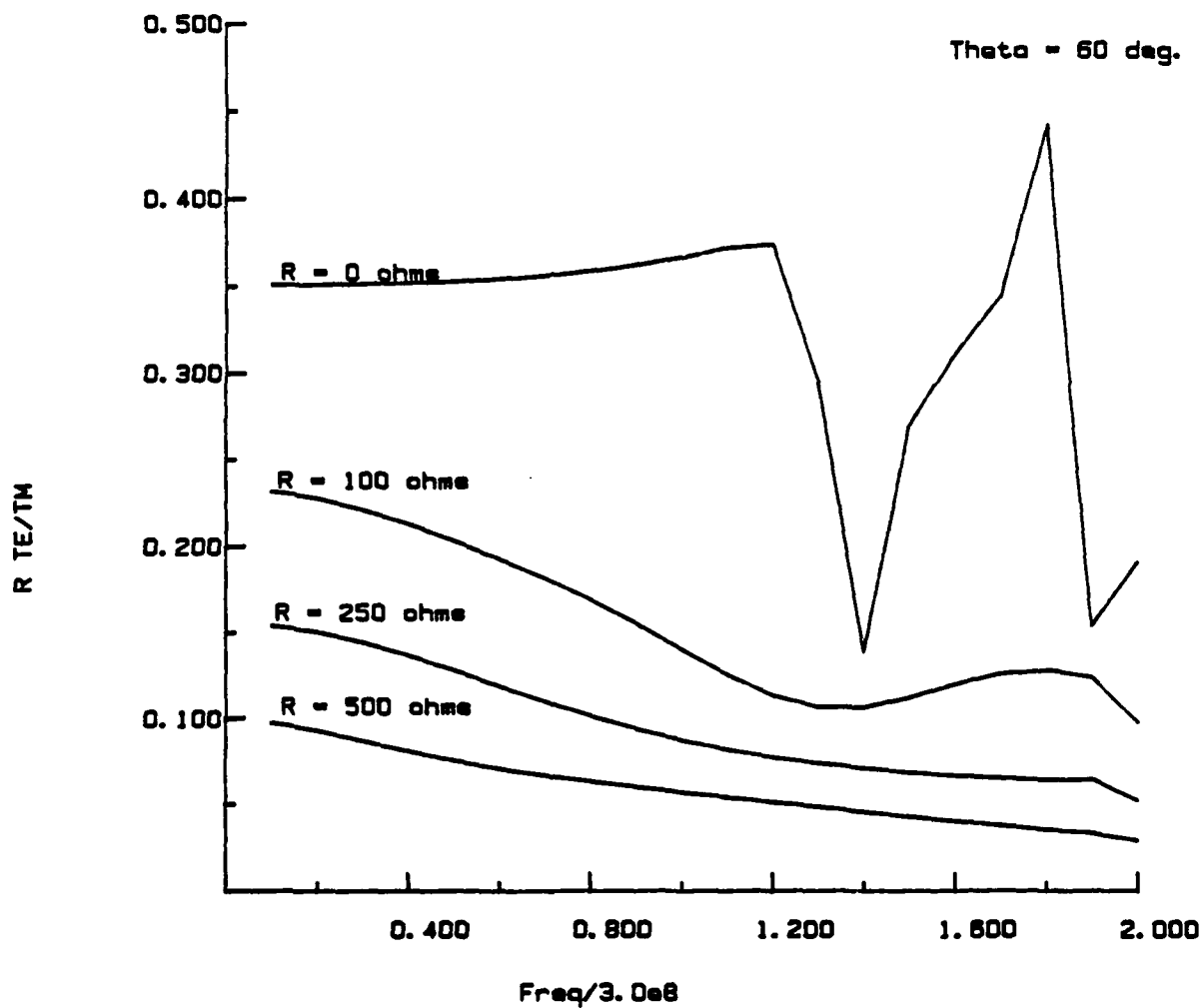


Figure 4.17 $|S_{11TE/TM}|$ versus normalized frequency for the zigzag plates of Figure 4.11 with a 60° bend. Plate resistance varies from lossless to $R = 500 \Omega$. The angles of the incident wave are $\theta_i = 45^\circ$, $\phi_i = 89.9^\circ$. The zeroth harmonic is shown.

Figures 4.18-4.21 show the effects of bending lossless strips on the reflection coefficient when the propagation vector of the incident wave is normal to the slab face, i.e., $\theta_i = 0.1^\circ$ and $\phi_i = 89.9^\circ$. With no bend, the TE wave is totally reflected at low frequencies and the TM wave, because it is incident on the edge of the strips and has an \vec{E} field perpendicular to the strip axis, is completely transmitted. There is no cross-coupling between the TE and TM waves.

Increasing the angle of bending to 30° in Figure 4.19, 60° in Figure 4.20, and 85° in Figure 4.21, the behavior discussed above, regarding the 45° incident field, is reinforced. The amount of cross-coupling between TE and TM polarizations increases with bend angle. The TE reflection coefficient at low frequencies becomes less as plate 2 is rotated out of alignment with the incident \vec{E} field. Correspondingly, the TM reflection coefficient becomes greater as plate 2 is rotated into alignment with the TM \vec{E} field. When the bend is 85° , the structure begins to appear, to both polarizations, like a square box which is disconnected at the corners. Plate 1 serves as the main scatterer for the TE wave with plate 2 serving chiefly as the connector between unit cells. For the TM case, the roles of the plates reverse. The coefficients for the TE and TM cases are, therefore, very similar over the entire frequency range. The second resonance phenomenon, which occurs for the non-normal incident wave, does not occur here. Bringing the strips closer together causes the resonances of the coefficients to become larger and sharper.

If a third plate is added to the zigzag plate structure of Figure 4.11, the honeycomb structure shown in Figure 4.22 results. The sizes of the three plates are the same ($d_s = 0.3$ m and $d_z = 0.25$ m) and the plates are separated angularly from each other by 120° , forming a regular hexagonal unit cell. The propagation vector of the incident wave is normal to the slab interface, i.e., $\theta_i = 0.1^\circ$ and $\phi_i = 89.9^\circ$.

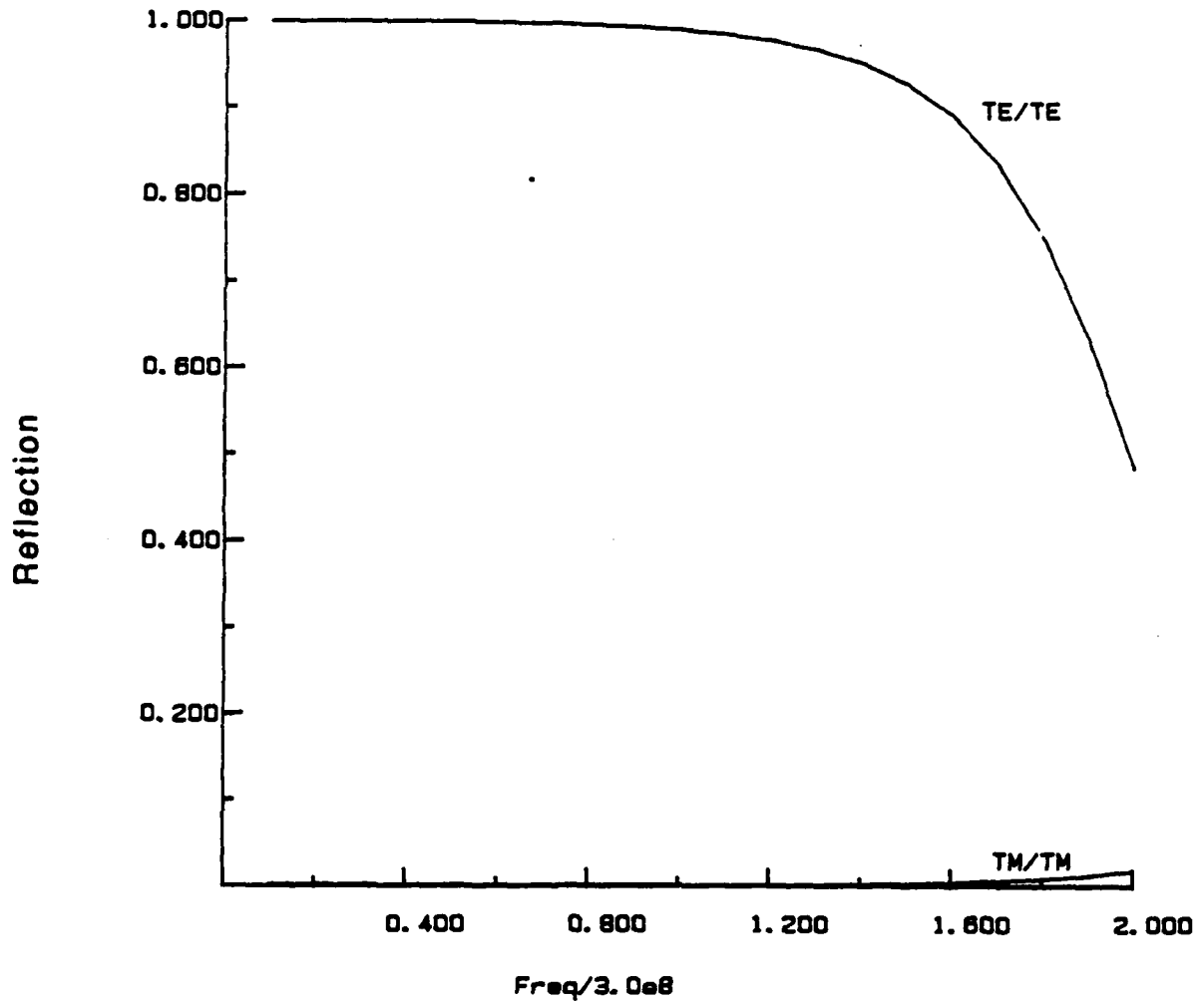


Figure 4.18 $|S_{11}|$ versus normalized frequency for the lossless zigzag plates of Figure 4.11 with no bend. Normal incidence, $\theta_i = 0.1^\circ$, $\phi_i = 89.9^\circ$. Note that the TM wave is transmitted through the structure and the TE wave is reflected from the structure. There is no cross-coupling of polarizations.

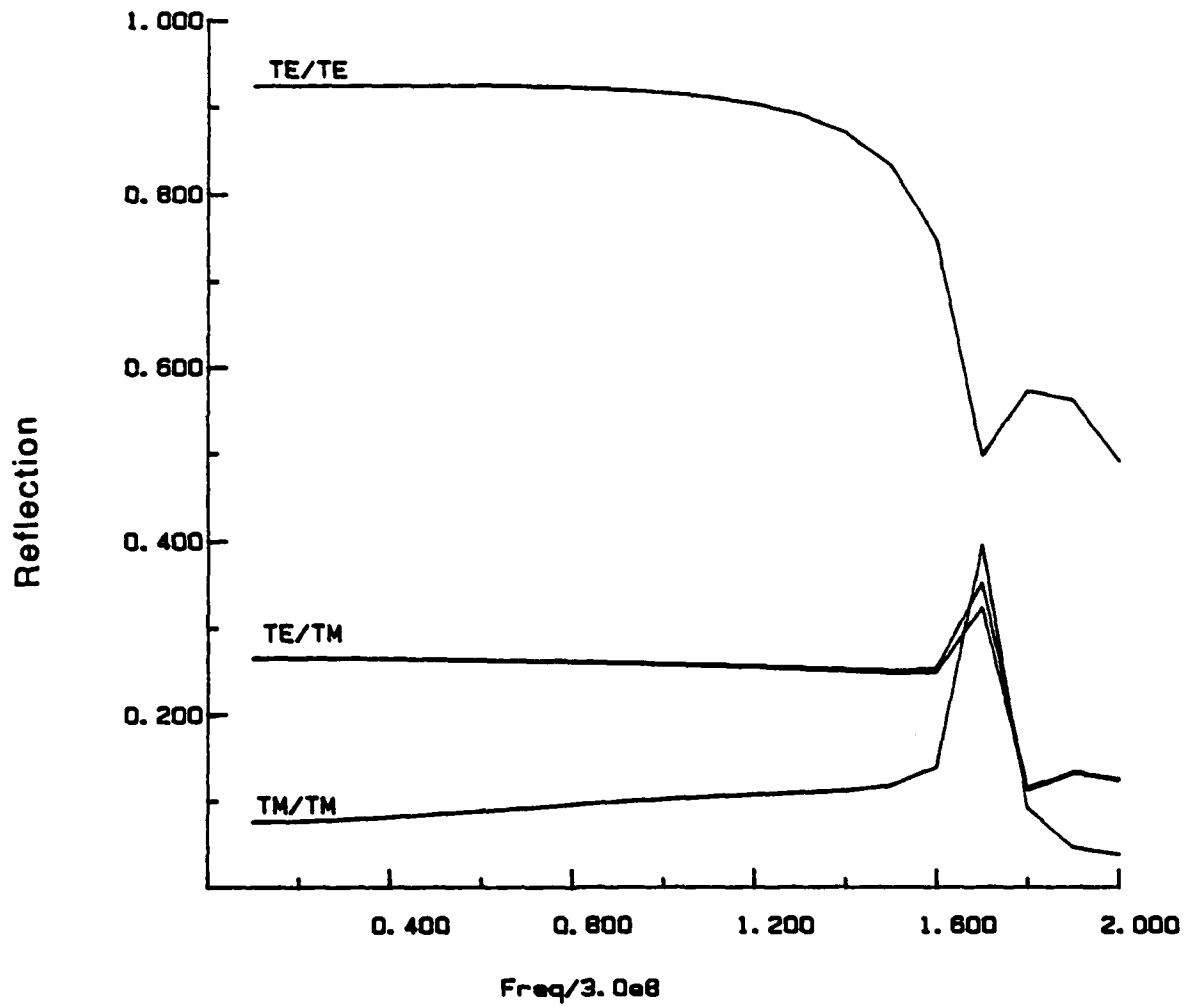


Figure 4.19 $|S_{11}|$ versus normalized frequency for lossless zigzag plates of Figure 4.11 with a 30° bend. Normal incidence, $\theta_i = 0.1^\circ$, $\phi_i = 89.9^\circ$. The TE/TE reflection coefficient decreases from that in Figure 4.18. The TE/TM and TM/TM reflection coefficients increase.

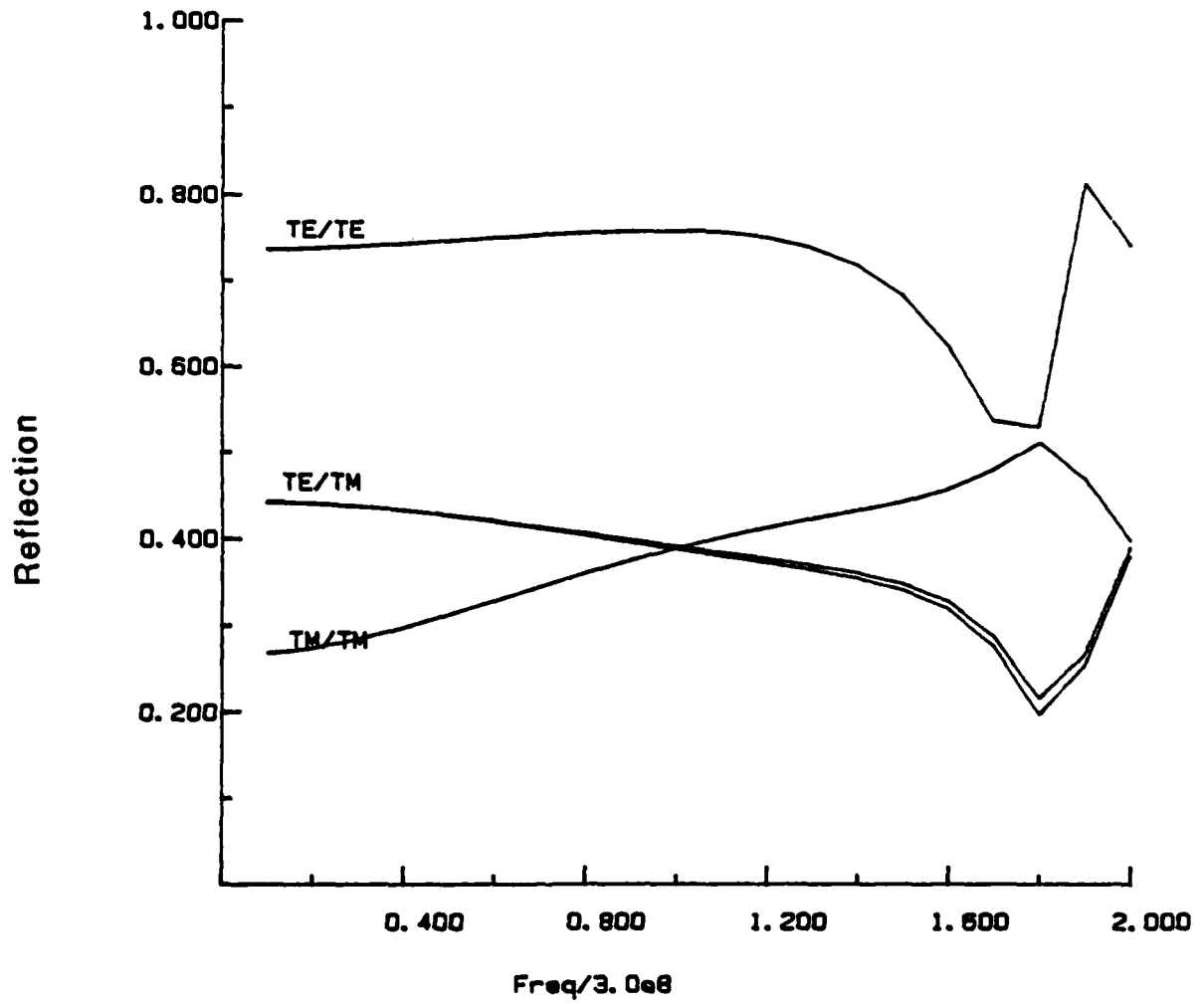


Figure 4.20 $|S_{11}|$ versus normalized frequency for lossless zigzag plates of Figure 4.11 with a 60° bend. Normal incidence, $\theta_i = 0.1^\circ$, $\phi_i = 89.9^\circ$. The trend of Figure 4.19 continues.

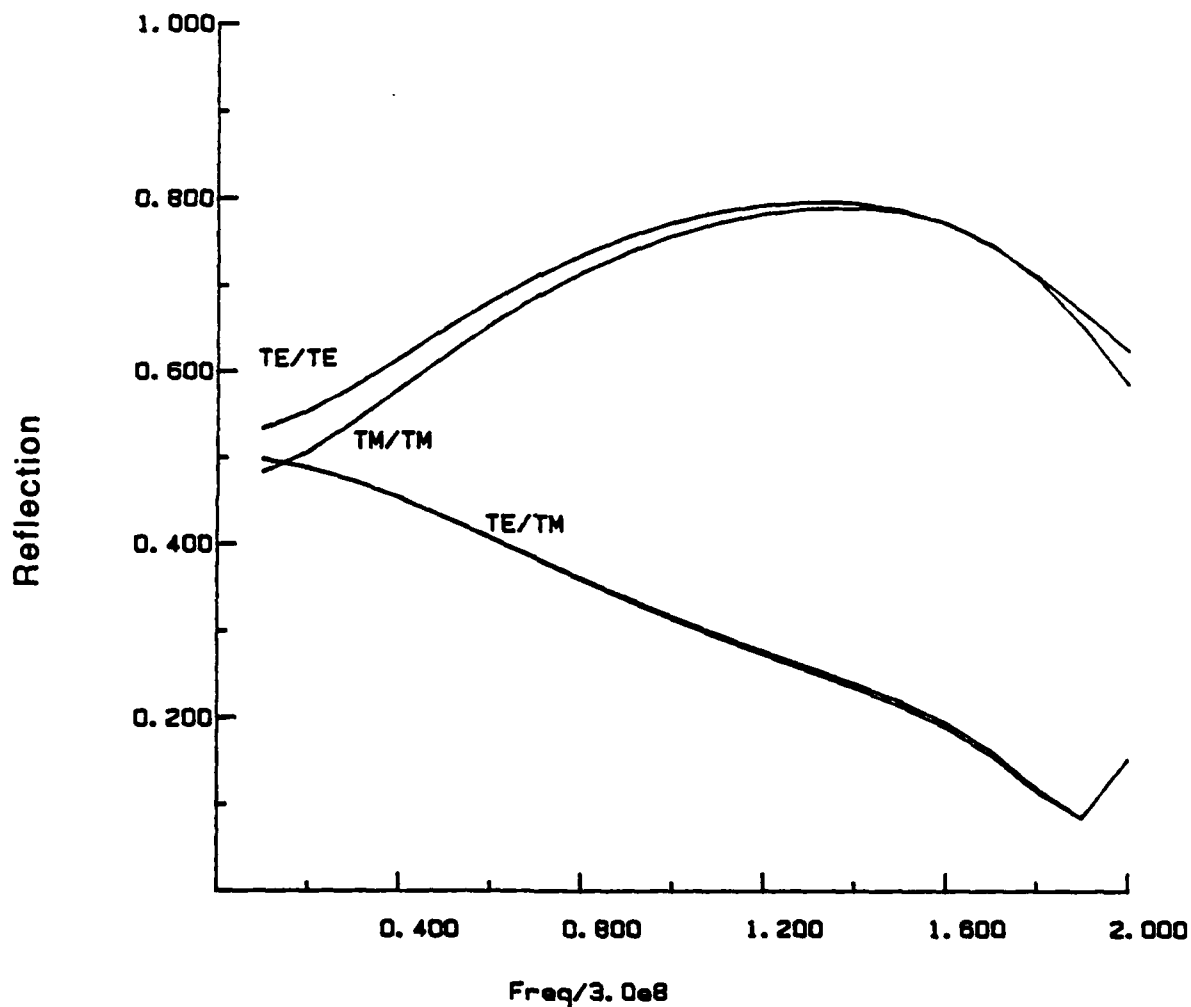


Figure 4.21 $|S_{11}|$ versus normalized frequency for lossless zigzag plates of Figure 4.11 with an 85° bend. Normal incidence, $\theta_i = 0.1^\circ$, $\phi_i = 89.9^\circ$. The TE/TE and the TM/TM reflection coefficients behave similarly because the unit cell "looks" the same to both of these waves.

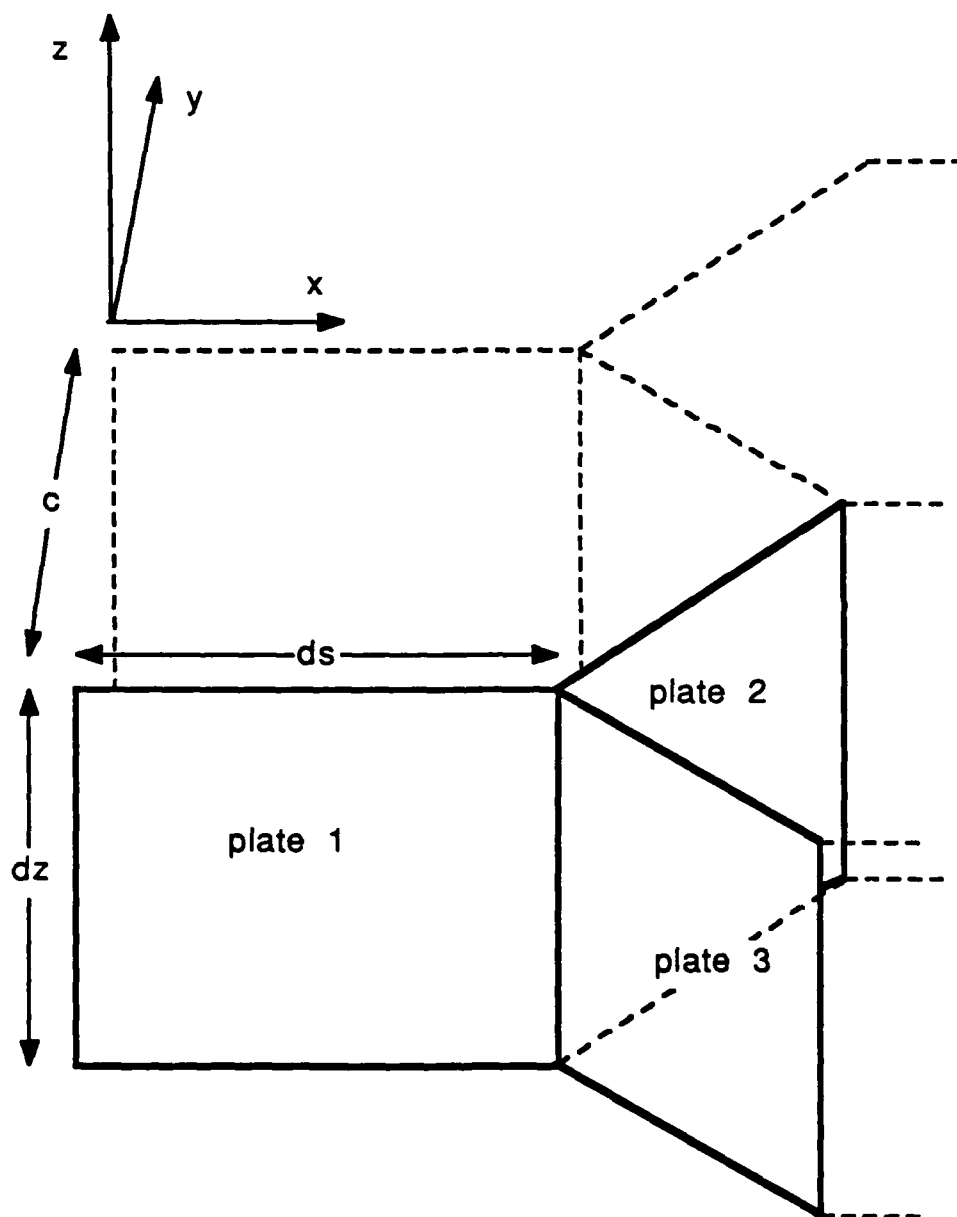


Figure 4.22 Unit cell for three plates connected to form a honeycomb. Plates 1, 2 and 3 are identical and separated angularly by 120° . The dimensions of a plate ($ds \times dz$) are 0.3×0.25 m. The plates are all connected to the neighboring cells.

The reflection characteristics of the lossless honeycomb are shown in Figure 4.23. The slab is totally reflecting at low frequencies because, unlike the parallel-strip structure whose unit cell can be viewed as a truncated parallel-plate waveguide, the hexagonal unit cell no longer supports a TEM mode. All modes that could exist within the structure are, therefore, cut off and there is no means to transport energy through the structure to transmit it on the other side. The characteristics of the honeycomb are relatively insensitive to polarization at this angle of incidence so plots of the TE and TM reflection coefficients overlay one another and there is no significant cross-coupling. Contrast this behavior with that of the same honeycomb structure with the third plate missing which is shown in Figure 4.24. As with other zigzag plate structures, the characteristics are sensitive to polarization and there is a large component of cross-coupling.

Adding loss to the honeycomb described above affects the reflection coefficients of the TE and TM polarizations differently as seen in Figure 4.25. The TM wave is reflected less than the TE wave at low frequencies. This can be explained by noting that in a macroscopic sense, the \vec{E} field associated with the TE wave interacts with a unit cell which has the resistance of plate 1 in series with two parallel resistances of plates 2 and 3. The \vec{E} field of the TM wave, on the other hand, interacts with the resistances of plates 2 and 3 in series. It is perpendicular to plate 1 and interacts very little with it. The total resistance interacting with the TE wave is, therefore, smaller than the total resistance interacting with the TM wave which leads to larger surface currents and larger scattered fields.

4.4 Conclusions

In this chapter, the techniques developed in Chapter 3 are extended to encompass geometries which are doubly periodic and composed of plates. The techniques consist of

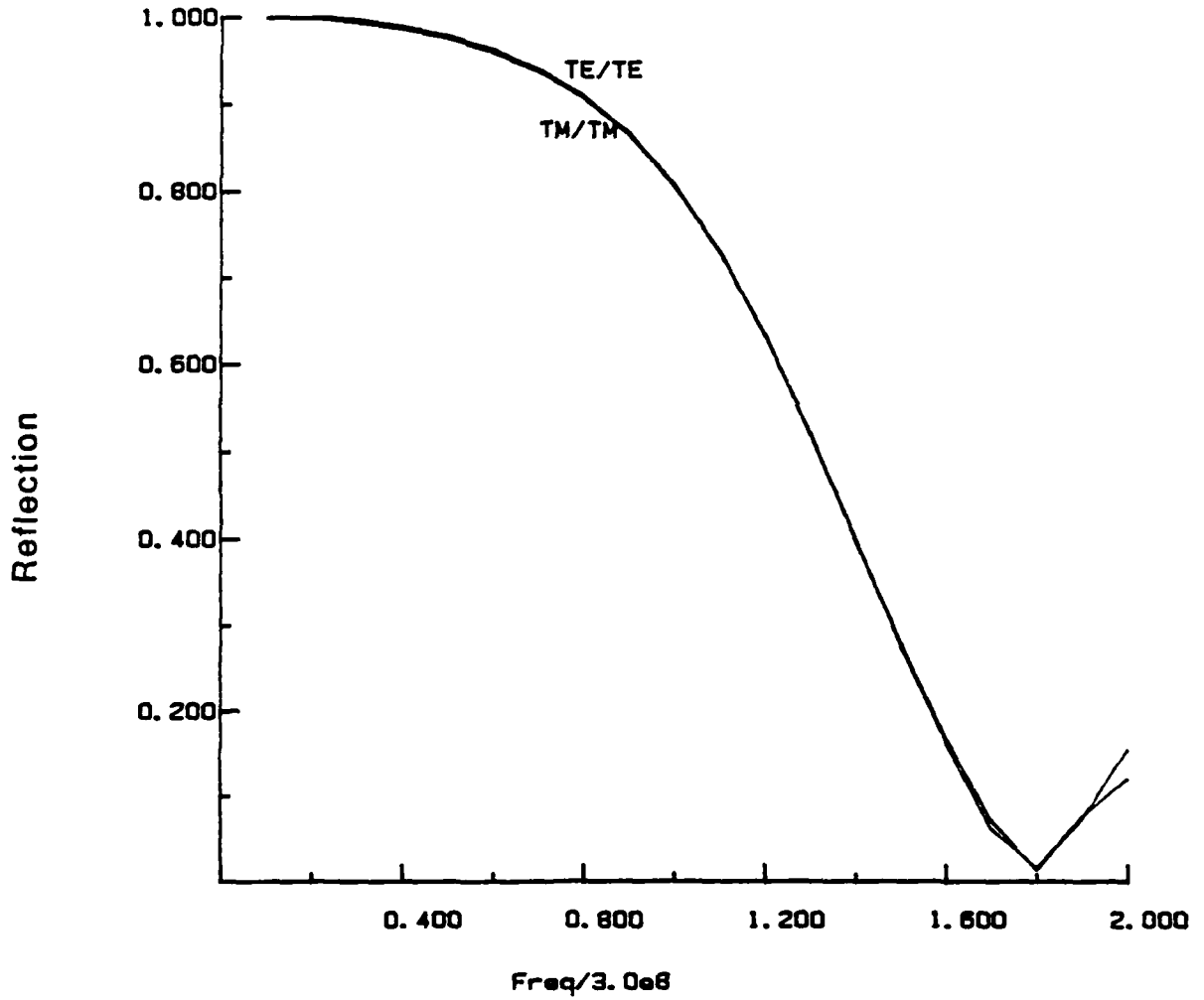


Figure 4.23 $|S_{11}|$ versus normalized frequency for the lossless honeycomb of Figure 4.22. Normal incidence, $\theta_i = 0.1^\circ$, $\phi_i = 89.9^\circ$. Note that the TE/TE and TM/TM reflection characteristics behave almost the same. There is no cross-coupling between polarizations.

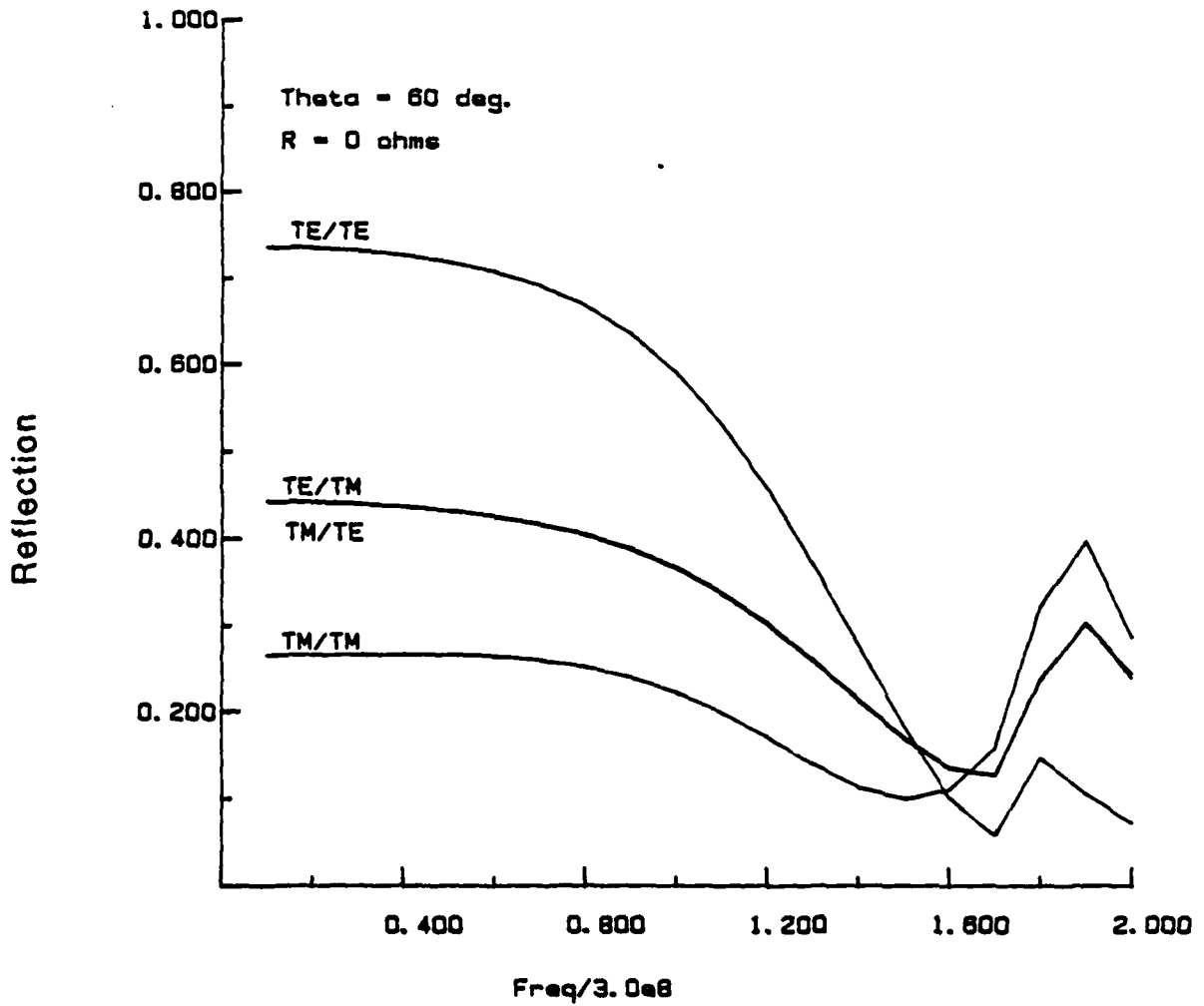


Figure 4.24 $|S_{11}|$ versus normalized frequency for the lossless honeycomb of Figure 4.22 with plate 3 missing. The geometry is that of a zigzag plate structure but with the spacing of a honeycomb. Normal incidence, $\theta_i = 0.1^\circ$, $\phi_i = 89.9^\circ$. In contrast to the curves of Figure 4.23, the TE/TE reflection coefficient and the TM/TM reflection coefficient behave quite differently.

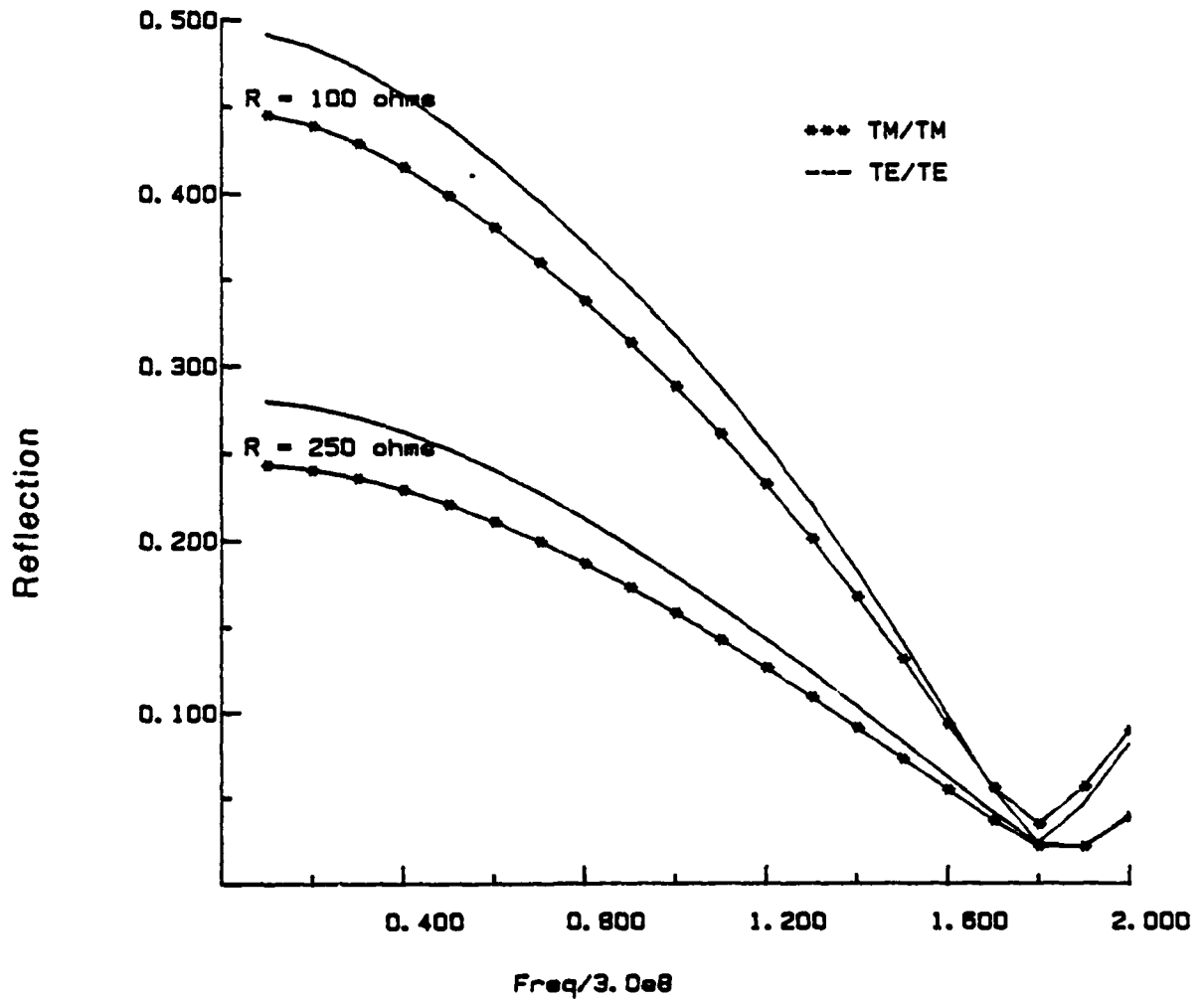


Figure 4.25 $|S_{11}|$ versus normalized frequency for honeycomb of Figure 4.22 with loss ($R = 100 \Omega$ and $R = 250 \Omega$) added. Normal incidence, $\theta_i = 0.1^\circ$, $\phi_i = 89.9^\circ$. Addition of loss causes the TM/TM and TE/TE reflection coefficients to behave differently in contrast to their behavior for the lossless honeycomb as shown in Figure 4.23.

formulating an EFIE, discretizing the equation using rooftop basis functions and razor testing functions, and solving the resulting matrix equation for the unknown currents flowing on the plates. The scattered field from the structure is described in terms of the generalized scattering matrix, harmonic by harmonic. The matrices for the plate array problems are larger and more difficult to fill than the strip array problems of Chapter 3. Therefore, acceleration techniques to efficiently calculate the Green's function and lookup tables to exploit the redundancy of the geometry become essential.

Results show the effect of continuity between unit cells. The TE waves for this angle of incidence are greatly affected by the presence or absence of cell-to-cell continuity at low frequencies while the TM waves are not. Next, the effect of bending the strip was demonstrated. Bending increases the amount of coupling between the TE and TM polarizations. In general, for the angles of incidence examined, increasing the bend angle decreases the TE reflection and increases the TM reflection until both polarizations behave similarly when the angle of bend approaches 90° . Adding loss decreases the magnitude of the reflection coefficients in general and smooths out the resonances caused by the unit cell geometry. The honeycomb slab was found, for normal incidence, to be independent of polarization and to have very little cross-coupling. Both TE and TM waves reflect totally at low frequencies. Addition of resistance to the plates causes some anisotropy with respect to polarization, although not as much as is caused by the deletion of one of the plates.

5. THICK PERIODIC PROBLEMS

5.1 Introduction

As discussed in Chapter 1, the size of the unit cell across the face of a honeycomb slab is typically on the order of a fraction of a wavelength. The slab thickness, on the other hand, is on the order of several wavelengths or more. Straightforward analysis of these slabs, in the manner discussed in Chapter 4, becomes prohibitive in terms of the number of unknowns required. An example is instructive.

Consider the honeycomb unit cell shown in Figure 4.22. If the unit cell is discretized at a density of ten basis functions per wavelength and the three plates composing the unit cell are dimensioned 0.6λ along \hat{s} by 0.5λ along \hat{z} , then 167 unknowns are needed to solve the problem. If this density of discretization is continued, then a one-wavelength thick slab would require 352 unknowns; a two-wavelength thick slab, 722 unknowns and so on. The problem quickly becomes large enough to overwhelm any computer system, not only from the standpoint of having to invert a large matrix, but also from filling the matrix in the first place. It should be pointed out, however, that since increasing the thickness of the slab builds on the block Toeplitz structure of the impedance matrix, filling the matrix is not as difficult a problem as it initially seems.

In this chapter, three methods will be discussed that are applicable to the solution of thick, structured slabs. Instead of using a brute-force approach to solve the problem, which would mean discretizing the entire slab, these methods attempt to extrapolate the solution of the thick slab from a rigorous solution of a thin slab having the same unit cell configuration along the interface. These slabs must be geometrically invariant in the thickness dimension. What must be kept in mind while weighing the advantages and disadvantages of these extrapolation procedures is that if the new method is no more efficient than the original brute-force method, it is not useful and need not be pursued.

The first method to be discussed calculates the solution to a thick slab by cascading the generalized scattering matrices of thin slabs. The limitations that were found in this method led to the search for alternative methods. In the second method, modes calculated for the interior of the lossy structure are matched to the Floquet harmonics outside the structure. This method is numerically intractable and, therefore, fails the criterion set forth above of needing to be more efficient than the straightforward moment method solution. The final method uses a moment method solution of a thin slab and Prony's method to construct large basis functions which model the physics of the current away from the interfaces of the slab. The method of moments is reapplied to a thicker slab using these constructed basis functions in the slab interior and subdomain basis functions near the interface. Of all the methods discussed, this method shows the most promise.

5.2 Cascading the Generalized Scattering Matrix

5.2.1 Definition of the scattering matrix

The generalized scattering matrix approach has been used successfully in the past to cascade FSSs with simple dielectric backings [33] or to cascade lossy strip structures with other similar structures [32]. It is, therefore, a natural candidate to be considered for extrapolating the characteristics of a thick slab of structured material from the characteristics of a thin slab. In order to understand the difficulty that arose using this method, it is best to return to the area in electromagnetics in which cascading the generalized scattering matrix was first applied—the area known as microwave networks [59],[60].

The generalized scattering matrix has its roots in the analysis of waveguide discontinuities and waveguide junctions. The fields within a simple waveguide can usually be completely described in terms of a single, propagating mode. Describing the fields within a region of the waveguide that has variation along the direction of propagation, on the other hand, requires, in addition to the propagating mode, an infinite number of nonpropagating modes. Because the nonpropagating modes are restricted to the region immediately surrounding the variation, this region can be replaced by a lumped equivalent circuit. The propagating mode is discontinuous across this circuit, so instead of having to deal with an infinite number of modes to describe in detail the fields within the region of variation, the effect that the variation has on the external region can be described by the discontinuity of a single mode.

The situation described in the paragraph above also exists when a plane wave is scattered from the structured slabs being studied in this thesis. The free space surrounding the slab may be thought of as a waveguide with walls separated by an infinite distance. The periodic nature of the slab dictates that the fields be represented as Floquet harmonics. Far away from the spatial discontinuity imposed by the slab, the fields are composed of a few propagating Floquet harmonics. Near the discontinuity, the fields are composed, in addition to the propagating Floquet harmonics, of an infinite number of nonpropagating harmonics. Because the nonpropagating harmonics are localized around the slab, the fields exterior to the slab can be described in terms of a microwave network in a manner analogous to that for the waveguide discontinuity.

The next step is to determine how to characterize the region of variation inside a waveguide as a microwave network. This usually involves solving a boundary-value problem. The use of the microwave network does not simplify the solution of the

boundary-value problem, it merely simplifies the description of its solution in the context of the overall problem. It is a fundamental theory of electromagnetics that a unique solution to electromagnetic fields inside a volume exists if the tangential components of either the magnetic or electric field are specified on the boundary surface [46]. A boundary surface for the waveguide discontinuity is defined, as shown in Figure 5.1, as a surface which encloses the entire discontinuity. The portion of the boundary that conforms to the metallic surface of the waveguide has the tangential component of the \vec{E} field equal to zero. It only remains to fix the boundary conditions at the terminal planes T_1 and T_2 in order to specify the field behavior uniquely within the volume.

The scattering matrix catalogues the amplitude of various Floquet harmonics which exist on the terminal planes. The total \vec{E} and \vec{H} fields tangent to either terminal plane can be described for each harmonic as a sum of the amplitudes of the incident harmonic (which is specified) and the scattered harmonics (which are calculated by solving the boundary-value problem). The uniqueness theorem as applied to the scattering matrix representation states that the amplitudes of the scattered harmonics at the terminal planes are uniquely related to the specified amplitude of the incident harmonic on them.

For the network under consideration with a single mode propagating in each guide, S_{mn} is a measure of the amplitude of the wave scattered into the m th guide by an incident wave of unit amplitude in the n th guide. The S matrix for the two-port network is, therefore, a 2X2 matrix. If more than one mode can propagate in the guides on either side of the discontinuity, then each element of the previous S matrix becomes a matrix itself in order to catalogue these additional modes. As the terminal planes are moved towards the region of discontinuity, evanescent modes may interact with the terminal planes and the order of the scattering matrix must again increase to accommodate these modes. Each new

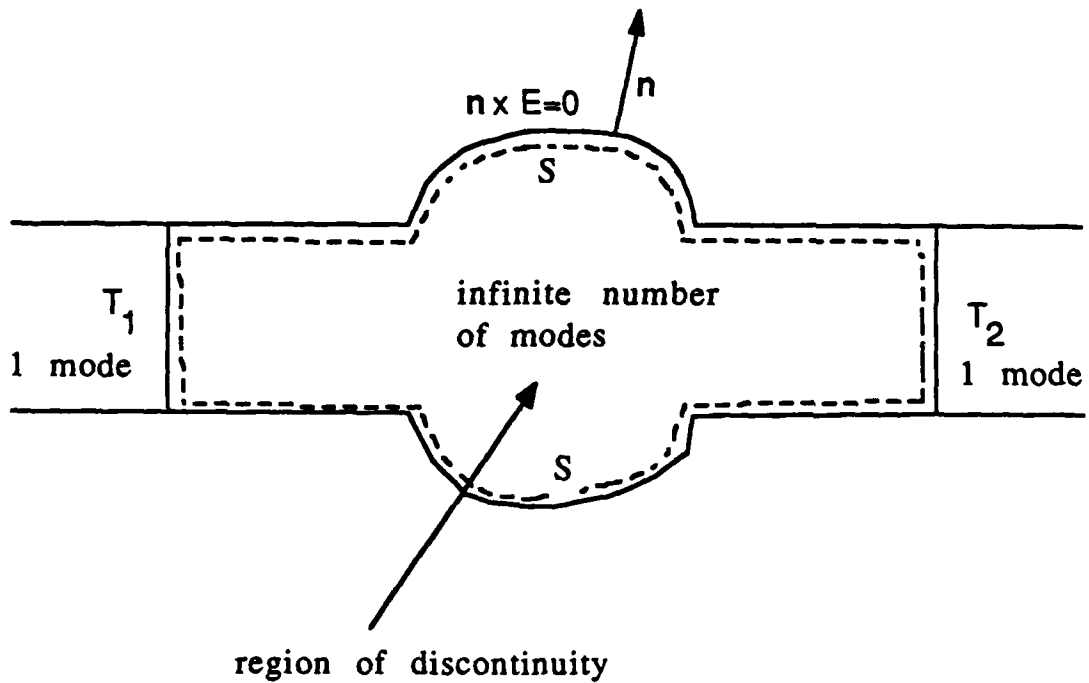


Figure 5.1 A two-port network modeling a region of discontinuity in the waveguide. The fields within the volume enclosed by the surfaces S , T_1 and T_2 are unique since the tangential \vec{E} field is zero on S and the scattering matrix specifies the fields on the terminal planes T_1 and T_2 .

mode, whether propagating or nonpropagating, only increases the effective number of ports needed to describe the junction under consideration.

The periodic slab can be thought of as a two-port network. The terminal planes are the infinite planes on each side of the slab. At these planes, the outgoing Floquet harmonics are calculated and catalogued as a function of an incident Floquet harmonic of unit amplitude by solving the boundary-value problem discussed in Chapters 3 and 4. The details of calculating the elements of the scattering matrix calculation are provided in Chapter 3 beginning on page 92 and in Chapter 4 beginning on page 132.

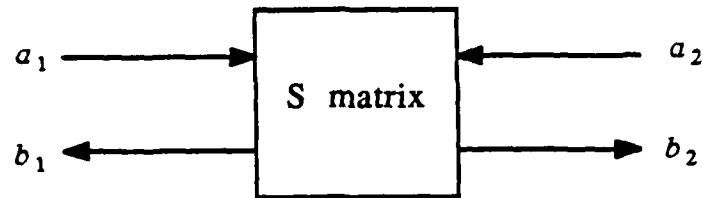
5.2.2 Cascading procedure

Suppose that several periodic slabs are stacked on top of each other in free space. The scattering matrix for each slab may be calculated using the concepts discussed above and the details from Chapters 3 and 4. The characteristics of the individual slabs, as represented by the scattering matrix, must now be cascaded in order to get the overall characteristics of the multislabs structure. The details of this operation are discussed next. It is understood when discussing cascading that the Floquet harmonics for each slab must be the same, which means that the size and shape of the unit cell across the face of each slab are identical.

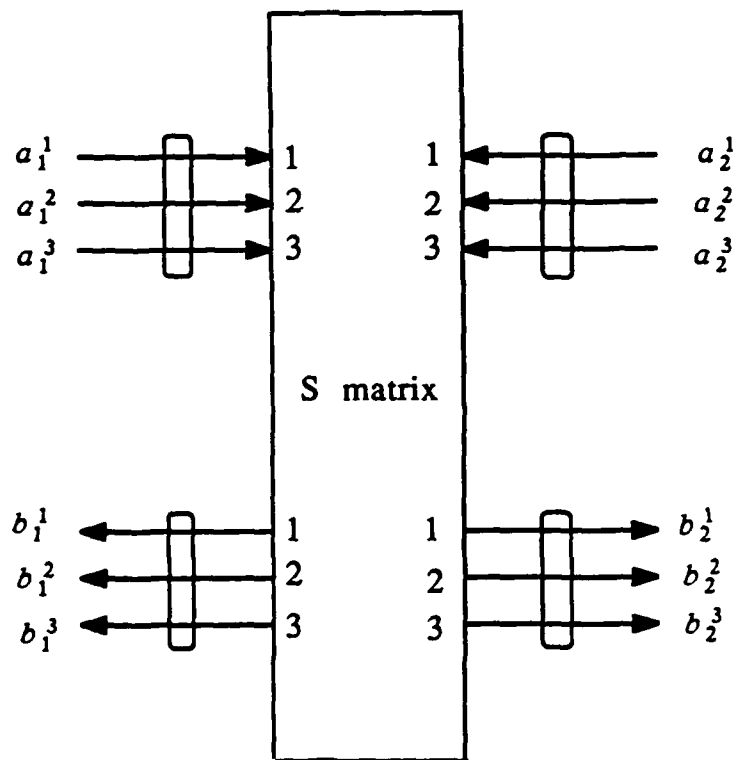
To cascade the generalized scattering matrices, researchers again turned to the methods used previously to cascade the characteristics of microwave circuits [55]. Referring to Figure 5.2, for a two-port network, if a_n represents the incoming waves and b_n represents the outgoing waves, then the S matrix takes the form of

$$\begin{bmatrix} b_1 \\ b_2 \end{bmatrix} = \begin{bmatrix} S_{11} & S_{12} \\ S_{21} & S_{22} \end{bmatrix} \begin{bmatrix} a_1 \\ a_2 \end{bmatrix} \quad (5.1)$$

As discussed previously, the elements a_n and b_n could be vectors while the elements S_{mn} could be matrices. This form is convenient for calculating, but not for cascading.



(a)



(b)

Figure 5.2 Input and output waves needed to define the S matrix for a two-port network. (a) is a simple S matrix where one harmonic models the fields on the terminal planes. (b) is a generalized S matrix where three harmonics are needed to model the fields on the terminal planes.

To cascade, it is desirable to have both the incident and scattered fields on one side of the discontinuity to be in terms of the incident and scattered fields on the other side. A linear transformation can be applied to the S matrix to get this relationship. The resulting matrix is known as a transmission or T matrix which can be expressed as

$$\begin{bmatrix} b_2 \\ a_2 \end{bmatrix} = \begin{bmatrix} T_{11} & T_{12} \\ T_{21} & T_{22} \end{bmatrix} \begin{bmatrix} a_1 \\ b_1 \end{bmatrix} \quad (5.2)$$

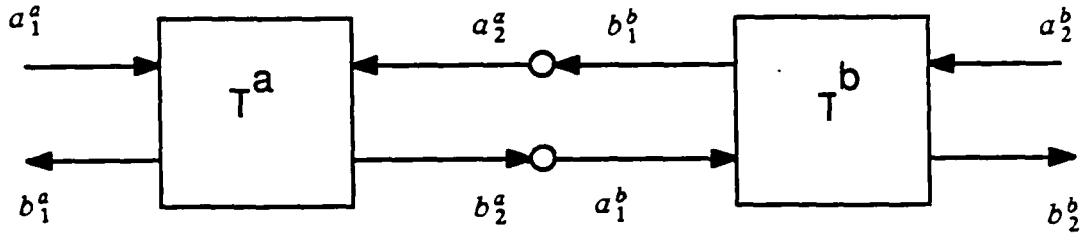
The linear transformation between the S and T matrices is given by [32]

$$T = \begin{bmatrix} S_{21} - S_{22}S_{12}^{-1}S_{11} & S_{22}S_{12}^{-1} \\ -S_{12}^{-1}S_{11} & S_{12}^{-1} \end{bmatrix} \quad (5.3a)$$

$$S = \begin{bmatrix} -T_{22}^{-1}T_{21} & T_{22}^{-1} \\ T_{11} - T_{12}T_{22}^{-1}T_{21} & T_{12}T_{22}^{-1} \end{bmatrix} \quad (5.3b)$$

where the matrix elements S_{mn} and T_{mn} are expressed in the form of submatrices to account for the possibility of needing more than one harmonic at the terminal plane to describe the field. The cascading procedure, demonstrated in Figure 5.3 [55], consists of multiplying together the T matrix for each slab to obtain the composite T matrix. The linear transformation of Equation (5.3b) returns the composite T matrix to the S matrix representation.

The problem with this procedure is that it is unstable numerically if higher-order harmonics are cascaded over large distances. The instability manifests itself by matrices with high condition numbers. The problem can be seen by examining Equation (5.3a) for one higher-order harmonic (so that matrix notation does not need to be used) and for a structure that is symmetric with respect to its thickness direction, i.e., $S_{11} = S_{22}$ and $S_{12} = S_{21}$. Equation (5.3a) becomes



$$\begin{bmatrix} b_2^a \\ a_2^a \end{bmatrix} = [T^a] \begin{bmatrix} a_1^a \\ b_1^a \end{bmatrix}$$

$$\begin{bmatrix} b_2^b \\ a_2^b \end{bmatrix} = [T^b] \begin{bmatrix} a_1^b \\ b_1^b \end{bmatrix}$$

Since $a_1^b = b_2^a$ and $a_2^a = b_1^b$, then

$$\begin{bmatrix} b_2^b \\ a_2^b \end{bmatrix} = [T^b] [T^a] \begin{bmatrix} a_1^a \\ b_1^a \end{bmatrix}$$

Figure 5.3 Cascading the characteristics of two microwave circuits using the T matrix representation [55].

$$T = \frac{1}{S_{12}} \begin{bmatrix} S_{12}^2 - S_{11}^2 & S_{11} \\ -S_{11} & 1 \end{bmatrix} \quad (5.4)$$

Since the higher-order harmonics are evanescent, they will decay to zero if they must travel too great a distance. The higher-order harmonics of S_{12} , because they travel between terminal planes, therefore, will decay to zero if the terminal planes are too far apart. When this happens, the rows of the T matrix in Equation (5.4) become dependent and T is ill-conditioned. The problem is compounded because the T matrix is multiplied together n times to cascade n slabs which means that the condition number of the overall T matrix is the condition number of the individual T matrix raised to the nth power. Because the final T matrix is so ill-conditioned, it is impossible to get meaningful answers.

If the unit cell of the cascaded structure lies entirely in the plane of periodicity, the instability problem is mitigated somewhat. If the planes are close to the structure, so that many harmonics are needed at the terminal planes to describe the field, the planes are also necessarily close to each other. In flat structures, therefore, the distances between planes and the number of harmonics required to model the fields have an inverse relationship. The same situation is not true if the unit cells are composed of plates or strips rotated out of the plane of periodicity. The distance between the terminal planes is fixed by the thickness of the slab but the number of harmonics needed to model the field is determined by the distance that the terminal plane is away from the structure. The slab may be quite thick, a situation where, for cascading stability, few harmonics would be desired, but the terminal plane may also be very close to the structure, a situation where, for field accuracy, many harmonics would be desired.

To study the above instability problem, the scattering matrix for two cascaded structured slabs is obtained using two methods. In the first method, both structured slabs are discretized at once and the scattering matrix is calculated for the entire problem. This

is called the exact scattering matrix. In the second method, the scattering matrix is found for a single structured slab and cascaded twice using the method discussed above. This is called the cascaded scattering matrix. Theoretically, the differences in the final scattering matrices obtained by these two methods should arise only from the fact that the number of harmonics accounted for in the interaction between the two structures is restricted by the order of the S matrix in one case and by the truncation of the periodic Green's function in the other. What actually dominates the error, however, is the numerical error that arises due to the instability of the cascade procedure.

In Figures 5.4 and 5.5, the relative errors between the individual elements of the exact and cascaded scattering matrices are plotted term-by-term, i.e., $\text{error}(S_{11})$, $\text{error}(S_{12})$, $\text{error}(S_{13})$, $\text{error}(S_{14})$, and so forth. The abscissa of the plot is the number of elements in the matrix. The problem geometry, as shown in Figure 5.4, consists of a TE wave incident on a strip array. The wave has a propagation vector lying in the plane normal to the strip axis and making an angle of 45° with the slab normal. The strips, which are rotated 90° out of the plane of periodicity, are 0.7λ long and are spaced 0.7λ apart. The two slabs are spaced 0.1λ apart. In Figure 5.4, the $-1, 0, +1$ harmonics are catalogued, so the S matrix has a total of 36 elements. The condition number for the overall T matrix is 1.0×10^6 . The relative error of the scattering matrix elements is below 40% for all elements and below 2% for most of the elements.

If the number of harmonics retained in the S matrix is increased to five ($-2, -1, 0, +1, +2$), in order to better model the terminal fields, the method breaks down. This is shown in Figure 5.5 in which the relative error for the S matrix elements is plotted. The elements in submatrices S_{11} and S_{12} become very accurate (below 1%). The elements in S_{21} and S_{22} become extremely inaccurate (more than $4.0 \times 10^8\%$ error). The condition number of the overall T matrix is 1.0×10^{14} , so the results cannot be trusted.

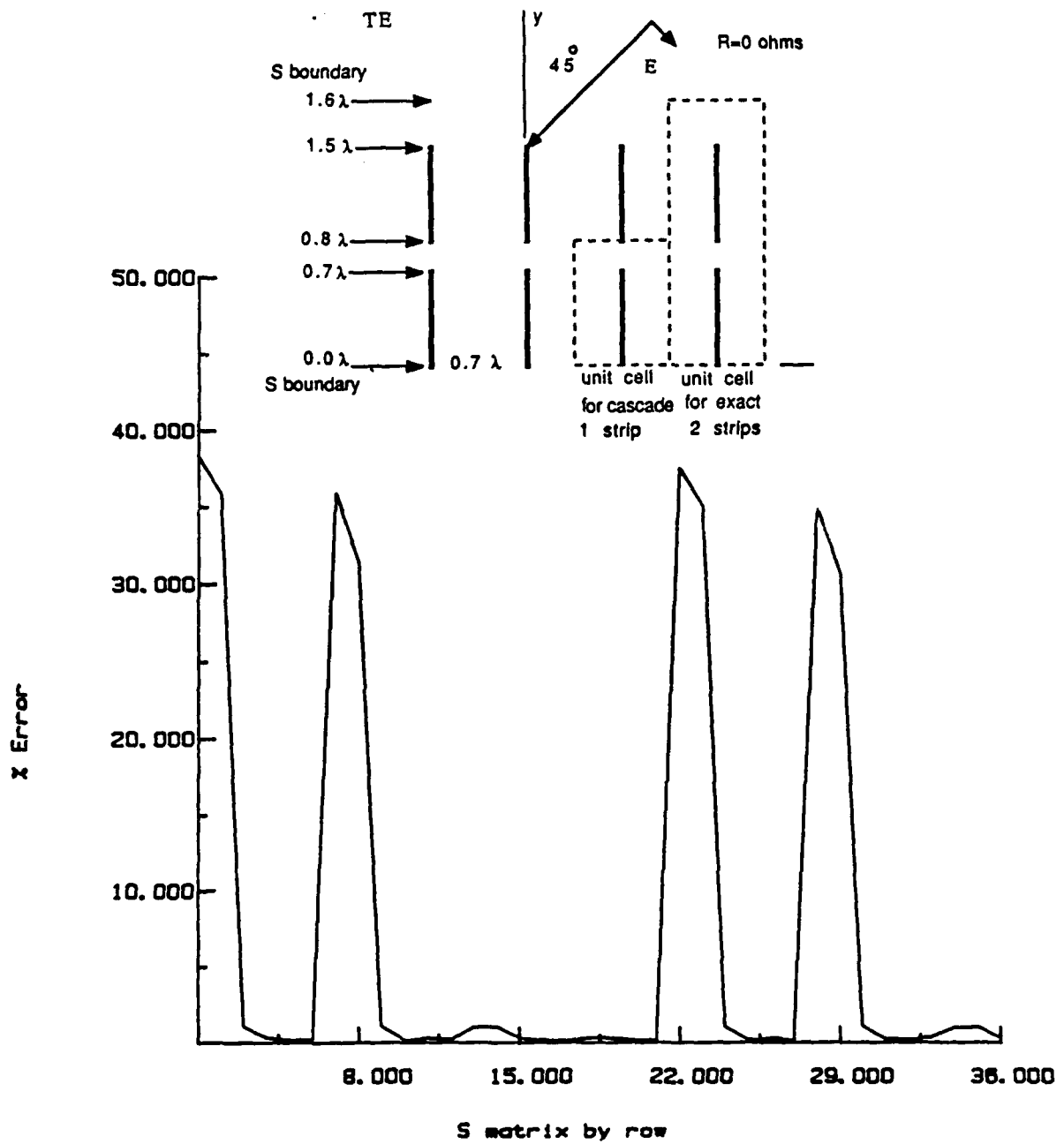


Figure 5.4 Relative error between the elements of the exact and cascaded S matrices plotted versus matrix element for the geometry shown. Three harmonics are retained so the number of elements in the S matrix is 36. The matrix elements are plotted by rows on the abscissa, i.e., $S_{11}, S_{12}, S_{13}, \dots, S_{21}, S_{22}, S_{23}$, etc...

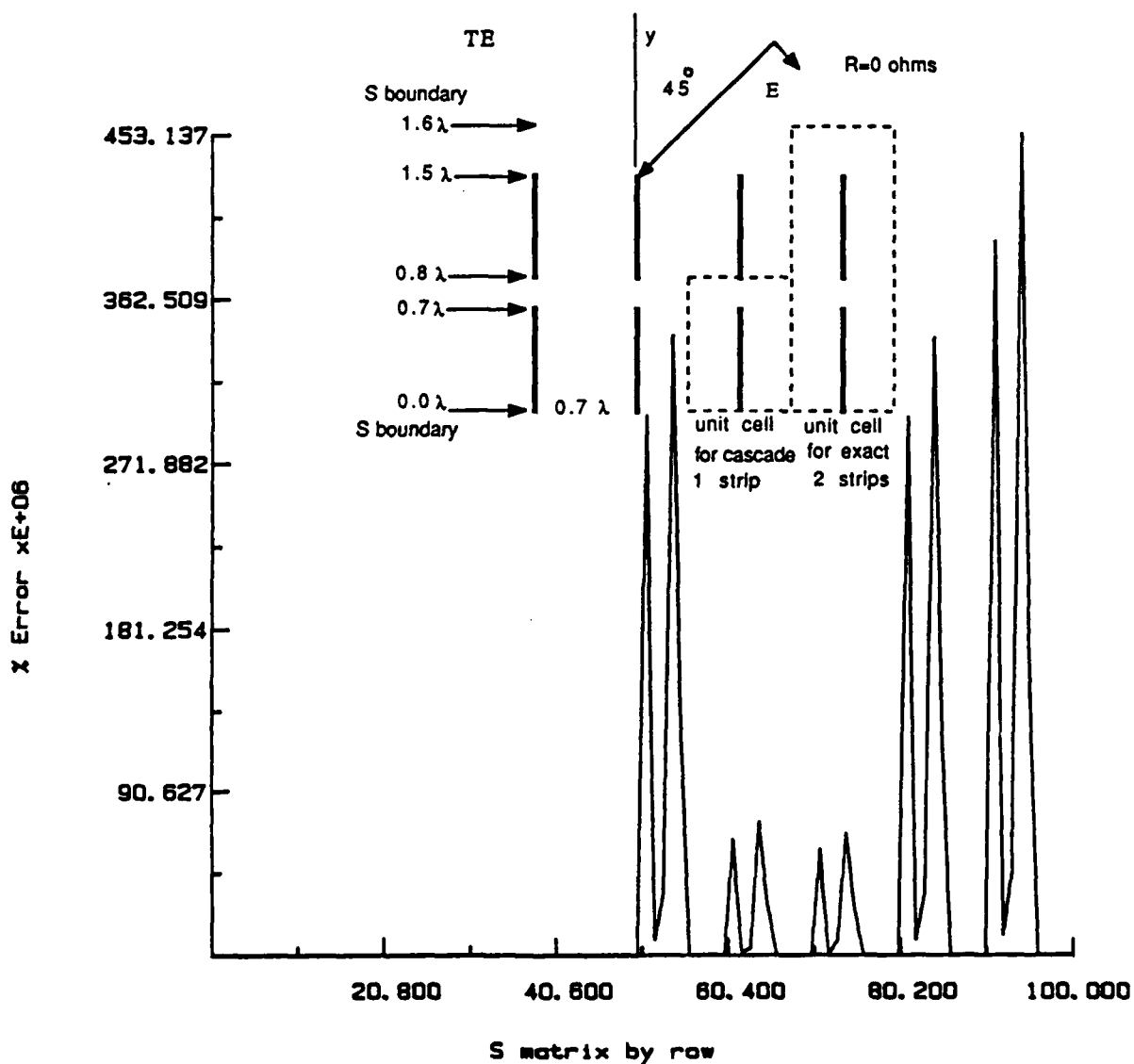


Figure 5.5 Relative error between the elements of the exact and cascaded S matrices plotted versus matrix element for the same geometry as shown in Figure 5.4. Five harmonics are retained so the number of elements in the S matrix is 100. The S_{11} and S_{21} submatrices are accurate but the S_{12} and S_{22} submatrices are extremely inaccurate because of the high condition number of the T matrix.

The way to avoid all these troubles is to cascade the S matrix directly without going to the T matrices [31]. This is done by cascading two S matrices at a time. The easiest way to see how the method works is to follow the operations on an incident wave Ψ^i on two structures shown in Figures 5.6 and 5.7. Figure 5.6 shows the procedure for calculating the composite S_{11} and S_{21} matrices while Figure 5.7 shows the calculations of S_{12} and S_{22} . S^a and S^b represent the scattering matrices of structures a and b, respectively. Referring to Figure 5.6, the amount of Ψ^i reflected from structure a is $S_{11}^a \Psi^i$. The wave $S_{21}^a \Psi^i$ is transmitted through structure a to become incident on structure b. Structure b transmits a portion of this wave ($S_{21}^b S_{21}^a \Psi^i$) and reflects the remainder ($S_{11}^b S_{21}^a \Psi^i$) back towards structure a. At structure a, the reflection and transmission occurs again. This sequence continues ad infinitum. The composite S_{11} matrix of the two structures is found by adding all the contributions of the wave leaving the left-hand side of the two structures in Figure 5.6. The composite S_{21} matrix is found by adding the transmitted contributions on the right-hand side. The result is

$$\begin{aligned} S_{11}^{comp} &= S_{11}^a + \sum_{n=0}^{\infty} S_{12}^a S_{11}^b [S_{22}^a S_{11}^b]^n S_{21}^a \\ &= S_{11}^a + S_{12}^a S_{11}^b \left[\tilde{I} - S_{22}^a S_{11}^b \right]^{-1} S_{21}^a \end{aligned} \quad (5.5)$$

$$\begin{aligned} S_{21}^{comp} &= \sum_{n=0}^{\infty} S_{21}^b [S_{22}^a S_{11}^b]^n S_{21}^a \\ &= S_{21}^b \left[\tilde{I} - S_{22}^a S_{11}^b \right]^{-1} S_{21}^a \end{aligned} \quad (5.6)$$

Each S_{mn} in the equations above is a matrix so it can account for more than one Floquet harmonic. \tilde{I} is the identity matrix. The closed form for the summation is valid because the summation is a convergent geometric series. The proof is given in [31]. The same

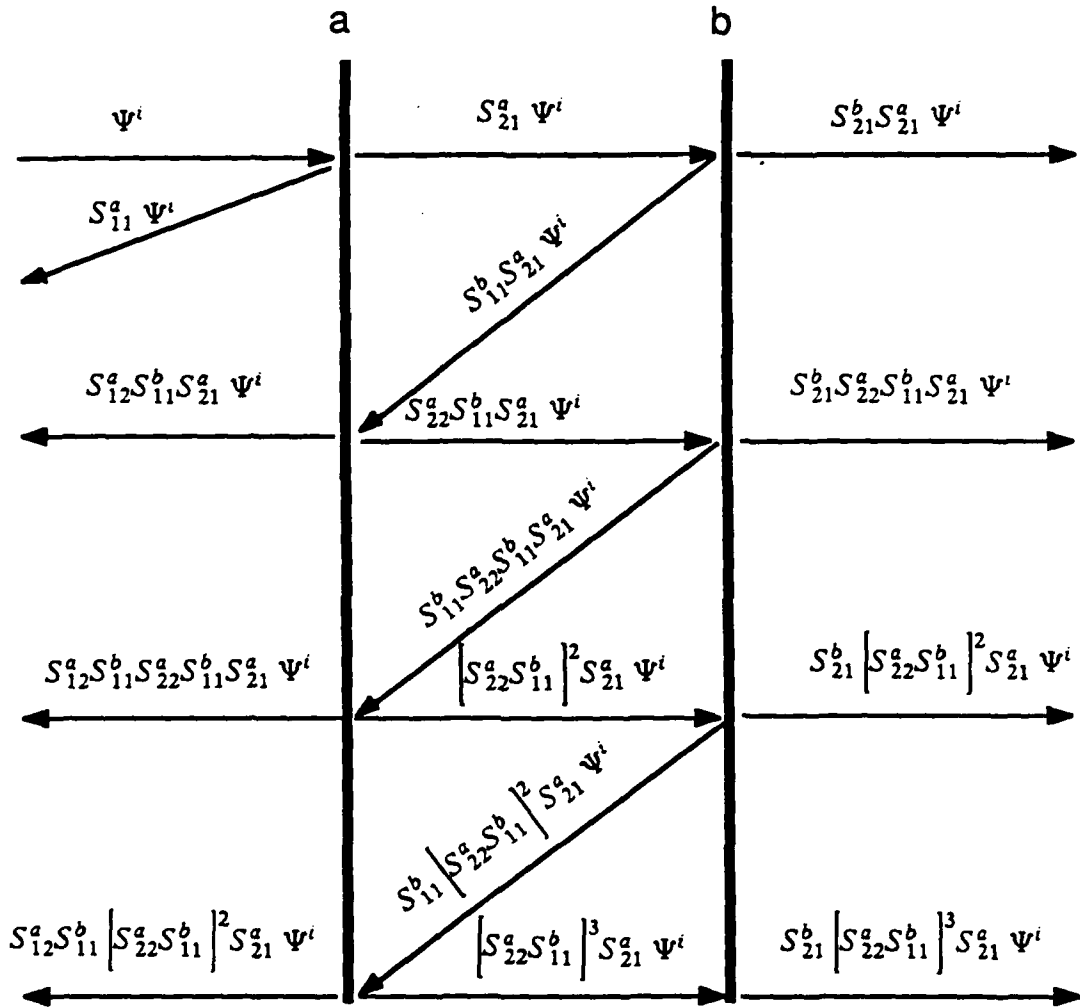


Figure 5.6 Cascading the S matrix directly without using the T matrix. The composite S_{11} and S_{21} submatrices are calculated for two networks represented by S^a and S^b .

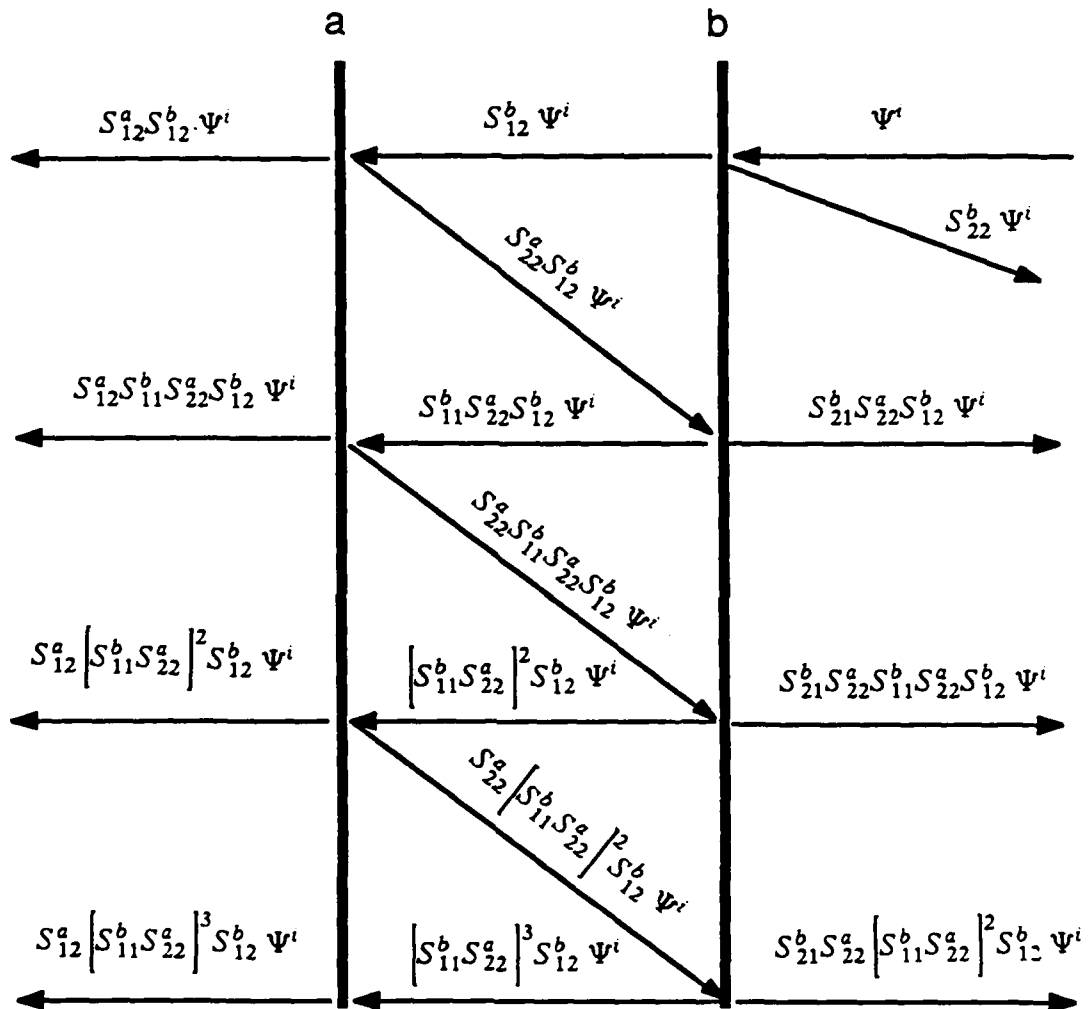


Figure 5.7 Cascading the S matrix directly without using the T matrix. The composite S_{22} and S_{12} submatrices are calculated for two networks represented by S^a and S^b .

procedure is applied to Figure 5.7 to obtain the remaining two composite S submatrices:

$$\begin{aligned} S_{22}^{comp} &= S_{22}^b + \sum_{n=0}^{\infty} S_{21}^b S_{22}^a \left[S_{11}^b S_{22}^a \right]^n S_{12}^b \\ &= S_{22}^b + S_{21}^b S_{22}^a \left[\vec{I} - S_{11}^b S_{22}^a \right]^{-1} S_{12}^b \end{aligned} \quad (5.7)$$

$$\begin{aligned} S_{12}^{comp} &= \sum_{n=0}^{\infty} S_{12}^a \left[S_{11}^b S_{22}^a \right]^n S_{12}^b \\ &= S_{12}^a \left[\vec{I} - S_{11}^b S_{22}^a \right]^{-1} S_{12}^b \end{aligned} \quad (5.8)$$

By first cascading two scattering matrices, then cascading the result with the next scattering matrix and so forth, the composite S matrix of an arbitrary number of slabs can be obtained. The programs are just as simple as the T matrix programs and the condition numbers associated with the matrices are on the order of one to ten instead of the condition numbers of millions associated with the T matrix.

5.2.3 Results of cascading

Next, the scattering matrix for the honeycomb slab shown in Figure 4.22 is cascaded. The unit cell is a regular hexagon with a side dimension of 0.3 m and a depth of 0.25 m. A plane wave is incident normally ($\theta_i = 0.1^\circ, \phi_i = 89.9^\circ$) on three stacked slabs of this structure. This geometry is shown from the side in Figure 5.8. The three slabs are in free space or are backed by a Perfect Electric Conductor (PEC). The slabs are infinitesimally close to each other, but are not touching, so that no current flows from slab to slab. The resistance of each slab is varied to see the effect that this has on the reflection coefficient.

Figure 5.9 shows a plot of the reflection coefficient for the zeroth harmonic versus frequency. The three slabs all have a resistance of 100 Ω . The PEC does not affect the reflection at low frequencies. This means that the wave is dissipated by the wall loss

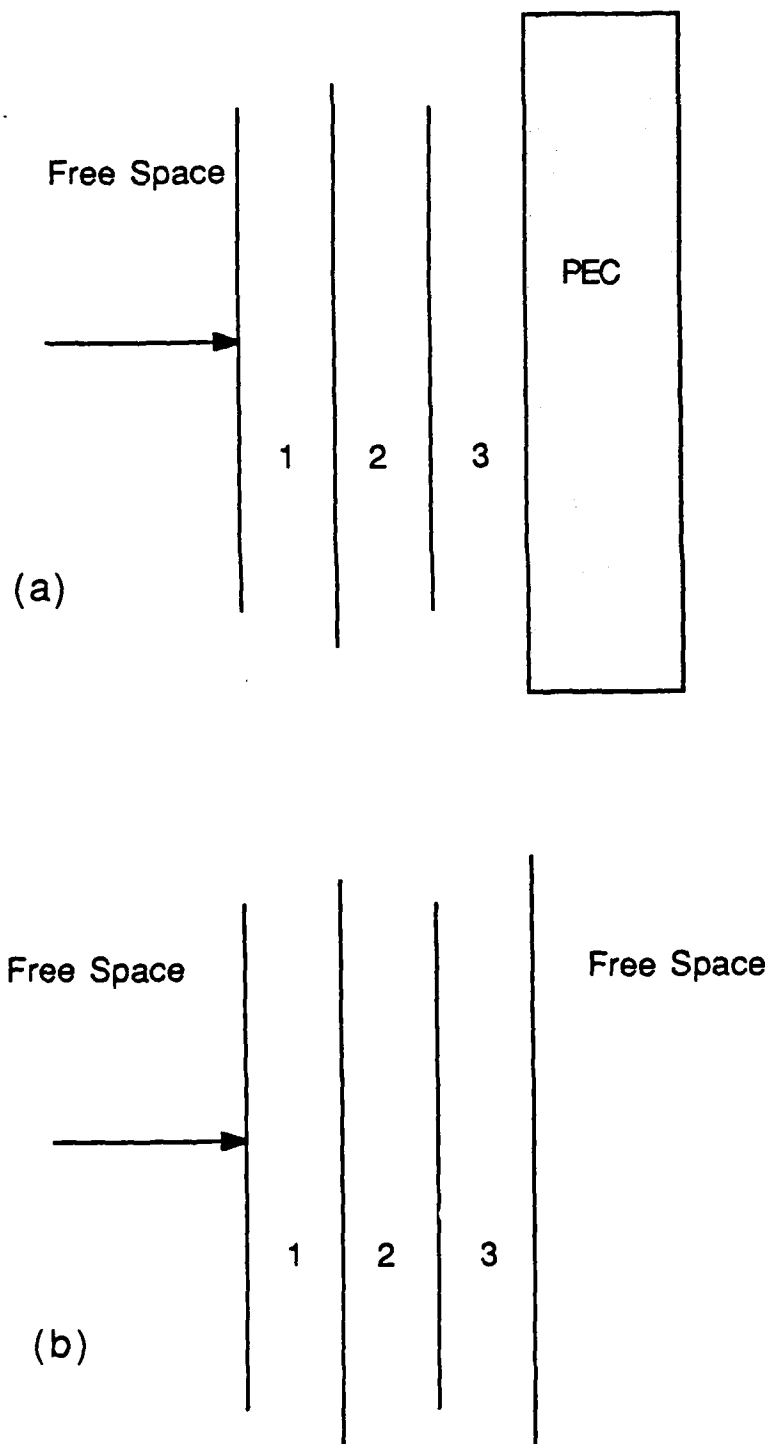


Figure 5.8 Side view of three honeycomb slabs which are infinitesimally close but not physically touching one another. The slabs are each 0.25 m thick and are lossy. The regular hexagon unit cell has a side length of 0.3 m. The slabs are backed by a PEC sheet (a) or are in free space (b).

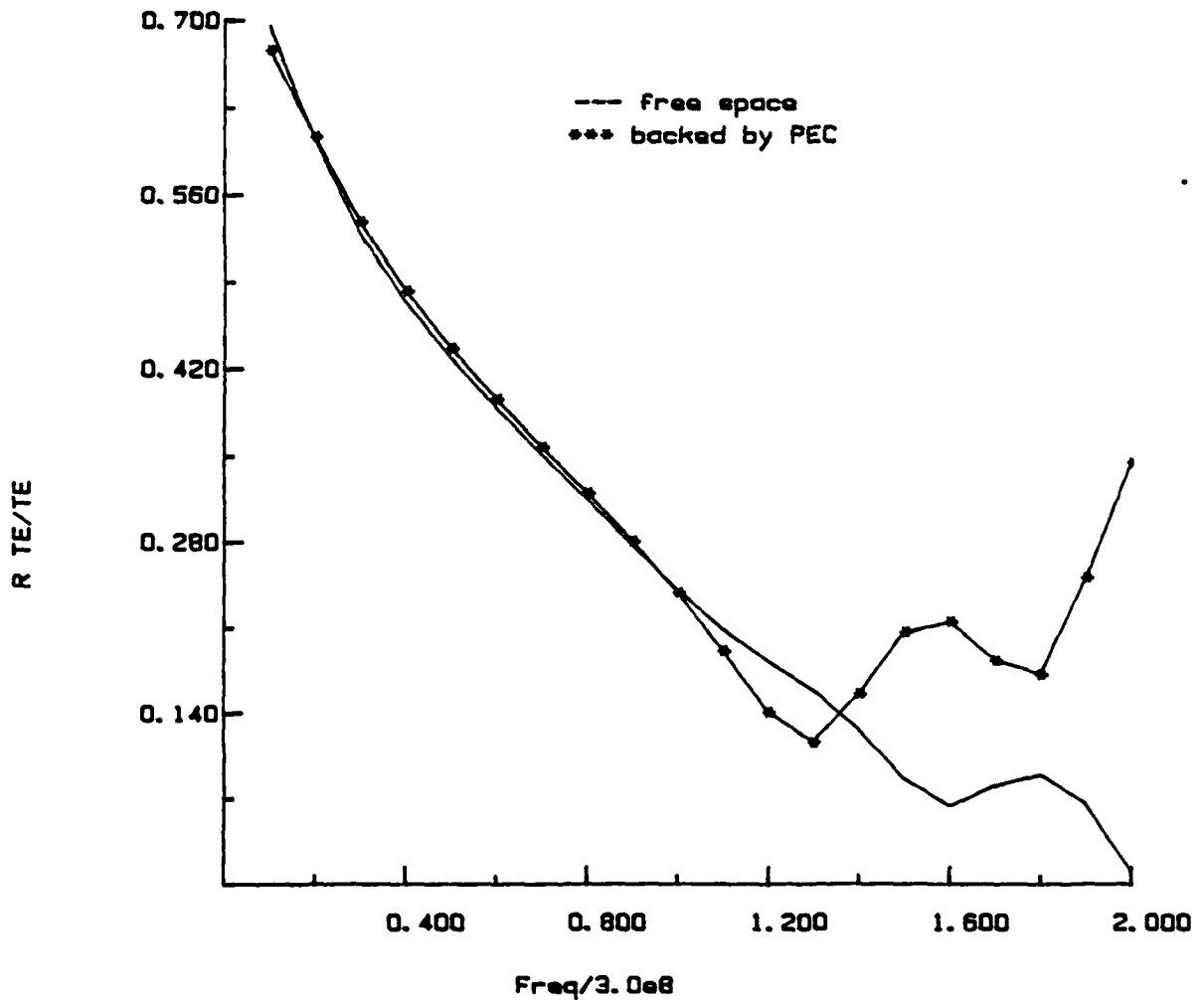


Figure 5.9 Plot of the zeroth harmonic of $|S_{11 TE/TE}|$ versus normalized frequency for the geometry of Figure 5.8. The incident wave makes angles of $\theta_i = 0.1^\circ, \phi_i = 89.9^\circ$. $R = 100 \Omega$ for all slabs. The slabs in free space and the slabs backed by PEC have similar characteristics which means that the incident wave does not interact with the back plane at low frequencies.

before it reaches the back plane. The reflected wave is due to the discontinuity in space imposed by the honeycomb itself. At around 4.8×10^8 Hz where the field is transmitted through the honeycomb (see Figures 4.23 and 4.25), the incident wave gets through all three layers of the honeycomb and is reflected by the PEC back through the honeycomb. At this frequency, the characteristics of the free space and the PEC backed honeycombs begin to differ.

Figure 5.10 is a plot of the same situation as Figure 5.9 except that the loss of the honeycomb slabs increases to 500Ω . For this case, the walls dissipate more energy, but the geometry of the honeycomb does not shield the back plane from the incident wave. The structure behaves like a lossy, simple dielectric on a PEC. The ripple effect in the reflection characteristics of the PEC case is due to the thickness of the dielectric changing by half a wavelength. The same effect happens to a lesser degree in the free standing slab. The ripples in this case are due to interaction of the waves reflected off the front and back planes of the slabs.

The idea behind RCS reduction is to match the impedance of the PEC to the impedance of free space gradually so that the matching material does not cause a reflection itself. This is attempted in Figure 5.11. Curve one shows the reflection characteristics when all three slabs have a resistance of 250Ω . This resistance of this case is approximately the average value of the resistances for curves two and three. Curve two shows what should not be done. The resistance is tapered, i.e., free space, 100Ω slab, 250Ω slab, 500Ω slab and PEC, but in the wrong direction. The highest resistance should be next to the free-space region to provide a smooth transition from free space to the region occupied by the honeycomb. Next to the PEC region, the resistance should be lowest to match the impedance of the PEC. This case is shown by the curve labeled three.

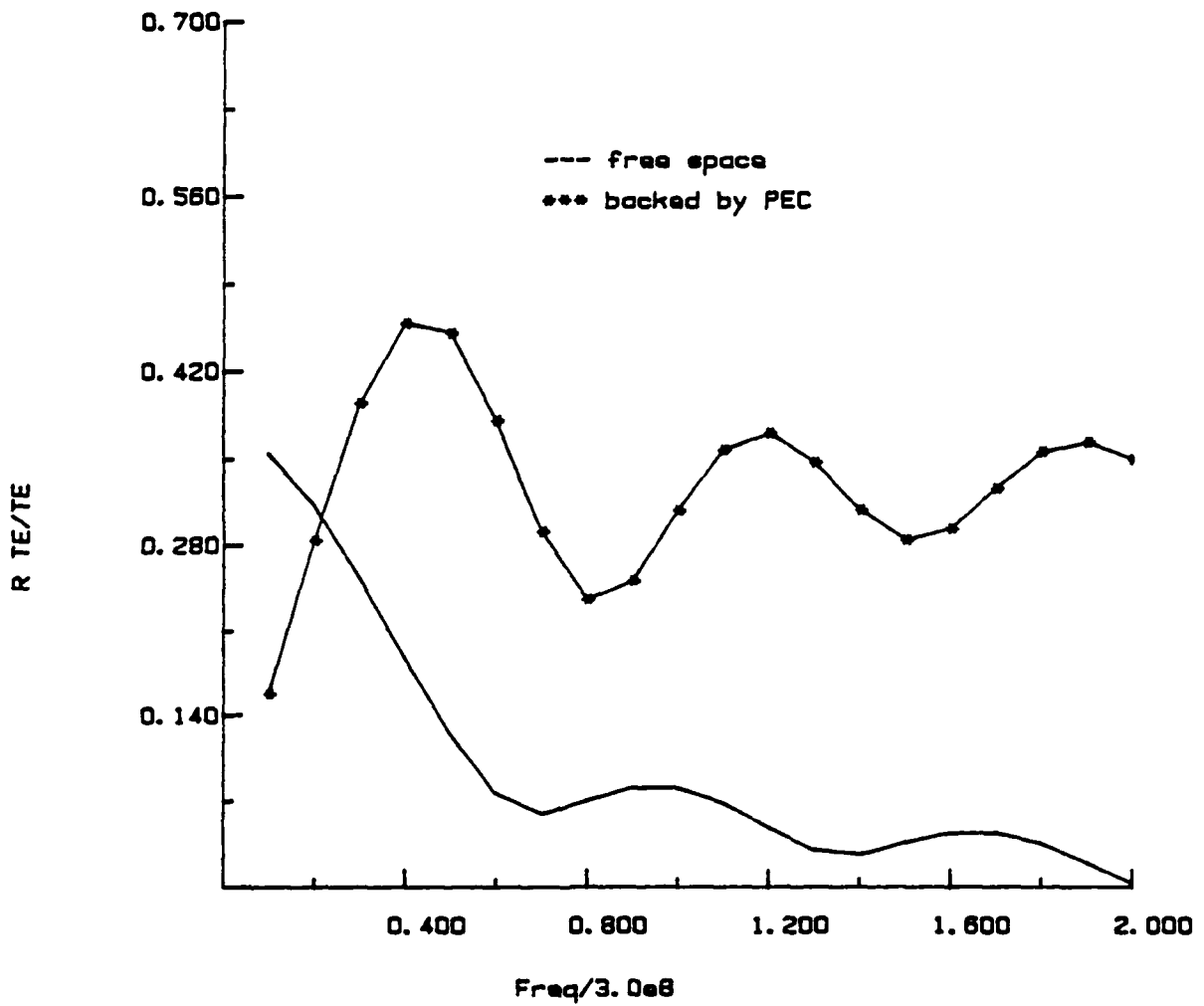


Figure 5.10 Plot of the zeroth harmonic of $|S_{11 TE/TE}|$ versus normalized frequency for the geometry of Figure 5.8. The incident wave makes angles of $\theta_i = 0.1^\circ$, $\phi_i = 89.9^\circ$. $R = 500 \Omega$ for all slabs. In contrast to Figure 5.9, the incident wave does interact with the back plane.

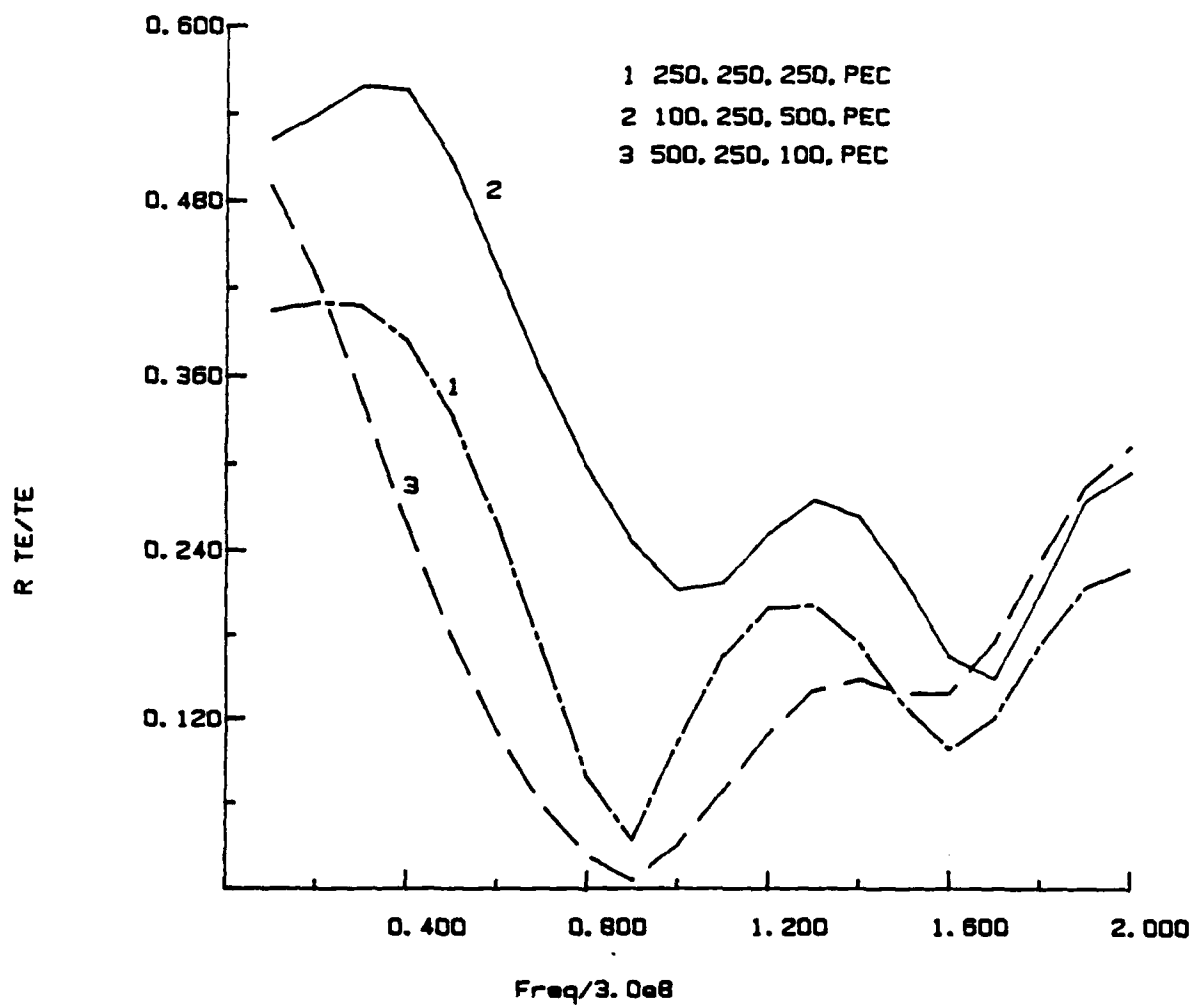


Figure 5.11 Plot of the zeroth harmonic of $|S_{11 TE/TE}|$ versus normalized frequency for the geometry of Figure 5.8. The incident wave makes angles of $\theta_i = 0.1^\circ$, $\phi_i = 89.9^\circ$. The results are shown for three different resistance combinations for the three slabs. For curve 1, all three slabs have a resistance of $R = 250 \Omega$. For curve 2, $R_1 = 100 \Omega$, $R_2 = 250 \Omega$ and $R_3 = 500 \Omega$. For curve 3, $R_1 = 500 \Omega$, $R_2 = 250 \Omega$ and $R_3 = 100 \Omega$. The slabs are backed by a PEC.

Curve three shows the best reflection characteristics of all three cases while curve two shows the worst. All curves have a ripple which shows the effect of the PEC backing, but the curve for the properly tapered resistance shows less ripple than the others. In order to get even better reflection characteristics, the resistance should be tapered more gradually.

5.2.4 Continuity problems with the S matrix

The problem that ultimately caused the abandonment of the S matrix as a way to model thick slabs of honeycomb is that the S matrix cannot model current continuity. If a structure is continuous in the thickness dimension, then the currents flowing in that dimension should also be continuous. The formulation in terms of an S matrix, however, breaks the thick, continuous slab into several identical thin slabs. The terminal planes can be infinitesimally close to the thin slab, but because of uniqueness problems, discussed below, the current-carrying elements of the thin slab cannot penetrate through the terminal planes.

Recall that the scattering matrix formulation comes about from applying the uniqueness principle to a volume which encloses the entire discontinuity in the waveguide. If a portion of the discontinuity protrudes through the terminal plane, then the incoming harmonic on the terminal plane is no longer due only to the known incident field, it is also due to the unknown scattered field from the currents on the protrusion. The incoming scattered field is dependent on the geometry internal and external to the volume and the incident field. The traditional scattering matrix catalogues the outgoing waves in terms of a known incoming wave. If the incoming wave is itself unknown and dependent on the geometry of the scatterer, then the scattering matrix cannot be defined. The scattering matrix representation, therefore, fails when a discontinuity penetrates the terminal plane.

Because the terminal planes must enclose the entire current-carrying structure of the thin slab, the current traveling normal to the terminal planes must go to zero before it reaches the terminal plane. This is contrary to what physically happens in a continuous structure where the currents would flow continuously through the mathematical surface formed by the terminal planes. The terminal planes behave as if they cut the slab physically. An example will clarify the issue.

A wave TE to the strip axis is incident on the array of strips, shown in Figure 5.12, whose unit cell is composed of one strip rotated 90° out of the plane of periodicity. The propagation vector of the incident wave makes an angle of 45° with respect to the slab normal. The strips have a resistance of 100Ω . Since the current due to the TE field flows along the thickness direction of the slab, this is the situation in which the S matrix will not work. A thin slab, 0.4λ thick, is solved by the method of moments and the scattering matrix is formed. This S matrix is cascaded 10 times in the manner described above to obtain the S matrix of a structure 4.0λ thick. The reflection coefficient found for this problem is compared to the reflection coefficient for two different problems. The first problem is a 4.0λ thick slab whose unit cell is composed of 10 separate strips, infinitesimally close to each other and each 0.4λ long. The relative error between the cascaded problem and this problem is plotted as a function of number of harmonics retained in the S matrix in Figure 5.13. As the number of harmonics increases, the cascaded reflection coefficient converges to that for the separated strip problem. The second problem is a 4.0λ thick slab whose unit cell is composed of a single strip. The relative error between the reflection coefficient for this problem and that for the cascaded reflection coefficient is shown in Figure 5.14. As the number of harmonics increases, the

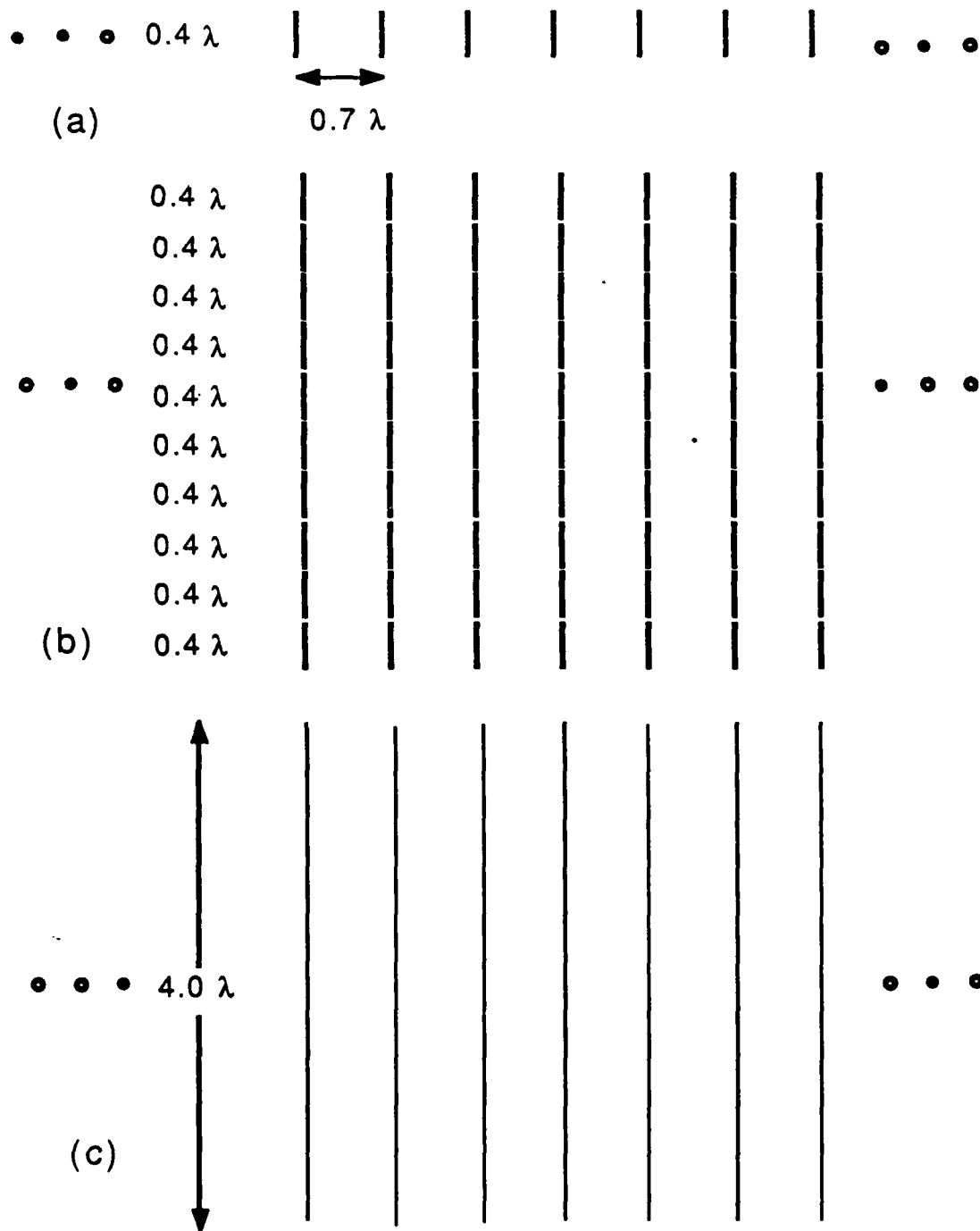


Figure 5.12 Three different rotated strip geometries to be compared. Strips with $R = 100 \Omega$ are rotated 90° out of the plane of periodicity. (a) shows the characteristics of a 0.4λ thick slab which is cascaded 10 times. (b) shows the characteristics of a 4.0λ thick slab made of ten 0.4λ thick slabs. (c) shows the characteristics of a 4.0λ thick slab made of continuous strips. A TE wave is incident on the slab and makes an angle of 45° with the slab normal. The current flows along the thickness of the slab.

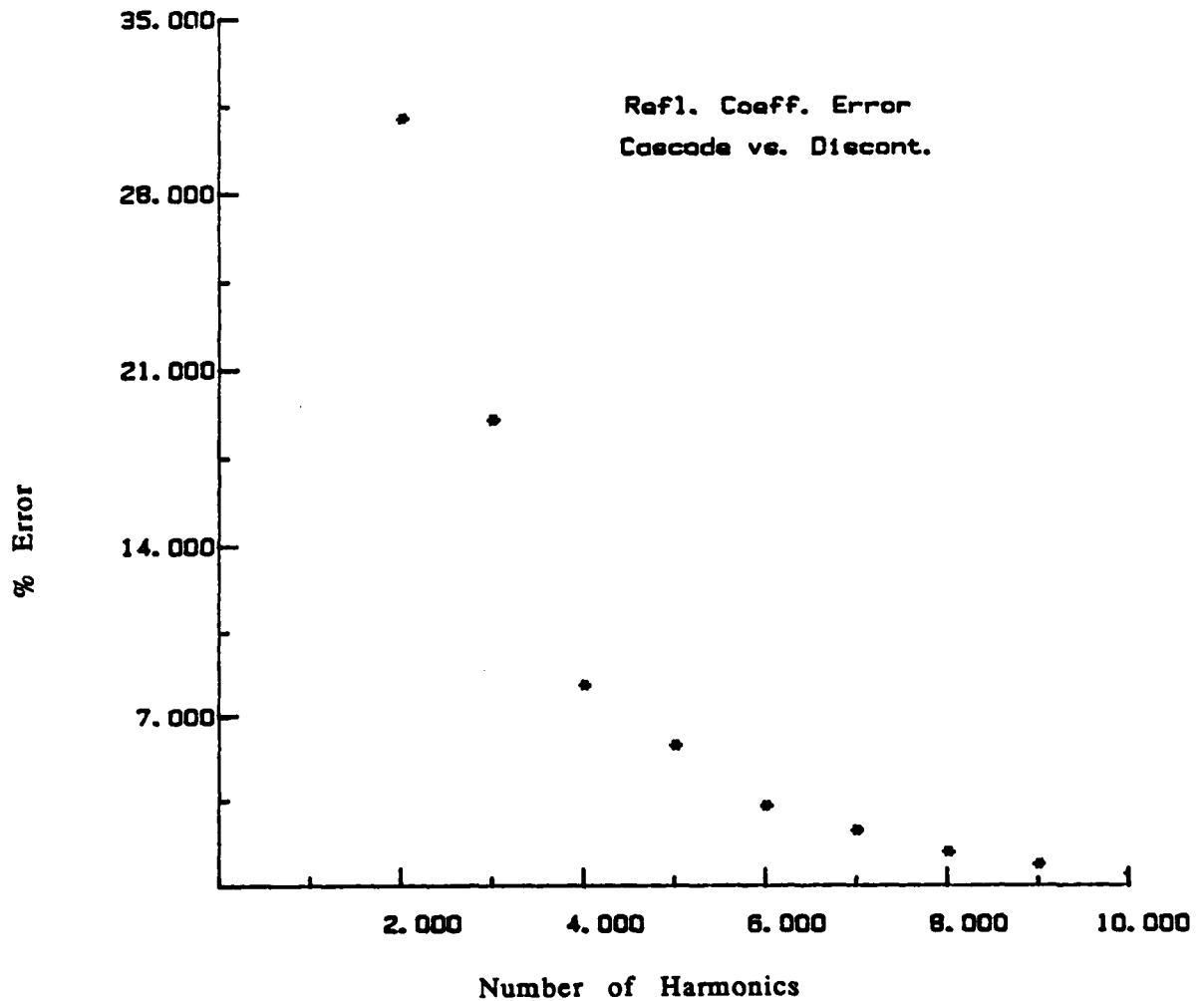


Figure 5.13 Relative error between the reflected TE power calculated by cascading (a) in Figure 5.12 ten times and the reflected TE power calculated for the discontinuous strip geometry of (b) in Figure 5.12. As the number of harmonics retained in the S matrix increases (abscissa), the cascaded result converges to the discontinuous strip result.

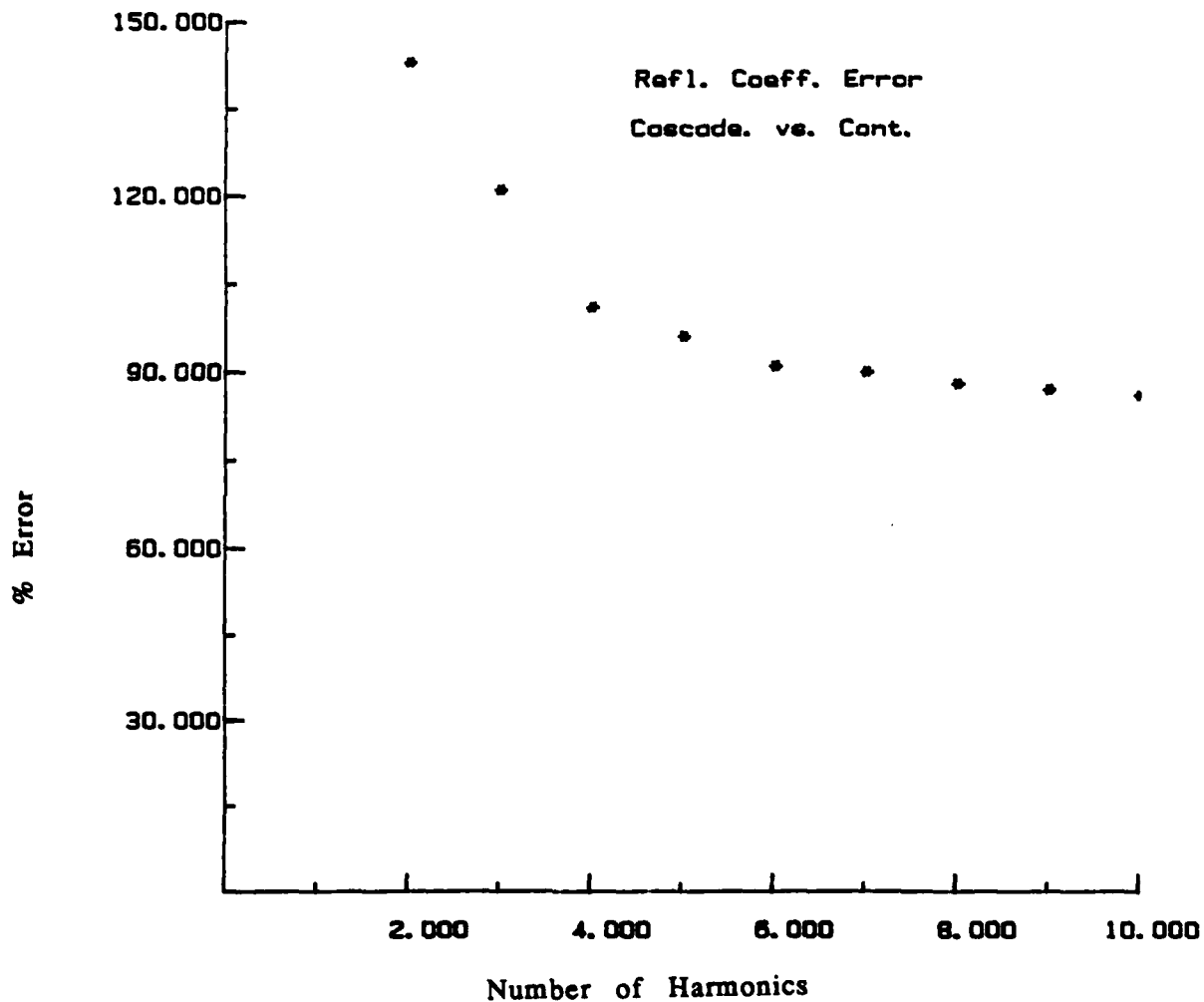


Figure 5.14 Relative error between the reflected TE power calculated by cascading (a) in Figure 5.12 ten times and the reflected TE power calculated for the continuous strip geometry of (c) in Figure 5.12. The cascaded result does not converge to the continuous strip result.

cascaded reflection coefficient converges, but not to the reflection coefficient of the continuous problem. The reflection coefficient is 87% in error.

To get a feel for the level of error involved, consider the following: the reflection coefficient for the continuous case is 0.009348 and for the transmission coefficient is 0.4940. For the discontinuous case, the reflection coefficient is 0.01732 and the transmission coefficient is 0.4888. In terms of relative error, the reflection coefficients do not agree, but in terms of absolute error, the coefficients are close. The S matrix has great flexibility in solving different configurations of resistance in the various slabs. If the absolute errors are most important to the reader, then the S matrix could be applied, but it should always be kept in mind what problem the S matrix is really modeling so that no unpleasant surprises occur.

5.3 The Modal Method

5.3.1 Introduction

As seen in the previous section, the S matrix works well for finding the characteristics of a thick slab which is composed of individual, thin slabs that are not physically connected to each other. It fails if the slab is continuous in the thickness dimension. Therefore, in order to model the characteristics of a continuous structure, an alternative method must be applied.

Deep within a thick, continuous slab, the fields exhibit a behavior that is unaffected by the presence of the slab interfaces. This behavior can be described in terms of a small number of modes of the structure. In the modal method, the structured slab of Chapter 4 is treated as if it were an infinite array of lossy, finite-length waveguides. First, the propagation constants of the modes are found for an array of lossy, infinite-length

waveguides having the same cross section as the finite waveguides. Next, the forms of the modes corresponding to each propagation constant are calculated. Finally, to find the coefficients of each of the modes, a mode-matching procedure is applied which enforces the continuity of the tangential \vec{E} and \vec{H} fields across the mouth of the guide.

The big advantage of the modal method is that once the coefficients, propagation constants and forms of the modes are known, the behavior of the field at any depth within the slab can be predicted with little additional calculation. The waveguide model is continuous in length so the current continuity problems faced by the S matrix method do not occur. Another attractive feature is that, since the structure in which the modes are found is infinite in length, the unknown surface current flowing on the waveguide walls needs to be discretized only around the circumference of the waveguide, not along the length of the waveguide. This reduces the number of unknowns needed to solve a typical waveguide problem to be on the same order as the number of unknowns needed to solve the strip problems discussed in Chapter 3.

The main disadvantage of this method is that virtually everything in this procedure, from determining the propagation constants to mode matching, must be done numerically. This makes the process costly in terms of computer time. As the loss in the structure increases, the propagation constants become more difficult to find and it is questionable if the modes even exist. It was hoped, however, that the loss in the structure would reduce the number of higher-order modes that exist in the guide, thereby mitigating the additional work needed to find the modes.

A half space filled with lossy, parallel-plate waveguides serves as a simple problem with which to introduce the modal method. Next, propagation constants are found for a one-dimensional array of rectangular waveguides and plotted as a function of wall loss

and angle of incidence. This geometry is closer to that of the honeycomb than is the parallel-plate geometry. Unfortunately, while many calculations for the parallel-plate waveguide could be done analytically, most of the calculations for this problem had to be done numerically.

5.3.2 Parallel-plate waveguide array

The problem geometry for lossy, parallel-plate waveguides that fill a half space is shown in Figure 5.15. Lossy plates that extend from $-\infty$ to $+\infty$ in \hat{z} and from $-\infty$ to 0 in \hat{y} are repeated periodically along the \hat{x} axis. The period of the structure is b meters. A plane wave having a propagation vector lying in the xy plane and making an angle of θ_i with respect to \hat{y} is incident on the structure. The incident wave is either TE or TM to \hat{z} . This problem has been done in the past by Lewis [37] and Hall [61] and is included here to demonstrate the modal method and show the steps which simplify the calculations due to the special geometry of the problem.

The first step of the mode-matching procedure is to find the propagation constants of the modes in an array of infinite, parallel-plate waveguides having wall loss which is modeled by the resistive boundary condition. It is assumed that the mode has a functional variation in the \hat{y} direction of $e^{-j\gamma y}$, where γ is the unknown which must be found. If this were a lossless problem, the form of the modes in a given waveguide would be known. A phase shift due to the incident field would then be imposed on these modes from guide-to-guide so that the continuity conditions of the \vec{E} and \vec{H} fields need to be applied only at the mouth of one guide. In the lossy case, the forms of the modes are unknown. The phase shift from cell-to-cell must be imposed prior to the solution of the modal propagation constants so that the fields that are eventually found will have the proper phase shift across the face of the slab. This makes the modal propagation constants dependent on the propagation constants of the incident field.

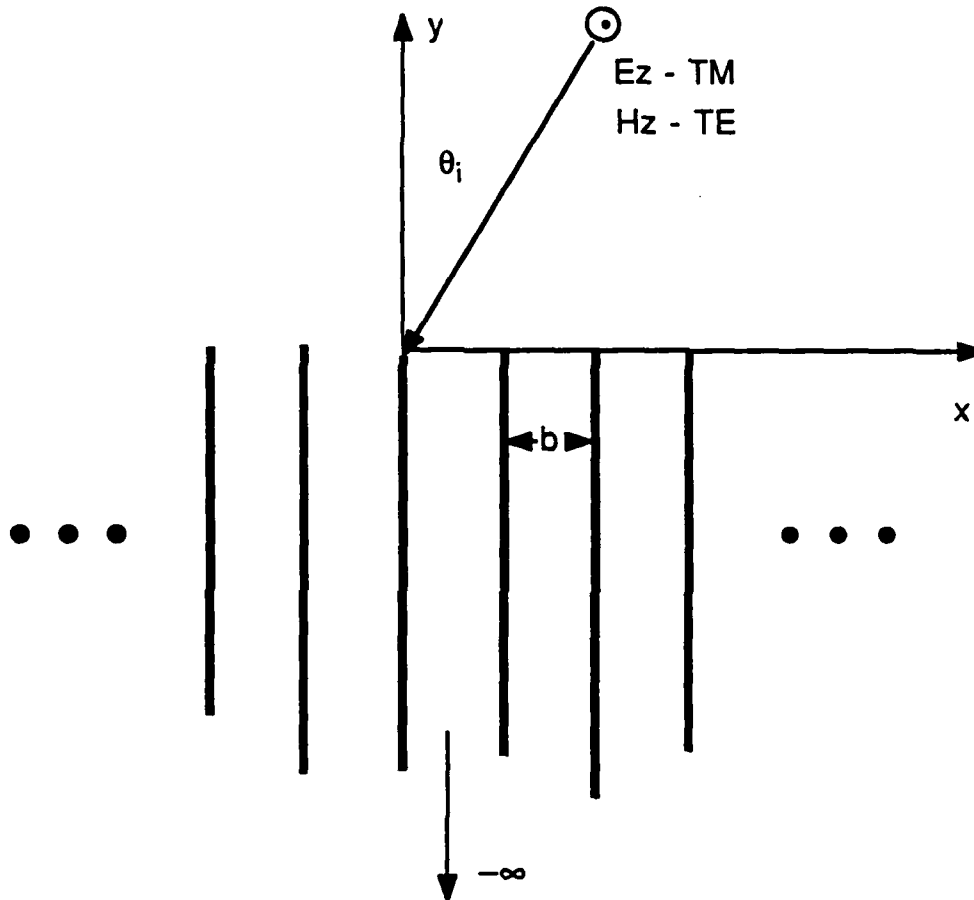


Figure 5.15 Geometry for an array of lossy parallel-plate waveguides which fill the half space $y < 0$. The propagation vector of the incident wave lies in the xy plane and makes an angle of θ_i with respect to \hat{y} . The wave is polarized TE or TM to \hat{z} .

When the incident field is polarized TM to \hat{z} , the E field and the current on the sheets are directed entirely in the \hat{z} direction. The total E field component (E_z^{tot}) can be related to the incident (E_z^{inc}) and the scattered (E_z^{scat}) fields by the equation

$$E_z^{tot} = E_z^{inc} + E_z^{scat} \quad (5.9)$$

E_z^{inc} is zero in this case because modes are the solution to the sourceless problem. By applying the resistive boundary condition to the wall at $x=0$, $E_z^{tot} = RJ_z$. E_z^{scat} is the E-field response at the point $x=0$ due to an infinite array of current sheets related to each other by Floquet's theorem.

By applying Floquet's theorem, Equation (5.9) becomes

$$RJ_z = J_z \sum_{m=-\infty}^{\infty} e^{-jk_x mb} G(mb) \quad (5.10)$$

where $k_x = -k_0 \sin \theta_i$ and $G(mb)$ is the E_z response at $x=0$ due to a current sheet of unit magnitude located at $x=mb$. Substituting for $G(mb)$ and cancelling J_z , the following equation is obtained

$$R + \frac{\omega\mu}{2\beta_x} \sum_{m=-\infty}^{\infty} e^{-jk_x mb} e^{\pm j\beta_x mb} = 0 \quad \text{for } m \leq 0 \quad (5.11)$$

where $\beta_x = \sqrt{k_0^2 - \gamma^2}$. Since the waveguide is lossy, both γ and β_x are complex. The signs are chosen so that the radiation condition holds. The summation can be expressed in closed form so Equation (5.11) becomes

$$2R\beta_x + j\omega\mu \frac{\sin\beta_x b}{(\cos\beta_x b - \cos k_x b)} = 0 \quad (5.12)$$

The unknown in Equation (5.12) is the propagation constant, γ , which is contained in the variable β_x and is located in the fourth quadrant of the complex plane. A set of γ 's is

found numerically by a routine such as Muller's method [62] which calculates the roots of a nonlinear equation.

In a similar manner, the equation needed to solve for the propagation constants for the TE incident wave is derived by applying the resistive boundary condition to the \hat{y} component of the E field on the $x=0$ sheet. The result is

$$2R - \frac{\beta_x}{j\omega\epsilon} \frac{\sin\beta_x b}{(\cos\beta_x b - \cos k_x b)} = 0 \quad (5.13)$$

Note that in both Equations (5.12) and (5.13) the propagation constant is a function of wall resistance and the angle of the incident wave as well as the spacing between the sheets.

The next step, after finding a set of γ 's which satisfy Equations (5.12) or (5.13), is to find the form of the modes corresponding to each propagation constant. This can be done, for the TM case, by calculating the E_z field due to all of the current sheets at points in a waveguide. Referring to Figure 5.16, this field is

$$E_z = -\frac{\omega\mu}{2\beta_x} \left[\dots + Ae^{-j\beta_x(2b+x)} + Be^{-j\beta_x(b+x)} + Ce^{-j\beta_x x} \right. \\ \left. + De^{+j\beta_x(x-b)} + Ee^{+j\beta_x(x-2b)} + Fe^{+j\beta_x(x-3b)} + \dots \right] \quad (5.14)$$

Applying Floquet's theorem to relate the current sheets and grouping terms reduce Equation (5.14) to

$$E_z = -C \frac{\omega\mu}{2\beta_x} \left\{ \left[\dots + e^{-j(\beta_x - k_x)2b} + e^{-j(\beta_x - k_x)b} + 1 \right] e^{-j\beta_x x} \right. \\ \left. + \left[e^{+j(\beta_x - k_x)b} + e^{+j(\beta_x - k_x)2b} + \dots \right] e^{+j\beta_x x} \right\} \\ = A^- e^{-j\beta_x x} + A^+ e^{+j\beta_x x} \quad (5.15)$$

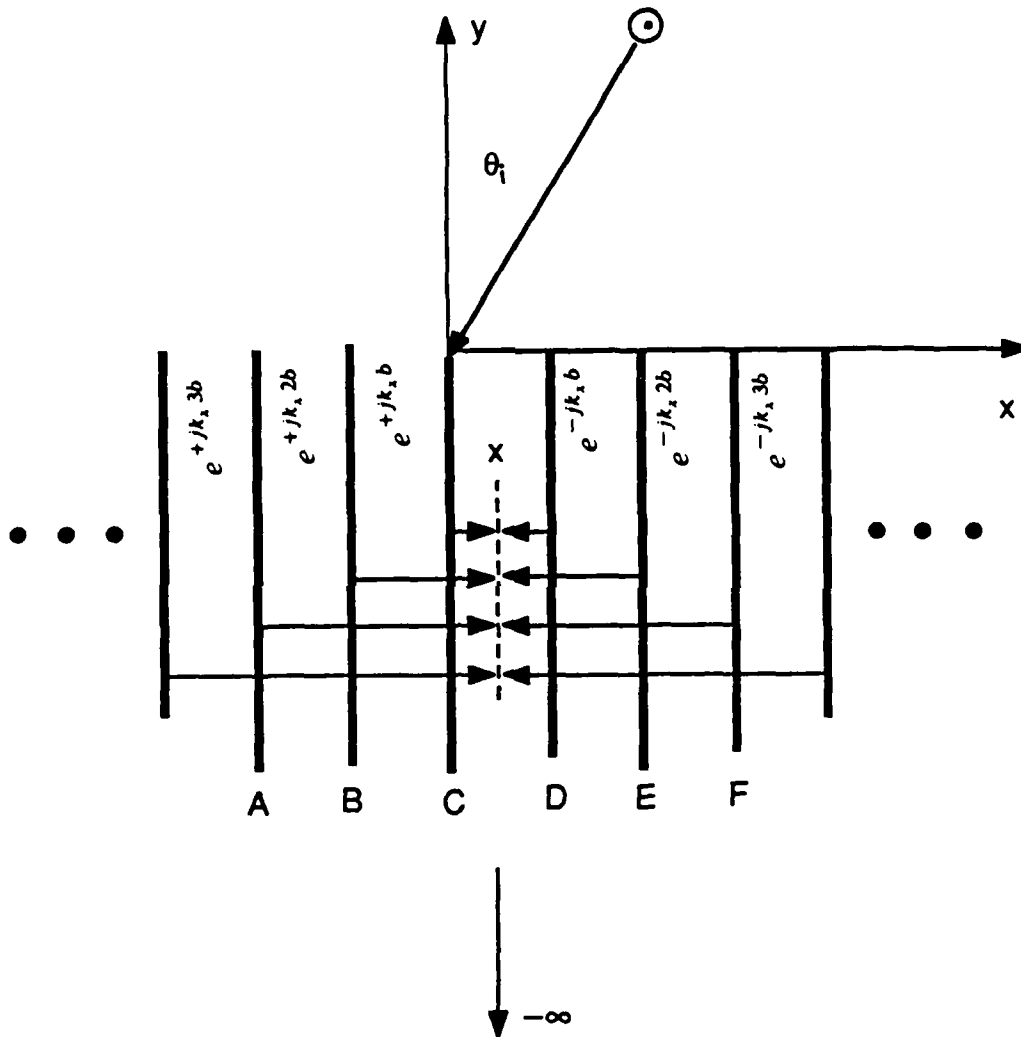


Figure 5.16 Contributions of the current sheets to the E field located at point x in a waveguide. The magnitudes of the current sheets are the same and the phases are related to each other by Floquet's theorem. The field at x can be expressed by two oppositely traveling plane waves.

Equation (5.15) shows that the fields within a waveguide can be expressed simply as two oppositely traveling waves. The relationship between A^+ and A^- can be found by knowing that the E field is continuous across a surface modeled by the resistive boundary condition and invoking Floquet's theorem.

$$E_z(0^+) = E_z(0^-) = E_z(b)e^{+jk_x b}, \quad (5.16)$$

therefore,

$$A^+ = A^- \left[\frac{e^{-j\beta_x b} - e^{-jk_x b}}{e^{-jk_x b} - e^{+j\beta_x b}} \right] \quad (5.17)$$

The actual value of A^+ is unimportant since it is the form of the modes that is being found. The coefficients of the modes are found by mode matching.

The final step — mode matching — is a standard procedure for matching the orthonormal modes of a lossless waveguide to the Floquet harmonics [34]-[36]. If the modes representing the field in one of the regions are not orthogonal to each other, which is the case here in the waveguide region, the procedure must be modified.

The problem is broken into two regions as shown in (a) of Figure 5.17. Region I is the free-space region exterior to the guides and region II is the region within the guides. Consider the solution in region one. A Huygens' surface is introduced at the plane $y=0$ and the fields within region II are set to zero (see (b) in Figure 5.17). Equivalent magnetic ($\vec{K} = \vec{E} \times \hat{n}$) and electric ($\vec{J} = \hat{n} \times \vec{H}$) currents are introduced on the surface to account for the discontinuity of the tangential fields. A PEC is introduced in the zero field region and removed using image theory (see (c) of Figure 5.17). The result is that the PEC shorts out \vec{J} and doubles \vec{K} . The incident field is also imaged. The same technique can be applied to region II with the same type of results. The difference between the two subproblems is that the field radiated by the magnetic current into region I is in terms of

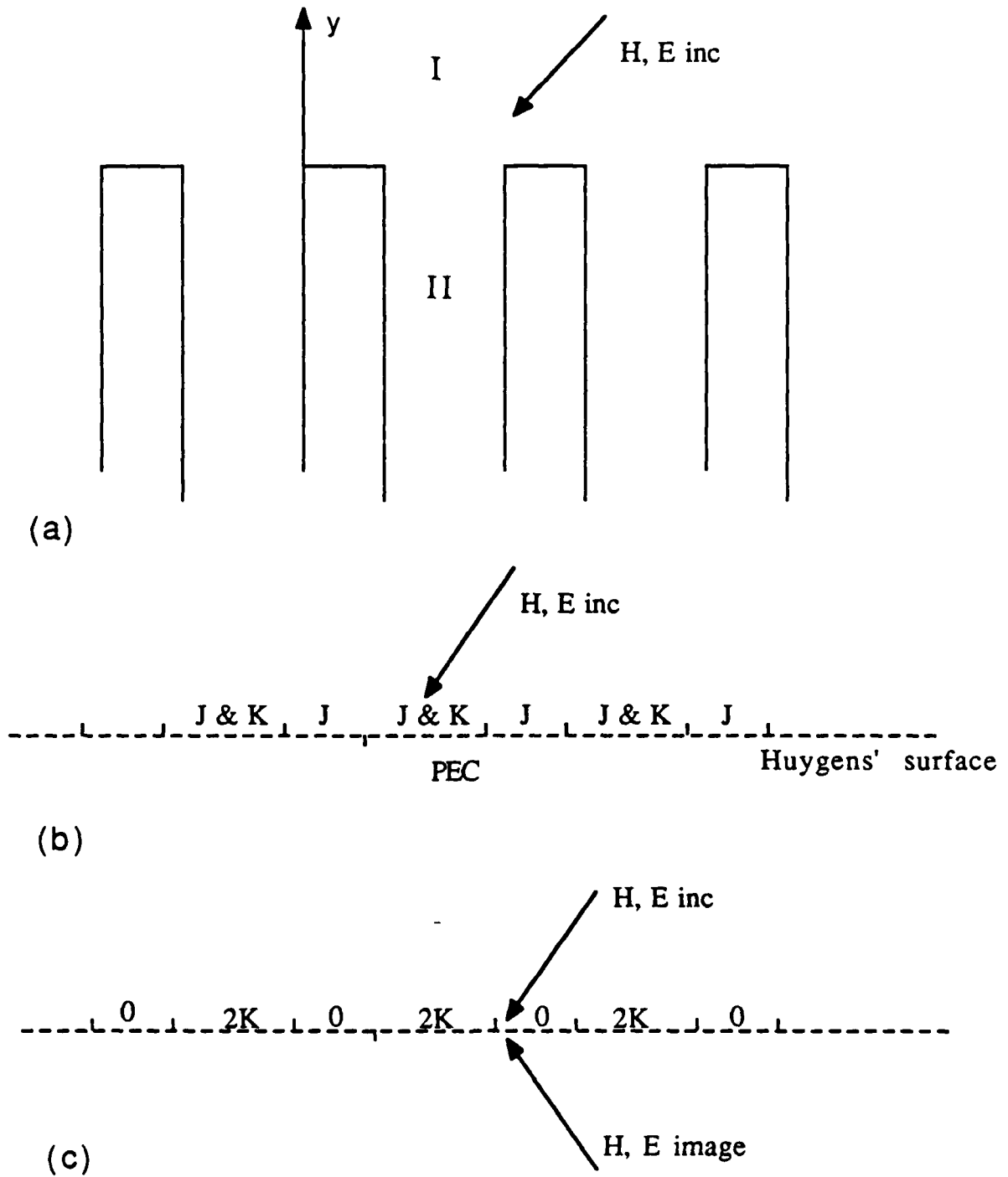


Figure 5.17 The steps needed to mode match. (a) the problem is broken into two regions labeled I and II. In (b) a Huygens' surface is introduced at $y=0$. The fields in region II are set to zero and their effect is modeled by currents on the Huygens' surface. A PEC is introduced in the zero field region. (c) the PEC is removed by image theory.

Floquet harmonics, while the field radiated into region II is in terms of the lossy waveguide modes.

Because the magnetic current radiating into both regions is the same, the continuity of the tangential \vec{E} field across the mouth of the guide has already been accounted for. Continuity of the tangential H field must be imposed numerically.

$$H_I^{inc} = -H_I^{scat} + H_{II}^{scat} \quad (5.18)$$

$$2 \frac{k_y}{\omega\mu} e^{-jk_x z} = \sum_m Y_m^{FL} \frac{K_m^{FL}}{2} \Psi_m^{FL} + \sum_m Y_m^{WG} \frac{K_m^{WG}}{2} \Psi_m^{WG} \quad (5.19)$$

where

$$Y_m^{FL} = \frac{\beta_y}{\omega\mu} \quad \text{and} \quad Y_m^{WG} = \frac{\gamma}{\omega\mu}$$

Y_m^{FL} is the wave admittance in the \hat{y} direction for the m th Floquet harmonic and Y_m^{WG} is the characteristic admittance of the m th waveguide mode. K_m^{FL} and K_m^{WG} are the coefficients of the waves in regions I and II, respectively. The function Ψ_m^{FL} represents the form of the Floquet harmonic while Ψ_m^{WG} represents the form of the waveguide mode.

The coefficient K_m is expressed in terms of the \vec{E} field across the aperture through the use of an inner product. If the field is expressed in terms of a set of modes

$$E = K_1 \Psi_1 + K_2 \Psi_2 + K_3 \Psi_3 + \dots = \langle \vec{K}, \vec{\Psi} \rangle \quad (5.20)$$

where \langle, \rangle denotes an inner product, then the coefficients are

$$\vec{K} = \vec{V}^{-1} E \quad (5.21)$$

where \vec{V} is a matrix with elements $V_{ij} = \langle \Psi_i, \Psi_j \rangle$ and $E_i = \langle \Psi_i, E \rangle$. \vec{V} accounts for the fact the the modes are independent but not orthonormal. If the modes are orthonormal, then \vec{V} becomes the identity matrix. Substituting Equation (5.21) into (5.19), the following integral equation results with the aperture E field as the unknown.

$$2 \frac{k_y}{\omega \mu} e^{-jk_x x} = \sum_m Y_m^{FL} \vec{V}_{FL}^{-1} \langle \Psi_m^{FL}, E \rangle \Psi_m^{FL} + \sum_m Y_m^{WG} \vec{V}_{WG}^{-1} \langle \Psi_m^{WG}, E \rangle \Psi_m^{WG} \quad (5.22)$$

The left-hand side of the above equation represents the incident H field. The first term on the right-hand side represents the coupling of H into the free-space Floquet harmonics while the second term represents the coupling of H into the waveguide modes.

If the above integral equation is solved by expanding the unknown aperture E field in basis functions B_l and testing the resulting equation with T_k , the following matrix equation results:

$$2 \frac{k_y}{\omega \mu} \int T_k(x) e^{-jk_x x} dx = \sum_l a_l \quad (5.23)$$

$$\left[\sum_m Y_m^{FL} \vec{V}_{FL}^{-1} \langle \Psi_m^{FL}, B_l \rangle \langle \Psi_m^{FL}, T_k \rangle + \sum_m Y_m^{WG} \vec{V}_{WG}^{-1} \langle \Psi_m^{WG}, B_l \rangle \langle \Psi_m^{WG}, T_k \rangle \right]$$

The basis and the testing functions may be any reasonable function, but often they are the Floquet harmonics or the modes of the waveguide. In the examples shown in this section, they are the modes that exist in the waveguide region.

Figure 5.18 shows what happens when one of the important modes is missed by Muller's method. The problem is solved in two ways: mode matching in the manner described above and solving a strip problem using the methods discussed in Chapter 3. The strips are rotated 90° with respect to the plane of periodicity and form a truncated parallel-plate structure, 4.0λ thick. Numerical experimentation shows that for this geometry, the back edge of the structure does not affect the fields in the aperture region; the fields behave as if the structure fills the entire half space. The plates are spaced 0.8λ apart and have a loss of 100Ω . A TM wave is incident on the structure at an angle of $\theta_i = 2^\circ$. The magnitude of the E_z field is plotted as a function of distance across the waveguide for various depths within the structure. The modal method does not model the fields correctly, especially the fields in the aperture.

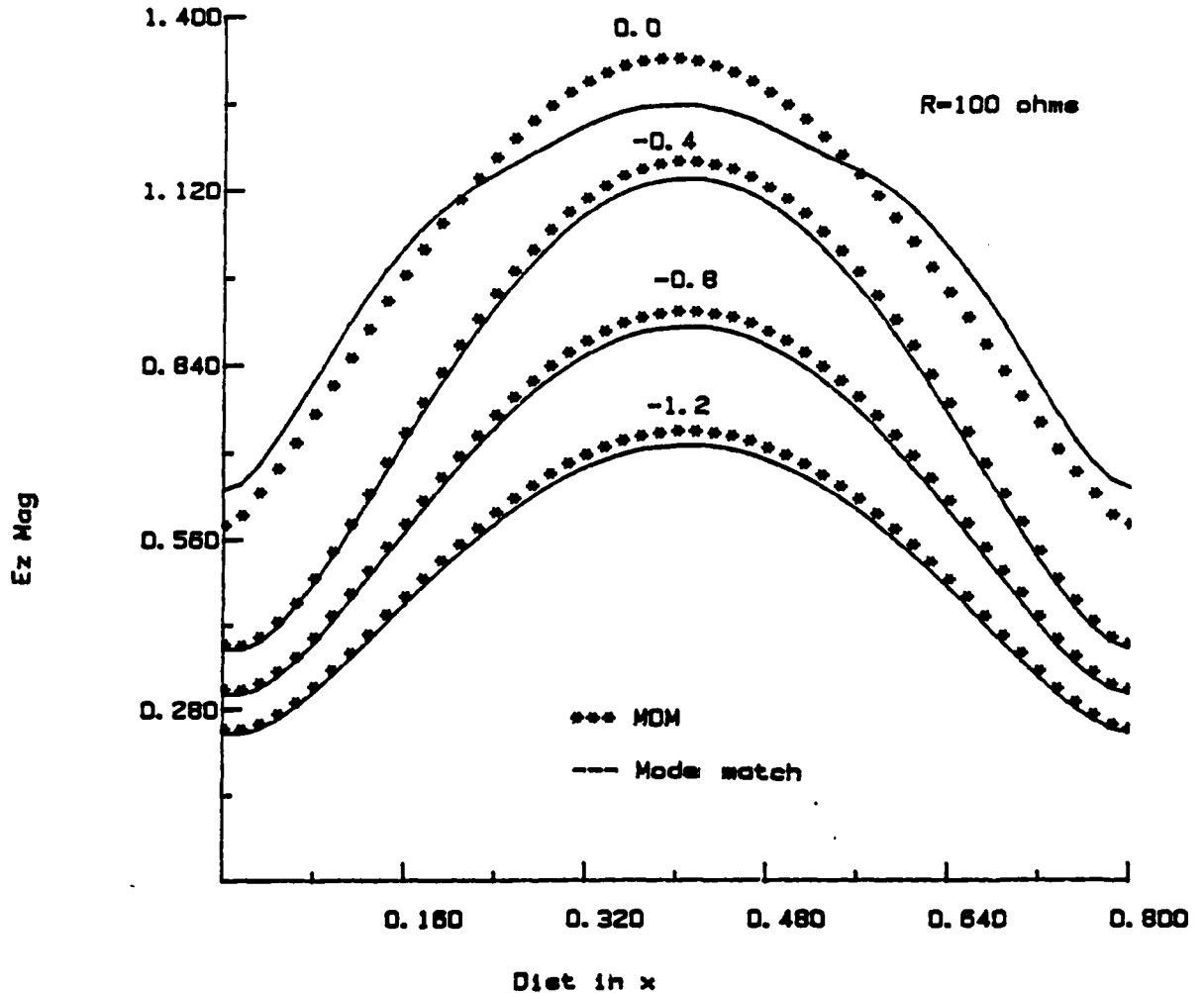


Figure 5.18 Missing an important mode in a mode-matching solution causes errors in the aperture field. A TM polarized wave is normally incident on a lossy parallel-plate array. $R = 100 \Omega$ and the plates are spaced 0.8λ apart. The E_z field is plotted as a function of distance across the waveguide for various depths into the structure. The mode matching solution is compared to a method of moments solution for a strip structure that was 4.0λ thick. The geometry is such that this appears like an infinitely thick slab.

The method used to find the propagation constants applies Muller's method to the lossless guides where the propagation constants are known, then gradually increases the wall loss and tracks the propagation constants as they slowly move in the complex plane. The propagation constants found for the previous loss value are input as the guesses for the present loss value. The problem is that occasionally the values of the propagation constants will change rapidly as the resistance is increased in a certain range. This is where Muller's method loses track of some of the modes.

Figure 5.19 shows that the fields within a lossy structure can be modeled as well by two waveguide modes as with 20 waveguide modes as long as the two modes chosen are the important modes of the waveguide. The E_x field is plotted over the aperture of a waveguide. A TE wave is incident at $\theta_i = 45^\circ$ on an array of lossy plates spaced 0.7λ apart and having a loss of $100\ \Omega$.

Note that in all the steps above, the only numerical work done was when Muller's method was used to find the propagation constants and when the matrices generated by the mode matching process were solved. The remainder of the steps could be done analytically. The sheets comprise a separable geometry so the currents on the sheets do not have to be discretized; one unknown describes the currents on all of the sheets. Because the infinite summation in Equation (5.11) reduces to closed form, a simple equation is entered into Muller's method. Once the propagation constants are found, the form of the modes can be simply described as a sum of two traveling waves. Because all the forms of the modes are known, the inner products needed for mode matching can be calculated analytically. The mode matching consists of multiplications and inversions of known matrices. Contrast this computation to what is needed to solve a one-dimensional array of rectangular waveguides.

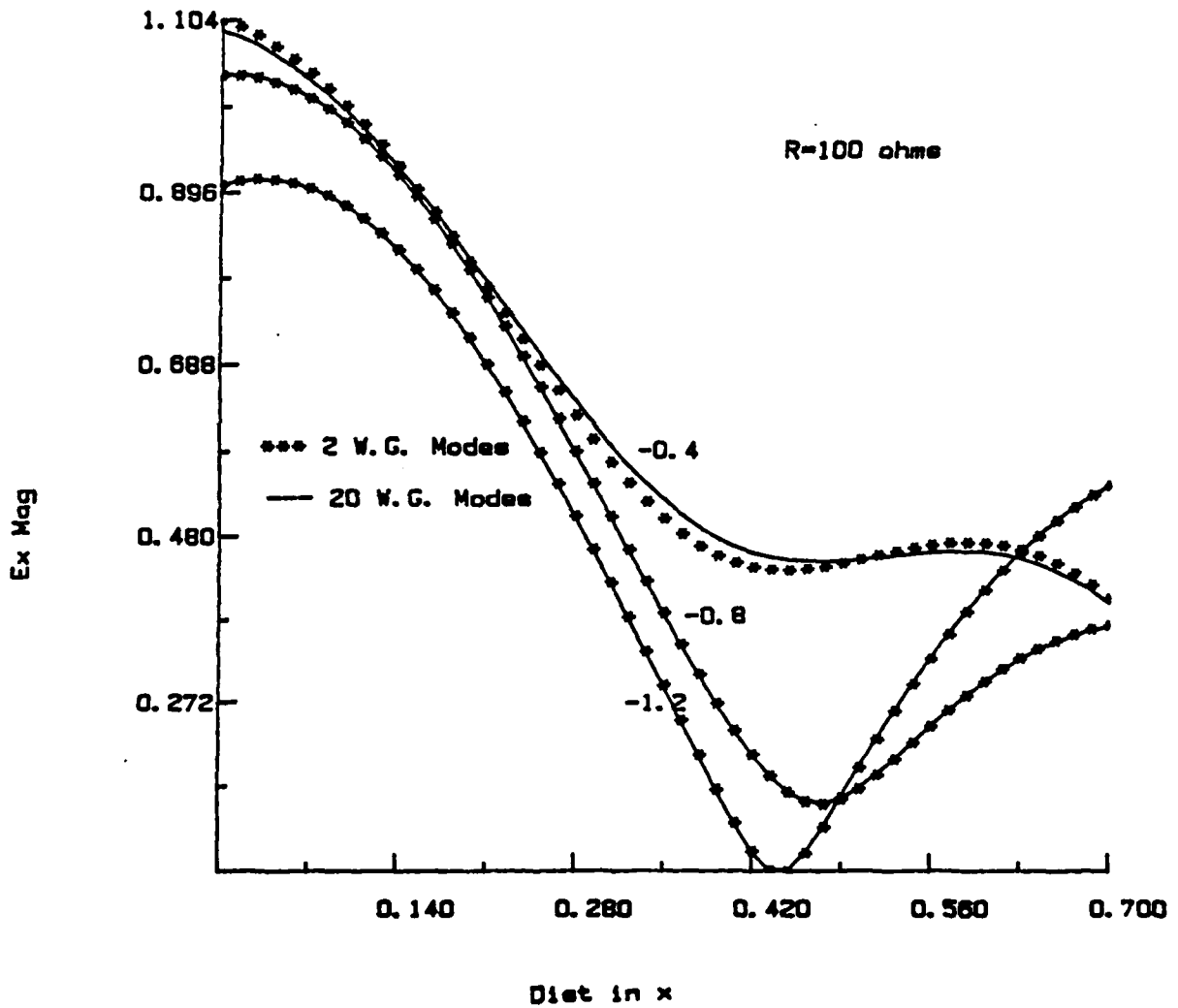


Figure 5.19 A figure showing that within the waveguide two modes model the fields adequately. The E_x field is plotted as a function of distance across the waveguide at various depths within the structure. $R = 100 \Omega$ and $b = 0.7 \lambda$. A TE wave is incident on the structure with $\theta = 45^\circ$. Within the guide, two modes model the fields as adequately as 20 modes.

5.3.3 One-dimensional array of rectangular waveguides

In this section, the one-dimensional array of rectangular waveguides shown in (a) of Figure 5.20 will be considered. Since this geometry is nonseparable, the method of moments must be used to discretize the unit cell shown in (b) of Figure 5.20. The equations that arise in the course of solving this problem are the same as those that arise in the problem of oblique scattering from a strip array solved previously in Chapter 3 with the following differences. The incident field is zero because modes of the structure are being sought. Consequently, the propagation constant along the waveguide is no longer a real number (k_z) set by the incident wave. The propagation constant is now the unknown of the problem and, since the walls of the guides are lossy, it is complex.

The equations needed for the lossy waveguide array are Equations (3.18a) and (3.18b) with the incident field set equal to zero. The quantity κ , which is part of the argument of the periodic Green's function and is defined in Equation (3.7b), is redefined as

$$\kappa = \sqrt{k_0^2 - \gamma^2} \quad (5.24)$$

κ is complex and represents the transverse wavenumber of the waveguide. It is chosen in the fourth quadrant of the complex plane to satisfy the radiation condition. The currents are discretized in the same manner as in Chapter 3 to form an impedance matrix.

The matrix equation formed by the procedure above is homogeneous. It has a non-trivial solution only if the determinant of the impedance matrix equals zero. In order to find the values of γ that correspond to modal propagation constants, a guess is made for γ , the impedance matrix is filled and the determinant of the matrix is calculated. This process is repeated until a value for γ is found which causes the absolute value of the

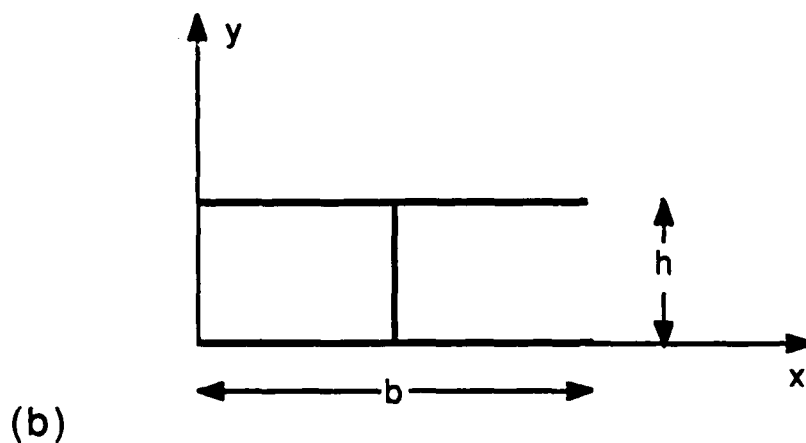
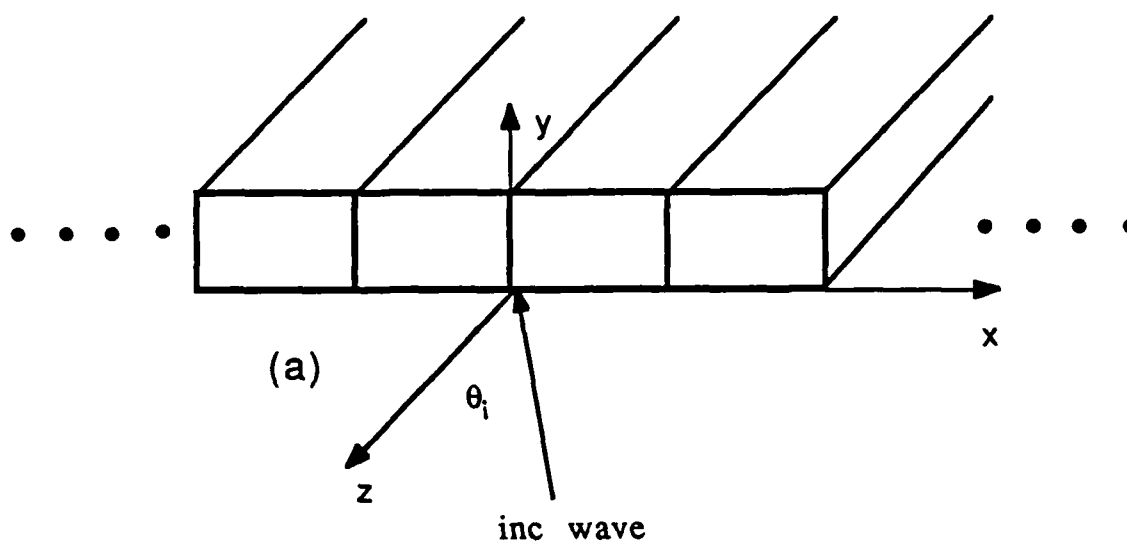


Figure 5.20 (a) Geometry for the array of rectangular waveguides. The propagation vector of the incident wave lies in the xz plane and makes an angle of θ_i with respect to \hat{z} . The array is composed of the unit cell shown in (b). The unit cell is composed of resistive strips joined to each other and to neighboring cells.

determinant to be a minimum. This γ is the modal propagation constant [53],[63]. The determinant will not go precisely to zero because the set of basis functions in this case is not complete on the domain of the operations performed on them. When the guide is lossless, the propagation constants are either purely real (propagating mode) or purely imaginary (evanescent mode). Therefore, the search for γ can take place along the real or imaginary axis. As loss is added to the waveguide walls, however, the search must be conducted over the complex plane.

Searching for the mode is more complicated in this case than it was for the parallel-plate case. In this case, many unknowns are needed to describe the current on the walls of the waveguide, while in the parallel-plate case only one unknown was needed. This means filling a matrix and finding its determinant rather than solving a simple equation. Also, unlike the parallel-plate case, the summations needed to fill the matrix cannot be expressed in closed form.

The form of the wall current corresponding to a given modal propagation constant is found numerically. First the impedance matrix for the propagation constant is filled. Then the eigenvectors of the impedance matrix are found using a numerical method. The eigenvector corresponding to the eigenvalue with the smallest modulus gives the coefficients of the basis functions corresponding to the wall currents for the mode.

The wall currents are substituted back into Equations (3.18a) and (3.18b) to obtain the form of the modal fields at discrete points across the waveguide. A separate integration around the waveguide wall must be done for every point and for every field component desired. In order to mode match, two tangential components of the \vec{E} and \vec{H} fields are needed at each point. This calculation is also much more intensive than that needed for the parallel-plate waveguide. In that case, the form of the field could be calculated by substituting the propagation constants in a simple equation.

Mode matching in the rectangular guide array must be done numerically. The values of the field components at the points across the waveguide aperture must be stored in vectors. The inner products of Equation (5.19), which could be performed analytically in the parallel-plate case, are performed numerically in this case. Because of the numerical intensity and numerical problems which will be discussed below, the modal method was dropped as being unpractical.

For all the results, the dimensions of a single guide in the array were $h = 0.25$ m and $b = 0.5$ m. The incident field has a frequency of 5.0×10^8 Hz. Its propagation vector lies in the xz plane and makes an angle of θ_i with respect to \hat{z} . For an array of lossless guides, only the TE_{10} mode propagates with $j\gamma = (0.0, 8.38)$ which can be determined analytically.

Numerically, as shown in Figure 5.21, $j\gamma = (0.0, 8.28)$. Figure 5.21 is a contour plot of the magnitude of the determinant of the impedance matrix versus the real value of $j\gamma$, which is plotted on the abscissa, and the imaginary value of $j\gamma$, which is plotted on the ordinate. The angle of incidence for this case is 20° . The determinant drops precipitously along the ordinate so the minimum is easy to find in this direction. Along the abscissa, the determinant drops very gradually so the minimum is difficult to find. This form of contour map is characteristic of the problem. Borrowing from the terminology of cartography, the plot of the determinant forms a narrow river valley. It is easy to find the lowest elevation of the valley across its width, but it is difficult to find the lowest elevation along its length.

In Figure 5.22, a wave is normally incident on a lossy waveguide array with a wall resistance of $R = 2.0 \Omega$, while in Figure 5.23, the same field is incident on a waveguide

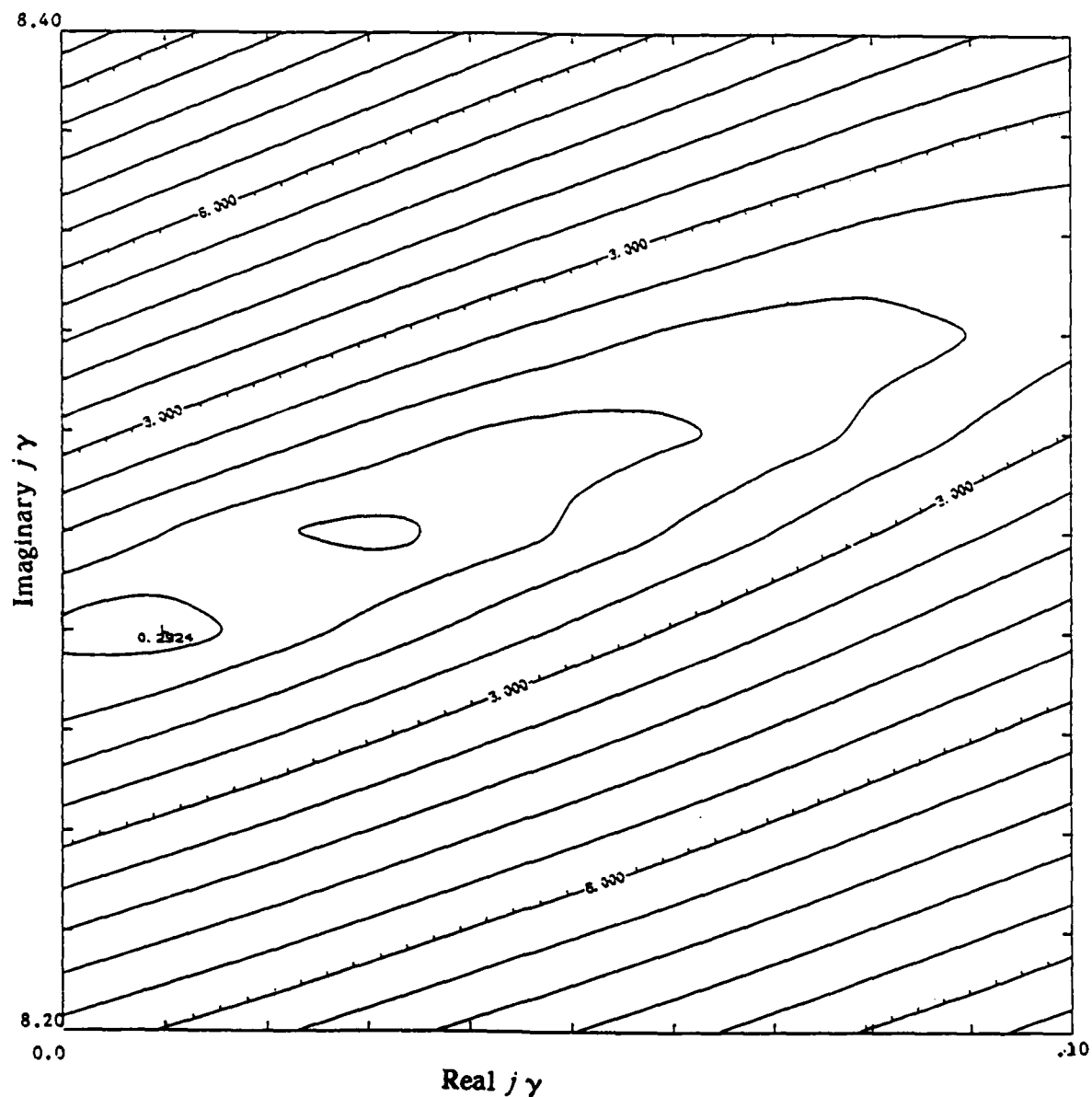


Figure 5.21 Contour map showing the magnitude of the determinant of the impedance matrix plotted versus $j\gamma$ where γ is complex. A wave with frequency 5.0×10^8 Hz is incident at an angle of $\theta_i = 20^\circ$ on a one-dimensional array of lossless rectangular waveguides. The waveguides are dimensioned $b = 0.5$ m and $h = 0.25$ m. The waveguide is discretized with four cells in b and two cells in h . This plot shows that a mode propagates at $j\gamma = (0.0, 8.28)$.

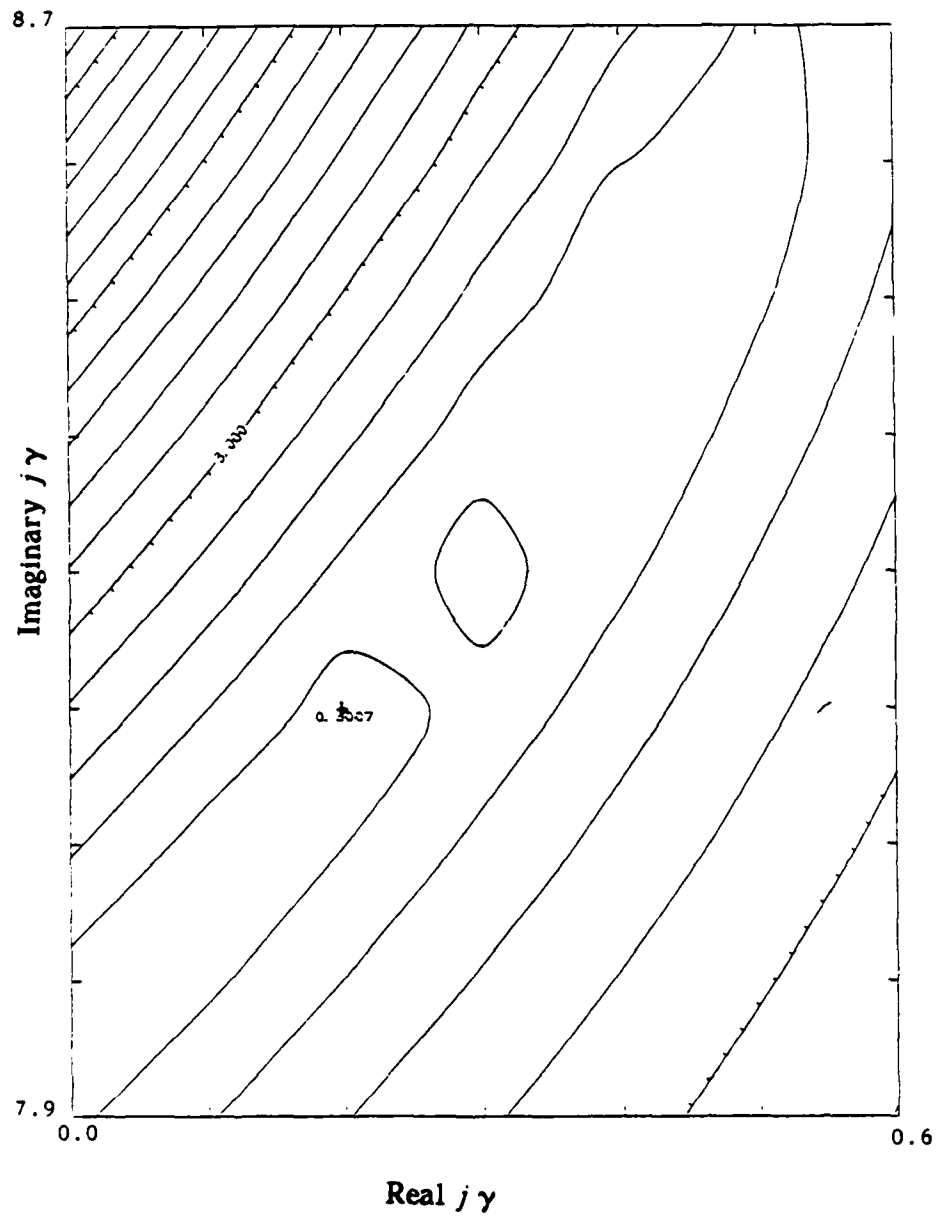


Figure 5.22 Same as Figure 5.21 except $R = 2.0 \Omega$ and $\theta_i = 1^\circ$. The contours are less steep in this case and the determinant minimum has moved to $j\gamma = (0.2, 8.2)$.

array with a wall resistance of $R = 10 \Omega$. The trend is that as R increases, the real and imaginary parts of $j\gamma$ for the minimum of the determinant increase, which means that a mode which is purely propagating in the lossless guide is propagating and attenuating in the lossy guide. Another trend is that the valley becomes wider and does not have as steep sides. This makes the minimum of the determinant even more difficult to find. Note that the error bound on γ in Figure 5.23, which has very little loss, could be as much as ± 0.2 .

Spurious modes are also a problem in this formulation. These modes were found by plotting the magnitude of the determinant for a lossless rectangular waveguide array as a function of real γ for different values of the incident angle. As the angle was varied from $\theta_i = 0^\circ$ to $\theta_i = 60^\circ$, the minimum corresponding to the true mode stayed constant at $j\gamma = (0.0, 8.28)$. A spurious mode appeared when $\theta_i = 10^\circ$ and moved around with increasing θ_i . When the walls are lossy and all the minimums move with changing incident angle, the only way to distinguish between true and spurious modes would be to find the fields associated with all the modes and see which ones do not satisfy the boundary conditions of the problem. These would be the spurious modes. This adds to the already heavy computational burden required by this method.

5.4 Large Basis Functions

5.4.1 Introduction

It would be advantageous if a mathematical model could be found that describes a thick, continuous structure like the modal method does, but whose calculations could be implemented efficiently like the scattering matrix method. The next method does just that; it bypasses the intense numerical calculation needed in the modal method, but

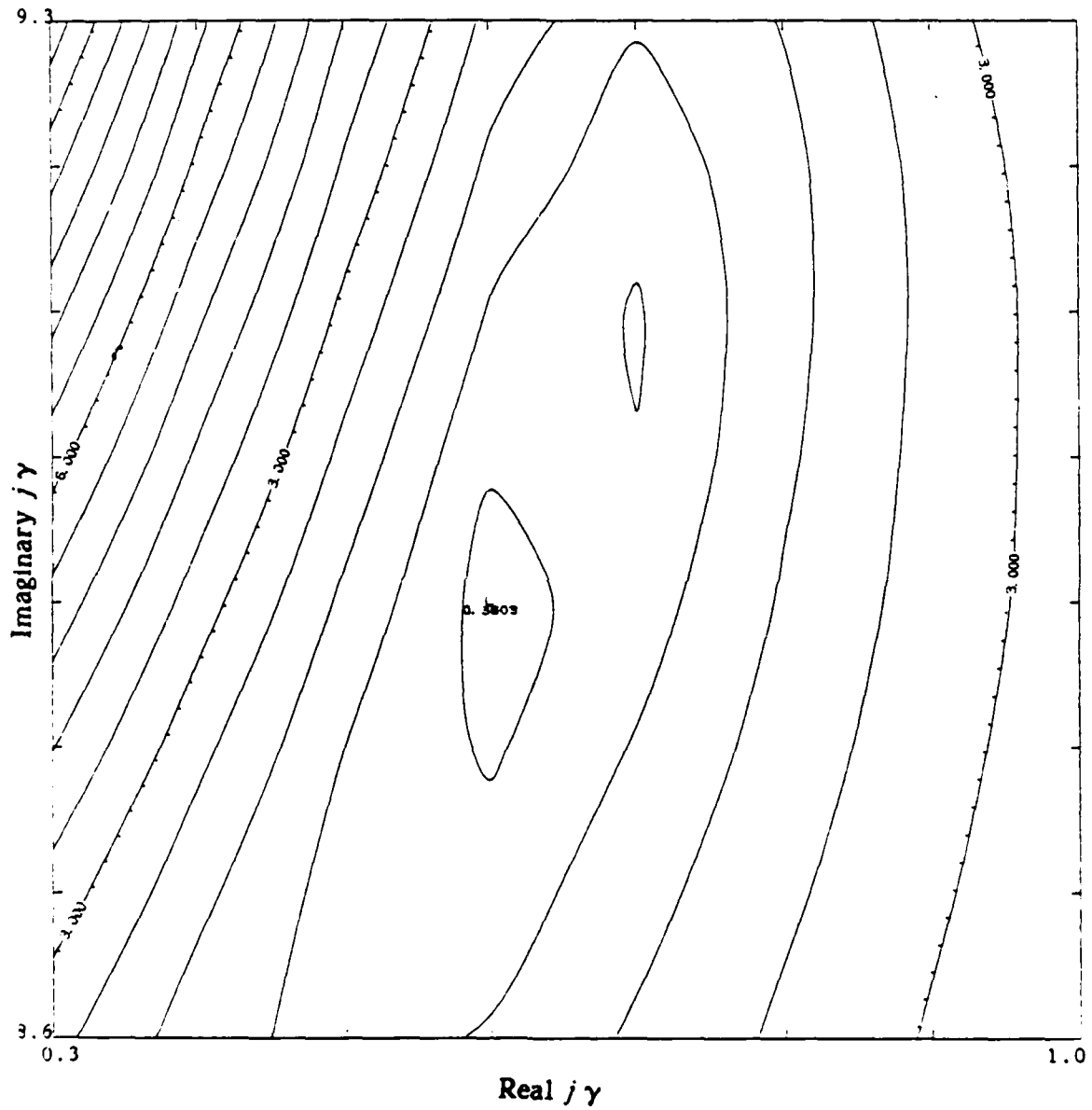


Figure 5.23 Same as Figure 5.22 except $R = 10 \Omega$. The contours have again flattened with respect to the previous cases. The determinant minimum has moved to $j\gamma = (0.6, 8.9)$.

models a continuous structure. In the remaining sections of this chapter, the method is described and results are presented which give some insight into the problem areas and accuracy of the method.

5.4.2 Description of the method

This method consists of applying the method of moments twice to two related problems using two different types of basis functions. First, the current is found for a thin slab using the procedure discussed in Chapter 4. This slab needs to be thick enough so that the current away from the slab interfaces settles down to a steady-state behavior as a function of distance, but at the same time thin enough so that it can be solved using the subdomain basis functions. Next, the current away from the slab interfaces is described in terms of a few simple functions using Prony's method [64]. Finally, the current for a thicker slab is found by the method of moments. Apart from the fact that it is thicker, the thick slab has the same unit cell geometry as the thin slab. The basis functions used in the interior of the thick slab are those functions found by Prony's method. The basis functions near the interface are the subdomain functions used previously. The objective of this method is to minimize the number of basis functions needed to model the interior current by using functions which accurately describe its behavior so that the current on slabs of arbitrary thickness can be found without increasing the required number of basis functions.

Prony's method is a curve-fitting algorithm which was initially used to succinctly represent input data to systems [65],[66]. It was not required, therefore, to have any relationship to the physics of the problem which generated the data. Later, Prony's method was used to extract poles and residues from time domain data [67]-[69], find scattering centers of a body [70], or find the propagation constants from measured data in

periodic structures [71]. In such cases, since physical quantities are being extrapolated from the data, it is essential that the method describes the underlying physics of the data. Prony's method as applied in this thesis also needs to capture the physics of the problem.

Prony's method, if properly applied, will extract the physical modes of a structure which are the same as those found by the modal method [72]. To demonstrate this, the modal method is used to find the modes of the lossy, parallel-plate array shown in Figure 5.15. The plates are spaced 0.7λ apart and have a wall resistance of $R = 0\ \Omega$ or $R = 100\ \Omega$. A plane wave which is TE to \hat{z} has a propagation vector which makes an angle of $\theta_i = 45^\circ$ with respect to \hat{y} . To find the modes via Prony's method, a finite-thickness (2.5λ), parallel-strip problem with the same parameters as the parallel-plate problem is solved by the method of moments. The interior current, which is further away from the slab interface than 0.5λ , is sampled and Prony's method is applied to extract the modes. As seen in Table 5.1 the modes found by the two methods agree with each other for $R = 100\ \Omega$. For the lossless case, the modes can be calculated analytically. Prony's method does not extract the mode $j\gamma_l = (0.0, 4.38)$ because this mode is not excited for this angle of incidence.

The mechanics of Prony's algorithm will not be discussed here since it is well established in the literature [64]-[71]. A particularly clear presentation of the algorithm can be found in [67]. Prony's method expresses a function as a weighted sum of complex exponentials.

$$f(z) = \sum_{l=0}^L A_l e^{j\gamma_l z} \quad (5.25)$$

The above equation has $2L$ unknowns (L residues A_l and L poles γ_l). Therefore, in order to generate the proper number of equations to solve for the unknowns, the function must be sampled at least $2L$ times.

Table 5.1 Comparison of the modes (j, γ_j) extracted analytically and numerically by the modal method and by Prony's method for a parallel-plate waveguide. A TE wave is incident on the geometry of Figure 5.15, in which $\theta_i = 45^\circ$ and $b = 0.7 \lambda$. Calculations were performed by L. Epp [72].

R	Analytical	Prony's Method	Modal method
0 Ω	(0.0, 6.283) (0.0, 4.397)	(0.002, 6.287)	(0.0, 6.283) (0.0, 4.397)
100 Ω		(0.699, 6.044) (0.006, 4.324)	(0.695, 6.044) (0.001, 4.397)

Sampling the current is a crucial step in finding the physical modes of the structure. The central problem is that the number of modes present in the structure is unknown. The user must guess at the number of modes needed before applying Prony's method. If an improper number of modes are postulated, the values of the poles and residues will adjust to give a best fit to the data. This, in turn, causes the representation of the true modes to be corrupted because either not enough functions are present to represent the modes or spurious modes are present which shift the position of the true modes.

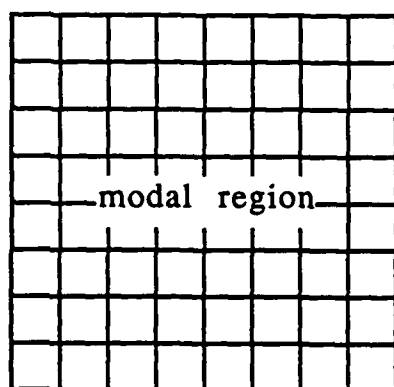
Fortunately, Prony's method is inexpensive to apply in terms of computer time. The practice, therefore, is to postulate a minimum number of modes initially, apply Prony's method, increase the number of modes by one and reapply Prony's method. This process is continued while the values of the poles are observed. Eventually, too many modes will be postulated and a spurious mode results. This mode can be distinguished from the true modes because the magnitude of the residue found by Prony's method for the spurious mode is an order of magnitude less than the magnitudes of the true modes.

Another problem in applying Prony's method is how to determine the sampling density of the current. As stated above, at least twice the number of samples as the number of modes are needed in order for Prony's method to work. At the same time, a Nyquist rate must apply. If a given propagation constant (γ_l) is present in the structure, the current must be sampled at a density at least twice that of the spatial frequency associated with γ_l in order to resolve that frequency. In order to capture the characteristics of the lowest-order mode, the sampling length must be long enough to capture a full wavelength of the mode. Finally, the location of the sampling area within a slab must be such that the higher-order modes excited by the interface do not penetrate

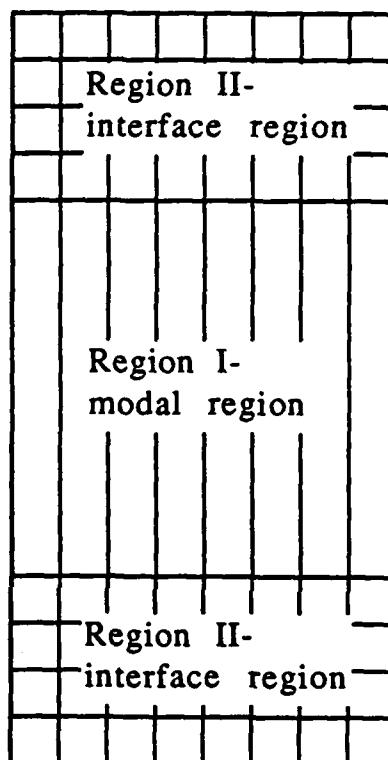
into this region and corrupt the steady-state behavior. Through numerical experimentation, it was found that at least half of a free-space wavelength of guard band needs to be applied at each side of the slab and a full free-space wavelength is required for sampling [73]. The slab thickness, therefore of the original thin problem must be at least two wavelengths in order to apply Prony's method. This can require too many unknowns especially if the unit cell has a complex geometry.

Much experimentation is needed in order to ensure that the poles extracted by Prony's method are true and accurate and can represent the physical process occurring in the interior of the waveguide. The sampling length, density and location can be varied while observing the values of the residues and poles. The true values can be taken as an average of the test values and the inconsistent poles can be eliminated. Prony's method is inaccurate in finding the decay of a function, but a rapidly decaying current does not penetrate far into the thick slab. The reflection coefficient of a thick slab having rapidly decaying current is the same as that for a thin slab because, in both cases, only the front part of the structure interacts with the incident wave.

Once the N values of γ_l and A_l are found, the information contained in the residues is discarded. The modal functions $e^{j\gamma_l z}$ are used as basis functions in the interior of a thicker slab, labeled region I in Figure 5.24, while the current in the interface region, labeled region II, is modeled again by subdomain basis functions. Using a mixture of basis functions to model the current has its precedence in scattering from large bodies in which entire domain basis functions are used to model regions where the current is slowly varying and subdomain basis functions are used to model the regions where the current is rapidly varying [74],[75]. In scattering problems, the use of Prony's method is ill-advised since the edges of the scatterer are the main contributors to the functional form of the



Unit cell of thin slab
subdomain basis functions



Unit cell of thick slab
mixed domain basis functions

Figure 5.24 On the left is shown the unit cell discretization of the thin slab using subdomain basis functions throughout the entire structure. On the right the thick slab discretization is shown. Subdomain basis functions are used in region II and the modal basis functions found from the thin slab problem are used in region I.

current in the center of the scatterer. For the problems in this thesis, it is the waveguide-like geometry of the slab that determines a functional form of the current independent of the slab interfaces. Prony's method, therefore, can be used to generate the interior basis functions.

The \hat{s} directed basis function for region I is shown in (a) of Figure 5.25. The function is a triangle in the \hat{s} direction and has an exponential behavior multiplied by a large pulse in the \hat{z} direction. The testing functions in the \hat{s} and \hat{z} directions are razor functions. As was done in the impedance matrix calculations in previous chapters, the vector potential calculation can be approximated so that the triangular portion of the basis function is replaced by a pulse and the pulse testing function is replaced by a delta function weighted by the support of the pulse. In the scalar potential calculation, one derivative is transferred onto the basis function yielding a pulse doublet in the \hat{s} direction. The other derivative is transferred onto the test function yielding a delta doublet. These approximations are shown in (b) and (c) of Figure 5.25.

The \hat{z} directed basis function for region I is shown in (a) of Figure 5.26. The function is a pulse in the \hat{s} direction and is made of three sections in the \hat{z} direction: a half triangle, followed by an exponential function multiplied by a pulse, followed by another half triangle. This gives the proper continuity and edge behavior to the function. Upon applying the standard approximations to the vector potential, the half triangles are approximated by pulses and the razor testing functions are approximated by delta functions multiplied by the support of the test pulse. In the scalar potential, the derivatives are transferred onto the basis and testing functions to yield calculations involving the response at a point due to pulses or pulses with exponential behavior calculated at a point. These approximations are shown in (b) and (c) of Figure 5.26.

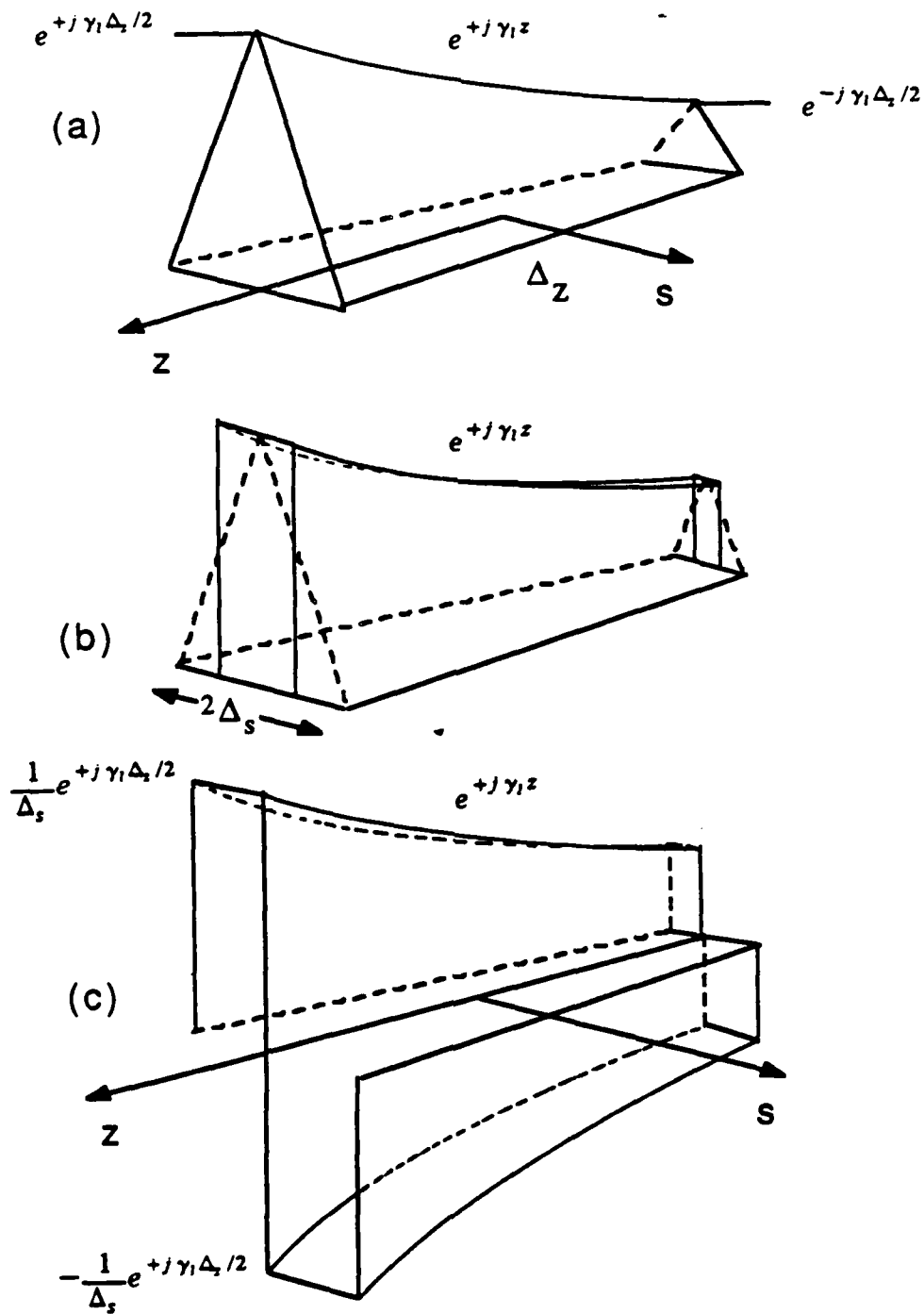


Figure 5.25 (a) The basis function representing J_s . The basis is a triangular function along \hat{s} and a truncated exponential function along \hat{z} . (b) The approximation for the vector potential calculation where the triangle is replaced by a pulse with the same moment. (c) The effect of one derivative in the \hat{s} direction.

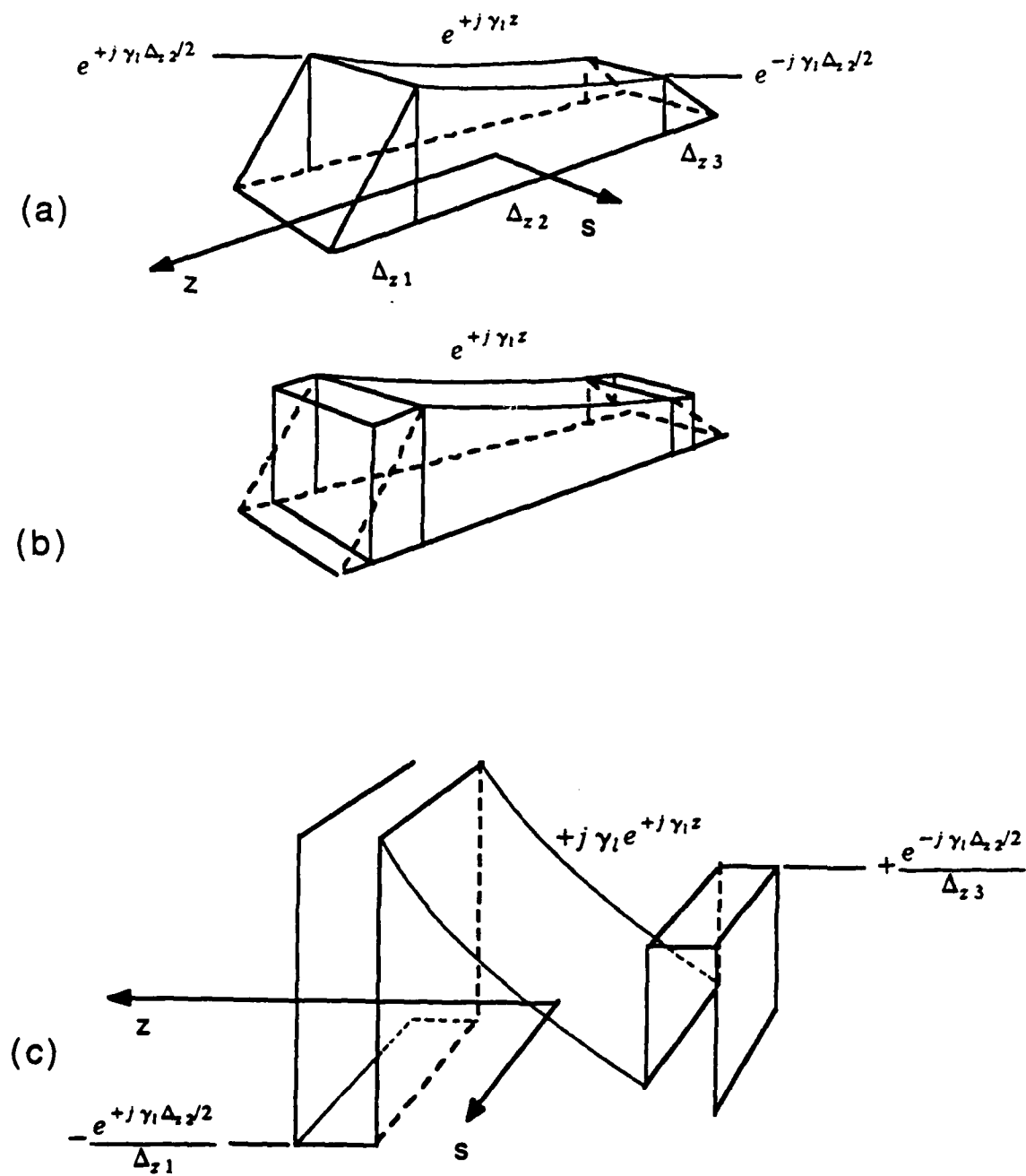


Figure 5.26 (a) The basis function representing J_z . The basis is a pulse function along \hat{s} and a truncated exponential function along \hat{z} . Half triangles are added to the ends of the function to give it the proper continuity. (b) The approximation for the vector potential calculation where the triangles are replaced by pulses with the same moment. (c) The effect of one derivative in the \hat{z} direction.

As seen in the paragraphs above, all impedance matrix calculations for the new modal basis functions involve either the response to two-dimensional pulses evaluated at a point, which has been discussed in Section 2.3, or the response at a point to the exponential pulse shown in Figure 5.27. The pulse is centered at the origin and is dimensioned Δ_x by Δ_z . The pulse is rotated with respect to the \hat{x} axis by the angle θ . The testing point is located at x_o, y_o, z_o . This calculation, which corresponds to Equation (2.63) in the two-dimensional pulse case, is done completely in the spectral domain. If $z_o > +\Delta_z/2$, the result is

$$\frac{1}{C.A.} \left| \begin{array}{c} 1 \\ 2 \end{array} \right| \left| \begin{array}{c} 1 \\ 2 \end{array} \right| \frac{e^{-j\gamma z_o}}{2j\gamma} \left| \frac{e^{+j(\gamma+\gamma_l)\frac{\Delta_z}{2}} - e^{-j(\gamma+\gamma_l)\frac{\Delta_z}{2}}}{j(\gamma+\gamma_l)} \right| \quad (5.26)$$

If $z_o < -\Delta_z/2$, then the result is

$$\frac{1}{C.A.} \left| \begin{array}{c} 1 \\ 2 \end{array} \right| \left| \begin{array}{c} 1 \\ 2 \end{array} \right| \frac{e^{+j\gamma z_o}}{2j\gamma} \left| \frac{e^{+j(\gamma_l-\gamma)\frac{\Delta_z}{2}} - e^{-j(\gamma_l-\gamma)\frac{\Delta_z}{2}}}{j(\gamma_l-\gamma)} \right| \quad (5.27)$$

If the testing point overlaps the basis function in the z direction, i.e., if $z_o < |\Delta_z/2|$, then the result is

$$\frac{1}{C.A.} \left| \begin{array}{c} 1 \\ 2 \end{array} \right| \left| \begin{array}{c} 1 \\ 2 \end{array} \right| \frac{1}{2j\gamma} \left| \frac{e^{-j\gamma z_o} \left[\frac{e^{+j(\gamma+\gamma_l)z_o} - e^{-j(\gamma+\gamma_l)\frac{\Delta_z}{2}}}{j(\gamma+\gamma_l)} \right]}{e^{+j\gamma z_o} \left[\frac{e^{+j(\gamma_l-\gamma)\frac{\Delta_z}{2}} - e^{+j(\gamma_l-\gamma)z_o}}{j(\gamma_l-\gamma)} \right]} \right| \quad (5.28)$$

where

$$\left| \begin{array}{c} 1 \\ 2 \end{array} \right| = \left| \frac{e^{+j(\beta_{xmn} \cos\theta + \beta_{ym} \sin\theta)\frac{\Delta_z}{2}} - e^{-j(\beta_{xmn} \cos\theta + \beta_{ym} \sin\theta)\frac{\Delta_z}{2}}}{j(\beta_{xmn} \cos\theta + \beta_{ym} \sin\theta)} \right|$$

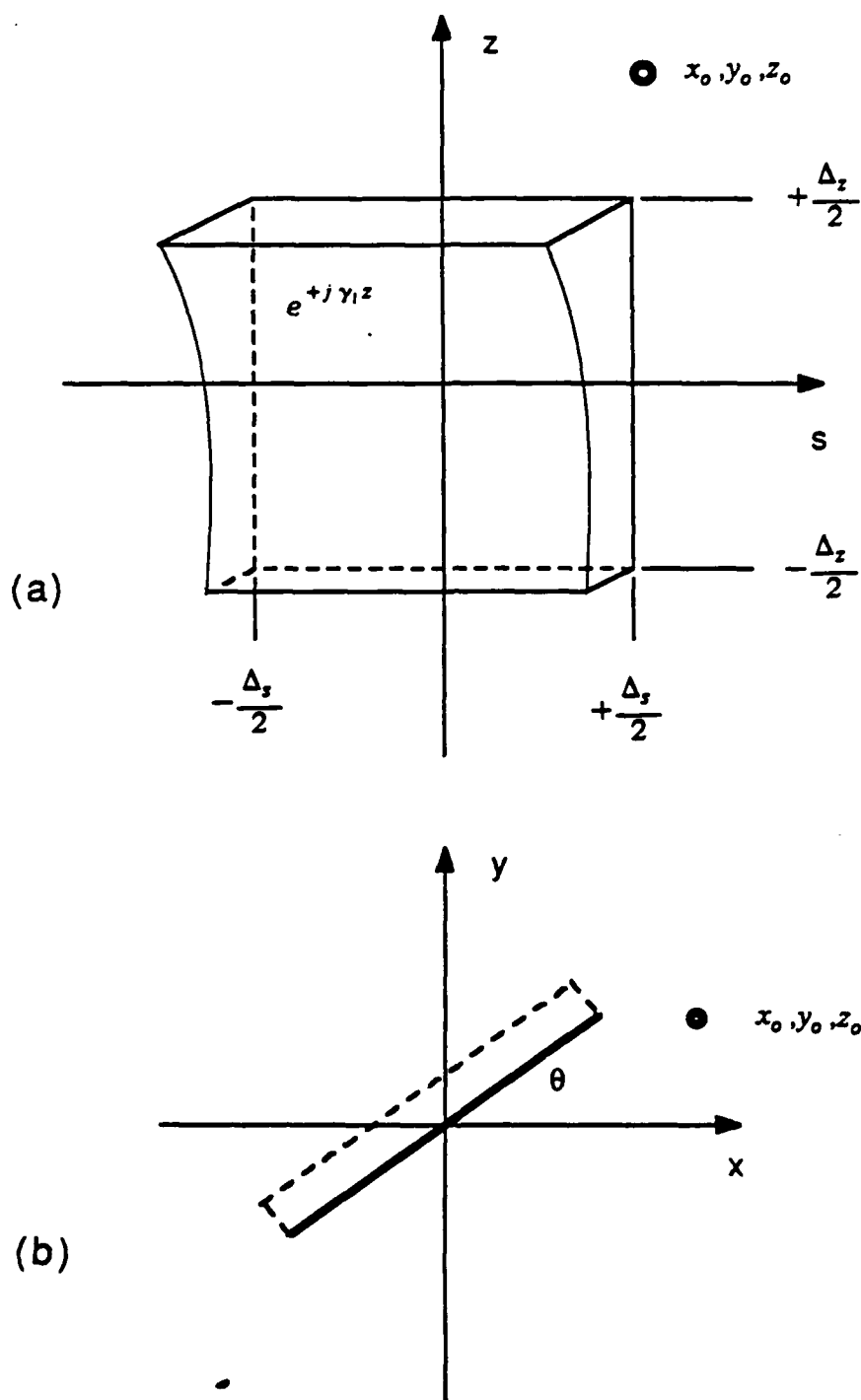


Figure 5.27 The large basis function with pulse behavior along \hat{s} and complex exponential behavior along \hat{z} . The function is dimensioned Δ_z by Δ_s , is centered at the origin and is rotated θ with respect to \hat{x} . The response is tested at the point x_0, y_0, z_0 . (a) shows the pulse from the side while (b) shows the top view.

$$\left[z \right] = e^{+j(\beta_{xmn} x_0 + \beta_{ym} y_0)}$$

C.A. denotes the area of the unit cell and β_{xmn} , β_{ym} , and γ are defined in Equation (2.57).

5.4.3 Results

In all of the results shown below, the magnitude of the surface current is plotted as a function of distance through the thickness dimension of the slab. The currents found by the method discussed in the previous section are compared to those currents found by using subdomain basis functions throughout the depth of the structure as discussed in Chapter 4. These results provide justification for using the interior current behavior of a thin slab to solve a thicker slab.

Figure 5.28 shows the magnitude of the \hat{z} directed current as a function of z for the slab shown in Figure 4.7. The plate that composes the unit cell is lossless and is dimensioned 0.2λ in \hat{x} by 4.0λ in \hat{z} . The plates are joined between the unit cells to form strips which are separated by 0.3λ . The incident plane wave is TM to \hat{z} . The propagation vector of the incident wave makes an angle of $\theta_i = 45^\circ$ with respect to \hat{z} and $\phi_i = 89.9^\circ$ with respect to \hat{x} . Figure 5.29 shows the magnitude of the \hat{s} directed current for this problem. Since the plates are joined to form strips and the incident field is nearly normal to the strip axis, the component of the \hat{s} directed current is much smaller than that for the \hat{z} component.

Prony's method extracted two modes from the solution of a 2.0λ slab. For the \hat{z} directed current, these modes were $j\gamma_l = (0.0, +6.39)$ and $j\gamma_l = (0.0, -6.35)$; for the \hat{s} current, the modes were $j\gamma_l = (0.0, 6.42)$ and $j\gamma_l = (0.0, -6.38)$. The coefficients of each of these modes extracted by Prony's method indicated that both modes were of equal importance in modeling the interior current. The modes were used as basis functions in

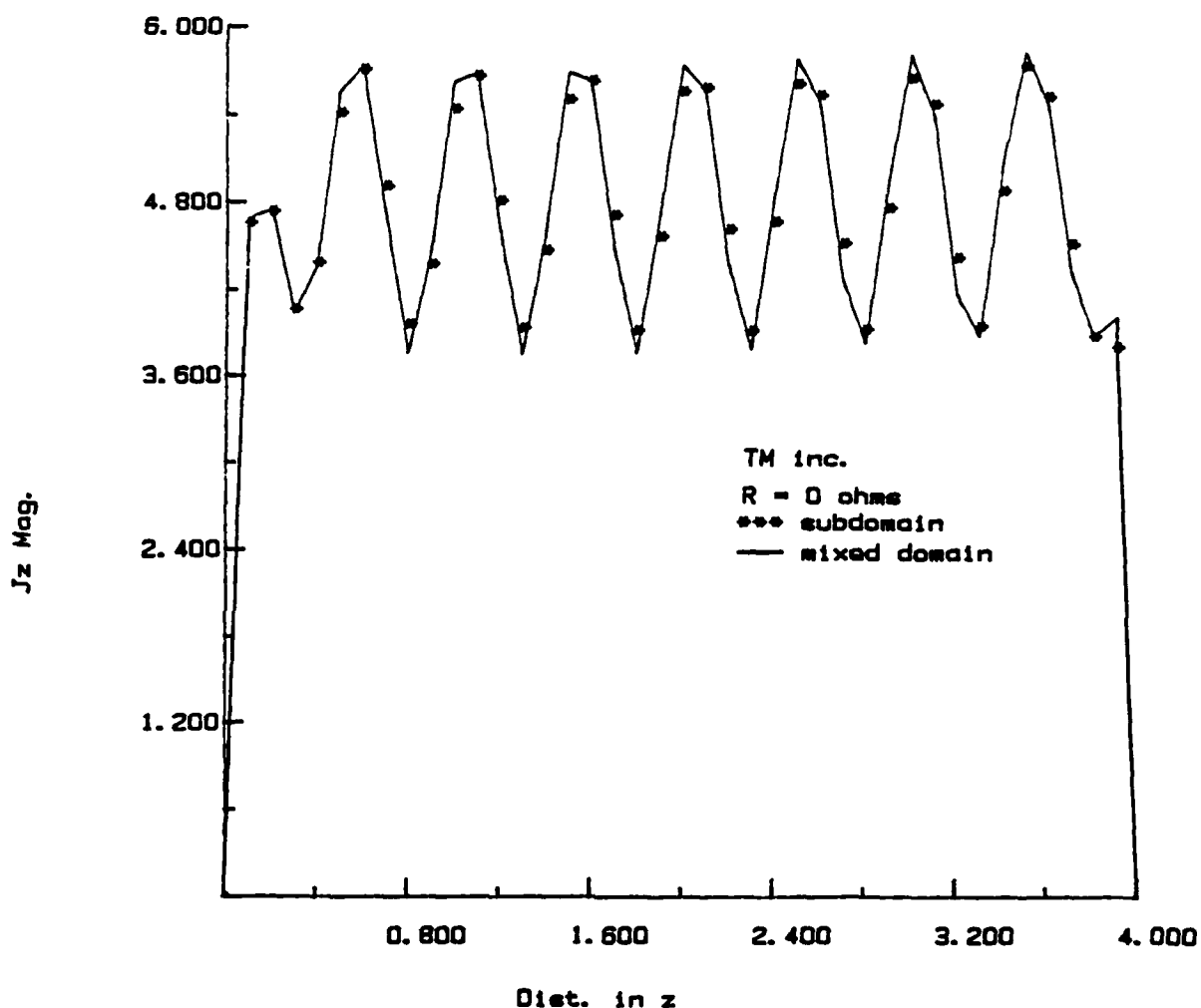


Figure 5.28 Magnitude of J_z versus z for the structure shown in Figure 4.7. The plates are connected between cells to form strips. The plates are dimensioned $ds = 0.2\lambda$, $dz = 4.0\lambda$ and $c = 0.3\lambda$. The incident wave is polarized TM to \hat{z} at angles $\theta_i = 45^\circ$, $\phi_i = 89.9^\circ$. $R = 0\ \Omega$. The current calculated using a mixture of subdomain basis functions and modal basis functions (extracted from a 2.0λ thick structure) agrees with the current calculated using all subdomain basis functions.

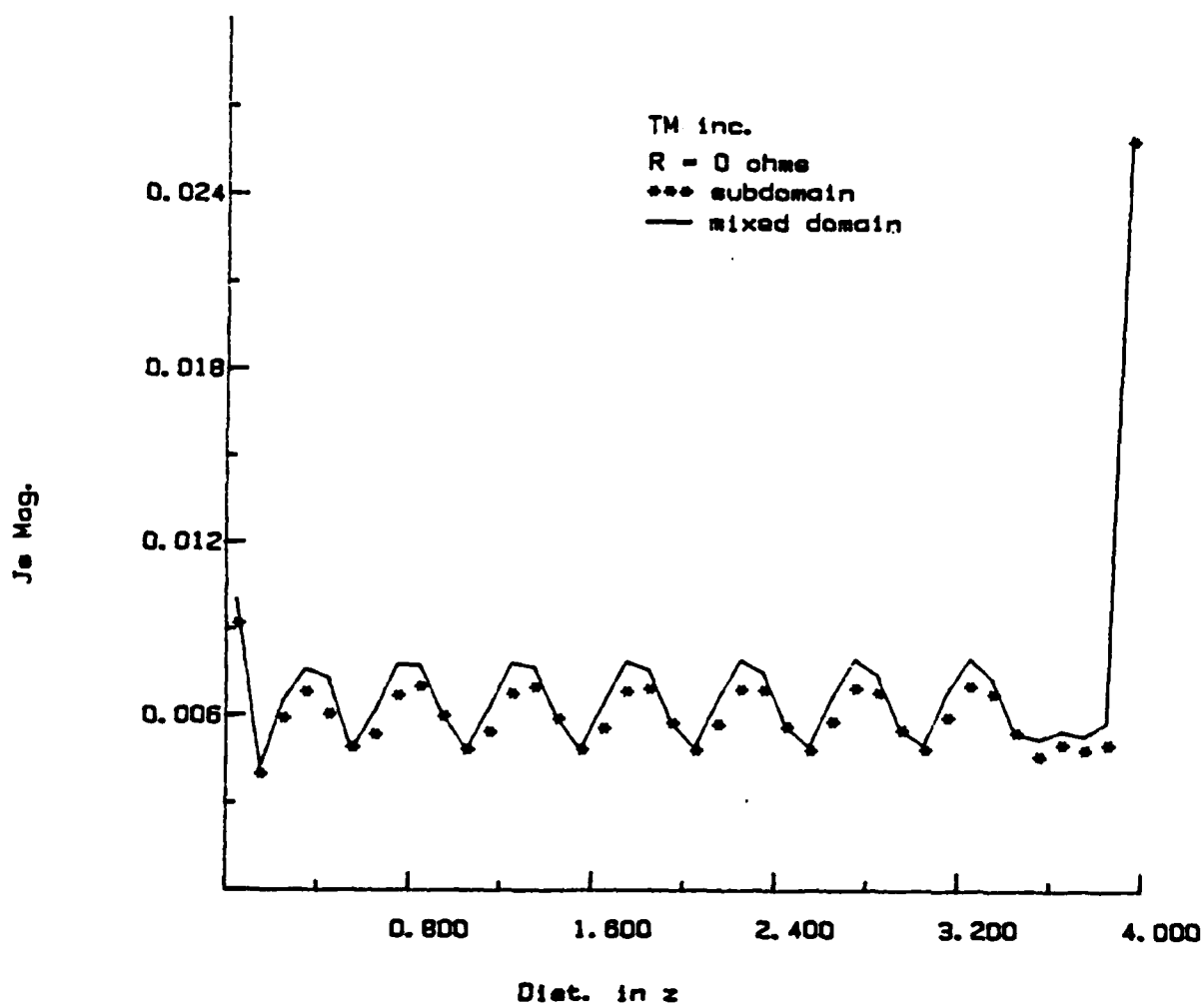


Figure 5.29 Magnitude of J_z versus z for the same situation as for Figure 5.28. The current calculated using a mixture of subdomain and modal basis functions is larger in magnitude with the current calculated using all subdomain basis functions. This error is insignificant since the major current component is in the \hat{z} direction.

the interior region ($0.5\lambda - 3.5\lambda$) of the 4.0λ thick problem. The \hat{z} directed current, shown in Figure 5.28, agrees well with the current found using the subdomain basis functions throughout the slab. The magnitude of the \hat{s} directed current, shown in Figure 5.29, is slightly greater than the magnitude of the subdomain results. This does not affect the scattered field significantly, however, because the magnitude of this current is three orders of magnitude below that of the \hat{z} current. The phase for both components, which is not shown, overlays the subdomain results.

In Figure 5.30, the magnitude of the \hat{s} directed current is plotted as a function of depth for the same lossless structure discussed in the paragraphs above. A TE polarized plane wave is incident on the structure. All of the modes in this case are below cutoff and, consequently, the current decreases exponentially within the structure. The single mode extracted from the 2.0λ thick slab by Prony's method is $j\gamma_l = (8.44, 0.0)$. This value represents an average of the values found by sampling the interior current over different lengths and at different locations because Prony's method does not accurately extract the characteristics of a rapidly decaying wave. In this case, the reflection coefficient of the thin slab could have been substituted for that of a thick slab because the current only interacts with the first 0.5λ of the structure.

Figures 5.31 and 5.32 show the \hat{z} and \hat{s} currents, respectively, plotted as a function of depth for a TM polarized wave incident on the structure discussed above. Loss ($R = 100\ \Omega$) is now added to the structure. Prony's method shows that again two modes are physically present in the structure, but due to the loss of the structure, the residue of one is an order of magnitude less than the other. This means that only one mode should be used to model the interior current. Use of two modes causes an oscillatory behavior of the current around the true value. The mode $j\gamma_l = (0.62, 6.36)$ was used to model J_s and $j\gamma_l = (0.66, 6.16)$ was used to model J_z .

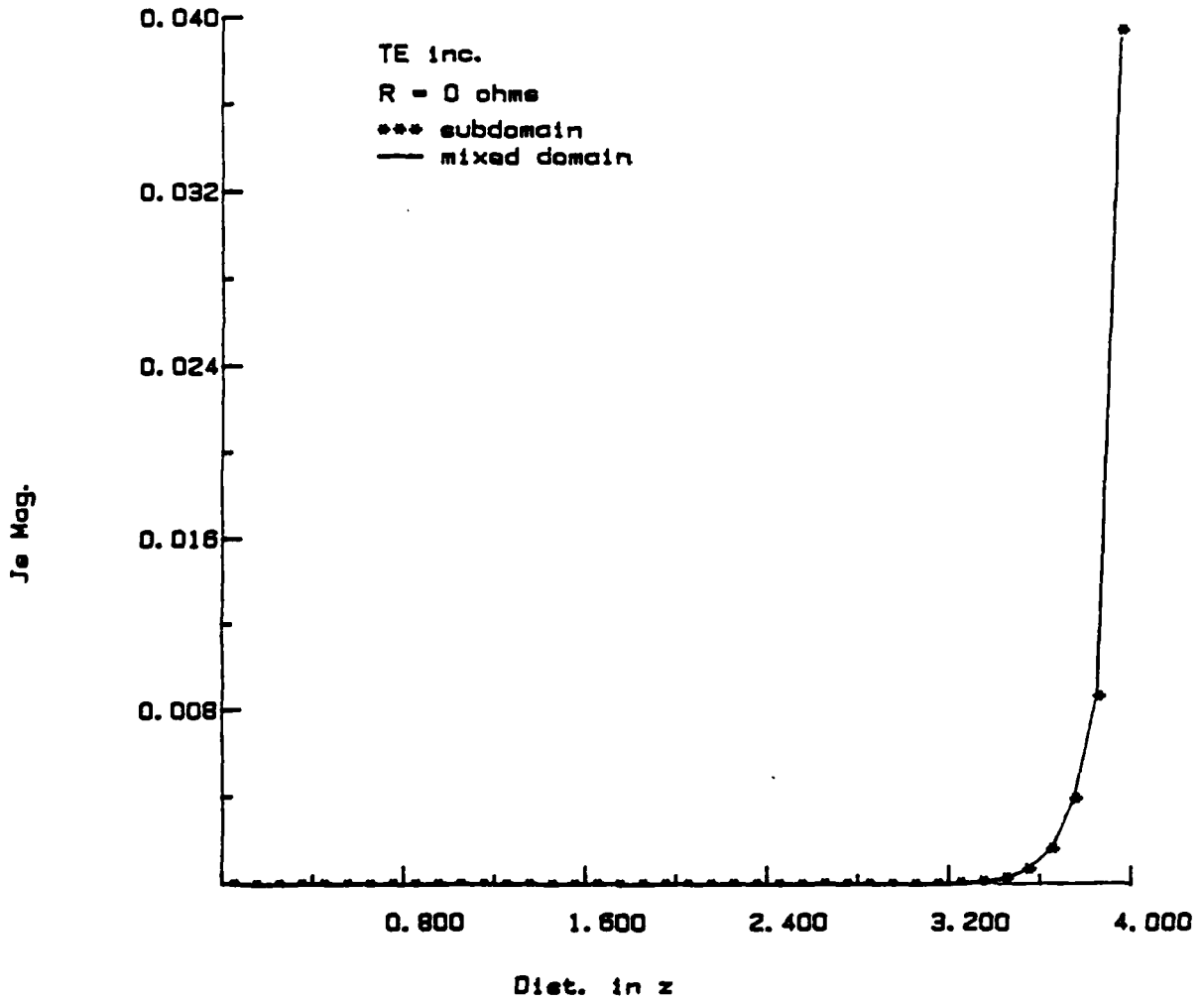


Figure 5.30 Magnitude of J_z versus z for the same geometry as for Figure 5.23. The incident field is polarized TE to \hat{z} . All modes in this structure are below cutoff so only the forward face of the slab interacts with the wave. A thin slab solution could, therefore, be used in this situation.

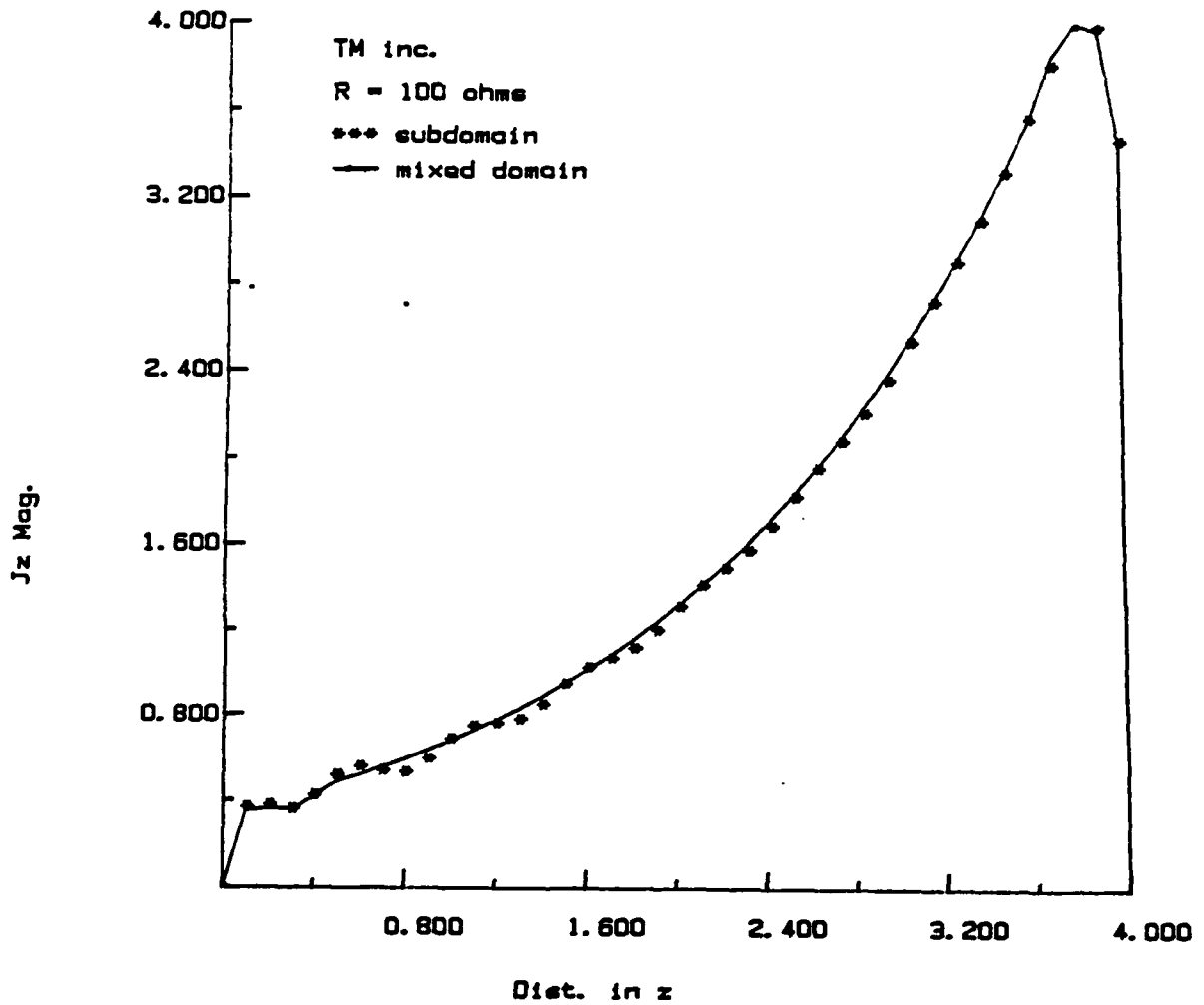


Figure 5.31 Magnitude of J_z versus z for the structure shown in Figure 4.7. The plates are connected between cells to form strips. The plates are dimensioned $ds = 0.2 \lambda$, $dz = 4.0 \lambda$ and $c = 0.3 \lambda$. The incident wave is polarized TM to \hat{z} at angles $\theta_i = 45^\circ$, $\phi_i = 89.9^\circ$. $R = 100 \Omega$. The actual current near the trailing face oscillates since the current reflects from the trailing edge and interacts with the forward traveling current. The modal basis functions do not model this.

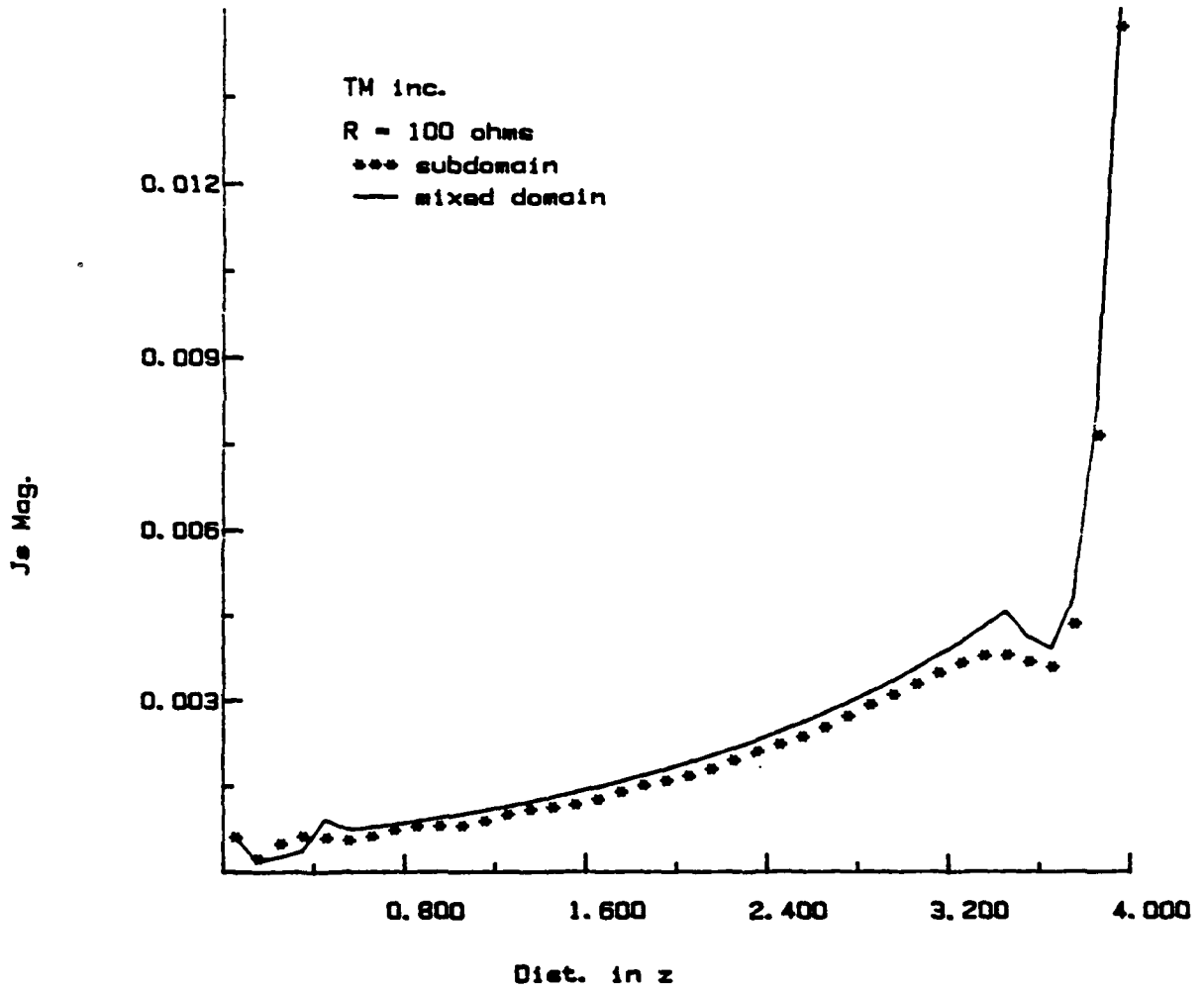


Figure 5.32 Magnitude of J_z versus z for the same situation as for Figure 5.32. The presence of peaks at around 0.5λ and 3.5λ shows that the method is having difficulty matching the currents in the transition region between the subdomain and modal regions.

Prony's method models the \hat{z} directed current well near the leading face of the slab, as shown in Figure 5.31, but since the interior current is composed of only one mode, the method cannot model the slight oscillations that occur in the region $0.5\lambda - 1.6\lambda$. These oscillations occur because the current is reflected from the back edge of the structure and interacts with the forward traveling current. This backward traveling current is absorbed by the loss in the walls as it travels. In Figure 5.32, Prony's method overestimates the current in the interior. At the points 0.5λ and 3.5λ , small peaks occur in the current because of difficulty in matching the level of the currents between the subdomain and modal regions.

The same type of current behavior is evident in the more complex zigzag structure of Figure 4.11 where $ds_1 = ds_2 = c = 0.2\lambda$ and $\theta = 60^\circ$. $R = 100\ \Omega$ and the angles of the incident wave are $\theta_i = 45^\circ$ and $\phi_i = 89.9^\circ$. Prony's method is applied to a 2.0λ thick structure and extrapolated to solve a 3.0λ thick structure. One mode is needed to model the current in the interior ($0.5\lambda - 2.5\lambda$) of the slab. Four basis functions are used to model the current variation in the \hat{s} direction. The magnitude of the current is plotted as a function of \hat{z} for the \hat{s} component of the current in Figure 5.33 and for the \hat{z} component in Figure 5.34. The worst-case results are shown. The behavior of the current is similar to the behavior in the strip case except that the two components of the current are the same order of magnitude and both components are inaccurate in the area between the subdomain and modal regions.

As shown above, Prony's method is able to extrapolate the current behavior in an arbitrarily thick structure from the solution of a thin structure. The method models a continuous structure and is straightforward to apply in concept. It has been shown that

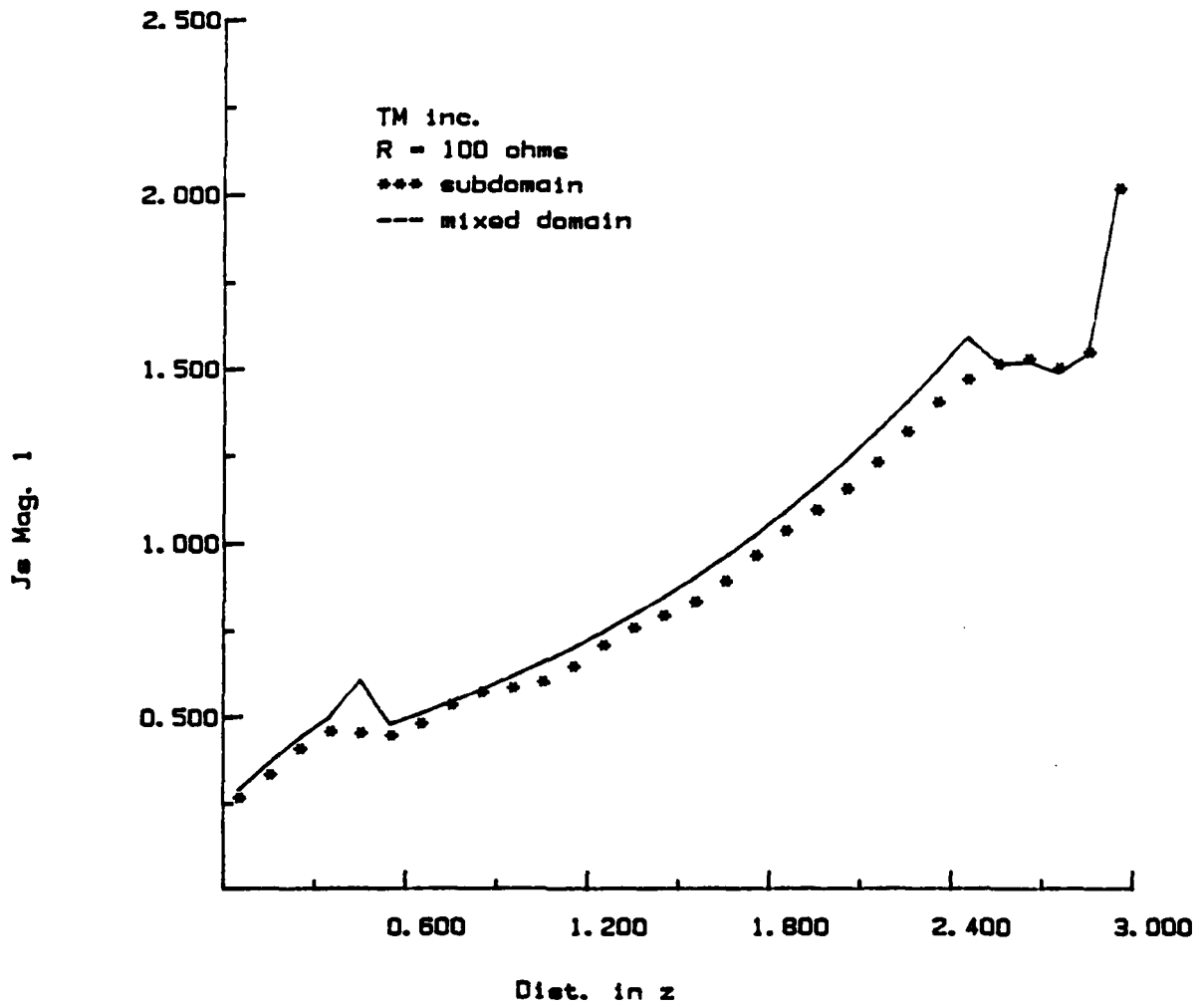


Figure 5.33 Magnitude of J_z versus z for the zigzag structure shown in Figure 4.11 when $ds_1=ds_2=c=0.2\lambda$, $\theta = 60^\circ$ and $R = 100\ \Omega$. The incident wave makes angles of $\theta_i = 45^\circ$ and $\phi_i = 89.9^\circ$. This plot is along the middle of plate one.

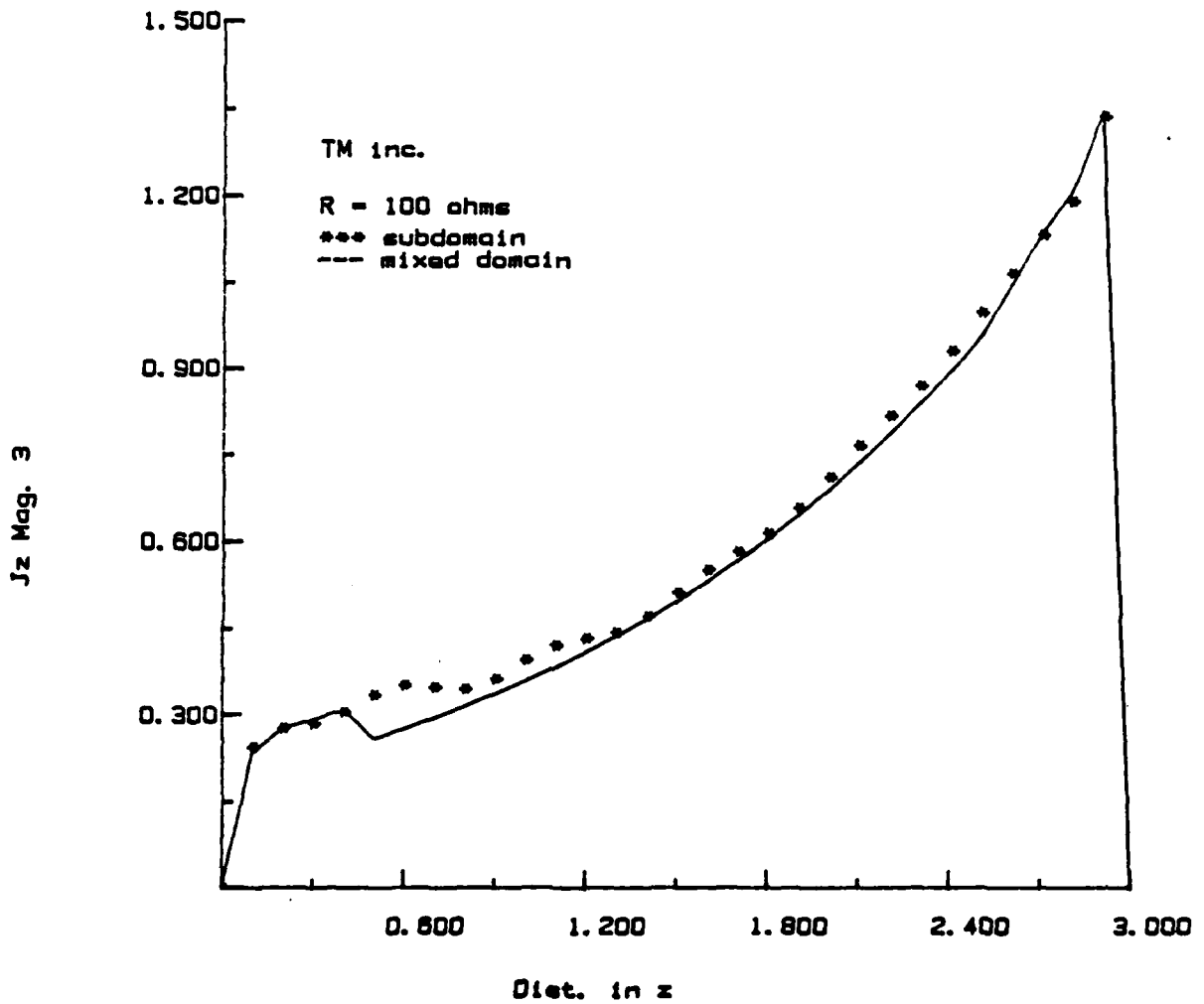


Figure 5.34 Magnitude of J_z versus z for the same situation as in Figure 5.33 except that this plot is along the middle of plate two.

the modes extracted by Prony's method are the same as those extracted by the more complex modal approach of Section 5.3. Upon finding these modes, a mode matching concept could have been applied, but it is desirable to work with a small number of modes in the interior of the problem rather than trying to find a large number of modes to mode match. Therefore, the moment method was reapplied to a thicker problem using modal basis functions to model the interior current.

The advantage of this method is that problems involving slabs of arbitrary thickness may be solved without increasing the order of the impedance matrix. The current shown in Figure 5.31, for example, required 40 mixed domain basis functions to solve. Discretizing the entire slab using subdomain basis functions required 158 functions. If the slab were increased in thickness to 10 wavelengths thick, the mixed domain discretization would still require 40 basis functions while the subdomain discretization would require 398 functions. Additionally, many of the impedance matrix calculations for the mixed domain involving the subdomain basis functions have been done when solving the initial thin-slab problem. These can be reused when solving the thick-slab problem.

The disadvantage of this method is that finding the true modes is very labor intensive. It is not easily automated and requires much intuition and physical insight on the part of the user. The second disadvantage is that using a mixture of subdomain and modal basis functions causes the impedance matrix to be no longer block Toeplitz in structure. Recall that in Chapter 4, once a portion of the impedance matrix was filled, the remainder of the impedance matrix could be filled using the calculations already performed. Therefore, the impedance matrix could be easily filled for thicker structures. The user therefore has to take this fact into consideration in calculating the tradeoff between discretizing entirely by subdomain basis functions or discretizing with a mixture

of subdomain and modal basis functions. The final disadvantage is that using subdomain functions, the geometry of the unit cell and the direction of the incident field cannot be varied without solving a new problem. With the use of large domain basis functions, the resistance distribution in the unit cell and the polarization of the incident field are also fixed.

6. CONCLUSIONS

In this thesis, a problem is investigated which is of great interest to people working in the area of RCS reduction: the problem of how a plane wave interacts with a lossy, periodic structure. The structure may be composed of thin strips repeated periodically along a one-dimensional lattice or thin plates repeated periodically along a two-dimensional lattice. A resistive boundary condition models the loss. The major difficulty of this work was in obtaining an efficient numerical solution to the problem.

Although structures with a wide variety of unit cell shapes, sizes and resistances were studied throughout the course of this thesis, the example problems should not be construed to have any relationship to actual RCS reduction problems. The parameters of these materials are sensitive pieces of information and are unknown to the general public. The purpose of this thesis is to describe phenomena associated with lossy, periodic structures and to develop techniques to solve these problems, not to solve practical problems for RCS reduction.

All periodic problems involve the calculation of a periodic Green's function, which consumes a large amount of computer time. Chapter 2 is devoted to a numerical study of how to compute the periodic Green's function efficiently by working in a combination of spectral and spatial domains. By properly selecting the weight given to each domain, the Green's function calculation may be optimized with respect to time. The codes written for the Chapter 2 study, which efficiently calculate the vector magnetic potential at a point due to a one- or two-dimensional array of current pulses, are applied to the problems in Chapters 3 and 4. Chapter 2 also discusses how the resistive boundary condition arises so the reader can make an intelligent selection of an appropriate boundary condition in future problems.

In Chapter 3, a study is conducted on how an oblique plane wave reflects from a one-dimensional array. The unit cell of the array is composed of resistive strips that are free-standing, connected to each other within the unit cell or connected between the unit cells. Oblique incidence on resistive structures causes cross-coupling between polarizations in the reflection coefficient. For example, the TE polarized reflection coefficient is dependent on a TM polarized incident wave. This situation does not occur if the structure is lossless, or if the propagation vector of the incident plane wave lies in the plane normal to the strip axis.

The cross-coupling between polarizations is minimal for oblique incidence when the following two conditions are met. First, the unit cell has to possess even symmetry with respect to a plane perpendicular to the direction of periodicity. Second, the propagation vector of the incident wave must be normal to the direction of periodicity. The cross-coupling increases to a level comparable to that of the co-coupling when either of these two conditions is violated. As resistance of the structure increases, the reflection coefficient showing the cross-coupling between TE and TM increases, while the one showing the co-coupling decreases until the resistance became larger than 500Ω , after which all the reflection coefficients decrease.

Plane-wave incidence on a structure made of unit cells repeated along a two-dimensional lattice is the subject of Chapter 4. The unit cells are made of resistive plates that are placed on edge, perpendicular to the plane of periodicity. The problems to be solved in this chapter require a large amount of computer time because of the large number of unknowns needed to discretize the problem and the difficulty in calculating each impedance matrix element.

The reflection coefficient versus frequency is plotted for unit cells made of two resistive plates which are bent with respect to each other. The plates are connected to each other and to adjacent unit cells to form a zigzag plate structure. This structure reflects power quite differently for different incident polarizations. At low frequencies, as the angle of the bend increases, the TE polarized reflection due to a TE incident field decreases, while the TM reflection due to a TM incident field increases. The cross-coupled reflection coefficient also increases with increasing bend angle. Adding resistance to the structure causes all of the reflection coefficients to decrease as the wave penetrates the structure and is dissipated. The dips and peaks in the reflection characteristics caused by the geometry of the structure flatten out with added resistance.

By adding a third plate to the zigzag plate structure, the unit cell of the honeycomb is formed. The co-coupled reflection coefficients (TE/TE and TM/TM) for a normally incident plane-wave structure overlay one another and the amount of cross-coupling is negligible. The addition of loss to the plates causes the two co-coupled responses to exhibit differences at low frequencies. This behavior is due to the difference in total resistance per unit cell "seen" by each polarization.

The straightforward solution of thick, structured slabs problems leads to large-order impedance matrices which are difficult to solve on today's computers. Chapter 5 discusses three methods which use the solution of a tractable thin slab to extrapolate the results of a thick slab. The first method, which involves cascading the generalized scattering matrices, is useful for obtaining characteristics of structures that have no current flowing continuously along the thickness dimension, i.e., structures that are composed of substructures physically separated from each other. Stability problems that arose in the past from cascading by first converting to transmission matrices are solved by cascading the scattering matrices directly.

In order to solve thick, structured slabs problems that have currents flowing in the thickness dimension, a modal solution was attempted. Modes were found in the interior of the lossy, guide structure which were matched to the Floquet harmonics outside of the structure. It was hoped that only a few modes would be sufficient in this scheme to keep the amount of calculation required to a minimum. Although the modal solution works well for the separable parallel-plate geometry, it is too costly in terms of computer time to apply to a general structure.

The first problem associated with the modal solution is that the propagation constants must be found numerically by guessing a propagation constant, filling an impedance matrix and solving for the determinant of the matrix. The propagation constant is found when the determinant is a minimum. This in itself is a lengthy process because several propagation constants have to be found, each of which involved hundreds of filling and solving sequences. Compounding the problem is that when the cell resistance is increased, the positions of the propagation constants migrate in the complex plane and the determinant minimums become shallower and harder to find. Once the propagation constants are found, the scattered fields are calculated numerically and stored in vector form. Finally, the inner products associated with the mode matching process must be calculated numerically. For the above reasons, the modal method is not a viable alternative to solve the thick, structured, slab problem.

The third method under consideration holds the most promise for solving a thick structured slab problem requiring current continuity throughout the structure. In this method, the problem of a thin slab, having the same unit cell characteristics across the slab face as the desired thick slab, is initially solved using the method of moments with

subdomain basis functions as discussed in Chapter 4. The surface current is sampled in the interior of the slab, i.e., away from the slab interfaces, where the currents have settled down to a steady-state behavior with respect to distance and the higher-order modes generated by the interaction with the interfaces are insignificant.

Prony's method is applied to the sampled current to describe the behavior of the current interior to the structure as a sum of a few complex, exponential functions. The exponential functions are used as basis functions which span the entire interior region of a thicker slab. It must be emphasized that the purpose of using Prony's method is to construct a basis function which contains the physical behavior of the interior current, not merely to construct a basis function which reproduces the interior current of the thin slab. With the physical behavior captured, the basis function may be used successfully to model the interior current of slabs of arbitrary thickness. The method of moments is then reapplied to the thicker problem using the new exponential basis functions in the interior and the previously used subdomain basis functions in the regions close to the interface. In such a scheme, slabs of arbitrary thickness may be solved without significantly increasing the number of basis functions required.

A problem associated with the third method is that the initial thin slab must be thick enough, such that the current in the slab interior is not influenced by the presence of the slab interfaces. This initial slab may require too many unknowns to be solved, especially when the unit cell has a complex geometry. The second problem is that, in addition to the desired functions, Prony's method outputs a set of functions which do not capture the physics of the interior current. These two types of functions must be separated from each another because the nonphysical basis functions will corrupt the final solution. The third problem is that the unit cell in the thick problem must be invariant in

2. The polarization and resistance as well as the incident field direction and cell geometry are fixed throughout the problem such that the current interior to the thin slab behaves in the same manner as the current interior to the thick slab. The final problem is that the introduction of the exponential basis functions caused the impedance matrix for the slab to lose its block Toeplitz structure — an attribute which was exploitable in filling and solving the matrix for the structure completely discretized by subdomain basis functions. In spite of the above problems, this method seems to be the only way at the present time to extend the solution of a thin structure to solve a thick structure.

The future work in this field consists of the following topics. The study of Chapter 2 is not complete. Although the study found the fastest way to calculate the summations in the spectral and spatial domains, what needs to be done is to balance the accuracy requirements throughout the problem solution. For example, it is useless to calculate the Green's function to four digit accuracy if the approximations on the basis function are only accurate to ten percent. When the accuracy requirements of the entire problem are taken into account, the optimum weighting of the two domains may be different than that found in Chapter 2.

A second area that could be explored is adapting these programs to one of the computers using parallel processing. The time needed to calculate the impedance matrix is the main stumbling block for these sets of problems. Since each impedance element calculation is independent of the other and consists of two independent parts, the spectral and spatial calculations, each of these parts could be assigned to a different processor in a parallel machine to speed up the overall calculation. Again, the weighting of the two domains would have to be re-examined for optimization.

This thesis examined geometries in which the axis of the unit cell was either parallel or perpendicular to the slab interface. A future geometry could have the axis of the unit cell at an angle with respect to the slab interface. The main difficulty with this problem would be in defining where the basis functions lie in space and how they are oriented. Once this is accomplished, Method 1, discussed in Section 2.3, could be applied with ease. More difficulty would be encountered in applying Methods 2 and 3 because a Fourier transform would have to be found for a current element in space which is more general in shape than those considered up to this point.

A large area of future interest, following the same trend as the FSS, is going to be the effect of truncating and curving the slab. Both of these procedures cause the structure to lose its periodicity. Also, due to manufacturing problems, the actual structure has cells that differ slightly from each other; again, periodicity is lost. A study of all of these effects could be accomplished simultaneously since the problems would require discretizing all the cells of the structure explicitly.

The final area of interest is that, in a macroscopic sense, the structured slab behaves as an anisotropic medium. How to characterize the slab as an anisotropic medium and how the wave behaves in this medium are important problems in order to bypass the numerical intensity of solving the full-wave problem. The regions of validity for these approximations must be carefully defined.

This thesis attempts to answer the basic questions concerning how an electromagnetic wave behaves in the presence of a periodic, lossy slab of material. As noted in the above paragraphs, there are many more untapped areas that remain as future research topics. It has been the author's experience that understanding the phenomena in this area of electromagnetics can be a slow and tedious process. In times of desperation, therefore, the

future researchers in this area should take heart from the words of Dr. Edgerton, inventor of stroboscopic photography, "If I knew what we'd find, I wouldn't bother to find it. People think research is like cutting wood and stacking it up....We worked and worked, didn't get anywhere. That's how you know you're doing research."

APPENDIX A. CODE VALIDATION

A.1 Introduction

Code validation — how well numerical results match the behavior of the physical world — is a subject of increasing concern in electromagnetic circles. Journal articles and entire conference sessions have been devoted to this topic since the computer is playing an ever-expanding role in electromagnetic analysis [76]-[78]. On a positive note, numerical electromagnetics has matured to such a level today that several different methods may be applied to a given problem. Unfortunately, the results of these different methods do not always agree with each other which necessitates including an error analysis with every numerical result [78].

Two themes arise whenever the subject of code validation is discussed. First, in all numerical solutions, assumptions and approximations are made in transitioning from the physical problem to a numerical model and finally to its solution. These approximations and assumptions must be explicitly put forth in the problem statement [78]. The portion of the results where the accuracy is questionable must also be pointed out. The reader will, therefore, be able to determine for himself which results are believable.

The second theme being discussed is that some validation procedure must be established which justifies the confidence placed in the code. Validation procedures fall into two categories [76]. Internal validation consists of checking the consistency within the code itself, which can include checking the satisfaction of the boundary condition, reciprocity and power conservation. External validation compares the results of the code to those of external sources such as analytical calculations, experimental results or results from other numerical solutions. Checking the code against other numerical solutions could be as simple as using different basis functions to solve the same numerical model.

or, for a more complete check, using a completely different numerical solution technique to solve the physical problem.

This appendix establishes a level of confidence in the results presented earlier in this thesis. First, the approximations and assumptions used to generate the results are consolidated and briefly presented. Second, the steps used to validate each code will be presented. Both internal and external checks are used. In this way, both areas of code validation are satisfied.

A.2 Assumptions and Approximations

The major assumption used throughout this thesis is that the resistive boundary condition correctly models the behavior of the fields on the surface of the honeycomb material. As discussed in Chapter 2, this assumption carries with it many sub-assumptions concerning the *geometry and composition of the scatterer*. For example, the surface must be a thin, electric shell and must not have kinks or sharp bends.

The surface current is approximated by a linear function along its direction of flow by using triangle or rooftop basis functions in a method of moments solution. A discretization of at least ten basis functions per wavelength is adhered to as recommended, for example, by Knott [12]. Because doubling the density of the basis functions does not change the reflection coefficient significantly in some example problems, convergence of the current is assumed. The vector potential portion of the impedance matrix element calculation further approximates the rooftop as a two-dimensional pulse and the triangle as a one-dimensional pulse. Justification for this approximation is given in Chapter 2. Numerical experimentation with the free-space Green's function also shows this to be a valid approximation. Since the operator for this class of problems is not positive or positive-definite, it is actually uncertain if convergence of the discretized problem implies

convergence of the original problem. Unfortunately, there is no other recourse but to be satisfied with numerical convergence [79].

The periodic Green's function involves a summation which is theoretically infinite. The truncation of this summation is another numerical approximation used to make the mathematical equations amenable to computer solution. The summation is truncated by observing the sum at three different truncation limits and calculating the relative error between the sum at the latest summation limit and the sum at the two preceding limits. The summing process stops when both errors fall within a given criterion set by the user—usually 0.1% to 1.0% relative error.

A similar type of truncation error is involved when cascading generalized scattering matrices. Truncating the summation in the periodic Green's function means that the information passed between basis and testing functions is contained essentially in a finite number of harmonics. Truncating the scattering matrix to a finite order means that the essential information passed between the entire structures enclosed by the terminal planes of the scattering matrix is contained in a finite number of harmonics. When the structures modeled by the scattering matrix are in each other's far field, only the propagating harmonics need be considered. As the structures are moved closer together, there is a trade-off between the accuracy of the scattering matrix model and the scattering matrix order as discussed in Chapter 5.

The modal solution of Chapter 5 involves finding the complex propagation constant of the structure by repeatedly filling an impedance matrix and solving for the determinant of that matrix while varying the value of the propagation constant. A mode is found when the value of the determinant goes to a minimum. The accuracy of finding the propagation constant is affected by all the assumptions and approximations discussed

above. Additionally, since the propagation constant is found in terms of discrete values rather than a continuous function, the value itself has a discretization error associated with it.

Once the propagation constant is found, the total field associated with this mode number is calculated. The total field is a continuous function in reality, but numerically it is a set of values found at discrete points across the unit cell. There is, therefore, a discretization error associated with the field. Finally, the modal fields across the unit cell are matched to the fields external to the structure. Theoretically, there are an infinite number of modes associated with the structure, but to allow the implementation of the procedure on the computer, only a few modes are retained. The resulting truncation error is similar in concept to truncating the number of Floquet harmonics considered in the generalized scattering matrix.

In Chapter 5, the large basis functions used to model the interior slab currents are found by applying the method of moments with subdomain basis functions. Therefore, the approximations discussed above in connection with the method of moments are also inherent in this procedure. A large approximation occurs when the modal behavior of the current interior to the slab is extracted numerically using Prony's method. The accuracy of this procedure depends on guessing the proper number of modes in the current, finding the region to sample and determining the proper sampling density. Finally, the current is rediscritized using the large, modal basis functions which depend on a very few modes accurately describing the current within the structure.

A.3 Validation

In this section, a description is given of the steps performed to validate the codes used in this thesis. The calculation of the periodic Green's function, derived in Chapter 2, is a

crucial part of all the codes. The calculation consists of two separate summations: the spectral portion and the spatial portion. The importance and number of terms in each portion are influenced by a factor (c) chosen by the user. To validate these subroutines, this factor is varied over a range of values. The spectral and spatial portions compensate each other exactly so that the final result is always the same. Only the time required to do the calculation changes since the factor determines the rate of convergence for each domain. If either of the contributors were to be in error, the final result would change as the factor changes. With this check, a major part of the subsequent codes using the periodic Green's function calculation is validated.

The strip codes of Chapter 3 are verified as follows. First, perfectly conducting strips are rotated so that they lie entirely in the plane of periodicity and fill the entire unit cell. If a component of the surface current flows perpendicularly to the strip axis, triangle basis functions are put between the cells so that there is no discontinuity in flow from cell to cell. The numerical solution of this problem is identical to the analytical solution of a plane wave incident on an infinite, perfectly conducting sheet. The surface current is the same as that calculated by physical optics $\vec{J} = 2 \hat{n} \times \vec{H}^{inc}$. The reflection coefficient is unity for the zeroth-order harmonic and insignificant for the higher-order harmonics. The transmission coefficient for all harmonics is insignificant. As loss is added to the strips, the results are identical to those for the corresponding thin, lossy dielectric plane problem. Internal validation for all strip codes is performed by a power check on the lossless structure. The propagating reflection and transmission coefficients add to equal one.

For the next strip code verification, perfectly conducting strips lie in the plane of periodicity and fill one-half of the unit cell ($a/b=0.5$). This problem can be solved

analytically using Wiener-Hopf methods [50] and compared to the solution using the code. The results for the TM reflection coefficient are shown in Figure A.1 and for the TE coefficient in Figure A.2. The exact solution and the codes used in this thesis agree with each other.

Also shown in Figures A.1 and A.2 are results for other strip-to-unit-cell size ratios ($a/b=0.25$ and $a/b=0.75$) calculated by using the method of moments with entire domain basis and testing functions as implemented by Hall [17]. In general, the results from Hall agree with results produced by the subdomain codes used in this thesis, but there are areas in which the two codes disagree. For example, the resonance dips predicted by the subdomain codes are deeper than those predicted by the entire domain codes because the subdomain basis functions have more degrees of freedom with which to model the current near resonance. The TE reflection coefficients predicted by the subdomain codes are always less than the ones predicted by the entire domain codes. Since the curve calculated by exact analysis also falls below the entire domain predicted curves, the subdomain curves can be considered more accurate.

Verification that the subdomain codes accurately model the scattering from strip structures where the strips are rotated out of the plane of periodicity is done by comparing the results to those of Hall's codes [30] which use entire domain basis functions. The comparisons have been shown previously in Chapter 3 and are mentioned here for completeness. The comparison for TM incidence on the cell geometry of Figure 3.3 shows excellent agreement between the two numerical results, as shown in Figure 3.6. The comparison for TE incidence on the lossy corrugated structure of Figure 3.4 is shown in Figure 3.7. The two results agree in form and level, but the resonance dip is shifted slightly. Because the subdomain code agrees with the exact solution for the flat case, it is taken to be more accurate in this case as well.

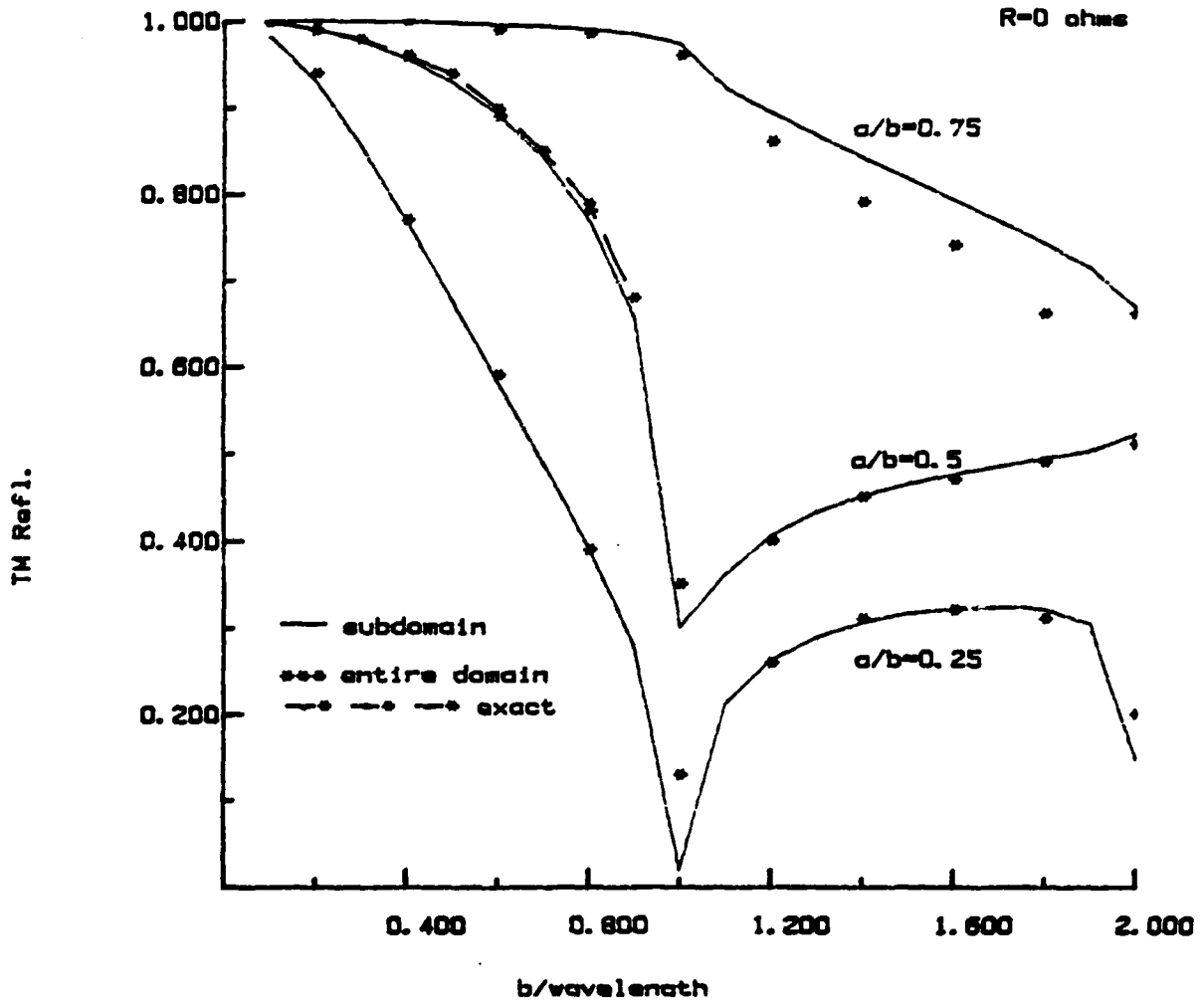


Figure A.1 TM reflection coefficient versus cell size for a lossless strip grating. The strips lie completely in the plane of periodicity and the propagation vector of the incident wave is normal to the plane of periodicity. The cell size is normalized to the incident wavelength. Curves for various ratios of strip size to unit cell size (a/b) are shown. The exact result, calculated by a Wiener-Hopf technique, is shown for $a/b=0.5$.

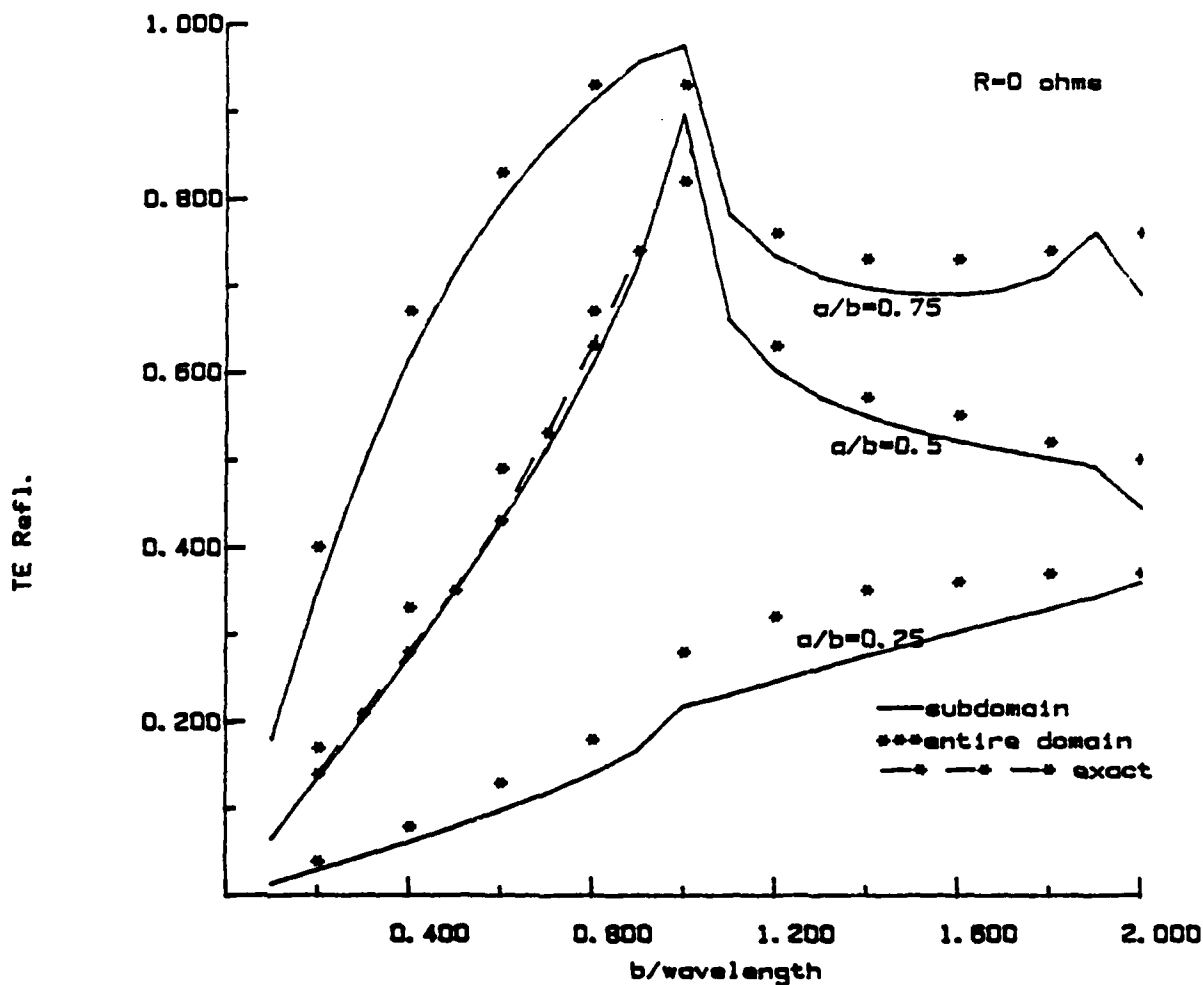


Figure A.2 TE reflection coefficient versus cell size for a lossless strip grating. The strips lie completely in the plane of periodicity and the propagation vector of the incident wave is normal to the plane of periodicity. The cell size is normalized to the incident wavelength. Curves for various ratios of strip size to unit cell size (a/b) are shown. The exact result, calculated by a Wiener-Hopf technique, is shown for $a/b=0.5$.

A final method used to validate the strip codes is to compare the results of the method of moments to the results of mode matching discussed in Chapter 5. Referring to Figure A.3, a single strip per unit cell is rotated 90° with respect to the plane of periodicity so that the structure looks like an infinite array of truncated, parallel-plate waveguides. The \vec{E} field tangent to the plane of periodicity (\hat{x} or \hat{z} direction) is found by the method of moments. A second geometry is constructed which consists of parallel-plate waveguides filling a half-space. This problem is solved by finding the modes supported by the waveguide structure and matching the waveguide modes to the Floquet harmonics in free space. The length of the truncated waveguide formed by the strips is adjusted so that the back edge of the waveguide does not affect the fields being observed. The \vec{E} field is plotted at various depths in the structure. As seen in Figure A.4 for the TM case and A.5 for the TE case, the results obtained by both methods agree. Slight differences occur for the fields at the mouth of the guide because both methods truncate the number of higher-order modes being observed. In the Figure A.5 there is a Gibbs phenomenon that occurs at the edge of the guide, particularly at the waveguide mouth.

The plate codes of Chapter 4 are checked by solving a structure having a unit cell filled with a single plate aligned along the \hat{x} axis. The plate is connected to neighboring cells in \hat{x} to form an array of strips rotated 90° out of the plane of periodicity and parallel to the \hat{x} axis. This is similar to the unit cell geometry shown in Figure A.3 except the strips are aligned with a different axis. The reflected fields calculated by the plate codes applied to this geometry are compared to those calculated by the strip codes. Figures A.6 and A.7 show the reflected TE and TM fields, respectively, for a plane wave incident at $\theta = 45^\circ$, $\phi = 89.9^\circ$ on a lossless array of parallel strips separated by 0.5 m. The

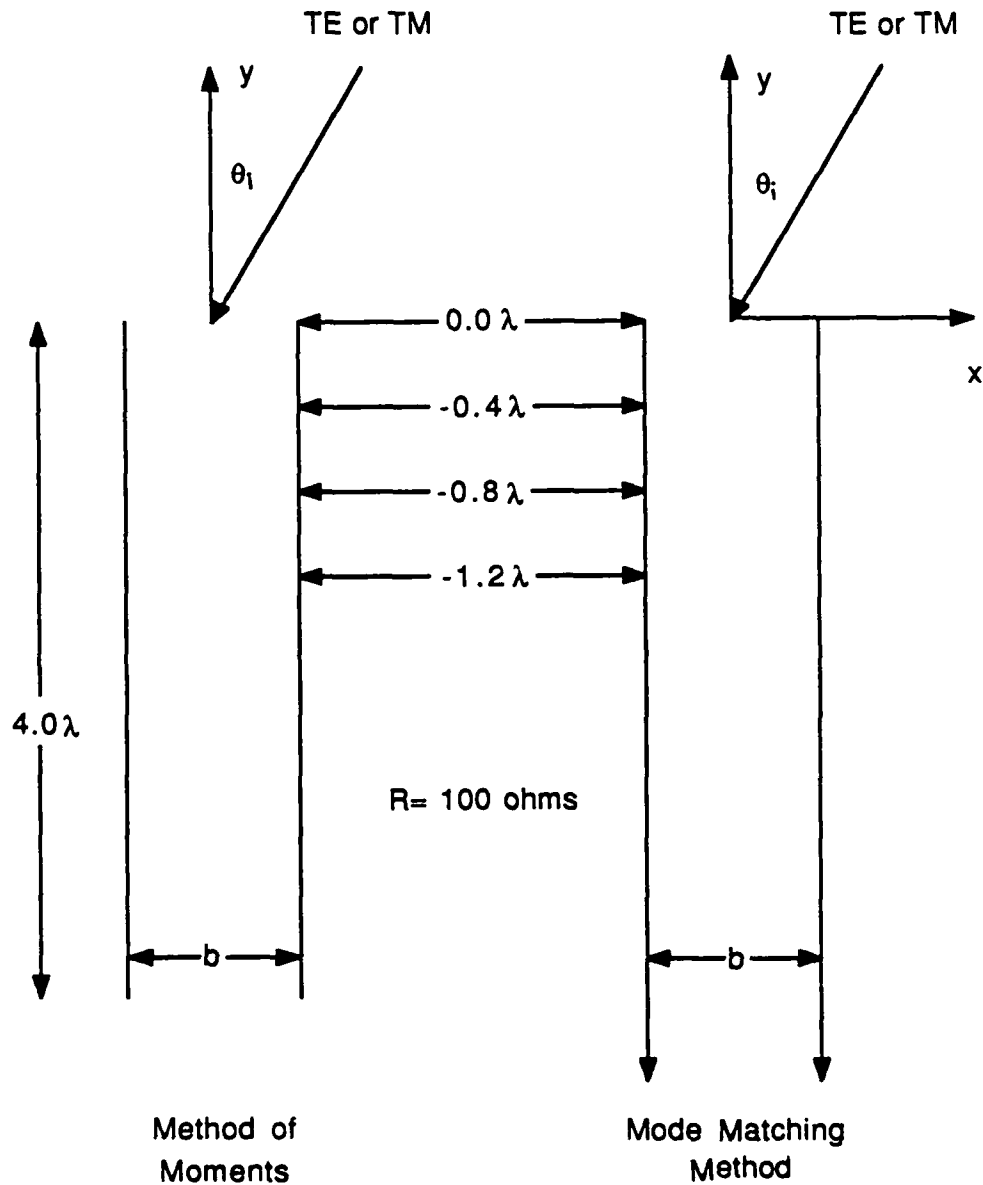


Figure A.3 The left figure shows the geometry of the unit cell for a strip array with the strips rotated 90° out of the plane of periodicity. This geometry is solved by the method of moments. The resulting slab is 4.0λ thick. The right figure shows the geometry for a parallel-plate array filling a half-space. This geometry is solved by mode matching the modes inside the waveguide to the Floquet harmonics outside the slab. The incident wave is either TE or TM to \hat{z} . The E field tangent to \hat{x} for the TE field and tangent to \hat{z} for the TM field is plotted at various depths within the structure. $R = 100 \Omega$.

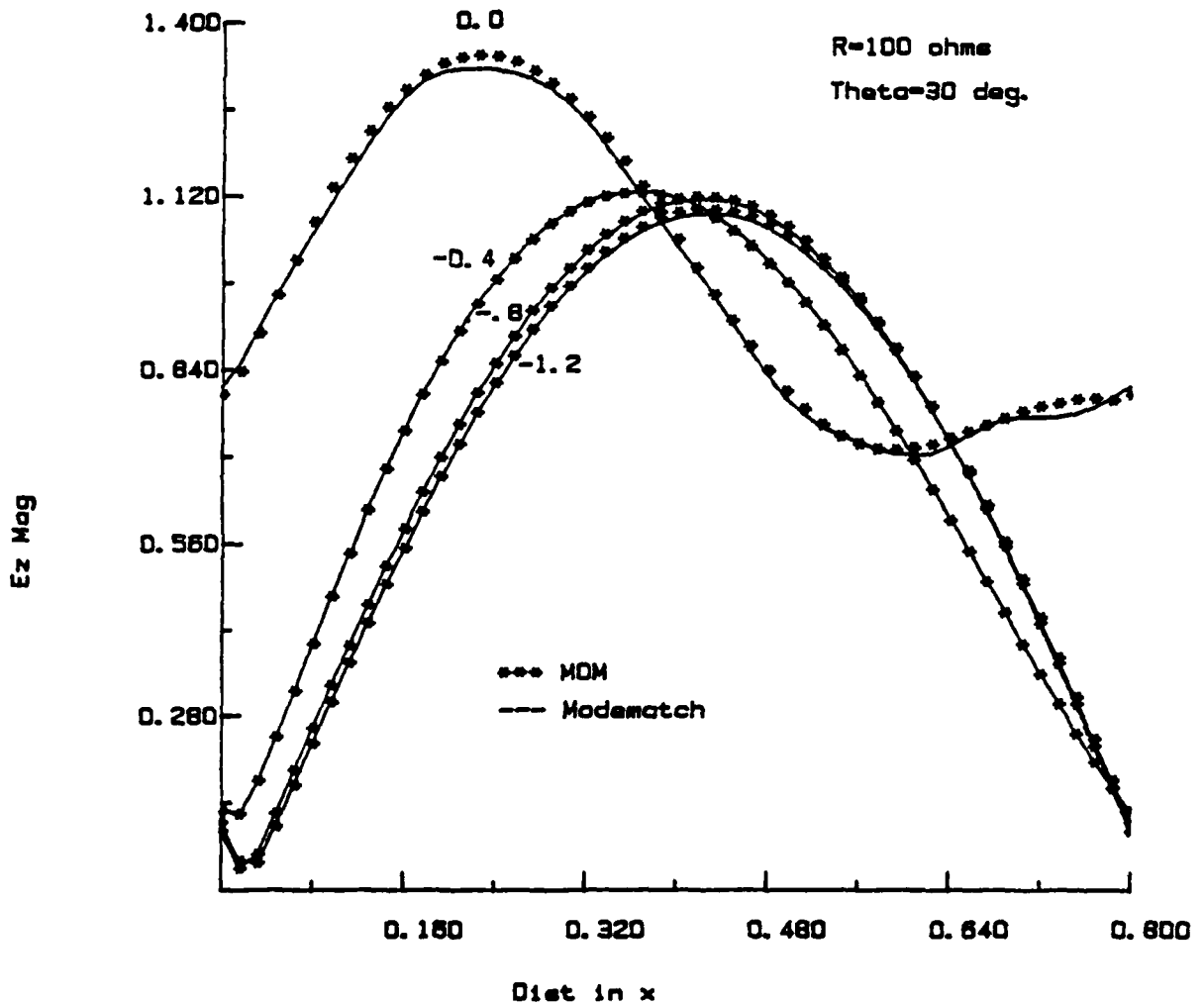


Figure A.4 Comparison of E_z plotted across the Figure A.3 unit cell as calculated by the method of moments and by mode matching. E_z is plotted at several depths into the structure. The incident wave is polarized TM to \hat{z} and makes an angle of 30° with respect to \hat{y} . The strip separation is 0.8λ and $R = 100 \Omega$.

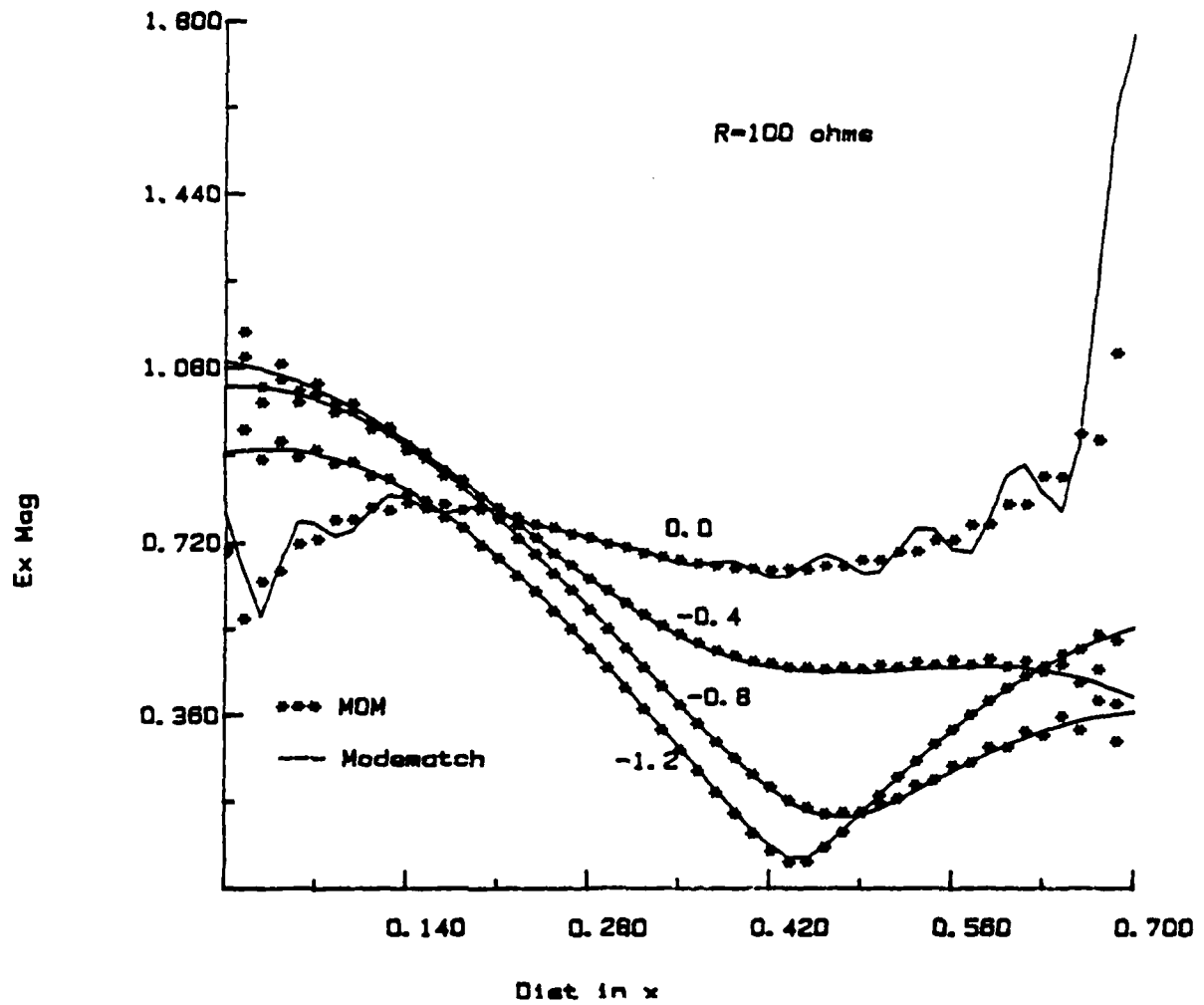


Figure A.5 Comparison of E_x plotted across the Figure A.3 unit cell as calculated by the method of moments and by mode matching. E_x is plotted at several depths into the structure. The incident wave is polarized TE to \hat{z} and makes an angle of 45° with respect to \hat{y} . The strip separation is 0.7λ and $R = 100 \Omega$.

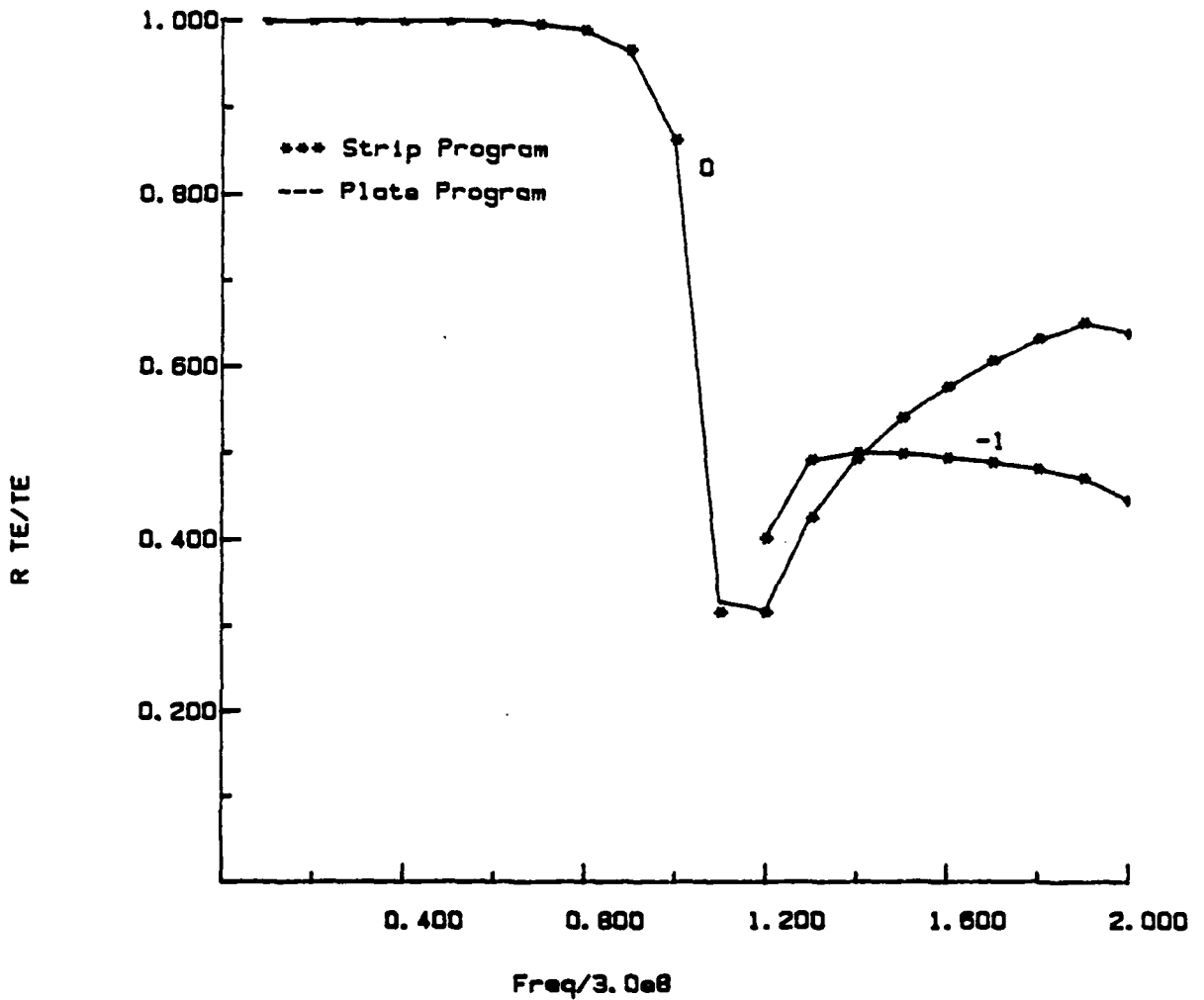


Figure A.6 Reflected TE coefficient versus frequency for an array of lossless strips rotated 90° with respect to the plane of periodicity. The strips are spaced 0.5λ apart and form a slab 0.5λ thick. $\theta_i = 45^\circ$, $\phi_i = 89.9^\circ$. The problem is solved by two methods. First, the strip code, which was verified previously, is applied. Next, the two-dimensional, plate array code is applied to a unit cell geometry consisting of a single plate attached to neighboring cells to form parallel strips.

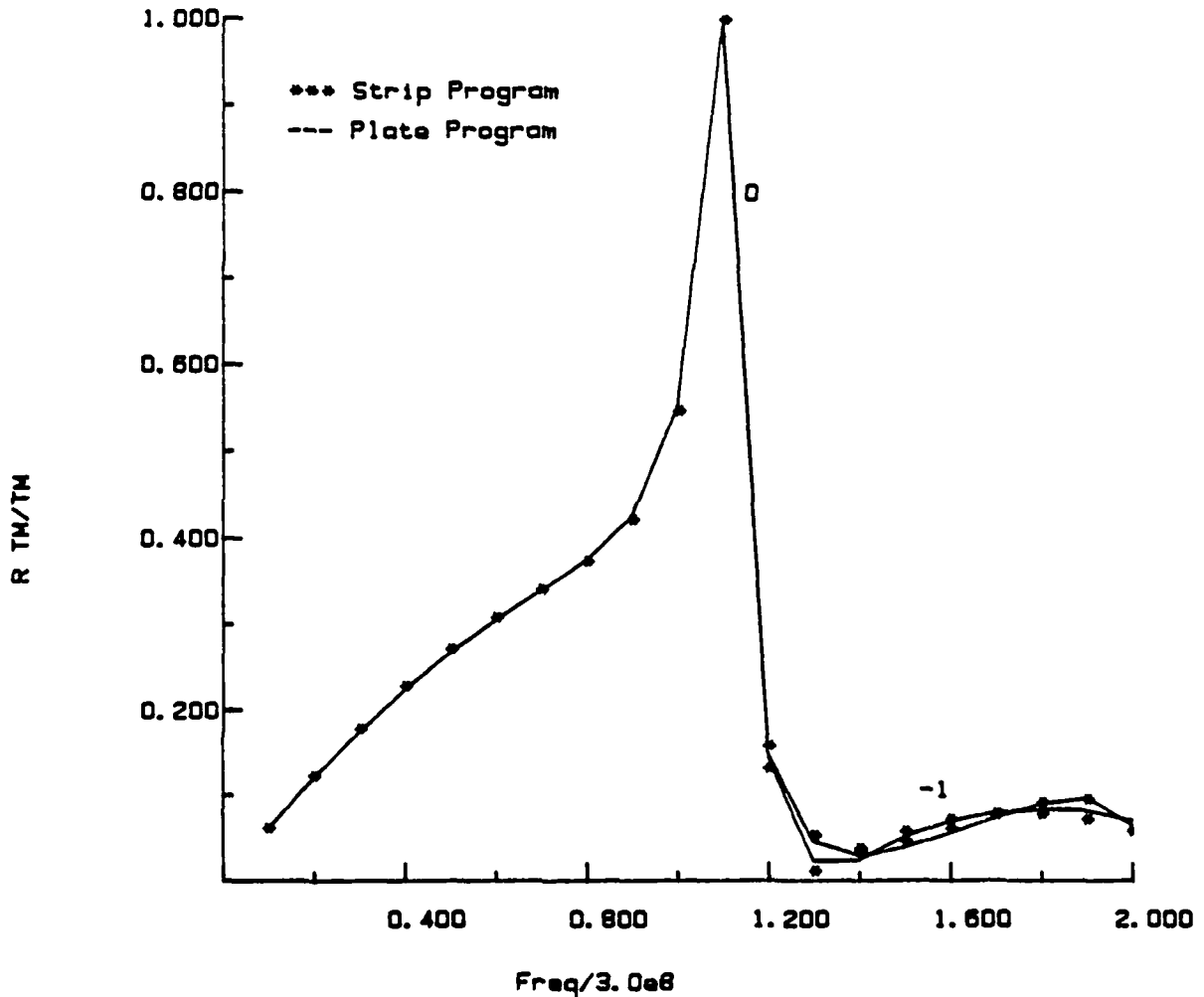


Figure A.7 Reflected TM coefficient versus frequency for an array of lossless strips rotated 90° with respect to the plane of periodicity. The strips are spaced 0.5λ apart and form a slab 0.5λ thick. $\theta_i = 45^\circ$, $\phi_i = 89.9^\circ$. The problem is solved by two methods. First, the strip code, which was verified previously, is applied. Next, the two-dimensional, plate array code is applied to a unit cell geometry consisting of a single plate attached to neighboring cells to form parallel strips.

resultant slab is 0.5 m thick. Figure A.8 shows that the addition of loss does not affect the agreement between the two codes. A power check was also successfully performed for the plate geometries.

Three different codes were written to cascade the generalized scattering matrices for three different types of geometries. The first type of geometry is composed of strips with an incident wave lying in the plane normal to the strip axes. These geometries require a single set of numbers to describe the Floquet harmonics and no coupling exists between the TE and TM polarizations. The second type of geometry is composed of strips with an obliquely incident plane wave. These geometries require a single set of numbers to describe the Floquet harmonics and coupling does exist between polarizations. Finally, geometries composed of a two-dimensional array of plates need two sets of numbers to describe the Floquet harmonics and coupling exists between the two polarizations.

To ensure that the codes cascading the generalized scattering matrix are operating correctly, the following procedure is used. First, two or more separate slabs of strip or plate arrays are solved using the method of moments to discretize the entire problem. The reflection coefficients of the propagating harmonics found using this method are compared to the coefficients found by cascading the scattering matrix of a single slab. To be more specific, first a single slab is discretized and solved by the method of moments. A generalized scattering matrix is found for the single slab and cascaded to find the reflection coefficients of the overall structure. The reflection coefficients found by the two methods approach each other as the order of the generalized scattering matrix is increased. A typical result, plotted in Figure A.9, shows the percent of relative error between the reflection coefficient found by the two methods discussed above applied to ten slabs of a lossless, parallel-strip structure. Each slab has a unit cell made of a single strip, 0.4

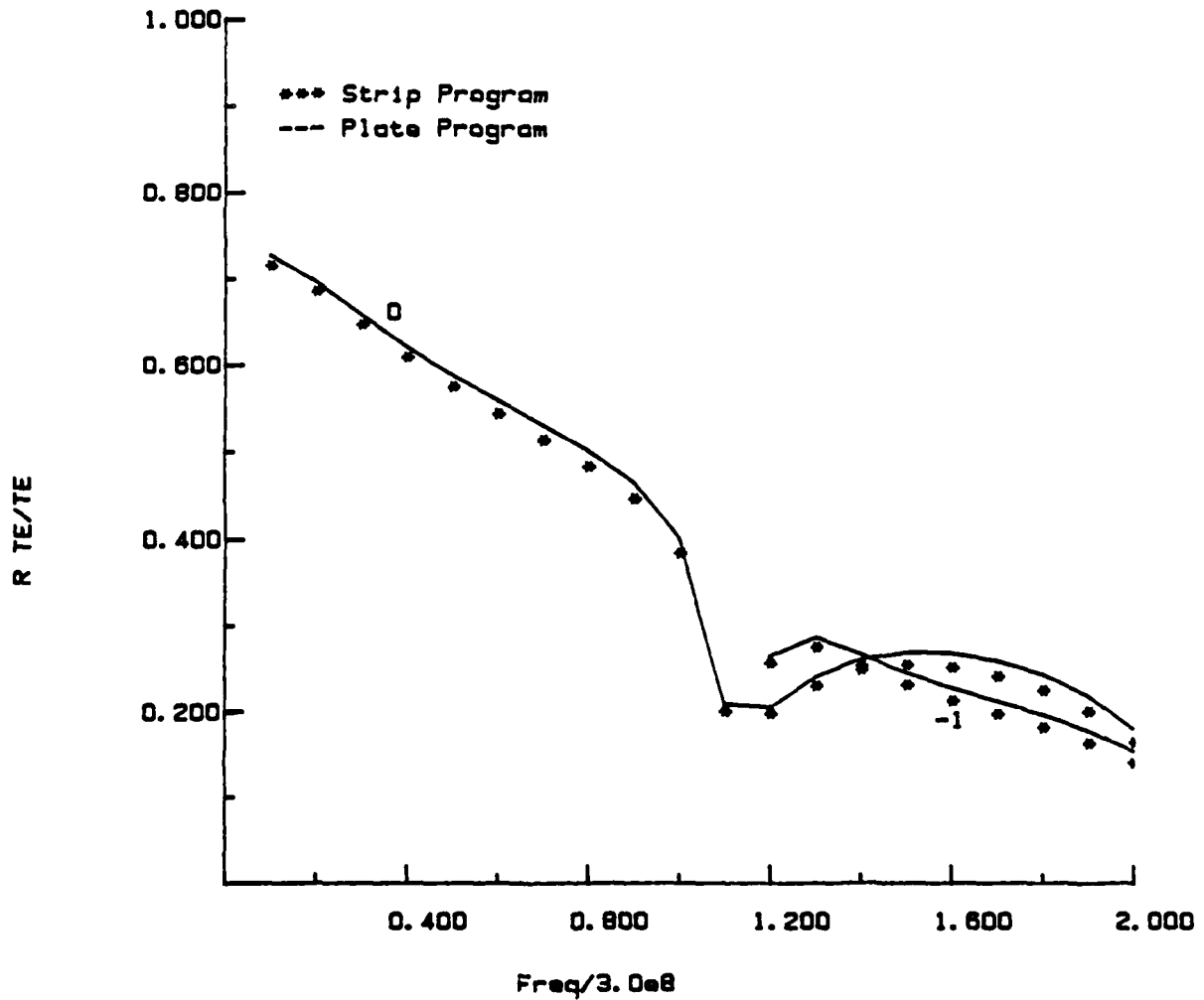


Figure A.8 Reflected TE coefficient versus frequency for an array of lossy strips rotated 90° with respect to the plane of periodicity. The strips are spaced 0.5λ apart and form a slab 0.5λ thick. $\theta_i = 45^\circ$, $\phi_i = 89.9^\circ$ and $R = 100 \Omega$. The problem is solved by two methods. First, the strip code, which was verified previously, is applied. Next, the two-dimensional, plate array code is applied to a unit cell geometry consisting of a single plate attached to neighboring cells to form parallel strips.

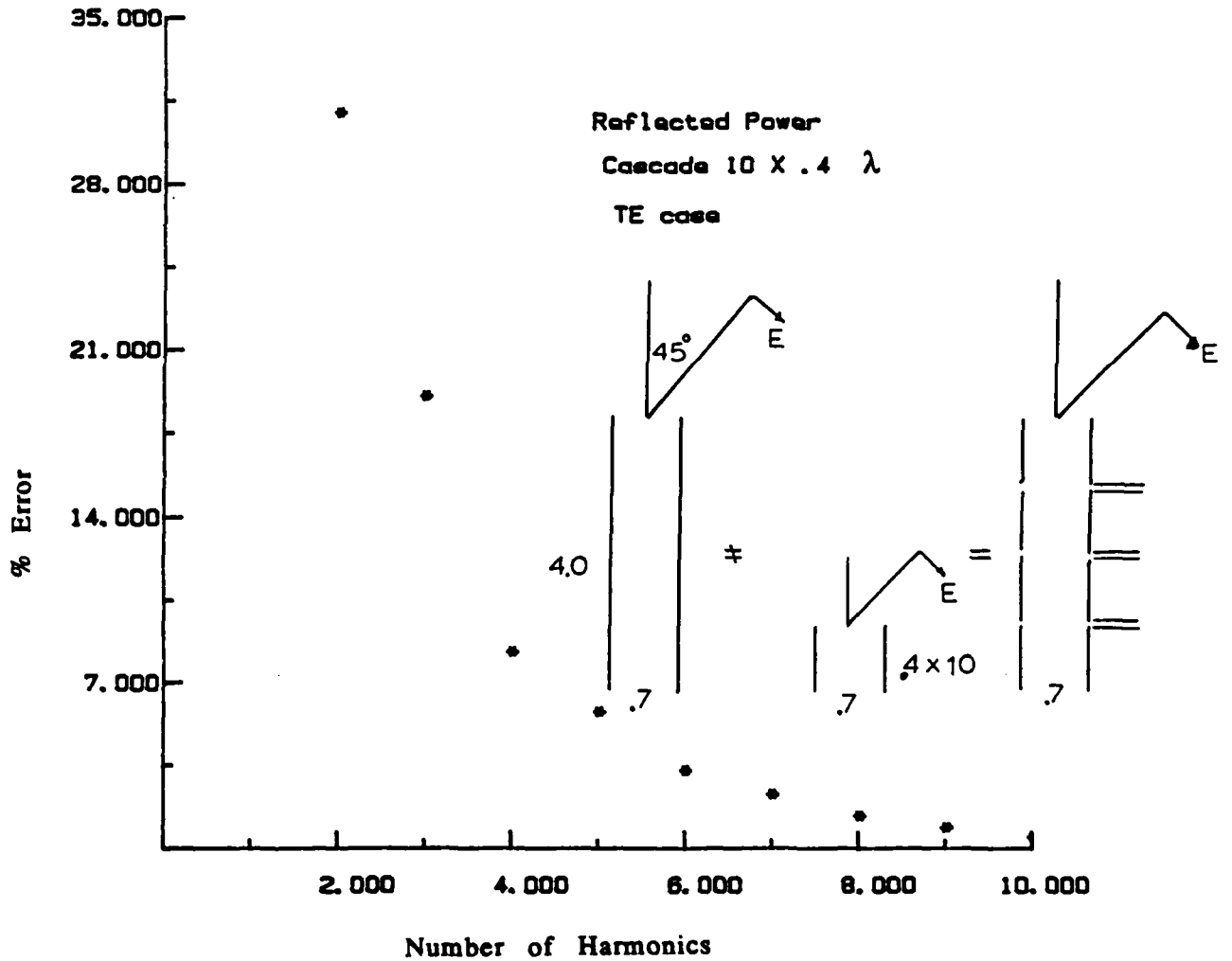


Figure A.9 Relative error between the reflected TE coefficient calculated by the method of moments applied to ten slabs of a strip array and the coefficient calculated by the method of moments applied to one slab and cascaded ten times. The error is plotted versus number of harmonics retained in the S matrix. The cascaded reflection coefficient converges to the reflection coefficient for the separated slab problem (above right), not to the coefficient for the continuous slab (above left). The reason for this is discussed in Chapter 5.

wavelength long and rotated 90° out of the plane of periodicity, like the structure of Figure A.3. The first method solves all ten slabs at one time, while the second method solves a single slab and cascades the generalized scattering matrix for the single slab, ten times. As the number of harmonics retained in the scattering matrix increases, the error between the two solution methods decreases.

The modal solution, discussed in Chapter 5, is verified in the following ways. The parallel strip case is verified by comparing the \vec{E} fields found by mode matching to those of the method of moments solution as discussed in the above paragraphs relating to Figures A.3-A.5. The propagation constant found using the modal method is compared in the lossless case to the propagation constant found analytically for a single parallel-plate waveguide. The solution to the one-dimensional waveguide array is verified by comparing the propagation constant found for the lossless case to the propagation constant calculated analytically for the single, lossless, rectangular waveguide. The routines used to fill the impedance matrix are the same as those used to fill the impedance matrix of the lossy, strip array with oblique incidence, which have been verified previously.

The codes using entire basis functions in the slab interior are verified by comparing the propagation constant found by Prony's method applied to parallel strips to the propagation constant found by applying the modal method. The stretching procedure, discussed in Chapter 5, is confirmed by the following method. First, a thick slab is solved by a straightforward application of the method of moments using subdomain basis functions. Next, the solution of a thin slab is used to construct large basis functions which physically model the current in the slab interior. Finally, the original thick problem is resolved using the constructed basis functions in the slab interior and

subdomain basis functions near the slab interface. The surface currents and fields due to these currents found by the two methods are compared. The current component perpendicular to the \vec{E} field is not modeled very well using the large basis functions. There are not enough degrees of freedom in these basis functions to correctly model the coupling between the dominant and minor component of current. The addition of loss to the structure, however, mitigates this problem.

REFERENCES

- [1] V. Lougheed, *Vehicles of the Air*. Chicago: Reilly and Britton Co., 1909, pp. 372-381.
- [2] E. M. Lenoë, "Comments on the status of composite structures technology," in *Fibrous Composites in Structural Design*, Proceedings of a conference on fibrous composites in structural design held in San Diego, CA, Nov. 14-17, 1978. New York: Plenum Press, 1980, pp. 1-6.
- [3] T. Tryckare, *The Lore of Flight*. Gothenburg, Sweden: Cagner and Co., 1970, p. 92.
- [4] Technical Publication, *Hexcel Honeycomb*, Hexcel Corp. Dublin, CA., 1983.
- [5] L. F. Vosteen, "Composite aircraft structures," *Fibrous Composites in Structural Design*, Proceedings of a conference on fibrous composites in structural design held in San Diego, CA, Nov. 14-17, 1978. New York: Plenum Press, 1980, pp. 7-24.
- [6] C. E. Covington and P. S. Baumgardner, "Design and production of fiberglass helicopter rotor blades," *Fibrous Composites in Structural Design*, Proceedings of a conference on fibrous composites in structural design held in San Diego, CA, Nov. 14-17, 1978. New York: Plenum Press, 1980, pp. 497-513.
- [7] Hughes Aircraft Co., "Measured effects of dielectric honeycomb support on FSS," Hughes report no. 856629-3, 1985.
- [8] V. Volpe and R. Carri, "Effects of lightning and nuclear electromagnetic pulse on an advanced composites aircraft," *Fibrous Composites in Structural Design*. Proceedings of a conference on fibrous composites in structural design held in San Diego, CA, Nov. 14-17, 1978. New York: Plenum Press, 1980, pp. 341-357.
- [9] F. L. Pitts, B. D. Fisher, and V. Mazur, "Lightning jolts aircraft," *IEEE Spectrum*, vol. 25, no. 7, pp. 34-38, July 1988.
- [10] B. Sweetman, *Stealth Aircraft*. Osceola, WI: Motorbooks International, 1986.
- [11] J. A. Adam, "How to design an invisible aircraft," *IEEE Spectrum*, vol. 25, no. 4, pp. 26-31, April 1988.
- [12] E. F. Knott, J. F. Shaeffer, and M. T. Tuley, *Radar Cross Section*. Norwood, MA: Artech House, Inc., 1985.
- [13] A. Hessel and A. A. Oliner, "A new theory of Wood's anomalies on optical gratings," *Appl. Opt.*, vol. 4, no. 10, pp. 1275-1297, Oct. 1965.
- [14] J. T. Mayhan and L. L. Tsai, "Reflection and transmission characteristics of thin periodic interfaces," *IEEE Trans. Antennas Propagat.*, vol. AP-24, no. 4, pp. 449-456, July 1976.

- [15] L. L. Tsai, T. K. Wu, and J. T. Mayhan, "Scattering by multi-layered lossy periodic strips with application to artificial dielectrics," *IEEE Trans. Antennas Propagat.*, vol. AP-26, no. 2, pp. 257-260, March 1978.
- [16] T. K. Wu, "Analysis and applications of multilayered periodic strips," *AEU*, vol. 33, no. 4, pp. 144-148, April 1979.
- [17] R. C. Hall and R. Mittra, "Scattering from a periodic array of resistive strips," *IEEE Trans. Antennas Propagat.*, vol. AP-33, no. 9, pp. 1009-1011, Sept. 1985.
- [18] B. J. Rubin and H. L. Bertoni, "Scattering from a periodic array of conducting bars of finite surface resistance," *Radio Sci.*, vol. 20, no. 4, pp. 827-832, July-Aug. 1985.
- [19] C. C. Chen, "Transmission through a conducting screen perforated periodically with apertures," *IEEE Trans. Microwave Theory Tech.*, vol. MTT-18, no. 9, pp. 627-632, Sept. 1970.
- [20] J. P. Montgomery, "Scattering by an infinite periodic array of thin conductors on a dielectric sheet," *IEEE Trans. Antennas Propagat.*, vol. AP-23, no. 1, pp. 70-75, Jan. 1975.
- [21] C. H. Tsao and R. Mittra, "Spectral-domain analysis of frequency selective surfaces comprised of periodic arrays of crossed dipoles and Jerusalem crosses," *IEEE Trans. Antennas Propagat.*, vol. AP-32, no. 5, pp. 478-486, May 1984.
- [22] B. J. Rubin and H. L. Bertoni, "Reflection from a periodically perforated plane using a subsectional current approximation," *IEEE Trans. Antennas Propagat.*, vol. AP-31, no. 6, pp. 829-836, Nov. 1983.
- [23] B. J. Rubin, "The propagation characteristics of signal lines in a mesh-plane environment," *IEEE Trans. Microwave Theory Tech.*, vol. MTT-32, no. 5, pp. 522-531, May 1984.
- [24] B. J. Rubin, "Scattering from a periodic array of apertures or plates where the conductors have arbitrary shape, thickness and resistivity," *IEEE Trans. Antennas Propagat.*, vol. AP-34, no. 11, pp. 1356-1365, Nov. 1986.
- [25] R. F. Harrington and J. R. Mautz, "An impedance sheet approximation for thin dielectric shells," *IEEE Trans. Antennas Propagat.*, vol. AP-23, no. 4, pp. 531-534, July 1975.
- [26] T. B. A. Senior, "Impedance boundary conditions for imperfectly conducting surfaces," *Appl. Sci. Res.*, vol. 8, Sec. B, pp. 419-436, 1961.
- [27] K. M. Mitzner, "An integral equation approach to scattering from a body of finite conductivity," *Radio Sci.*, vol. 2, no. 12, pp. 1459-1470, Dec. 1967.

- [28] K. M. Mitzner, "Effective boundary conditions for reflection and transmission by an absorbing shell of arbitrary shape," *IEEE Trans. Antennas Propagat.*, vol. AP-16, no. 6, pp. 706-712, Nov. 1968.
- [29] T. A. Senior, "Backscattering from resistive strips," *IEEE Trans. Antennas Propagat.*, vol. AP-27, no. 6, pp. 808-813, Nov. 1979.
- [30] R. C. Hall, R. Mittra, and K. M. Mitzner, "Scattering from finite thickness resistive strip gratings," *IEEE Trans. Antennas Propagat.*, vol. AP-36, no. 4, pp. 504-510, April 1988.
- [31] R. Mittra and S. W. Lee, *Analytical Techniques in the Theory of Guided Waves*. New York: MacMillan, 1971, pp. 207-217.
- [32] R. C. Hall, R. Mittra, and K. M. Mitzner, "Analysis of multilayered periodic structures using generalized scattering matrix theory," *IEEE Trans. Antennas Propagat.*, vol. AP-36, no. 4, pp. 511-517, April 1988.
- [33] T. A. Cwik and R. Mittra, "The cascade connection of planar periodic surfaces and lossy dielectric layers to form an arbitrary periodic screen," *IEEE Trans. Antennas Propagat.*, vol. AP-35, no. 12, pp. 1397-1405, Dec. 1987.
- [34] N. Amitay and V. Galindo, "The analysis of circular waveguide phased arrays," *The Bell Syst. Tech. J.*, vol. 47, no. 9, pp. 1903-1932, Nov. 1968.
- [35] V. Galindo and C. P. Wu, "Numerical solutions for an infinite phased array of rectangular waveguides with thick walls," *IEEE Trans. Antennas Propagat.*, vol. AP-16, no. 2, pp. 149-158, March 1966.
- [36] N. Amitay, C. P. Wu, and V. Galindo, "Methods of phased array analysis," in *Phased Array Antennas*, A. A. Oliner and G. H. Knittel, Eds. Norwood, MA: Artech House Inc., 1972.
- [37] L. R. Lewis and A. Hessel, "Propagation characteristics of periodic arrays of dielectric slabs," *IEEE Trans. Microwave Theory Tech.*, vol. MTT-19, no. 3, pp. 276-286, March 1971.
- [38] R. E. Collin, *Field Theory of Guided Waves*. New York: McGraw-Hill Co., 1960.
- [39] R. W. Lampe, "A method of moments solution of stripline discontinuity problems," Ph.D. dissertation, University of Illinois, Urbana, IL, 1984.
- [40] R. Lampe, P. Klock, and P. Mayes, "Integral transforms useful for the accelerated summation of periodic, free-space Green's functions," *IEEE Trans. Microwave Theory Tech.*, vol. MTT-33, no. 8, pp. 734-736, August 1985.
- [41] S. M. Wright, "Efficient analysis of infinite microstrip arrays on electrically thick substrates," Ph.D. dissertation, University of Illinois, Urbana, IL, 1984.

- [42] W. F. Richards, K. McInturff, and P. S. Simon, "An efficient technique for computing the potential Green's functions for a thin, periodically excited parallel-plate waveguide bounded by electric and magnetic walls," *IEEE Trans. Microwave Theory Tech.*, vol. MTT-35, no. 3, pp. 276-281, March 1987.
- [43] N. G. Alexopoulos and I. E. Rana, "Mutual impedance computation between printed dipoles," *IEEE Trans. Antennas Propagat.*, vol. AP-29, no. 1, pp. 106-111, Jan. 1981.
- [44] R. Gabel and R. Roberts, *Signals and Linear Systems*. New York: Wiley and Sons, 1973.
- [45] C. Kittel, *Introduction to Solid State Physics*. New York: Wiley and Sons, 1976.
- [46] R. F. Harrington, *Time-Harmonic Electromagnetic Fields*. New York: McGraw-Hill, 1961.
- [47] A. W. Glisson and D. R. Wilton, "Simple and efficient numerical methods for problems of electromagnetic radiation and scattering from surfaces," *IEEE Trans. Antennas Propagat.*, vol. AP-28, no. 5, pp. 593-603, Sept. 1980.
- [48] L. N. Medgyesi-Mitschang and P. L. Huddleston, "Stochastic impedance boundary condition method," in *1988 URSI Radio Science Meeting Program and Abstracts*, Syracuse, NY, p. 453, June 6-10, 1988.
- [49] D. Wang and P. L. Huddleston, "Radiation from large coated bodies," in *1988 URSI Radio Science Meeting Program and Abstracts*, Syracuse, NY, p. 373, June 6-10, 1988.
- [50] L. A. Weinstein, *The theory of diffraction and the factorization method*. Boulder, CO: The Golem Press, 1969, pp. 267-290.
- [51] W. H. Kent and S. W. Lee, "Diffraction by an infinite array of parallel strips," *J. Math. Phys.*, vol. 13, pp. 1926-1930, 1972.
- [52] J. P. Montgomery, "Scattering by an infinite array of multiple parallel strips," *IEEE Trans. Antennas Propagat.*, vol. AP-27, pp. 798-807, Nov. 1979.
- [53] R. F. Harrington, *Field Computation by Moment Methods*. New York: Krieger, 1983.
- [54] M. G. Andreasen, "Scattering from cylinders with arbitrary surface impedance," *Proc. IEEE*, vol. 53, no. 8, pp. 812-817, Aug. 1965.
- [55] S. Ramo, J. R. Whinnery and T. Van Duzer, *Fields and Waves in Communication Electronics*. New York: Wiley, 1965.
- [56] R. Mittra, R. C. Hall and C. H. Tsao, "Spectral-domain analysis of circular patch frequency selective surfaces," *IEEE Trans. Antennas Propagat.*, vol. AP-32, no. 5, pp. 533-536, May 1984.

- [57] T. A. Cwik and R. Mittra, "Scattering from a periodic array of free-standing arbitrarily shaped conducting or resistive patches," *IEEE Trans. Antennas Propagat.*, vol. AP-35, no. 11, pp. 1226-1234, Nov. 1988.
- [58] C. H. Chan and R. Mittra, "On the analysis of frequency selective surfaces using subdomain basis functions," submitted to *IEEE Trans. Antennas Propagat.*
- [59] N. Marcuvitz, *Waveguide Handbook*. London: Peter Peregrinus Ltd., 1986.
- [60] D. M. Sarzonov, A. Gridin, and B. A. Mishustin, *Microwave Circuits*. Moscow: Mir, 1982.
- [61] R. C. Hall and F. E. Gardiol, "Formulation of the eigenvalue problem for an infinite medium of planar resistive sheets," *1988 IEEE AP-S International Symposium Digest*, vol. II, pp. 1126-1129, June 15-19, 1987.
- [62] R. Beckett and J. Hurt, *Numerical Calculations and Algorithms*. New York: McGraw-Hill, 1967.
- [63] B. E. Spielman and R. F. Harrington, "Waveguides of arbitrary cross section by solution of a nonlinear integral eigenvalue equation," *IEEE Trans. Microwave Theory Tech.*, vol. MTT-20, no. 9, pp. 578-585, Sept. 1972.
- [64] L. Weiss and R. N. McDonough, "Prony's method, z-transforms, and Pade approximation," *SIAM Rev.*, vol. 5, no. 2, pp. 145-149, April 1963.
- [65] R. N. McDonough and W. H. Huggins, "Best least-squares representation of signals by exponentials," *IEEE Trans. Automat. Contr.*, vol. AC-13, no. 4, pp. 408-412, Aug. 1968.
- [66] T. Y. Young and W. H. Huggins, "On the representation of electro-cardiograms," *IEEE Trans. Bio-Med. Electron.*, vol. BME-10, no. 3, pp. 86-95, July 1963.
- [67] M. L. Van Blaricum, "Techniques for extracting the complex resonances of a system directly from its transient response," Ph.D. dissertation, University of Illinois, Urbana, IL, 1976.
- [68] A. J. Poggio, M. L. Van Blaricum, E. K. Miller, and R. Mittra, "Evaluation of a processing technique for transient data," *IEEE Trans. Antennas Propagat.*, vol. AP-26, no. 1, pp. 165-173, Jan. 1978.
- [69] M. L. Van Blaricum and R. Mittra, "Problems and solutions associated with Prony's method for processing transient data," *IEEE Trans. Antennas Propagat.*, vol. AP-26, no. 1, pp. 174-182, Jan. 1978.
- [70] M. P. Hurst and R. Mittra, "Scattering center analysis via Prony's method," *IEEE Trans. Antennas Propagat.*, vol. AP-35, no. 8, pp. 986-988, Aug. 1987.

- [71] R. Mittra and K. E. Jones, "Resolution of multimode data in periodic structures and waveguides," *IEEE Trans. Antennas Propagat.*, vol. AP-13, no. 2, p. 325, March 1965.
- [72] R. E. Jorgenson, L. Epp, R. Mittra and K. M. Mitzner, "A technique for solving the problem of scattering by thick periodic structures," *Abstracts of the 1988 URSI National Radio Science Meeting*, Syracuse, NY, p. 140, June 1988.
- [73] L. Epp, private discussions.
- [74] J. M. Bornholdt and L. N. Medgyesi-Mitschang, "Mixed-domain Galerkin expansions in scattering problems," *IEEE Trans. Antennas Propagat.*, vol. AP-36, no. 2, pp. 216-227, Feb. 1988.
- [75] A. H. Chang, "Numerical methods for solving the problem of electromagnetic scattering from large bodies," Ph.D. dissertation, University of Illinois, Urbana, IL, 1988.
- [76] E. K. Miller, "Development of EM modeling software performance standards," in *1988 IEEE AP-S International Symposium Digest*, vol. III, pp. 1340-1343, June 6-10, 1988.
- [77] E. K. Miller, "Electromagnetic modeling software committee," *IEEE Antennas and Propagation Society Newsletter*, vol. 30, no. 4, pp. 36-38, Aug. 1988.
- [78] L. B. Felsen, "Benchmarks: an option for quality assessment," in *1988 IEEE AP-S International Symposium Digest*, vol. III, pp. 1344-1346, June 6-10, 1988.
- [79] D. G. Dudley, "Error minimization and convergence in numerical methods," *Electromagnetics*, vol. 5, pp. 89-97, 1985.